Development of a cell centred upwind finite volume algorithm for a new conservation law formulation in structural dynamics.

Lee, Chun Hean

Swansea University
Prifysgol Abertawe

Development of a Cell Centred Upwind Finite Volume Algorithm for a New Conservation Law Formulation in Structural Dynamics

by

Chun Hean Lee

Submitted to the College of Engineering
in partial fulfillment of the requirements for the degree of

Doctor of Philosophy

at

Swansea University

February 5, 2012

ProQuest LLC.
789 East Eisenhower Parkway
P.O. Box 1346
Ann Arbor, MI 48106 – 1346

DECLARATION

This work has not previously been accepted in substance for any degree and is not being concurrently submitted in candidature for any degree.

Signed ..... (candidate)
Date ..... 8/3/12 .....

STATEMENT 1

This thesis is the result of my own investigations, except where otherwise stated. When correction services have been used, the extent and nature of the correction is clearly marked in a footnote(s).
Other sources are acknowledged by footnotes giving explicit references. A bibliography is appended.

Signed ..... (candidate)
Date ..... 8/3/12 .....

STATEMENT 2

I hereby give consent for my thesis, if accepted, to be available for photocopying and for inter-library loan, and for the title and summary to be made available to outside organisations.

Signed ..... (candidate)
Date ..... 8/3/12 .....

Acknowledgements

I would like to express my profound gratitude to my main supervisor, Dr. Antonio J. Gil, who has guided me all along the course of the program with great enthusiasm and patience. I would also like to thank Prof. Javier Bonet, my co-supervisor, for consistently providing me technical guidance throughout the research. I am indebted to them for introducing me to the world of numerical modelling. They were very approachable and showed great personal dedication to the work. I could not have done it without them.

I am gratefully acknowledge the financial support received from Overseas Research Students Awards Scheme (ORSAS), which allowed me to concentrate thoroughly towards the completion of this research.

Special thanks go to my girlfriend Lee Ling for her continuous support and making me believe in my success. Many thanks to all my friends in Swansea, specially to Karim Abd. Izian, Miquel, Dhruba, Shankha, Mota, Kenny and Andy.

Last but not least, I would like to thank my parents (Kem San and Chai Hong) for their blessings and active support all through my academic career. Without their sacrifices and initiatives, it would have been extremely hard for me to avail such a great opportunity of learning and experience. I am grateful to all my sisters (Sei Neay, Say Yen, Eng Tee and Eng Hwei) who have been really concerned and helpful over the past few years. This work is completely dedicated to them.

To Neay, Yen, Tee, Hwei, Ling and my parents
for all their love and understanding

Abstract

Over the past few decades, dynamic solid mechanics has become a major field of interest in industrial applications involving crash simulation, impact problems, forging and many others to be named. These problems are typically nonlinear due to large deformations (or geometrical nonlinearity) and nonlinear constitutive relations (or material nonlinearity). For this reason, computer simulations for such problems are of practical importance. In these simulations, the Lagrangian formulation is typically used as it automatically satisfies the mass conservation law. Explicit numerical methods are considered to be efficient in these cases.

Most of the numerical methods employed for such simulations are developed from the equation of motion (or momentum balance principle). The use of low-order elements in these numerical methods often exhibits the detrimental locking phenomena in the analysis of nearly incompressible applications, which produces an undesirable effect leading to inaccurate results. Situations of this type are usual in the solid dynamics analysis for rubber materials and metal forming processes. In metal plasticity, the plastic deformation is isochoric (or volume-preserving) whereas, the compressible part is due only to elastic deformation.

Recently, a new mixed formulation has been established for explicit Lagrangian transient solid dynamics. This formulation, involving linear momentum, deformation gradient and total energy, results in first order hyperbolic system of equations. Such conservation-law formulation enables stresses to converge at the same rate as velocities and displacements. In addition, it ensures that low order elements can be used without volumetric locking and/or bending difficulty for nearly incompressible applications.

The new mixed formulation itself shows a clear advantage over the classical displacement-based formulation, due to its simplicity in incorporating state-of-the-art shock capturing techniques. In this research, a curl-preserving cell centred finite volume computational methodology is presented for solving the first order hyperbolic system of conservation laws on quadrilateral cartesian grids. First, by assuming that the approximation to the unknown variables is constant within each cell. This will lead to discontinuities at cell edges which will motivate the use of a Riemann solver by introducing an upwind bias into the evaluation of the numerical flux function. Unfortunately, the accuracy is severely undermined by an excess of numerical dissipation. In order to alleviate this, it is vital to introduce a linear reconstruction procedure for enhancing the accuracy of the scheme. However the second-order spa-

tial method does not prohibit spurious oscillation in the vicinity of sharp gradients. To circumvent this, a nonlinear slope limiter will then be introduced.

It is now possible to evolve the semi-discrete evolutionary system of ordinary equations in time with the aid of the family of explicit Total Variation Diminishing Runge Kutta (TVD-RK) time marching schemes. Moreover, a correction procedure involving minimisation algorithm for conservation of the total angular momentum is presented. To this end, a number of interesting examples will be examined in order to demonstrate the robustness and general capabilities of the proposed approach.

"You can know the name of a bird in all the languages of the world, but when you're finished, you'll know absolutely nothing whatever about the bird. So let's look at the bird and see what it's doing – that's what counts. I learned very early the difference between knowing the name of something and knowing something".

Richard Feynman (1918 – 1988)

Contents

List of Figures

List of Tables

Nomenclature

$\boldsymbol{F}, F_{iI}$	Deformation gradient tensor, $F_{iI} = \partial x_i / \partial X_I$
$\bar{\boldsymbol{F}}, \bar{F}_{iI}$	Modified deformation gradient tensor, $\bar{F}_{iI} = (\bar{J}/J)^{1/3} F_{iI}$
J	Jacobian, $J = \det(\partial x_i / \partial X_I)$
$\bar{J}$	Dilatational parameter, $\bar{J} = \int_V J dV / \int_V dV$
$\boldsymbol{H}, H_{iI}$	Displacement gradient tensor, $H_{iI} = \partial u_i / \partial X_I$
$\tilde{\boldsymbol{H}}, \tilde{H}_{iI}$	Enhanced displacement gradient tensor
$\boldsymbol{u}$	Displacement field, $\boldsymbol{u} = \boldsymbol{x} - \boldsymbol{X}$
$\boldsymbol{X}, X_I$	Material or Lagrangian coordinates
$\boldsymbol{x}, x_i$	Spatial or Eulerian coordinates
V	Material or reference volume
v	Spatial or current volume
$\boldsymbol{p}, p_i$	Linear momentum per unit of undeformed volume, $p_i = \rho_0 v_i$
$\boldsymbol{v}, v_i$	Velocity field
ρ_0	Material density
E_T	Total energy
$\boldsymbol{b}, b_i$	Body force per unit mass
$\boldsymbol{t}, t_i$	Surface traction vector, $t_i = P_{iI} N_I$
$\boldsymbol{P}, P_{iI}$	First Piola-Kirchhoff stress tensor
$\boldsymbol{\sigma}, \sigma_{ij}$	Cauchy or engineering stress tensor
$\boldsymbol{N}, N_I$	Material outward-pointing unit normal vector
$\boldsymbol{n}, n_i$	Spatial outward-pointing unit normal vector
$\boldsymbol{\nabla}_0$	Gradient operator in undeformed space, $[\nabla_0]_I \equiv \partial / \partial X_I$
$\boldsymbol{\nabla}_{\boldsymbol{x}}$	Gradient operator in deformed space, $[\nabla_{\boldsymbol{x}}]_i \equiv \partial / \partial x_i$
$\boldsymbol{I}, \delta_{ij}$	Second-order identity tensor, $I_{ij} = \delta_{ij}$
$\boldsymbol{\mathcal{I}}, \mathcal{I}_{ijkl}$	Fourth-order identity tensor, $\mathcal{I}_{ijkl} = \delta_{ik}\delta_{jl}$
$\hat{\boldsymbol{\mathcal{I}}}, \hat{\mathcal{I}}_{ijkl}$	Transposition fourth-order tensor, $\hat{\mathcal{I}}_{ijkl} = \delta_{il}\delta_{jk}$
ψ	Helmholtz free energy function, $\psi = e - \theta\eta$
e	Internal energy
η	Entropy
θ	Temperature
D_{int}	Internal dissipation rate
I, II, III	First, second and third invariants
$\boldsymbol{C}, C_{IJ}$	Right Cauchy-Green deformation tensor, $C_{IJ} = F_{iI} F_{iJ}$
$\boldsymbol{b}, b_{ij}$	Left Cauchy-Green deformation tensor, $b_{ij} = F_{iI} F_{jI}$

p	Pressure
μ	Shear modulus
κ	Bulk modulus
λ	Lamé constant
E	Young's modulus
ν	Poisson's ratio
$\boldsymbol{E}, E_{IJ}$	Green-Lagrange strain tensor, $E_{IJ} = (C_{IJ} - \delta_{IJ})/2$
$\boldsymbol{e}, e_{ij}$	Eulerian strain tensor, $e_{ij} = (\delta_{ij} - b_{ij}^{-1})/2$
$\boldsymbol{\varepsilon}, \varepsilon_{ij}$	True or engineering strain tensor, $\varepsilon_{ij} = 1/2(\partial u_i/\partial x_j + \partial u_j/\partial x_i)$
$\boldsymbol{\mathcal{U}}$	Vector of unknown variable
$\boldsymbol{\mathcal{F}}_I$	Vector of conservative flux
$\boldsymbol{S}$	Vector of source term
$\boldsymbol{\mathcal{A}}_N$	Flux Jacobian matrix, $\boldsymbol{\mathcal{A}}_N = \boldsymbol{\mathcal{A}}_I N_I = (\partial \boldsymbol{\mathcal{F}}_I / \partial \boldsymbol{\mathcal{U}})\, N_I$
$\boldsymbol{\mathcal{F}}_N$	Interface flux, $\boldsymbol{\mathcal{F}}_N = \boldsymbol{\mathcal{F}}_I N_I$
$\boldsymbol{\mathcal{C}}, \mathcal{C}_{iIjJ}$	Material fourth-order constitutive tensor, $\mathcal{C}_{iIjJ} = \partial P_{iI}/\partial F_{jJ}$
$\boldsymbol{\mathcal{R}}, \boldsymbol{\mathcal{L}}$	Right and left eigenvectors
$\boldsymbol{U}, \boldsymbol{V}$	Right and left stretch tensors
$\boldsymbol{\mathcal{W}}$	Characteristic variable, $\boldsymbol{\mathcal{W}} = \boldsymbol{\mathcal{R}}^{-1}\boldsymbol{\mathcal{U}}$
U_p, U_s	Volumetric and shear waves
$\boldsymbol{Q}, Q_i$	Heat flow vector
$\lambda_{e,\alpha}$	Elastic principle stretches
$\tau_{\alpha\alpha}$	Principal component of Kirchhoff stress tensor, $\tau_{\alpha\alpha} = J\sigma_{\alpha\alpha}$
f	Yield function of elasto-plastic constitutive model
H	Hardening modulus
$\bar{\varepsilon}_p$	Hardening variable
τ_y^0	Initial yield stress
$\boldsymbol{b}_e$	Elastic left Cauchy-Green deformation tensor
$\boldsymbol{C}_p$	Plastic right Cauchy-Green deformation tensor
$\boldsymbol{G}_e$	Gradient operator or slope vector at cell e
ϕ_e	Slope limiter scalar value
$\boldsymbol{R}$	Residual vector
α_{CFL}	Courant-Friedrichs-Lewy number
h_{min}	Minimum grid size
$\boldsymbol{A}$	Total angular momentum of a system, $\boldsymbol{A} = \int_V \boldsymbol{x} \times \boldsymbol{p}\, dV$
$\boldsymbol{L}$	Linear momentum of a system, $\boldsymbol{L} = \int_V \boldsymbol{p}\, dV$
$\hat{N}_a$	Standard shape function
$\boldsymbol{M}_{ab}^C, [M_{ab}^C]_{ij}$	Consistent mass matrix, $[M_{ab}^C]_{ij} = (\int_V \rho_0 \hat{N}_a \hat{N}_b dV)\delta_{ij}$
$\boldsymbol{M}_a^L, [M_a^L]_{ij}$	Lumped mass matrix, $[M_a^L]_{ij} = (\int_V \rho_0 \hat{N}_a dV)\delta_{ij}$
$\boldsymbol{K}_{\mathscr{C},ab}$	Material or constitutive stiffness matrix
$\boldsymbol{K}_{\sigma,ab}$	Initial stress or geometric stiffness matrix
$\boldsymbol{K}_{\kappa,ab}$	Dilatational stiffness matrix

Part I

Preliminaries

Chapter 1

Introduction

"There is one thing one has to have: either a soul that is cheerful by nature, or a soul made cheerful by work, love, art and knowledge".

Friedrich Nietzsche (1844 – 1900)

1.1 Motivation

Solid mechanics is concerned with the behaviour of a general solid continuum problem subjected to external actions. Historically, solid mechanics was of primary interest for the constructions of buildings and structures, starting with the pioneering works of Leonardo da Vinci (1452-1519), Galileo Galilei (1564-1642) and Isaac Newton (1642-1727). Following the successful achievement by Isaac Newton in stating the laws of motion, great progress was made from the early seventeenth to the late nineteenth century, notably by James Bernoulli (1654-1705), John Bernoulli (1667-1748), Euler (1707-1783), Charles-Augustine Coulomb (1736-1806), Augustin Louis Cauchy (1789-1857), Robert Hooke (1635-1703) and others. At present, there exists a considerable number of principles in continuum mechanics [1].

An understanding of the fundamental laws of solid mechanics is of practical importance in mechanical, aeronautical and civil engineering. Additionally, with the advent of modern materials, it is necessary to develop more sophisticated constitutive theories[1] in order to describe the phenomenological responses of materials [2–7]. In general, a solid typifies a body with a firm shape, as opposed to a fluid[2], while a structure refers to a solid which is comprised of cables[3], beams[4] and plates [8–11].

In practice, structural analysis is an indispensable tool that can drive an engineering design process without having to test it. Its objective is to analyse a structural system so as to predict the behaviour (i.e. deformations and stresses) of the structure due to external forces. The relation of the analysis process to other processes is depicted in Figure 1.1. In this thesis, the structural modelling and analysis will be considered, but more focus is placed on the latter.

There are two broad classes of external loads, namely static and dynamical loading [12]. Static forces are those that are applied slowly to a structure and thus of steady-state in character. In contrast, dynamic forces[5] are time-varying forces which can cause the vibration of a structure. Many engineering problems in which the dynamic effects are of particular importance are transportation, manufacturing and civil engineering structures under environmental loadings (i.e. wind and snow load). One of the most striking examples that has had a lasting effect on the field of structural dynamics is due to the collapse of the Tacoma Narrows suspension bridge that took place in Washington on November 7, 1940 (see Figure 1.2). The

[1] In civil engineering structures, some modern design codes are based on Limit State Design (LSD) where plastic analysis has been pointed out. This analysis reveals that the structure is capable of resisting loads after the elastic limit and will only collapse under the extent of plasticity.

[2] A fluid is a substance that continuously deforms under an applied shear stress.

[3] Cables are flexible structural elements. The deformed shape depends on the nature and magnitude of the applied load. When a cable is pulled at either end, a straight shape is achieved. This is known as tie-rod.

[4] Beams are the horizontal elements that carry loads by bending since the loads are applied transversely to their longitudinal axis.

[5] In dynamic analysis, it is necessary to consider the inertial forces produced by the accelerating masses.

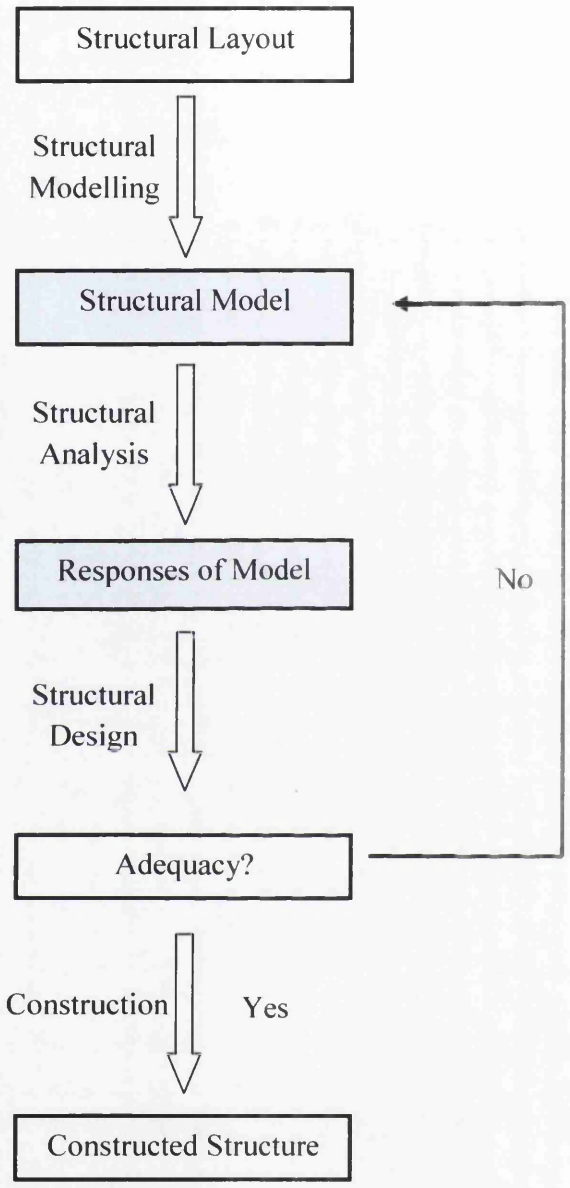

Figure 1.1: Role of structural analysis in the design process of a structure.

destruction is used as a lesson in the necessity to consider both aerodynamics and resonance effects in civil and structural engineering.

From an analytical viewpoint, the conventional linear analysis is restricted to infinitesimal strain deformation theory; for instance, concrete and steel civil structures.[6] Unfortunately, many problems of practical interest, such as forging, machining, crash and collision tests (see Figure 1.3), typically involve a considerable change of shape and are often accompanied by nonlinear material behaviour [3, 4, 6, 7]. In order to simulate these convoluted nonlinear problems, the displacement-based formulation is used [17].

The traditional solid dynamics formulation, where its primary variable is the displacement field, is solved by standard finite element spatial discretisation together with a family of Newmark time integration schemes. However, the resulting space-time discretised formulation presents a series of shortcomings. First, Newmark's method has a tendency for high frequency noise to persist in the solution and most importantly, its accuracy is remarkably degraded once artificial damping is employed. Some minor modifications were introduced to improve the accuracy of numerical dissipation without the inclusion of a discontinuity sensor, which consequently made the Newmark scheme unsuitable for problems where shocks are present [18–21]. Additionally, it is well known that using linear elements in displacement-based FE leads to second order convergence for displacements but one order less for strains and stresses.

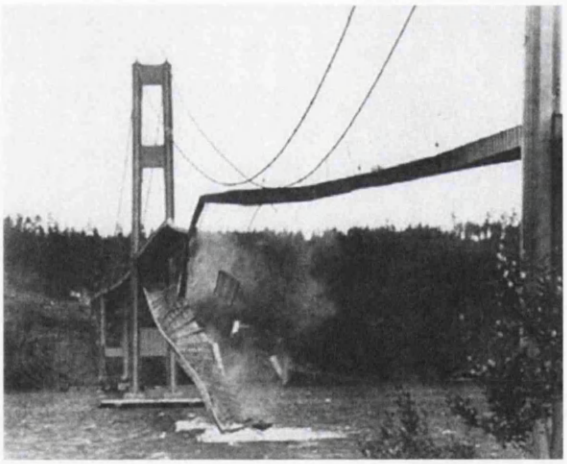

Figure 1.2: Aeroelastic instabilities of the Tacoma Narrows suspension bridge.

It is also known that constant stress elements exhibit volumetric locking in incompressible or nearly incompressible applications; for instance, plastic flows involving large isochoric strains. In order to eliminate the locking phenomena, a variety of different approaches have been developed. First, p-refinement can be introduced where high order interpolating functions are adopted [22]. Another general approach

[6] Infinitesimal strain theory deals with the small deformations in a continuum body [1, 13–16].

(a) (b)

Figure 1.3: (a) Crash test; and (b) Collision test

is to introduce a multi-field Veubeke-Hu-Washizu (VHW) type variational principle, which enables the use of independent kinematic descriptions for the volumetric and deviatoric deformations [7]. In particular, the mean dilatation technique, in which a constant interpolation for volumetric variables over an element is involved, is widely accepted. This specific technique can be identified as a particular case of Selective Reduced Integration (SRI), where the volumetric stress components are suitably underintegrated. Unfortunately, this scheme cannot be applied within the context of low order elements (i.e. linear triangles and linear tetrahedrons) as these elements have already used the simplest Gaussian quadrature rule. In [23], Bonet and Burton suggested that the volumetric strain energy is approximated by evaluating averaged nodal pressures in terms of nodal volumes while the deviatoric component is treated in a standard manner. However, the resulting solution behaved poorly in bending dominated cases. To circumvent this difficulty, Dohrmann *et al.* [22] proposed a new linear tetrahedron by applying nodal averaging process to the whole small strain tensor. Furthermore, Bonet *et al.* extended this application to large strain regime with the idea of employing an averaged nodal deformation gradient tensor as the main kinematic variable [24].

This thesis offers an alternative computational framework to prevent the detrimental locking effects by developing a mixed formulation that permits the use of any low order elements. Insofar as the formulation is expressed as a system of conservation laws, where both the velocities and deformation gradient tensor are the primary conserved variables, stresses converge at the same rate as velocities and displacements. Moreover, this system of equations can be discretised using a cell centred Finite Volume Method (FVM), typically based on the use of Riemann solvers and shock capturing schemes. A wealth of research has been carried out for developing the FVM in Computational Solid Dynamics (CSD). The literature on this topic has mushroomed in recent years and will be briefly summarised in the next section.

1.2 State of the Art

1.2.1 Finite Volume Method vs Finite Element Method

Traditionally, Finite Element Method (FEM) has been extensively used for problems in Computational Solid Mechanics (CSM) [10]. As a contemporary, Finite Volume Method (FVM) has established itself within the field of Computational Fluid Dynamics (CFD) [25, 26]. Both schemes can be considered as methods of weighted residuals where they differ in the choice of weighting functions [27]. The finite element Galerkin method treats the shape function as the weighting function and can be easily extended to higher order by increasing the order of polynomial interpolation. In contrast, the finite volume method results by selecting the weighting function as element piecewise unit constant. These two numerical techniques are equivalent in many applications [28].

Over the past few decades a number of authors have used the FVM to discretise the traditional displacement-based equation in solid mechanics. It is now possible to classify this method into two approaches: vertex-based [27, 29–32] and cell-centred [33–37]. The first approach is based upon standard FEM [38] and employs shape functions to describe the variation of the displacement field over an element and is very well suited to complex geometries [29, 32]. This approach can be generally classified as cell-vertex FVM [25, 27]. However, it should be noted that there is a specific class of cell-vertex methods that employs non-overlapping control volumes [28, 39, 40], which will be referred to as a vertex-based FVM. The second approach is based upon traditional FVM [41] that has been widely used in CFD [25]. This particular technique has been applied in CSM involving structured [33, 34] and unstructured meshes [35–37, 42].

Unfortunately, both of the finite volume approaches discussed above are restricted to the second order dynamic equilibrium equation for the displacement field [43, 44], which subsequently do not make use of any upwind-biased numerical flux [45–57]. Recently, a new mixed-formulation based upon first order hyperbolic system of conservation laws has been proposed for explicit solid dynamics [58, 59]. Numerical methods for solving nonlinear systems of hyperbolic conservation laws require a monotone numerical flux [60]. The choice of the flux computation has a profound influence on the properties of the resulting schemes [61, 62]. A refined approach in utilising wave propagation information contained in the new mixed formulation to construct the numerical flux is introduced in [63, 64].

1.2.2 Locking

The standard low order elements exhibit severe locking for incompressible or nearly incompressible materials. Rubber or rubber-like materials experience nearly incompressible material behaviour and are characterised by a large ratio of bulk modulus to shear modulus [65–68] (see Figure 1.4). In metal plasticity, the plastic deforma-

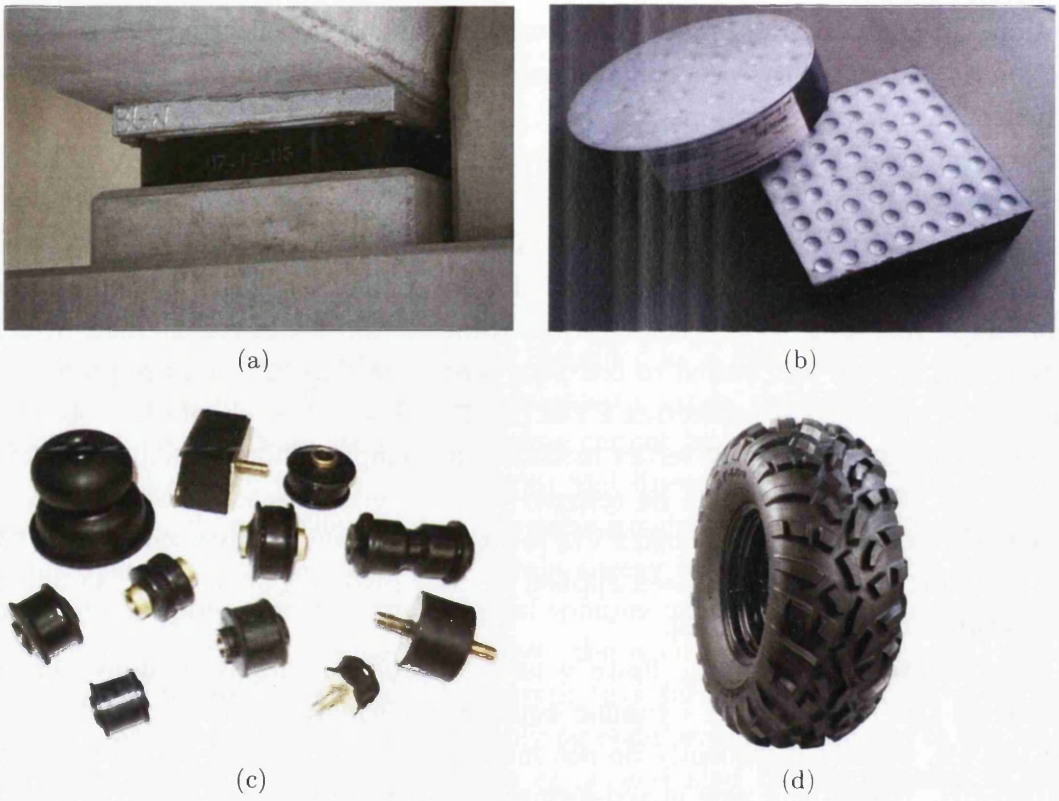

(a) (b)

(c) (d)

Figure 1.4: Rubber or rubber-like materials: (a) Bridge bearing pad; (b) Structural bearings; (c) Engine mountings; and (d) Tyre.

tion is isochoric and the compressible part is due to elastic deformations that remain small in many applications [7].

Problems can arise in the presence of incompressibility which lead to the so-called volumetric locking phenomenon [22–24]. In this case, the standard linear elements are not able to enforce a complete nullity of the volumetric strain. This leads to an overestimation of the stiffness related to the volumetric part, which results in overly stiff behaviour [38,69,70].

To alleviate this, different approaches have been developed. Simo *et al.* [71] proposed a three-field variational method with independent constant pressure and constant dilatation. However, this proposed element is hampered by hourglassing[7] under certain conditions [72]. In the so-called F-bar methodology, the standard deformation gradient $\boldsymbol{F}$ is replaced by a modified deformation gradient $\bar{\boldsymbol{F}} = (\bar{J}/J)^{1/3}\boldsymbol{F}$ with $J = \det\boldsymbol{F}$ and $\bar{J} = const.$ Nagtegaal *et al.* [73] introduced the dilatation parameter $\bar{J} = \int_V JdV/\int_V dV$, which coincides with the three-field variational method discussed above. This method is widely known as mean dilatation approach. A slightly different definition for $\bar{J} = J_e = \det\boldsymbol{F}_e$ at the centroid of the element is also performed in [74,75]. First by noting that a family of geometrically linear Enhanced Assumed Strain (EAS) elements has been developed by [76,77]. Simo and Armero [78] extended the original idea to finite strain range, where the independent displacement gradient field is redefined as $\boldsymbol{H} = \boldsymbol{\nabla}_0\boldsymbol{u} + \tilde{\boldsymbol{H}}$ where $\tilde{\boldsymbol{H}}$ denotes the enhanced displacement gradient tensor. Another attractive alternative in the treatment of nearly incompressible models is Selective Reduced Integration (SRI) method. The crucial idea underlying SRI is that a full numerical integration is employed for the isochoric terms while a selective reduced integration is imposed for the volumetric stress component [69,79,80].

A clear advantage of using mixed variational, F-bar or EAS approaches is that they are directly applicable to all constitutive models. In contrast, SRI method is used for models with decoupled isochoric and volumetric behaviours. Insofar as an isochoric-volumetric decoupled material behaviour is assumed for most practical applications, the SRI method can be employed without any difficulties. All methods described above are capable of producing locking-free results, but only restricted to both four-node quadrilateral and eight-node hexahedron elements. Efforts to develop linear triangular and linear tetrahedral elements that are effective in nearly incompressible applications have only been partially successful, as the resulting formulations suffer from artificial mechanisms similar to hourglassing [22–24].

1.3 Scope of the Thesis

This thesis deals with the numerical technique required to simulate the responses of Lagrangian fast dynamic problems. The aim of this technique is to enable the

[7]Hourglassing is described as spurious zero-energy modes of deformation [6,38,69]. The existence of low-energy modes can only be detected via an eigenvalue analysis of the tangent matrix.

development of a computer program that is capable of alleviating the problems elucidated as follows:

- Non-physical oscillation in the vicinity of shock discontinuities.
- Volumetric or shear locking in nearly incompressible deformations or bending dominated situations.

Furthermore, the proposed methodology should be able to predict the following properties with respect to time:

- Deformed shape at particular time instant t.
- Other internal quantities such as pressure, internal and kinetic energy, linear and angular momentum.
- Numerical dissipation.

The formulation of a Lagrangian fast dynamic analysis is based on a first order hyperbolic system of conservation laws[8], which is crucially governed by two physical laws, namely the momentum balance principle[9] and the deformation gradient conservation principle. Both phycial laws are coupled with each other; typical of a so-called mixed formulation[10] [38]. In the case of reversible process, these balance principles have to be supplemented by an isothermal elastic constitutive law in order to describe the mechanical behaviour of a particular class of materials. Nonetheless, many problems of physics and engineering have implications for irreversible processes (i.e. thermal effects and dissipative inelastic mechanisms). In order to underline such phenomenon, it is essential to solve for an additional state variable, namely the first law of thermodynamics (or energy balance principle), where the constitutive models are more refined than those of isothermal elasticity. It is worth noting that, during a reversible process, the energy balance principle can be obtained by suitable integration of the momentum conservation principle [3, 4].

Unfortunately, it is practically almost impossible to find analytical solutions that satisfy the system of conservation laws for the majority of problems due to geometric and material nonlinearities[11] [3, 6, 7]. In order to solve the system of equations approximately, a cell centred FVM is used. The spatial semi-discretisation is performed on a standard cell-centred cartesian grid, where the primary variables are

[8]The non-conservative form of governing equations is not suitable for numerical solutions with strong discontinuities [26, 60, 81–84].

[9]The momentum balance principle is also known as the balance of momentum principle or the momentum conservation principle.

[10]The mixed formulation is defined by the fact that the number of dependent unknowns can be reduced in the governing equations by suitable algebraic operation. Otherwise, an irreducible formulation is recovered.

[11]The material nonlinearity is defined as the stress-strain behaviour which is given by an inelastic constitutive relationship whereas, the geometric nonlinearity is important in large deformation behaviour.

defined at the centroid of the cells. Under this circumstance, any control volume can be identified with the existing grid and typically, the field variables are approximated in every cell by means of piecewise constant shape functions, which yield first order accuracy in space [85].

Higher order spatial accuracy can be achieved by introducing a suitable reconstruction procedure for conservative variables within each cell, which then requires the neighbouring or adjacent information relative to the particular cell under consideration. A piecewise linear approximation to the solution variables is sufficient to be considered. However, the linear approximation does not prohibit unphysical oscillations in shock dominated problems [26, 60, 84]. In order to rectify this, a modern shock capturing technique which incorporates a nonlinear limiter is introduced [84, 86, 87]. A general predictor-corrector reconstruction procedure will be presented.

The discontinuity at every cell interface motivates the use of a Riemann solver to evaluate the interface fluxes. Hence, a Lagrangian contact algorithm for the computation of such fluxes will also be derived. Furthermore, the semidiscrete nonlinear evolution equations will be advanced forward in time by using a family of Total Variation Diminishing Runge-Kutta (TVD-RK) time stepping schemes [88]. For consistency, the order of accuracy in time should be matched with the order of spatial accuracy.

In order to guarantee the existence of a single-valued continuous displacement field, it is essential to obtain a zero-curl deformation gradient tensor to ensure compatible deformations[12]. Commonly available finite volume updated schemes in [26, 60, 84] introduce disturbances in the solution as the treatment of this constraint is not handled properly. To alleviate this, it is necessary to control curl errors in order to develop a robust and accurate scheme. A new conservative FVM that is locally curl-preserving will be presented.

The proposed computational methodology mentioned above does not necessarily preserve the total angular momentum of a system, which then induces energy loss under long-term analysis. For this purpose, a correction procedure involving a minimisation technique will be introduced.

To this end, a series of examples will be examined in order to demonstrate the robustness and general capabilities of this numerical technique. Comparisons of the proposed approach with the traditional displacement-based formulation will also be performed.

1.4 Outline

In order to elaborate the objectives indicated in the previous section, this thesis is organised as follows:

[12]In the classical infinitesimal strain deformation, these constraints are expressed by Saint-Venant's compatibility equations [89]; that is, $\nabla \times (\nabla \times \boldsymbol{\varepsilon}) = \mathbf{0}$.

- ***Chapter II*** explores the fundamentals of reversible Lagrangian elastodynamics [43,44,90]. The discussion starts with the derivations of the laws of physics for Lagrangian fast dynamics. The physical laws are valid for any continuum body, regardless of the material of which the body is made. A constitutive model is introduced so as to distinguish between different types of material [6]. These physical laws can then be combined into a single system of conservative equations [82,91].[13] It becomes a basic ingredient for studying the eigenstructure, which in turn leads to the development of a linearised Riemann solver that is required at interface fluxes [84].

- ***Chapter III*** discusses irreversible processes[14] that are always encountered in nature where constitutive relations are more complex than in isothermal elasticity [3]. In such cases, thermal effects and other dissipative mechanisms cannot be neglected. Laws of thermodynamics, hyperelastic-plastic materials and the Rankine-Hugoniot relations will be introduced [2,7].

- ***Chapter IV*** presents the numerical techniques required to solve the system of conservative equations. These include: cell-centred based discretisation [25,60,92]; Monotone Upstream Scheme for Conservation Law reconstruction procedure [93–95]; nonlinear slope limiter [86,87]; a family of TVD Runge-Kutta time stepping schemes [88,96,97] and maximum time increment [98].

- ***Chapter V*** presents a general framework for describing the highly nonlinear numerical interface flux function. This framework generalises the linearised Riemann solver and is derived based upon the Rankine-Hugoniot jump condition of the linear momentum variable.

- ***Chapter VI*** examines the proposed computational methodology required to conserve the total angular momentum of a system in order to ensure that physically meaningful solutions are produced under long-time integration [99–103].

- ***Chapter VII*** presents a new locally curl-preserving finite volume updated scheme in a treatment for satisfying the compatibility condition of strains [104,105].

- ***Chapter VIII*** deals with consistency and Von-Neumann stability analysis of the one-dimensional linear convection equation [25,60]. Once the method is proven to be consistent and stable, it shall automatically satisfy the convergence requirement [106].

[13]Navier-Stokes equations is widely used in computational fluid dynamics. A particular case, known as Euler equations, is recovered if the viscosity and heat conduction are neglected. Discussions about these mathematical models can be found in any CFD textbooks.

[14]Irreversible process is also regarded as natural process.

- ***Chapter IX*** simplifies the general formulations derived previously for 1D problems such as: governing equations; flux Jacobian matrix; eigenstructure; linearised Riemann solver; predictor-corrector reconstruction procedure and characteristic theory. Some 1D rod examples will be demonstrated.

- ***Chapter X*** is devoted to some practically interesting 2D examples: plate; beam and column in bending application; a punch test; tensile case and impact problems.

- ***Chapter XI*** concludes the thesis by summarising the main points and indicating some suggestions for future research works.

Part II

General Formulation of the Problem

Chapter 2

Reversible Lagrangian Elastodynamics

"Mathematics are well and good but nature keeps dragging us around by the nose".

Albert Einstein (1879 – 1955)

2.1 Introductory Remarks

This chapter is devoted to a general discussion on several formal aspects of explicit Lagrangian fast dynamic analysis within the context of elastic wave propagation[1]. There are many references available on the basic theory of elastodynamics (see [32,37,90,107–112]). In spite of that, a great deal of literature is focussed on steady-state (or elastostatic) problems [29,30,35,113], .

The classical displacement-based formulation is typically solved by standard finite element spatial discretisation together with a family of Newmark time integrators. It is well known that constant stress elements exhibit volumetric locking in incompressible or nearly incompressible dynamic applications and also perform poorly in bending dominated situations [23,24,69,75,80,114]. One of the approaches to surmount these difficulties is to treat deformation gradient tensor as an independent variable [58].

This chapter begins with problem variables that constitute a new mixed formulation for reversible elastodynamics. The conservative equations (also known as balance principles) are then derived. Inasmuch as a rubber (or rubber-like) material is considered, the most appropriate constitutive law for describing its behaviour (such that the model can withstand very large strains without any permanent deformation) will be the nearly incompressible Neo-Hookean (NH) hyperelastic material. The conservation-law formulation is subsequently presented which motivates the study of eigenstructure so that a linearised Riemann solver can be derived.

In order to achieve a better understanding of the sections that follow, it is necessary to briefly discuss some mathematical preliminaries[2]. The flowchart in Figure 2.1 illustrates the structure of this chapter.

2.2 Problem Variables

Motion of a continuum body is defined by a deformation mapping from a reference volume V to the corresponding current volume $v(t)$ (see Figure 2.2). During motion $\boldsymbol{\phi}$, the position $\boldsymbol{x}$ of a material particle $\boldsymbol{X}$ at any arbitrary time t is of the form $\boldsymbol{x} = \boldsymbol{\phi}(\boldsymbol{X}, t)$; material coordinate $\boldsymbol{X}$ is used to label any particle of a body at time $t = 0$. The deformation gradient tensor, $\boldsymbol{F}(\boldsymbol{X}, t)$, is generally expressed as

$$\boldsymbol{F}(\boldsymbol{X}, t) = \frac{\partial \boldsymbol{\phi}(\boldsymbol{X}, t)}{\partial \boldsymbol{X}} = \frac{\partial \boldsymbol{x}(\boldsymbol{X}, t)}{\partial \boldsymbol{X}}. \tag{2.1}$$

This tensor is said to be a two-point tensor due to its ability to transform a vector from the undeformed configuration to the deformed configuration [7] and transpires that a body will experience a homogeneous deformation if $\boldsymbol{F}$ itself is independent of $\boldsymbol{X}$. In addition, the determinant of $\boldsymbol{F}$ (denoted by Jacobian J) relates differential

[1]Elastic wave propagation is alternatively known as elastodynamics.

[2]The basic knowledge of mathematical preliminaries (i.e. linear algebra, continuum mechanics and hyperbolic equations) is summarised in Appendices (A - C).

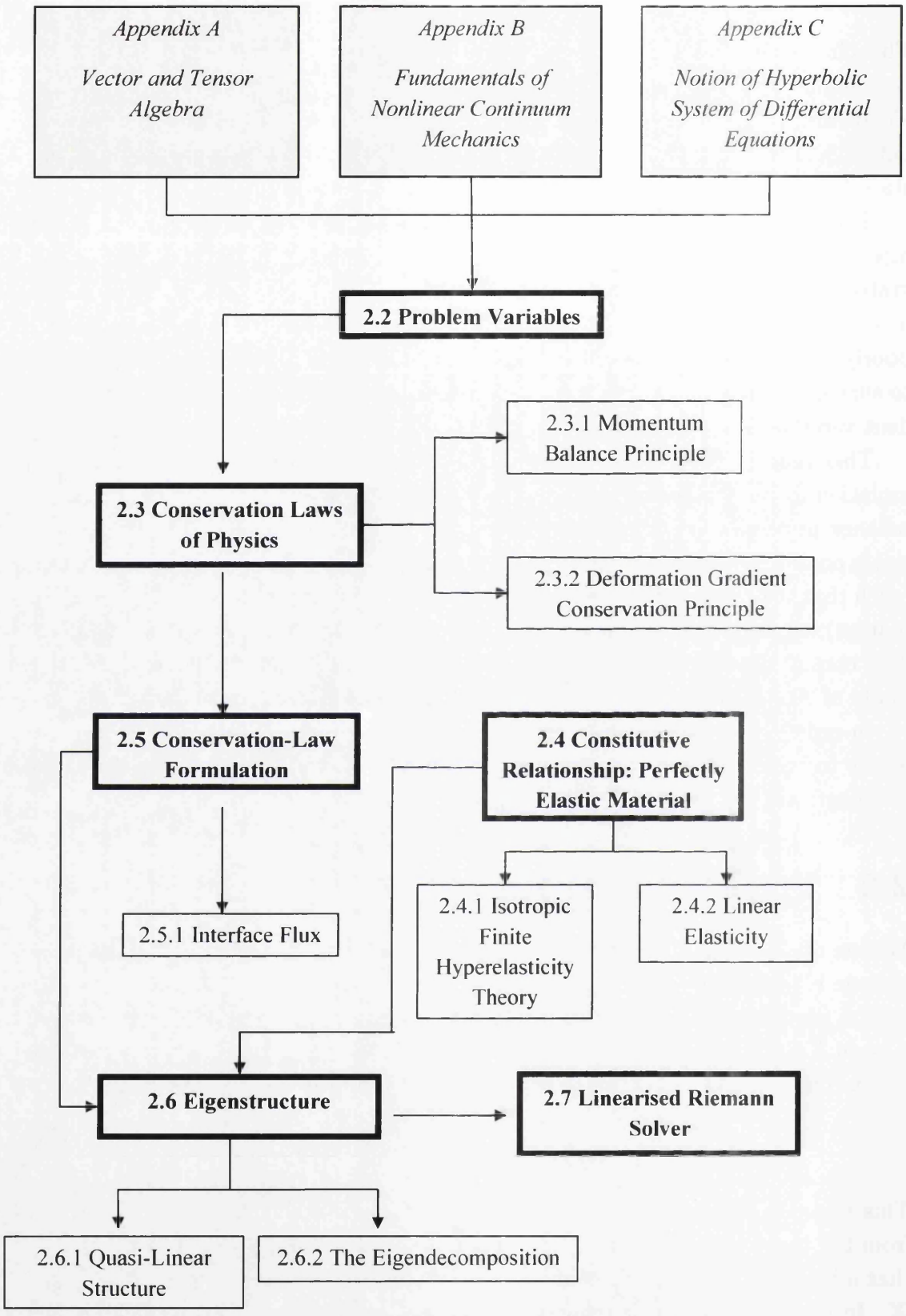

Figure 2.1: Guide to this chapter.

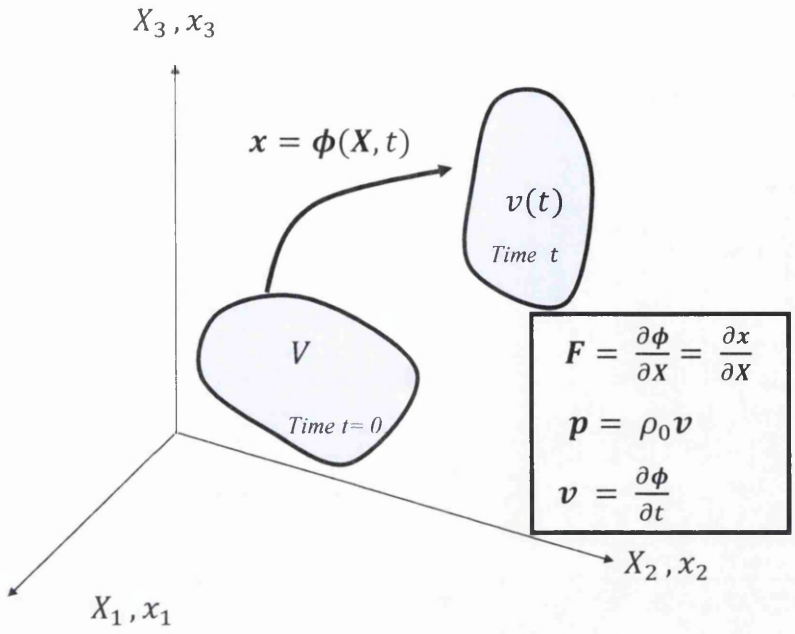

Figure 2.2: Motion of a body.

volumes in both material and spatial configurations $dv = JdV$. More precisely, the condition, $J \in \mathbb{R}^+$, has to be satisfied since a body is not allowed to penetrate itself [115]. A situation in which $J \leq 0$ is physically unacceptable. The material velocity $\boldsymbol{v}(\boldsymbol{X}, t)$ and linear momentum per unit of undeformed volume, $\boldsymbol{p}(\boldsymbol{X}, t)$, are given as

$$\boldsymbol{v}(\boldsymbol{X}, t) = \frac{\partial \boldsymbol{\phi}(\boldsymbol{X}, t)}{\partial t}, \qquad \boldsymbol{p}(\boldsymbol{X}, t) = \rho_0 \boldsymbol{v}(\boldsymbol{X}, t). \tag{2.2}$$

During isothermal process, it is sufficient to consider $\boldsymbol{p}$ and $\boldsymbol{F}$ as problem variables for which the corresponding standard conservation laws can be derived. This process allows the energy balance principle, E_T, to be uncoupled from the rest of the conservation laws [1,3]. A general energy principle will be presented in Section 3.2 with the aid of the laws of Thermodynamics.

2.3 Conservation Laws of Physics

This section presents the Total Lagrangian description[3] for a new mixed formulation of Lagrangian explicit dynamics solid mechanics. The formulation is crucially governed by two physical laws, namely the momentum balance principle [3, 4, 6, 7, 116] and the deformation gradient conservation principle [58, 59, 63, 64, 117, 118]. In essence, these physical laws are collectively known as a general statement which is not restricted in their application to any class of material.

[3]In Total Lagrangian Formulation (TLF), all variables are referred to undeformed configuration. The decisive advantage is that all derivatives with respect to spatial co-ordinates are calculated based upon an original undeformed configuration [115].

2.3.1 Momentum Balance Principle

For a continuum, momentum balance principle states that the rate of change of linear momentum of particles (which lie within a material volume V) is equal to resultant forces applied to these particles. Mathematically, this principle is expressed as

$$\frac{d}{dt}\int_V \boldsymbol{p}(\boldsymbol{X},t)\,dV = \int_V \rho_0 \boldsymbol{b}(\boldsymbol{X},t)\,dV + \int_{\partial V} \boldsymbol{t}\,dA; \qquad \boldsymbol{p}(\boldsymbol{X},t) = \rho_0 \boldsymbol{v}(\boldsymbol{X},t), \quad (2.3)$$

where $\boldsymbol{p}$ is the linear momentum per unit of material volume, ρ_0 represents the constant material density, $\boldsymbol{v}$ is the velocity field, $\boldsymbol{b}$ stands for the body force per unit mass and $\boldsymbol{t}$ denotes the nominal traction vector. Since the material volume integral does not evolve in time[4], (2.3) then leads to a local differential momentum conservation law

$$\frac{\partial \boldsymbol{p}(\boldsymbol{X},t)}{\partial t} - \boldsymbol{\nabla}_0 \cdot \boldsymbol{P}(\boldsymbol{X},t) = \rho_0 \boldsymbol{b}(\boldsymbol{X},t); \qquad [\boldsymbol{\nabla}_0 \cdot \boldsymbol{P}]_i = [\mathrm{DIV}\boldsymbol{P}]_i = \frac{\partial P_{iI}}{\partial X_I}, \quad (2.4)$$

with the help of $\boldsymbol{t} = \boldsymbol{P}\boldsymbol{N}$ together with the divergence theorem [3, 7, 115]. The two-point tensor $\boldsymbol{P}$ describes the first Piola-Kirchhoff stress tensor, $\boldsymbol{N}$ represents the material outward unit normal vector and $\boldsymbol{\nabla}_0$ denotes the gradient operator in undeformed space. It is worth noting that (2.4) is a standard Lagrangian equation of motion for continuum mechanics and most importantly, it reduces to the equilibrium equation if the inertial term is neglected [1, 6]. Note that the partial derivative of $\boldsymbol{p}(\boldsymbol{X},t)$ is taken at constant $\boldsymbol{X}$, or in other words, (2.4) is derived by following the material particle $\boldsymbol{X}$.[5]

2.3.2 Deformation Gradient Conservation Principle

Deformation gradient tensor, $\boldsymbol{F}$, plays a key role in describing kinematics for large deformation analysis[6] [3, 6, 7, 115, 116, 123, 124]. In order to alleviate shear locking

[4] If a control volume deforms with body motion, the volume will be transformed from a spatial representation to a reference representation. This procedure is known as Reynolds Transport Theorem (RTT). Literature such as [1, 13, 115, 119–122] review this concept.

[5] In a purely mechanical reversible process, an energy equation can be derived as follows. Multiplying the momentum conservation law by a velocity vector $\boldsymbol{v}$ gives

$$\frac{\partial \boldsymbol{p}}{\partial t} \cdot \boldsymbol{v} - (\boldsymbol{\nabla}_0 \cdot \boldsymbol{P}) \cdot \boldsymbol{v} = \rho_0 \boldsymbol{b} \cdot \boldsymbol{v}.$$

Then, integrating over an arbitrary domain V with the aid of divergence theorem yields

$$\frac{d}{dt}\int_V \frac{1}{2}\rho_0 \boldsymbol{v}\cdot\boldsymbol{v}\,dV + \int_V \boldsymbol{P}\colon\frac{\partial \boldsymbol{v}}{\partial \boldsymbol{X}}\,dV = \int_{\partial V} \boldsymbol{t}\cdot\boldsymbol{v}\,dA + \int_V \rho_0 \boldsymbol{b}\cdot\boldsymbol{v}\,dV.$$

By noting that $\boldsymbol{P}\colon\frac{\partial \boldsymbol{v}}{\partial \boldsymbol{X}} = \boldsymbol{P}\colon\dot{\boldsymbol{F}}$, equation above can be re-written as

$$\frac{d}{dt}\int_V \frac{1}{2}\rho_0 \boldsymbol{v}\cdot\boldsymbol{v}\,dV + \int_V \boldsymbol{P}\colon\dot{\boldsymbol{F}}\,dV = \int_{\partial V} \boldsymbol{t}\cdot\boldsymbol{v}\,dA + \int_V \rho_0 \boldsymbol{b}\cdot\boldsymbol{v}\,dV. \quad (2.5)$$

This energy balance principle will be revisited in Section 3.2.

[6] In linear elasticity, deformation gradient tensor is approximated by $\boldsymbol{F} \approx \boldsymbol{I}$, which implies that the magnitude of the engineering strain $\boldsymbol{\varepsilon}$ is restricted to an infinitesimal value.

as well as volumetric locking, one of the locking-free methods is to treat $\boldsymbol{F}$ as an independent variable with the aim of increasing the degrees of freedom (or flexibility) of a problem [24]. For this purpose, conservation of deformation gradient tensor has to be derived by noting that the time derivative of $\boldsymbol{F}(\boldsymbol{X}, t)$ is related to the velocity vector $\boldsymbol{v}(\boldsymbol{X}, t)$ as

$$\frac{\partial \boldsymbol{F}}{\partial t} = \boldsymbol{\nabla}_0 \boldsymbol{v}. \tag{2.6}$$

With the help of the identity tensor $\boldsymbol{I}$, (2.6) can be alternatively written as

$$\frac{\partial \boldsymbol{F}}{\partial t} - \boldsymbol{\nabla}_0 \cdot (\boldsymbol{v} \otimes \boldsymbol{I}) = \boldsymbol{0}. \tag{2.7}$$

This can be considered as a generalisation of continuity equation in fluid dynamics.[7] Nonetheless, it is essential to express (2.7) in a general integral form

$$\frac{d}{dt} \int_V \boldsymbol{F}\, dV = \int_{\partial V} \boldsymbol{v} \otimes \boldsymbol{N}\, dA; \qquad \boldsymbol{v} = \boldsymbol{p}/\rho_0,$$

with the aid of the divergence theorem.

2.4 Constitutive Relationship: Perfectly Elastic Material

In order to close the coupled system, viz. (2.4) and (2.7), both derived balance principles have to be supplemented by a constitutive law satisfying two fundamental requirements, namely frame invariance[8] (or objectivity) and the laws of Thermodynamics [80].

Rubber[9] (or rubber-like) materials are used in various engineering applications, like engine mounts, building and bridge bearings, tyres and vibration-isolation devices (see Figure 1.4). In general, these materials are characterised by high deformability and reversibility of deformation. As a result, they exhibit a nonlinear hyperelastic behaviour. Theoretical analysis of hyperelasticity has been performed in [65–68]. From a phenomenological viewpoint, the strain energy function ψ is

[7] Eulerian description of mass conservation law in fluid mechanics is

$$\frac{\partial \rho}{\partial t} + \boldsymbol{\nabla}_{\boldsymbol{x}} \cdot (\rho \boldsymbol{v}) = 0,$$

where $\boldsymbol{\nabla}_{\boldsymbol{x}} = \partial/\partial \boldsymbol{x}$.

[8] Constitutive equations must remain invariant when rigid body motion is superimposed on a deformed configuration. A basic review of this concept can be found in [1, 3, 6].

[9] Rubber has flexible molecular structures which able to be stretched up to several times its original length. This material can be treated as a linearly elastic model at small strains. However, a nonlinear elasticity should be considered when analysing rubber behaviour in large deformations.

postulated as a function which depends wholly on $\boldsymbol{F}$, $\psi = \psi(\boldsymbol{F})$. Additionally, ψ can also be represented in terms of invariants[10] for isotropic behaviour[11].

2.4.1 Isotropic Finite Hyperelasticity Theory

For a hyperelastic (or Green-elastic) model, the existence of a Helmholtz free energy functional, which is defined per unit of undeformed volume, is postulated [3]. Based on the definition of Legendre transformation, a general free energy functional is expressed as

$$\psi(\boldsymbol{F}, \theta) = e(\boldsymbol{F}, \eta) - \theta\eta. \tag{2.8}$$

Under isothermal process, thermodynamic variables (i.e. entropy η and temperature θ) are neglected. The above equation is thus reduced to $\psi(\boldsymbol{F}) = e(\boldsymbol{F})$ where e is the internal energy.

By using Clausius-Planck inequality, an internal dissipation rate is generally denoted as

$$D_{\text{int}} = \boldsymbol{P} : \dot{\boldsymbol{F}} - \dot{e} + \theta\dot{\eta} \geq 0. \tag{2.9}$$

Note that internal dissipation D_{int} is zero in a reversible process. For the class of isothermal perfectly elastic materials, (2.9) degenerates to the following equality

$$D_{\text{int}} = \boldsymbol{P} : \dot{\boldsymbol{F}} - \dot{\psi} = \left(\boldsymbol{P} - \frac{\partial \psi(\boldsymbol{F})}{\partial \boldsymbol{F}} \right) : \dot{\boldsymbol{F}} = 0. \tag{2.10}$$

Since $\dot{\boldsymbol{F}}$ can assume arbitrary values, the First Piola-Kirchhoff stress tensor is deduced as

$$\boldsymbol{P} = \frac{\partial \psi(\boldsymbol{F})}{\partial \boldsymbol{F}}. \tag{2.11}$$

Laws of Thermodynamics within the context of irreversible processes will be discussed in the next chapter.

The strain (or stored) energy functional can be conveniently decomposed into the summation of deviatoric[12] $\psi_{dev}(J^{-1/3}\boldsymbol{F})$ and volumetric components $\psi_{vol}(J)$ as

$$\psi(\boldsymbol{F}) = \psi_{dev}(J^{-1/3}\boldsymbol{F}) + \psi_{vol}(J), \tag{2.12}$$

which in turn, leads to

$$\boldsymbol{P} = \boldsymbol{P}_{dev} + \boldsymbol{P}_{vol}; \quad \boldsymbol{P}_{dev} = \frac{\partial \psi_{dev}}{\partial \boldsymbol{F}}; \quad \boldsymbol{P}_{vol} = \frac{\partial \psi_{vol}}{\partial \boldsymbol{F}}. \tag{2.13}$$

[10] It is easy to demonstrate that invariants of $\boldsymbol{C}$ are identical to invariants of $\boldsymbol{b}$: [7]

$$\begin{aligned} I_{\boldsymbol{C}} &= \text{tr}(\boldsymbol{C}) = \text{tr}(\boldsymbol{F}^T\boldsymbol{F}) = \text{tr}(\boldsymbol{F}\boldsymbol{F}^T) = \text{tr}(\boldsymbol{b}) = I_{\boldsymbol{b}}; \\ II_{\boldsymbol{C}} &= \text{tr}(\boldsymbol{C}\boldsymbol{C}) = \text{tr}(\boldsymbol{F}^T\boldsymbol{F}\boldsymbol{F}^T\boldsymbol{F}) = \text{tr}(\boldsymbol{F}\boldsymbol{F}^T\boldsymbol{F}\boldsymbol{F}^T) = \text{tr}(\boldsymbol{b}\boldsymbol{b}) = II_{\boldsymbol{b}}; \\ III_{\boldsymbol{C}} &= \det(\boldsymbol{C}) = \det(\boldsymbol{F}^T\boldsymbol{F}) = \det(\boldsymbol{F}\boldsymbol{F}^T) = \det(\boldsymbol{b}) = III_{\boldsymbol{b}}. \end{aligned}$$

Here, the right and left Cauchy-Green deformation tensors are defined by $\boldsymbol{C} = \boldsymbol{F}^T\boldsymbol{F}$ and $\boldsymbol{b} = \boldsymbol{F}\boldsymbol{F}^T$, respectively.

[11] Isotropy is defined by requiring the constitutive behaviour to be identical in any material direction.

[12] Deviatoric is alternatively known as isochoric or volume-preserving.

The volumetric stress term can also be further developed by introducing pressure p,

$$\boldsymbol{P}_{vol} = \frac{d\psi_{vol}}{dJ}\frac{\partial J}{\partial \boldsymbol{F}} = pJ\boldsymbol{F}^{-T}; \quad p = \frac{d\psi_{vol}(J)}{dJ}; \quad J = \det\boldsymbol{F}. \tag{2.14}$$

The simplest model satisfying the conditions described above is the nearly incompressible Neo-Hookean (NH) material. Its deviatoric and volumetric parts are described as[13]

$$\psi_{dev} = \frac{1}{2}\mu\left[J^{-2/3}(\boldsymbol{F}:\boldsymbol{F}) - 3\right]; \quad \psi_{vol} = \frac{1}{2}\kappa(J-1)^2. \tag{2.15}$$

Here, κ is the bulk modulus which only appears in the volumetric term whereas the shear modulus μ, on the other hand, appears in the deviatoric counterpart. In addition, the expressions for deviatoric component of stress tensor and pressure p can be obtained as

$$\boldsymbol{P}_{dev} = \mu J^{-2/3}[\boldsymbol{F} - \frac{1}{3}(\boldsymbol{F}:\boldsymbol{F})\boldsymbol{F}^{-T}], \qquad p = \kappa(J-1), \tag{2.16}$$

respectively.[14]

2.4.2 Linear Elasticity

Engineering materials (i.e. concrete, steel and metal) usually undergo a very small change in shape. Under this circumstance, there is no difference between deformed and undeformed configurations.

To this effect, a linear elastic constitutive relationship is considered as an excellent model to describe small deformation behaviour for these engineering materials. The stored energy functional, ψ, is defined by[15]

$$\psi(\boldsymbol{\varepsilon}) = \frac{1}{2}\lambda\left(\mathrm{tr}\boldsymbol{\varepsilon}\right)^2 + \mu\left(\boldsymbol{\varepsilon}:\boldsymbol{\varepsilon}\right), \tag{2.17}$$

where μ and λ are the so-called Lamé constants. It is worth mentioning that Saint-Venant Kirchhoff material is recovered if $\boldsymbol{\varepsilon}$ is replaced by the Green-Lagrange strain tensor $\boldsymbol{E}$, which is defined as $\boldsymbol{E} = (\boldsymbol{C} - \boldsymbol{I})/2$ where $\boldsymbol{C} = \boldsymbol{F}^T\boldsymbol{F}$.

In general, a deformation gradient tensor is conveniently split into a displacement gradient $\boldsymbol{H} = \partial\boldsymbol{u}/\partial\boldsymbol{X}$ and a unit (or identity) matrix $\boldsymbol{I}$; that is, $\boldsymbol{F} = \boldsymbol{I} + \boldsymbol{H}$. In

[13]The strain energy functional of Neo-Hookean material can be alternatively denoted in an invariant form:

$$\psi(I_{\boldsymbol{C}}, II_{\boldsymbol{C}}, III_{\boldsymbol{C}}) = \frac{1}{2}\mu\left(III_{\boldsymbol{C}}^{-1/3}I_{\boldsymbol{C}} - 3\right) + \frac{1}{2}\kappa\left(III_{\boldsymbol{C}}^{1/2} - 1\right)^2.$$

[14]Note that the deviatoric nature of $\boldsymbol{P}_{dev}$ implies that $\boldsymbol{P}_{dev}:\boldsymbol{F} = 0$, instead of $\mathrm{tr}(\boldsymbol{P}_{dev}) = 0$ (see [7]).

[15]In linear elasticity, material description of strain energy functional can be expressed in an invariant form as

$$\psi(I_{\boldsymbol{\varepsilon}}, II_{\boldsymbol{\varepsilon}}, III_{\boldsymbol{\varepsilon}}) = \frac{1}{2}\lambda I_{\boldsymbol{\varepsilon}}^2 + \mu II_{\boldsymbol{\varepsilon}}.$$

the context of infinitesimal strain, an assumption is made such that only linear contributions of $\boldsymbol{H}$ are considered. In what follows, the engineering (or true) strain $\boldsymbol{\varepsilon}$ and its trace can be further developed as

$$\boldsymbol{\varepsilon} = \frac{1}{2}\left(\boldsymbol{H} + \boldsymbol{H}^T\right) = \frac{1}{2}\left(\boldsymbol{F} + \boldsymbol{F}^T - 2\boldsymbol{I}\right); \quad \operatorname{tr}(\boldsymbol{\varepsilon}) = \operatorname{tr}(\boldsymbol{H}) = \operatorname{tr}(\boldsymbol{F}) - 3. \tag{2.18}$$

In the absence of deformation ($\boldsymbol{F} = \boldsymbol{I}$), the stored energy functional vanishes as expected ($\psi(\boldsymbol{\varepsilon}) = 0$). Based on (2.11), after some simple algebraic manipulations, the stress tensor is easily obtained as

$$\boldsymbol{P}(\boldsymbol{F}) = \boldsymbol{\sigma}(\boldsymbol{F}) = \mu\left[\boldsymbol{F} + \boldsymbol{F}^T - \frac{2}{3}\operatorname{tr}(\boldsymbol{F})\boldsymbol{I}\right] + \kappa\left(\operatorname{tr}(\boldsymbol{F}) - 3\right)\boldsymbol{I}. \tag{2.19}$$

The above stress tensor (widely known as engineering stress $\boldsymbol{\sigma}$) is clearly a symmetric tensor field [1, 6, 7, 13, 115, 120, 121, 125].

2.5 Conservation-Law Formulation

The physical laws for linear momentum and deformation gradient are summarised here for convenience:[16]

$$\frac{\partial \boldsymbol{p}}{\partial t} - \boldsymbol{\nabla}_0 \cdot \boldsymbol{P} = \rho_0 \boldsymbol{b}, \tag{2.20a}$$

$$\frac{\partial \boldsymbol{F}}{\partial t} - \boldsymbol{\nabla}_0 \cdot (\boldsymbol{v} \otimes \boldsymbol{I}) = \boldsymbol{0}, \tag{2.20b}$$

where $\boldsymbol{v} = \boldsymbol{p}/\rho_0$. These laws of physics[17] can then be combined into a single system of first order hyperbolic equations as

$$\frac{\partial \boldsymbol{\mathcal{U}}}{\partial t} + \frac{\partial \boldsymbol{\mathcal{F}}_I}{\partial X_I} = \boldsymbol{\mathcal{S}}, \quad \forall I = 1, 2, 3; \tag{2.21}$$

[16] An alternative notation, $\boldsymbol{\nabla}_0 \cdot (\cdot) \equiv \mathrm{DIV}(\cdot)$, is also used in [7, 92].

[17] Conservation law in differential form is characterised by all space derivative terms grouped as a divergence operator.

where their components are illustrated as

$$\boldsymbol{\mathcal{U}} = \begin{pmatrix} p_1 \\ p_2 \\ p_3 \\ F_{11} \\ F_{12} \\ F_{13} \\ F_{21} \\ F_{22} \\ F_{23} \\ F_{31} \\ F_{32} \\ F_{33} \end{pmatrix}, \qquad \boldsymbol{\mathcal{F}}_I = \begin{pmatrix} -P_{1I}(\boldsymbol{F}) \\ -P_{2I}(\boldsymbol{F}) \\ -P_{3I}(\boldsymbol{F}) \\ -\delta_{I1}v_1 \\ -\delta_{I2}v_1 \\ -\delta_{I3}v_1 \\ -\delta_{I1}v_2 \\ -\delta_{I2}v_2 \\ -\delta_{I3}v_2 \\ -\delta_{I1}v_3 \\ -\delta_{I2}v_3 \\ -\delta_{I3}v_3 \end{pmatrix}, \qquad \boldsymbol{\mathcal{S}} = \begin{pmatrix} \rho_0 b_1 \\ \rho_0 b_2 \\ \rho_0 b_3 \\ 0 \\ 0 \\ 0 \\ 0 \\ 0 \\ 0 \\ 0 \\ 0 \\ 0 \end{pmatrix}. \tag{2.22}$$

Here, a homogeneous equation is simply recovered in the absence of body force $\boldsymbol{b}$. The conservation-law (2.21-2.22) is capable of yielding the physically correct values in problems where discontinuities are present.

2.5.1 Interface Flux

At a given interface defined by the material outward unit normal vector $\boldsymbol{N} = (N_1, N_2, N_3)^T$, the interface flux will be denoted as

$$\boldsymbol{\mathcal{F}}_N = \boldsymbol{\mathcal{F}}_I N_I = \begin{pmatrix} -t_1(\boldsymbol{F}) \\ -t_2(\boldsymbol{F}) \\ -t_3(\boldsymbol{F}) \\ -N_1 v_1 \\ -N_2 v_1 \\ -N_3 v_1 \\ -N_1 v_2 \\ -N_2 v_2 \\ -N_3 v_2 \\ -N_1 v_3 \\ -N_2 v_3 \\ -N_3 v_3 \end{pmatrix}, \qquad \forall I = 1, 2, 3, \tag{2.23}$$

with the help of $\boldsymbol{t} = \boldsymbol{P}\boldsymbol{N}$.

2.6 Eigenstructure

2.6.1 Quasi-Linear Structure

The Flux Jacobian matrix is generally given as

$$\boldsymbol{\mathcal{A}}_N = \boldsymbol{\mathcal{A}}_I N_I = \frac{\partial \boldsymbol{\mathcal{F}}_I}{\partial \boldsymbol{\mathcal{U}}} N_I = \frac{\partial \boldsymbol{\mathcal{F}}_N}{\partial \boldsymbol{\mathcal{U}}}, \qquad \forall I = 1,2,3, \tag{2.24}$$

where $\boldsymbol{\mathcal{A}}_I = \partial \boldsymbol{\mathcal{F}}_I / \partial \boldsymbol{\mathcal{U}}$ and $\boldsymbol{\mathcal{F}}_N = \boldsymbol{\mathcal{F}}_I N_I$.

In order to fully understand the eigenstructure of this matrix, it is useful to separate the momentum and deformation gradient components of $\boldsymbol{\mathcal{U}}$ and $\boldsymbol{\mathcal{F}}_N$ as

$$\boldsymbol{\mathcal{U}} = \begin{pmatrix} \boldsymbol{p} \\ \boldsymbol{F} \end{pmatrix}, \qquad \boldsymbol{\mathcal{F}}_N = \begin{pmatrix} -\boldsymbol{t} \\ -\boldsymbol{v} \otimes \boldsymbol{N} \end{pmatrix}, \qquad \boldsymbol{t} = \boldsymbol{P}\boldsymbol{N}, \qquad \boldsymbol{v} = \frac{1}{\rho_0}\boldsymbol{p}, \tag{2.25}$$

where the tensors in the above expression should be interpreted as column vectors of 9 entries corresponding to each of the tensor components, as explained in *Remark 2.1.* Consequently, $\boldsymbol{\mathcal{A}}_N$ can be written as

$$\boldsymbol{\mathcal{A}}_N = \begin{pmatrix} -\frac{\partial(\boldsymbol{P}\boldsymbol{N})}{\partial \boldsymbol{p}} & -\frac{\partial(\boldsymbol{P}\boldsymbol{N})}{\partial \boldsymbol{F}} \\ -\frac{\partial\left(\frac{1}{\rho_0}\boldsymbol{p}\otimes\boldsymbol{N}\right)}{\partial \boldsymbol{p}} & -\frac{\partial\left(\frac{1}{\rho_0}\boldsymbol{p}\otimes\boldsymbol{N}\right)}{\partial \boldsymbol{F}} \end{pmatrix} = \begin{pmatrix} \boldsymbol{0}_{3\times 3} & -\boldsymbol{\mathcal{C}}_N \\ -\frac{1}{\rho_0}\boldsymbol{I}_N & \boldsymbol{0}_{9\times 9} \end{pmatrix}, \tag{2.26}$$

where

$$[\boldsymbol{\mathcal{C}}_N]_{ijJ} = \frac{\partial P_{iI}}{\partial F_{jJ}} N_I, \quad [\boldsymbol{I}_N]_{iIk} = \delta_{ik} N_I. \tag{2.27}$$

Note that $\boldsymbol{\mathcal{C}}_N$ denotes a normal component of any constitutive material fourth-order tensor $\boldsymbol{\mathcal{C}} = \partial \boldsymbol{P} / \partial \boldsymbol{F}$. For the case of nearly incompressible Neo-Hookean (NH) material, recall first that the stress tensor is formulated as

$$\boldsymbol{P}(\boldsymbol{F}) = \mu J^{-2/3}\left[\boldsymbol{F} - \frac{1}{3}(\boldsymbol{F} : \boldsymbol{F})\boldsymbol{F}^{-T}\right] + \kappa(J-1)J\boldsymbol{F}^{-T}, \tag{2.28}$$

the nonlinear elasticity tensor $\boldsymbol{\mathcal{C}}$ can then be derived as

$$\begin{aligned} \boldsymbol{\mathcal{C}}(\boldsymbol{F}) = \frac{\partial \boldsymbol{P}}{\partial \boldsymbol{F}} = &-\frac{2}{3}\mu J^{-2/3}\boldsymbol{F}\otimes\boldsymbol{F}^{-T} + \frac{2}{9}\mu J^{-2/3}(\boldsymbol{F}:\boldsymbol{F})\boldsymbol{F}^{-T}\otimes\boldsymbol{F}^{-T} \\ &+ \mu J^{-2/3}\boldsymbol{\mathcal{I}} - \frac{1}{3}\mu J^{-2/3}(\boldsymbol{F}:\boldsymbol{F})\boldsymbol{\mathcal{H}} - \frac{2}{3}\mu J^{-2/3}\boldsymbol{F}^{-T}\otimes\boldsymbol{F} \\ &+ \kappa J(2J-1)\boldsymbol{F}^{-T}\otimes\boldsymbol{F}^{-T} + \kappa J(J-1)\boldsymbol{\mathcal{H}}. \end{aligned} \tag{2.29}$$

Here, $\boldsymbol{\mathcal{H}} = \partial \boldsymbol{F}^{-T}/\partial \boldsymbol{F} = -F_{iJ}^{-T}F_{jI}^{-T}$, $\partial J/\partial \boldsymbol{F} = J\boldsymbol{F}^{-T}$ and $\boldsymbol{\mathcal{I}} = \delta_{ij}\delta_{IJ}$. More specifically, some of the engineering problems exhibit relatively small deformation behaviour. Hence, the linear elasticity tensor[18] is usually simplified to

$$\boldsymbol{\mathcal{C}}(\boldsymbol{F} \approx \boldsymbol{I}) = \lambda \boldsymbol{I}\otimes\boldsymbol{I} + \mu(\boldsymbol{\mathcal{I}} + \bar{\boldsymbol{\mathcal{I}}}), \tag{2.30}$$

with the equivalent indicial notations

[18]This is a standard linear isotropic elasticity tensor which can be found in references such as [1,6,7,115,121,125,126].

$$\boldsymbol{I} \otimes \boldsymbol{I} = \delta_{iI}\delta_{jJ}; \qquad \bar{\boldsymbol{\mathcal{I}}} = \delta_{iJ}\delta_{Ij}. \tag{2.31}$$

It is worth mentioning that (2.30) is conspicuously a constant material elasticity tensor. In addition, the Lamé constants μ and λ are expressed in terms of other physical measurements as

$$\mu = \frac{E}{2(1+\nu)}, \qquad \lambda = \frac{\nu E}{(1+\nu)(1-2\nu)}, \qquad \kappa = \lambda + \frac{2}{3}\mu, \tag{2.32}$$

where E is the Young's modulus, ν represents the Poisson's ratio and κ denotes the bulk modulus.

Remark 2.1 *Let $\boldsymbol{S}$ be a second order tensor and its components are shown as:*

$$\boldsymbol{S} = \begin{pmatrix} S_{11} & S_{12} & S_{13} \\ S_{21} & S_{22} & S_{23} \\ S_{31} & S_{32} & S_{33} \end{pmatrix} = \begin{pmatrix} \boldsymbol{S}_1^T \\ \boldsymbol{S}_2^T \\ \boldsymbol{S}_3^T \end{pmatrix}, \tag{2.33}$$

where

$$\boldsymbol{S}_1 = \begin{pmatrix} S_{11} \\ S_{12} \\ S_{13} \end{pmatrix}, \quad \boldsymbol{S}_2 = \begin{pmatrix} S_{21} \\ S_{22} \\ S_{23} \end{pmatrix}, \quad \boldsymbol{S}_3 = \begin{pmatrix} S_{31} \\ S_{32} \\ S_{33} \end{pmatrix}. \tag{2.34}$$

The tensor $\boldsymbol{S}$ is then reshaped into a column vector as

$$\boldsymbol{S} = \begin{pmatrix} \boldsymbol{S}_1 \\ \boldsymbol{S}_2 \\ \boldsymbol{S}_3 \end{pmatrix} = \begin{pmatrix} S_{11} \\ S_{12} \\ S_{13} \\ S_{21} \\ S_{22} \\ S_{23} \\ S_{31} \\ S_{32} \\ S_{33} \end{pmatrix}. \tag{2.35}$$

This sort of convention is very useful in studying the eigenstructure of a matrix.

2.6.2 The Eigendecomposition

With the above definitions at hand, it is now possible to study the eigendecomposition of a Flux Jacobian matrix in order to develop the linearised Riemann solver that will be used to calculate the interface flux. It is well known that the right and left eigenvectors of $\boldsymbol{\mathcal{A}}_N$, namely $\boldsymbol{\mathcal{R}}_\alpha$ and $\boldsymbol{\mathcal{L}}_\alpha$, and their corresponding eigenvalues U_α are solutions of equations as follows:

$$\boldsymbol{\mathcal{A}}_N \boldsymbol{\mathcal{R}}_\alpha = U_\alpha \boldsymbol{\mathcal{R}}_\alpha \tag{2.36a}$$

$$\boldsymbol{\mathcal{L}}_\alpha^T \boldsymbol{\mathcal{A}}_N = U_\alpha \boldsymbol{\mathcal{L}}_\alpha^T. \tag{2.36b}$$

The orthogonality condition[19] between the left and right eigenvectors allows the flux Jacobian (or decoupling) matrix to be expressed as:

$$\boldsymbol{\mathcal{A}}_N = \sum_{\alpha=1}^{12} U_\alpha \frac{\boldsymbol{\mathcal{R}}_\alpha \boldsymbol{\mathcal{L}}_\alpha^T}{\boldsymbol{\mathcal{R}}_\alpha^T \boldsymbol{\mathcal{L}}_\alpha}. \tag{2.37}$$

In order to derive expressions for these eigenvectors, it is of paramount importance to separate their components into

$$\boldsymbol{\mathcal{R}}_\alpha = \begin{pmatrix} \boldsymbol{p}_\alpha^R \\ \boldsymbol{F}_\alpha^R \end{pmatrix}, \quad \boldsymbol{\mathcal{L}}_\alpha = \begin{pmatrix} \boldsymbol{p}_\alpha^L \\ \boldsymbol{F}_\alpha^L \end{pmatrix}. \tag{2.38}$$

Substituting the explicit expression for $\boldsymbol{\mathcal{A}}_N$, viz. (2.26b), into (2.36a), it becomes

$$-\boldsymbol{\mathcal{C}}_N : \boldsymbol{F}_\alpha^R = U_\alpha \boldsymbol{p}_\alpha^R \tag{2.39a}$$

$$-\frac{1}{\rho_0} \boldsymbol{p}_\alpha^R \otimes \boldsymbol{N} = U_\alpha \boldsymbol{F}_\alpha^R. \tag{2.39b}$$

Eliminating $\boldsymbol{F}_\alpha^R$ by inserting (2.39b) into (2.39a) then yields a symmetric eigenvalue problem for $\boldsymbol{p}^R$ as

$$\boldsymbol{\mathcal{C}}_{NN} \boldsymbol{p}_\alpha^R = \rho_0 U_\alpha^2 \boldsymbol{p}_\alpha^R, \tag{2.40}$$

where the symmetric 3×3 tensor $\boldsymbol{\mathcal{C}}_{NN}$ (also known as acoustic tensor) is given as

$$[\boldsymbol{\mathcal{C}}_{NN}]_{ij} = \sum_{I,J}^{3} \mathcal{C}_{iIjJ} N_I N_J. \tag{2.41}$$

In the present nonlinear elastic context, the eigenproblem discussed above leads to 3 pairs of wave speeds, which correspond to the volumetric (or P-wave) U_p and shear (or S-wave) U_s:

$$U_{1,2} = \pm U_p, \tag{2.42a}$$

$$U_{3,4} = U_{5,6} = \pm U_s, \tag{2.42b}$$

where

$$U_p = \sqrt{\frac{\beta + \left(\frac{\alpha}{\Lambda^2} + 2\gamma\right)}{\rho_0}}; \quad U_s = \sqrt{\frac{\beta}{\rho_0}}, \tag{2.43}$$

with further expansions of

$$\alpha = \kappa J^2 + \frac{5}{9} \mu J^{-2/3} (\boldsymbol{F} : \boldsymbol{F}), \tag{2.44a}$$

$$\beta = \mu J^{-2/3}, \tag{2.44b}$$

$$\gamma = -\frac{2}{3} \mu J^{-2/3}, \tag{2.44c}$$

$$\Lambda = \frac{1}{\|\boldsymbol{F}^{-T} \boldsymbol{N}\|}. \tag{2.44d}$$

[19] Orthogonality is discussed in Appendix C.

Here, μ denotes the shear modulus, κ describes the bulk modulus and ρ_0 represents the mass density. Expression (2.42) concludes that the remaining six eigenvalues of matrix $\boldsymbol{\mathcal{A}}_N$ are zero. The matrix $\boldsymbol{\mathcal{A}}_N$ can thus be reconstructed in terms of non-zero wave speeds as

$$\boldsymbol{\mathcal{A}}_N = \sum_{\alpha=1}^{6} U_\alpha \frac{\boldsymbol{\mathcal{R}}_\alpha \boldsymbol{\mathcal{L}}_\alpha^T}{\boldsymbol{\mathcal{R}}_\alpha^T \boldsymbol{\mathcal{L}}_\alpha}. \tag{2.45}$$

Moreover, the eigenvalue structure, viz. (2.40), also leads to 3 pairs of orthogonal eigenvectors, in which the first one $\boldsymbol{n}$ corresponds to the outward unit normal vector in spatial configuration associated to material vector $\boldsymbol{N}$ and the remaining two are arbitrary tangential vectors $\boldsymbol{t}_{1,2}$ orthogonal to $\boldsymbol{n}$. These orthogonal eigenvectors are given by

$$\boldsymbol{\mathcal{R}}_{1,2} = \begin{pmatrix} \boldsymbol{n} \\ \pm\frac{1}{\rho_0 U_p}\boldsymbol{n}\otimes\boldsymbol{N} \end{pmatrix}; \quad \boldsymbol{\mathcal{R}}_{3,4} = \begin{pmatrix} \boldsymbol{t}_1 \\ \pm\frac{1}{\rho_0 U_s}\boldsymbol{t}_1\otimes\boldsymbol{N} \end{pmatrix} \tag{2.46a}$$

and

$$\boldsymbol{\mathcal{R}}_{5,6} = \begin{pmatrix} \boldsymbol{t}_2 \\ \pm\frac{1}{\rho_0 U_s}\boldsymbol{t}_2\otimes\boldsymbol{N} \end{pmatrix}. \tag{2.46b}$$

On the other hand, the following set of left eigenvectors is obtained in an analogous manner as

$$\boldsymbol{\mathcal{L}}_{1,2} = \begin{pmatrix} \boldsymbol{n} \\ \pm\frac{1}{U_p}\boldsymbol{\mathcal{C}} : (\boldsymbol{n}\otimes\boldsymbol{N}) \end{pmatrix}; \quad \boldsymbol{\mathcal{L}}_{3,4} = \begin{pmatrix} \boldsymbol{t}_1 \\ \pm\frac{1}{U_s}\boldsymbol{\mathcal{C}} : (\boldsymbol{t}_1\otimes\boldsymbol{N}) \end{pmatrix} \tag{2.47a}$$

and

$$\boldsymbol{\mathcal{L}}_{5,6} = \begin{pmatrix} \boldsymbol{t}_2 \\ \pm\frac{1}{U_s}\boldsymbol{\mathcal{C}} : (\boldsymbol{t}_2\otimes\boldsymbol{N}) \end{pmatrix}. \tag{2.47b}$$

In the case of infinitesimal elastic deformations where $\boldsymbol{n} \approx \boldsymbol{N}$, the volumetric and shear waves can be reduced to

$$U_p = \sqrt{\frac{\lambda + 2\mu}{\rho_0}}; \quad U_s = \sqrt{\frac{\mu}{\rho_0}}, \tag{2.48}$$

due to the fact that $\boldsymbol{F} \approx \boldsymbol{I}$ and $J \approx 1$. Both waves propagate at constant velocity with their shape unchanged. See Appendix D for a detailed derivation of linear and nonlinear elastic wave speeds.

Noting that $\boldsymbol{\mathcal{R}}_\alpha^T \boldsymbol{\mathcal{L}}_\alpha = 2$ for $\alpha = 1, 2, \ldots, 6$, the Flux Jacobian matrix $\boldsymbol{\mathcal{A}}_N$ can now be re-written as

$$\mathcal{A}_N = \frac{1}{2}\sum_{\alpha=1}^{6} U_\alpha \mathcal{R}_\alpha \mathcal{L}_\alpha^T \tag{2.49a}$$

$$= \frac{1}{2}(\mathcal{R}_1, \ldots, \mathcal{R}_6) \begin{pmatrix} U_p & 0 & 0 & 0 & 0 & 0 \\ 0 & -U_p & 0 & 0 & 0 & 0 \\ 0 & 0 & U_s & 0 & 0 & 0 \\ 0 & 0 & 0 & -U_s & 0 & 0 \\ 0 & 0 & 0 & 0 & U_s & 0 \\ 0 & 0 & 0 & 0 & 0 & -U_s \end{pmatrix} \begin{pmatrix} \mathcal{L}_1^T \\ \vdots \\ \mathcal{L}_6^T \end{pmatrix} \tag{2.49b}$$

$$= \frac{1}{2}\left[U_p(\mathcal{R}_1\mathcal{L}_1^T - \mathcal{R}_2\mathcal{L}_2^T) + U_s(\mathcal{R}_3\mathcal{L}_3^T - \mathcal{R}_4\mathcal{L}_4^T + \mathcal{R}_5\mathcal{L}_5^T - \mathcal{R}_6\mathcal{L}_6^T)\right]. \tag{2.49c}$$

This expression is very useful in deriving a linearised Riemann solver due to the necessity of evaluating the matrix $|\mathcal{A}_N|$.

2.7 Linearised Riemann Solver

The use of Flux Jacobian matrix $\mathcal{A}_N$ (2.49) enables development of an accurate Riemann solver. In general, the interface flux across a surface defined by the material outward-pointing unit normal vector $\boldsymbol{N}$ (where there is a physical or computational discontinuity in the problem variables $\boldsymbol{\mathcal{U}}^- \neq \boldsymbol{\mathcal{U}}^+$) is written as[20]

$$\mathcal{F}_N = \underbrace{\frac{1}{2}\left[\mathcal{F}_N(\boldsymbol{\mathcal{U}}^-) + \mathcal{F}_N(\boldsymbol{\mathcal{U}}^+)\right]}_{\text{unstable flux}} \underbrace{-\frac{1}{2}\int_{\boldsymbol{\mathcal{U}}^-}^{\boldsymbol{\mathcal{U}}^+} |\mathcal{A}_N|\, \mathrm{d}\boldsymbol{\mathcal{U}}}_{\text{stabilising term}}, \tag{2.50}$$

where the above integral is taken along an arbitrary path from $\boldsymbol{\mathcal{U}}^-$ to $\boldsymbol{\mathcal{U}}^+$. From equation above, the first term denotes the unstable flux (simple arithmetic average from the left and right states), implying no consideration for wave directional character. The second (stabilising) term can be interpreted as artificial diffusion that damps the instabilities arising in the first term. It is worth pointing out that the integration paths of Osher's numerical flux are taken to be integral curves associated with a set of right eigenvectors [53–57]. Another conventional Roe's approximate Riemann solver reveals that an averaged Jacobian matrix $\hat{\mathcal{A}}_N$ is first sought, which then leads to the calculations of averaged eigenvalues, eigenvectors and wave strengths [45–52].

[20]The flux computation can be identified as a particular case of Jameson-Schmidt-Turkel (JST) scheme.

Firstly, the Jacobian matrix $|\boldsymbol{\mathcal{A}}_N|$ reads as follows:

$$|\boldsymbol{\mathcal{A}}_N| = \frac{1}{2}\sum_{\alpha=1}^{6} |U_\alpha| \boldsymbol{\mathcal{R}}_\alpha \boldsymbol{\mathcal{L}}_\alpha^T \tag{2.51a}$$

$$= \frac{1}{2}(\boldsymbol{\mathcal{R}}_1, \ldots, \boldsymbol{\mathcal{R}}_6) \begin{pmatrix} U_p & 0 & 0 & 0 & 0 & 0 \\ 0 & U_p & 0 & 0 & 0 & 0 \\ 0 & 0 & U_s & 0 & 0 & 0 \\ 0 & 0 & 0 & U_s & 0 & 0 \\ 0 & 0 & 0 & 0 & U_s & 0 \\ 0 & 0 & 0 & 0 & 0 & U_s \end{pmatrix} \begin{pmatrix} \boldsymbol{\mathcal{L}}_1^T \\ \vdots \\ \boldsymbol{\mathcal{L}}_6^T \end{pmatrix} \tag{2.51b}$$

$$= \frac{1}{2}\left[U_p(\boldsymbol{\mathcal{R}}_1\boldsymbol{\mathcal{L}}_1^T + \boldsymbol{\mathcal{R}}_2\boldsymbol{\mathcal{L}}_2^T) + U_s(\boldsymbol{\mathcal{R}}_3\boldsymbol{\mathcal{L}}_3^T + \boldsymbol{\mathcal{R}}_4\boldsymbol{\mathcal{L}}_4^T + \boldsymbol{\mathcal{R}}_5\boldsymbol{\mathcal{L}}_5^T + \boldsymbol{\mathcal{R}}_6\boldsymbol{\mathcal{L}}_6^T)\right]. \tag{2.51c}$$

Substituting (2.46) and (2.47) into (2.51), after some simple but lengthy algebra, leads to the following expression:

$$|\boldsymbol{\mathcal{A}}_N| = \begin{pmatrix} U_s\boldsymbol{I}_{3\times3} & \boldsymbol{0}_{3\times9} \\ \boldsymbol{0}_{9\times3} & \frac{1}{\rho_0 U_s}\boldsymbol{\mathcal{C}}^* \end{pmatrix} + \begin{pmatrix} (U_p - U_s)\boldsymbol{n}\otimes\boldsymbol{n} & \boldsymbol{0}_{3\times9} \\ \boldsymbol{0}_{9\times3} & (\frac{1}{\rho_0 U_p} - \frac{1}{\rho_0 U_s})(\boldsymbol{n}\otimes\boldsymbol{N})\otimes[\boldsymbol{\mathcal{C}}\colon(\boldsymbol{n}\otimes\boldsymbol{N})] \end{pmatrix}$$

where the tensor $\boldsymbol{\mathcal{C}}^*$ is shown as

$$[\boldsymbol{\mathcal{C}}^*]_{iIjJ} = \sum_a \boldsymbol{\mathcal{C}}_{iajJ} N_a N_I.$$

Since U_s grows with $\sqrt{\mu}$ and $\boldsymbol{\mathcal{C}}$ grows with μ, $|\boldsymbol{\mathcal{A}}_N|$ will not become unbounded in the absence of shear strength (terms appeared as divided or multiplied by U_s will simply vanish). The integral of stabilising term across the discontinuity can be reduced to

$$\int_{\boldsymbol{\mathcal{U}}^-}^{\boldsymbol{\mathcal{U}}^+} |\boldsymbol{\mathcal{A}}_N|\, d\boldsymbol{\mathcal{U}} = \int_{\boldsymbol{\mathcal{U}}^-}^{\boldsymbol{\mathcal{U}}^+} \begin{pmatrix} U_s\, d\boldsymbol{p} \\ \frac{1}{\rho_0 U_s}\, d\boldsymbol{t}\otimes\boldsymbol{N} \end{pmatrix} + \begin{pmatrix} (U_p - U_s)\boldsymbol{n}\, dp_n \\ (\frac{1}{\rho_0 U_p} - \frac{1}{\rho_0 U_s})(\boldsymbol{n}\otimes\boldsymbol{N})\, dt_n \end{pmatrix} \tag{2.52}$$

where

$$d\boldsymbol{t} = (\boldsymbol{\mathcal{C}}\colon d\boldsymbol{F})\,\boldsymbol{N} = (d\boldsymbol{P})\boldsymbol{N}; \qquad dp_n = d\boldsymbol{p}\cdot\boldsymbol{n}; \qquad dt_n = d\boldsymbol{t}\cdot\boldsymbol{n}.$$

It is normally impossible to integrate (2.52) exactly in a nonlinear case. However, the assumption of linearity in engineering analysis (for which the wave speeds are independent of the state of deformation (2.48)) enables (2.52) to be evaluated exactly as

$$\int_{\boldsymbol{\mathcal{U}}^-}^{\boldsymbol{\mathcal{U}}^+} |\boldsymbol{\mathcal{A}}_N|\, \mathrm{d}\boldsymbol{\mathcal{U}} = \begin{pmatrix} U_s(\boldsymbol{p}^+ - \boldsymbol{p}^-) \\ \frac{1}{\rho_0 U_s}(\boldsymbol{t}^+ - \boldsymbol{t}^-)\otimes\boldsymbol{N} \end{pmatrix} + \begin{pmatrix} (U_p - U_s)(p_n^+ - p_n^-)\boldsymbol{n} \\ \left(\frac{1}{\rho_0 U_p} - \frac{1}{\rho_0 U_s}\right)(t_n^+ - t_n^-)(\boldsymbol{n}\otimes\boldsymbol{N}) \end{pmatrix}. \tag{2.53}$$

A generalisation of this linearised Riemann solver will be described in Chapter 5 (a method for nonlinear cases).

Chapter 3

Irreversible Processes and Elements of Lagrangian Rapid Dynamics

"Although mechanical energy is indestructible, there is a universal tendency to its dissipation, which produces throughout the system a gradual augmentation and diffusion of heat, cessation of motion and exhaustion of the potential energy of the material Universe".

Lord Kelvin (1824 – 1907)

3.1 Introductory Remarks

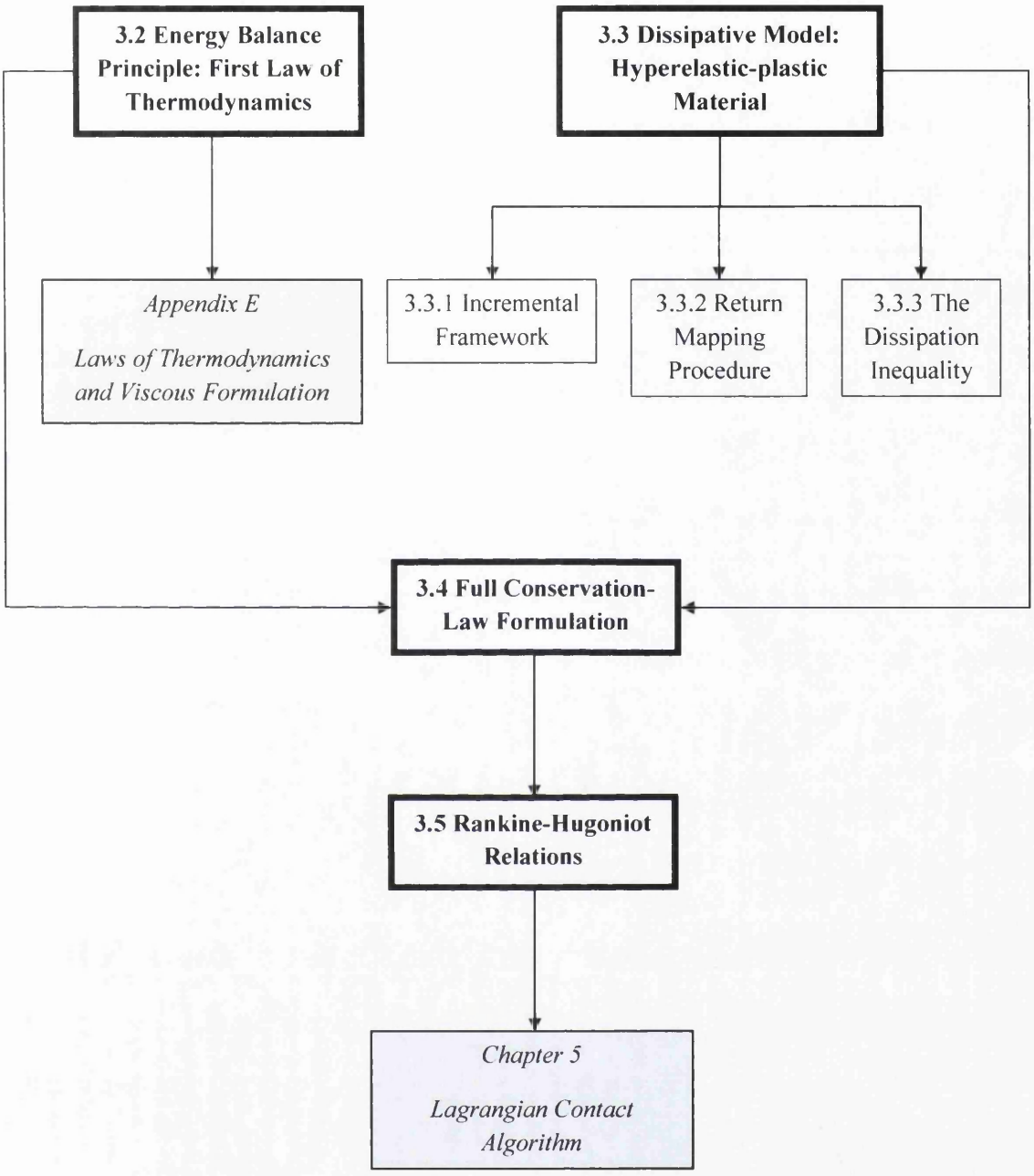

Figure 3.1: Content and guide to this chapter.

Many applications in engineering and physics deal with irreversible processes, where the constitutive models are more sophisticated than those of isothermal elasticity. Under such circumstances, thermal effects and inelastic dissipative mechanism cannot be neglected.

Recently, problems concerned with non-isothermal elasticity are arising in connection with materials and structures employed in aerospace, nuclear fields and other specialised applications. These problems are generally known as thermoelasticity.

In principle, thermoelasticity deals with the interaction between temperature, stress and elastic deformation due to mechanical and thermal loadings. A wealth of literature has been devoted to the numerical solutions of dynamic thermoelasticity. These numerical methods include Laplace-transform FEM and semi-discrete methods [127–129]. In recent years, Discontinuous Galerkin (DG) method has been used by [130–132] for solving coupled thermoelastic problems. For simplicity, this thesis only deals with an isothermal process where the thermodynamic variables (i.e. entropy η and temperature θ) can be ignored. In order to achieve a complete understanding on non-isothermal process, it is necessary to include a chapter dealing with entropy and Second Law of Thermodynamics (see Appendix E).

Many materials of practical importance do not behave in an elastic manner at high level of stress. They exhibit plastic (or irrecoverable) behaviour by virtue of the fact that these materials fail to return to their undeformed state when surface forces are relaxed.[1] A conservative Eulerian formulation of plasticity was first proposed by Plohr and Sharp [133]. Numerical solutions for elastoplastic flows based on this formulation[2] have been discussed in [118, 134–136].

This chapter is organised as follows. In order to describe an equation governs such irreversible processes, it is essential to solve for an additional state variable, namely the energy, by using the First Law of Thermodynamics (or energy balance principle[3]), which does not specify the direction of energy transfer. With the inclusion of this principle a complete conservation-law formulation will be developed. Moreover, the Rankine-Hugoniot relations are introduced in dealing with the behaviour of shocks waves. In particular, the jump condition of linear momentum variable will be used to derive a general Riemann solver which is applicable to nonlinear cases. Figure 3.1 shows the suggested roadmap to this chapter.

3.2 Energy Balance Principle: First Law of Thermodynamics

The rate of change of the total energy in a continuum is formulated mathematically as

$$\frac{d}{dt}\int_V E_T\, dV = \int_{\partial V} \boldsymbol{t}\cdot\boldsymbol{v}\, dA - \int_{\partial V} \boldsymbol{Q}\cdot\boldsymbol{N}\, dA, \tag{3.1}$$

where E_T is the total energy per unit of undeformed volume, $\boldsymbol{t}$ describes the traction vector, $\boldsymbol{v}$ stands for the velocity vector, $\boldsymbol{Q}$ denotes the heat flow vector and $\boldsymbol{N}$ represents the outward-pointing unit normal vector in reference configuration. For

[1]The irrecoverable behaviour depends on the deformation history of an inelastic material.

[2]The use of Eulerian coordinates avoids the problems of mesh tangling and remeshing. In contrast, Lagrangian formulation is simpler and faster in computation, but it suffers from severe mesh distortions especially in problems having large deformations.

[3]The famous quote made by Clausius in 1865: *The energy of the universe is constant.* This statement is rather loose from rigorous theoretical standpoint.

simplicity, the heat source term is neglected in the equation above. The corresponding differential balance law of (3.1) is given by

$$\frac{\partial E_T}{\partial t} + \boldsymbol{\nabla}_0 \cdot \left(\boldsymbol{Q} - \boldsymbol{P}^T \boldsymbol{v}\right) = 0. \tag{3.2}$$

In order to derive a more physically meaningful equation, it is useful to combine (2.4) and (2.7) into (3.2), which yields

$$\frac{\partial e}{\partial t} = \boldsymbol{P} : \frac{\partial \boldsymbol{F}}{\partial t} - \boldsymbol{\nabla}_0 \cdot \boldsymbol{Q}, \quad e = E_T - \psi_{kin} - \psi_{ext}, \tag{3.3}$$

where $\psi_{ext} = -\rho_0 \boldsymbol{b} \cdot \boldsymbol{x}$ is the potential energy due to body force, $\psi_{kin} = (\boldsymbol{p} \cdot \boldsymbol{p})/2\rho_0$ represents the kinetic energy and e denotes the internal energy per unit of undeformed volume. For the case of thermoelasticity, e contains both the elastic strain energy and the heat component.

3.3 Dissipative Model: Hyperelastic-plastic Material

Many practical applications often exhibit some permanent inelastic deformations. In order to describe this irrecoverable behaviour, the simplest case of rate-independent Von-Mises plasticity with isotropic hardening will be considered [2, 6, 7].

First, it is essential to define a strain energy functional in terms of the elastic principal stretches $\lambda_{e,\alpha}$:[4]

$$\psi(\lambda_{e,1}, \lambda_{e,2}, \lambda_{e,3}) = \psi_{dev}(J^{-1/3}\lambda_{e,1}, J^{-1/3}\lambda_{e,2}, J^{-1/3}\lambda_{e,3}) + \psi_{vol}(J), \tag{3.4}$$

where

$$\psi_{dev} = \mu\left[(\ln \lambda_{e,1})^2 + (\ln \lambda_{e,2})^2 + (\ln \lambda_{e,3})^2\right] - \frac{1}{3}\mu(\ln J)^2 \tag{3.5}$$

and

$$\psi_{vol} = \frac{1}{2}\kappa(\ln J)^2; \qquad \kappa = \lambda + \frac{2}{3}\mu; \qquad \ln J = \sum_{\alpha=1}^{3} \ln \lambda_{e,\alpha}. \tag{3.6}$$

The Kirchhoff stress tensor is conveniently decomposed into its principal components as

$$\tau_{\alpha\alpha} = J\sigma_{\alpha\alpha} = \tau'_{\alpha\alpha} + Jp, \qquad \forall \quad \alpha = 1, 2, 3. \tag{3.7}$$

Here, the deviatoric stress component $\tau'_{\alpha\alpha}$ is

$$\tau'_{\alpha\alpha} = \frac{\partial \psi_{dev}}{\partial \ln \lambda_{e,\alpha}} = 2\mu \ln \lambda_{e,\alpha} - \frac{2}{3}\mu \ln J \tag{3.8}$$

and the pressure p is defined as

$$p = \frac{d\psi_{vol}}{dJ} = \kappa \frac{\ln J}{J}. \tag{3.9}$$

[4]Formulations can be greatly simplified if the principal directions are used.

3.3.1 Incremental Framework

The typical initial hypothesis in plasticity is postulated such that no further permanent deformation takes place during the motion from time n to $n+1$. This hypothesis then leads to a trial left Cauchy-Green tensor[5] which is established as

$$\boldsymbol{b}_{e,n+1}^{trial} = \boldsymbol{F}_{n+1}\boldsymbol{C}_{p,n}^{-1}\boldsymbol{F}_{n+1}^{T}. \tag{3.10}$$

The expression above represents an exact time integration of $\boldsymbol{b}_e$ that results from the overall change in deformation based on the assumption that there is no further change in irrecoverable strain, that is, $[d\boldsymbol{b}_e(\boldsymbol{F},\boldsymbol{C}_p)/dt]_{\boldsymbol{C}_p}$.

Insofar as the principal direction is being used, a spectral decomposition can be performed on $\boldsymbol{b}_{e,n+1}^{trial}$, which yields

$$\boldsymbol{b}_{e,n+1}^{trial} = \sum_{\alpha=1}^{3} \left(\lambda_{e,\alpha}^{trial}\right)^2 \boldsymbol{n}_{\alpha}^{trial} \otimes \boldsymbol{n}_{\alpha}^{trial}, \tag{3.11}$$

where $\lambda_{e,\alpha}^{trial}$ describes the trial elastic stretches and $\boldsymbol{n}_{\alpha}^{trial}$ denotes the principal directions. With the help of $\lambda_{e,\alpha}^{trial}$, the trial deviatoric Kirchhoff stress tensor can be subsequently computed:

$$\boldsymbol{\tau}^{'trial} = \sum_{\alpha=1}^{3} \tau_{\alpha\alpha}^{'trial} \boldsymbol{n}_{\alpha}^{trial} \otimes \boldsymbol{n}_{\alpha}^{trial}; \qquad \tau_{\alpha\alpha}^{'trial} = 2\mu \ln \lambda_{e,\alpha}^{trial} - \frac{2}{3}\mu \ln J_{n+1}. \tag{3.12}$$

By virtue of the equation above, no plastic deformation involved during time increment $\Delta t = t^{n+1} - t^{n}$. However, further permanent behaviour will generally occur in order to accommodate the inelastic constitutive requirement. To this effect, the so-called return mapping procedure should be carried out to ensure that the trial deviatoric stress tensor returns to the yield surface. This represents the change of $\boldsymbol{b}_e$ at constant $\boldsymbol{F}$ but varying $\boldsymbol{C}_p$ (that is, $[d\boldsymbol{b}_e(\boldsymbol{F},\boldsymbol{C}_p)/dt]_{\boldsymbol{F}}$) and the total evolution of $\boldsymbol{b}_e$ is

$$\frac{d\boldsymbol{b}_e}{dt} = \left.\frac{d\boldsymbol{b}_e}{dt}\right|_{\boldsymbol{C}_p} + \left.\frac{d\boldsymbol{b}_e}{dt}\right|_{\boldsymbol{F}}. \tag{3.13}$$

Since the Von Mises plasticity is considered, its plastic flows is restricted to behave in a purely isochoric manner, $\det(\boldsymbol{F}_p) = 1$. Under such circumstance, $J_{n+1} = J_{e,n+1} = \det(\boldsymbol{F}_{n+1})$. This plasticity is defined by a yield criterion which depends on deviatoric Kirchhoff stress tensor $\boldsymbol{\tau}'$ and the hardening variable $\bar{\varepsilon}_p$:

$$f(\boldsymbol{\tau}', \bar{\varepsilon}_p) = \sqrt{\frac{3}{2}(\boldsymbol{\tau}' : \boldsymbol{\tau}')} - \bar{\tau}_y \leq 0; \quad \bar{\tau}_y = \bar{\tau}_y^0 + H\bar{\varepsilon}_p, \tag{3.14}$$

where $\bar{\tau}_y^0$ is the initial yield stress and H denotes the constant hardening parameter. The yield function, viz. (3.14), is basically determined by a generalised scalar Von Mises equivalent stress $\sqrt{\frac{3}{2}(\boldsymbol{\tau}' : \boldsymbol{\tau}')}$ and this inequality has to be satisfied. Otherwise,

[5]The left Cauchy-Green deformation tensor is often called the Finger deformation tensor.

$\Delta\gamma$ and ν_α^{n+1} need to be evaluated to ensure that $\boldsymbol{\tau}'$ returns back to the yield surface (which will be discussed in the following section).

Now assume that an updated elastic stretch $\lambda_{e,\alpha}^{n+1}$ has been accomplished, it is then easy to determine the resulting elastic left Cauchy-Green tensor $\boldsymbol{b}_{e,n+1}$ (which includes an additional change in regard to the permanent deformation) as

$$\boldsymbol{b}_{e,n+1} = \sum_{\alpha=1}^{3} \left(\lambda_{e,\alpha}^{n+1}\right)^2 \boldsymbol{n}_\alpha^{n+1} \otimes \boldsymbol{n}_\alpha^{n+1}, \tag{3.15}$$

where $\boldsymbol{n}_\alpha^{n+1} = \boldsymbol{n}_\alpha^{trial}$ [7]. Consequently, the updated inverse plastic right Cauchy-Green strain tensor is obtained as

$$\boldsymbol{C}_{p,n+1}^{-1} = \boldsymbol{F}_{n+1}^{-1} \boldsymbol{b}_{e,n+1} \boldsymbol{F}_{n+1}^{-T}. \tag{3.16}$$

3.3.2 Return Mapping Procedure

As discussed previously, some modifications are made to the elastic stretch $\lambda_{e,\alpha}^{n+1}$ and the deviatoric Kirchhoff stress $\tau_{\alpha\alpha}^{'}$ under the condition of $f(\boldsymbol{\tau}^{'trial}, \bar{\varepsilon}_{p,n}) > 0$.

The updated deviatoric Kirchhoff stress in principal direction is corrected as follows:

$$\tau_{\alpha\alpha}^{'} = \tau_{\alpha\alpha}^{'trial} - 2\mu\Delta\gamma\nu_\alpha^{n+1}. \tag{3.17}$$

Equation above indicates that $\boldsymbol{\tau}^{'}$ is proportional to $\boldsymbol{\tau}^{'trial}$ with a corrected magnitude of $-2\mu\Delta\gamma$. This is obviously known as radial return mapping [6,7] (see Figure 3.2). The dimensionless direction vector $\boldsymbol{\nu}$ is represented as

$$\nu_\alpha^{n+1} = \frac{\tau_{\alpha\alpha}^{'trial}}{\sqrt{\frac{2}{3}}\|\boldsymbol{\tau}^{'trial}\|}; \quad \|\boldsymbol{\tau}^{'trial}\| = \sqrt{\boldsymbol{\tau}^{'trial} : \boldsymbol{\tau}^{'trial}}, \tag{3.18}$$

and eventually, the only remaining unknown in (3.17) is $\Delta\gamma$. With the aid of $\Delta\bar{\varepsilon}_p = \Delta\gamma$ [7], the incremental plastic multiplier, $\Delta\gamma$, can be derived as

$$\Delta\gamma = \begin{cases} \frac{f(\boldsymbol{\tau}^{'trial}, \bar{\varepsilon}_{p,n})}{3\mu + H} & \text{if } f(\boldsymbol{\tau}^{'trial}, \bar{\varepsilon}_{p,n}) > 0; \\ 0 & \text{if } f(\boldsymbol{\tau}^{'trial}, \bar{\varepsilon}_{p,n}) \leq 0. \end{cases} \tag{3.19}$$

Once $\Delta\gamma$ and ν_α^{n+1} are known, the elastic stretch is readily computed

$$\lambda_{e,\alpha}^{n+1} = \text{Exp}\left(\ln \lambda_{e,\alpha}^{trial} - \Delta\gamma\nu_\alpha^{n+1}\right). \tag{3.20}$$

By substituting (3.18) into (3.17) for ν_α^{n+1}, the corrected deviatoric stress yields

$$\tau_{\alpha\alpha}^{'} = \left(1 - \frac{2\mu\Delta\gamma}{\sqrt{2/3}\|\boldsymbol{\tau}^{'trial}\|}\right) \tau_{\alpha\alpha}^{'trial}. \tag{3.21}$$

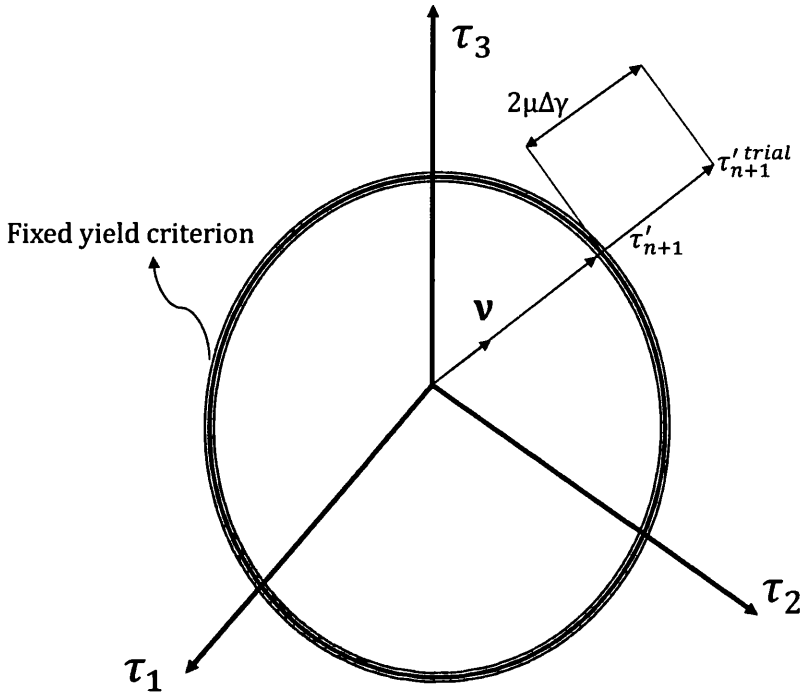

(a)

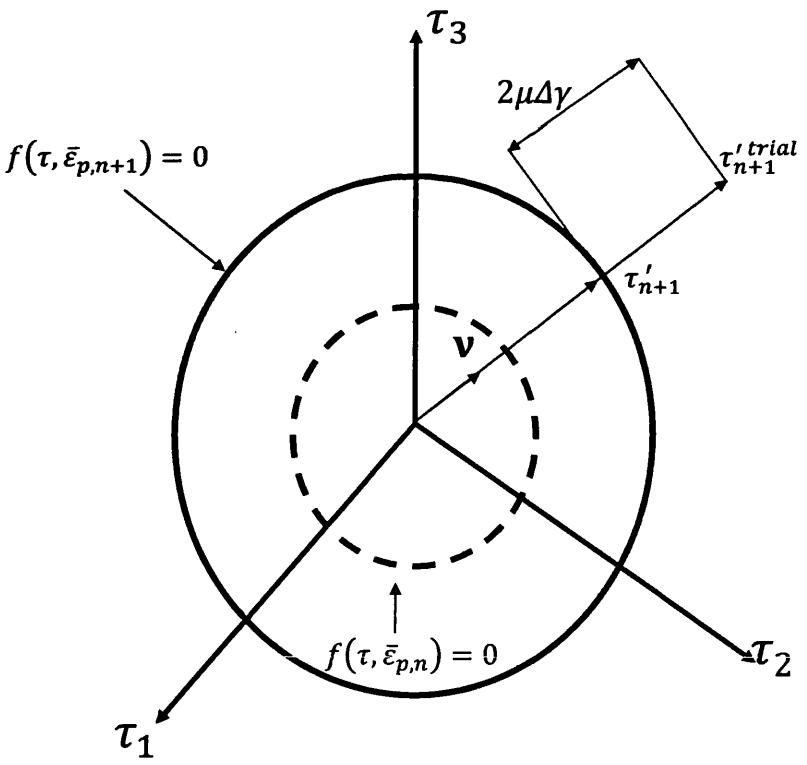

(b)

Figure 3.2: Radial return mapping procedure: (a) Perfect plasticity; (b) Isotropic linear hardening plasticity.

Recall that within the elastic domain ($\Delta\gamma = 0$), no further update for $\boldsymbol{b}_{e,n+1}$ is required:

$$\lambda_{e,\alpha}^{n+1} = \lambda_{e,\alpha}^{trial}; \qquad \tau_{\alpha\alpha}^{'} = \tau_{\alpha\alpha}^{'trial}. \tag{3.22}$$

In order to move on to the next time step, it is necessary to record the current state of inelastic deformations as

$$\bar{\varepsilon}_{p,n+1} = \bar{\varepsilon}_{p,n} + \Delta\gamma, \tag{3.23}$$

where $\bar{\varepsilon}_{p,n+1}$ is the updated value of Von Mises equivalent plastic strain.

An algorithmic procedure for implementing the rate-independent Von Mises plasticity with isotropic hardening is illustrated in Algorithm (3.3.1).

Algorithm 3.3.1: EVALUATION OF $\boldsymbol{P}(\boldsymbol{F}_{n+1}, \boldsymbol{C}_{p,n}^{-1}, \bar{\varepsilon}_{p,n})$

(1). Given $\boldsymbol{F}_{n+1}$, $\boldsymbol{C}_{p,n}^{-1}$ and $\bar{\varepsilon}_{p,n}$.
(2). Initiate $\Delta\gamma = \nu_{\alpha}^{n+1} = 0$.
(3). Evaluate $J_{n+1} = \det \boldsymbol{F}_{n+1}$.
(4). Solve pressure $p = \kappa \frac{\ln J_{n+1}}{J_{n+1}}$.
(5). Compute trial left strain tensor $\boldsymbol{b}_{e,n+1}^{trial} = \boldsymbol{F}_{n+1}\boldsymbol{C}_{p,n}^{-1}\boldsymbol{F}_{n+1}^{T}$.
(6). Spectral decomposition: $\boldsymbol{b}_{e,n+1}^{trial} = \sum_{\alpha=1}^{3}(\lambda_{e,\alpha}^{trial})^2\, \boldsymbol{n}_{\alpha}^{trial} \otimes \boldsymbol{n}_{\alpha}^{trial}$.
(7). Set $\boldsymbol{n}_{\alpha}^{n+1} = \boldsymbol{n}_{\alpha}^{trial}$.
(8). Trial Kirchhoff stress: $\tau_{\alpha\alpha}^{'trial} = 2\mu \ln \lambda_{e,\alpha}^{trial} - \frac{2}{3}\mu \ln J_{n+1}$.
if $(f(\boldsymbol{\tau}^{'trial}, \bar{\varepsilon}_{p,n}) > 0)$
then
(9). Direction vector: $\nu_{\alpha}^{n+1} = \frac{\tau_{\alpha\alpha}^{'trial}}{\sqrt{\frac{2}{3}}\|\boldsymbol{\tau}^{'trial}\|}$.
(10). Plastic Multiplier: $\Delta\gamma = \frac{f(\boldsymbol{\tau}^{'trial}, \bar{\varepsilon}_{p,n})}{3\mu + H}$.
(11). Elastic stretch: $\lambda_{e,\alpha}^{n+1} = \mathrm{Exp}\,(\ln \lambda_{e,\alpha}^{trial} - \Delta\gamma\nu_{\alpha}^{n+1})$.
(12). Return map: $\tau_{\alpha\alpha}' = \left(1 - \frac{2\mu\Delta\gamma}{\sqrt{2/3}\|\boldsymbol{\tau}^{'trial}\|}\right)\tau_{\alpha\alpha}^{'trial}$.
(13). Update stress: $\tau_{\alpha\alpha} = \tau_{\alpha\alpha}' + Jp; \quad \boldsymbol{\tau} = \sum_{\alpha=1}^{3}\tau_{\alpha\alpha}\boldsymbol{n}_{\alpha}^{n+1} \otimes \boldsymbol{n}_{\alpha}^{n+1}$.
(14). First Piola-Kirchhoff stress tensor: $\boldsymbol{P} = \boldsymbol{\tau}\boldsymbol{F}^{-T}$.
(15). Update $\boldsymbol{b}_{e,n+1} = \sum_{\alpha=1}^{3}(\lambda_{e,\alpha}^{n+1})^2\, \boldsymbol{n}_{\alpha}^{n+1} \otimes \boldsymbol{n}_{\alpha}^{n+1}$.
(16). Update $\boldsymbol{C}_{p,n+1}^{-1} = \boldsymbol{F}_{n+1}^{-1}\boldsymbol{b}_{e,n+1}\boldsymbol{F}_{n+1}^{-T}; \quad \bar{\varepsilon}_{p,n+1} = \bar{\varepsilon}_{p,n} + \Delta\gamma$.
return $(\boldsymbol{P}_{n+1})$

3.3.3 The Dissipation Inequality

The strain energy functional of Von Mises plasticity with isotropic hardening is postulated as:

$$\psi = \psi(\boldsymbol{\varepsilon}_e, \bar{\varepsilon}_p); \qquad \boldsymbol{\varepsilon}_e = \ln \boldsymbol{V}_e = \frac{1}{2}\ln \boldsymbol{b}_e, \tag{3.24}$$

where $\boldsymbol{\varepsilon}_e$ denotes the elastic logarithmic stretch tensor and $\bar{\varepsilon}_p$ represents the accummulated plastic strain. The time derivative of (3.24) gives

$$\dot{\psi} = \frac{\partial\psi}{\partial\boldsymbol{\varepsilon}_e} : \dot{\boldsymbol{\varepsilon}}_e + \frac{\partial\psi}{\partial\bar{\varepsilon}_p}\dot{\bar{\varepsilon}}_p; \qquad \frac{\partial\psi}{\partial\bar{\varepsilon}_p} = H\bar{\varepsilon}_p, \tag{3.25}$$

where the scalar-valued function, $\partial\psi/\partial\bar{\varepsilon}_p$, associated to isotropic hardening curve [2]. The evolution of the internal variable, $\bar{\varepsilon}_p$, is described as $\dot{\bar{\varepsilon}}_p = \dot{\gamma}$, which follows from the hypothesis of associativity [6]. By employing chain rule to $\boldsymbol{\varepsilon}_e$ in (3.25a) yields

$$\dot{\psi} = \frac{1}{2}\frac{\partial\psi}{\partial\boldsymbol{\varepsilon}_e} : \frac{\partial(\ln \boldsymbol{b}_e)}{\partial \boldsymbol{b}_e} : \dot{\boldsymbol{b}}_e + \dot{\gamma} H \bar{\varepsilon}_p \tag{3.26a}$$

$$= \frac{1}{2}\underbrace{\frac{\partial\psi}{\partial\boldsymbol{\varepsilon}_e} : \frac{\partial(\ln \boldsymbol{b}_e)}{\partial \boldsymbol{b}_e}\boldsymbol{b}_e}_{\partial\psi/\partial\boldsymbol{\varepsilon}_e} : \dot{\boldsymbol{b}}_e\boldsymbol{b}_e^{-1} + \dot{\gamma} H \bar{\varepsilon}_p \tag{3.26b}$$

$$= \frac{1}{2}\frac{\partial\psi}{\partial\boldsymbol{\varepsilon}_e} : \dot{\boldsymbol{b}}_e\boldsymbol{b}_e^{-1} + \dot{\gamma} H \bar{\varepsilon}_p \tag{3.26c}$$

$$= \frac{\partial\psi}{\partial\boldsymbol{\varepsilon}_e} : \boldsymbol{l}_e + \dot{\gamma} H \bar{\varepsilon}_p \tag{3.26d}$$

$$= \boldsymbol{\tau} : \boldsymbol{l}_e + \dot{\gamma} H \bar{\varepsilon}_p. \tag{3.26e}$$

where $\boldsymbol{l}_e = \dot{\boldsymbol{F}}_e\boldsymbol{F}_e^{-1}$ is the velocity gradient and $\boldsymbol{b}_e = \boldsymbol{F}_e\boldsymbol{F}_e^T = \boldsymbol{F}\boldsymbol{F}_p^{-1}\boldsymbol{F}_p^{-T}\boldsymbol{F}^T$. During isothermal process, the Clausius-Planck inequality simplifies to

$$D_{\text{int}} = \boldsymbol{P} : \dot{\boldsymbol{F}} - \dot{\psi} \geq 0 \tag{3.27a}$$

$$= \boldsymbol{\tau} : \boldsymbol{l} - \dot{\psi} \geq 0. \tag{3.27b}$$

Substituting (3.26e) into above expression gives

$$D_{\text{int}} = \boldsymbol{\tau} : (\boldsymbol{l} - \boldsymbol{l}_e) - \dot{\gamma} H \bar{\varepsilon}_p \geq 0 \tag{3.28a}$$

$$= \boldsymbol{\tau} : \boldsymbol{l}_p - \dot{\gamma} H \bar{\varepsilon}_p \geq 0 \tag{3.28b}$$

$$= \dot{w}_p \left(1 - \frac{H\bar{\varepsilon}_p}{\bar{\tau}}\right) \geq 0, \tag{3.28c}$$

where $\boldsymbol{l}_p = \boldsymbol{l} - \boldsymbol{l}_e$. Here, $\dot{w}_p = \boldsymbol{\tau} : \boldsymbol{l}_p = \dot{\gamma}\bar{\tau}$ describes the rate of plastic dissipation and the Von Mises equivalent stress, $\bar{\tau}$, is defined as

$$\bar{\tau} = \sqrt{\frac{3}{2}\boldsymbol{\tau}' : \boldsymbol{\tau}'}.$$

For the case of perfectly plastic material, that is $H = 0$, (3.28) reduces further to

$$D_{\text{int}} = \dot{w}_p = \boldsymbol{\tau} : \boldsymbol{l}_p \geq 0.$$

3.4 Full Conservation-Law Formulation

More generally, the conservation-law formulation can be further developed by including the energy balance principle E_T (or First Law of Thermodynamics). For the sake of convenience, the differential laws of these balance principles are presented as follows:

$$\frac{\partial \boldsymbol{p}}{\partial t} - \boldsymbol{\nabla}_0 \cdot \boldsymbol{P} = \rho_0 \boldsymbol{b}, \tag{3.29a}$$

$$\frac{\partial \boldsymbol{F}}{\partial t} - \boldsymbol{\nabla}_0 \cdot (\boldsymbol{v} \otimes \boldsymbol{I}) = \boldsymbol{0}, \tag{3.29b}$$

$$\frac{\partial E_T}{\partial t} - \boldsymbol{\nabla}_0 \cdot (\boldsymbol{P}^T \boldsymbol{v} - \boldsymbol{Q}) = 0, \tag{3.29c}$$

where $\boldsymbol{p} = \rho_0 \boldsymbol{v}$ is the linear momentum per unit of material volume, ρ_0 represents the material density, $\boldsymbol{v}$ is the velocity field, $\boldsymbol{b}$ stands for the body force per unit mass, $\boldsymbol{F}$ indicates the deformation gradient tensor, $\boldsymbol{P}$ is the first Piola-Kirchhoff stress tensor, E_T is the total energy per unit of undeformed volume, $\boldsymbol{Q}$ is the heat flux vector and $\boldsymbol{\nabla}_0$ denotes the material gradient operator in undeformed space.

The above laws can be formulated in a first order system of conservative equations as

$$\frac{\partial \boldsymbol{\mathcal{U}}}{\partial t} + \frac{\partial \boldsymbol{\mathcal{F}}_I}{\partial X_I} = \boldsymbol{\mathcal{S}}, \qquad \forall I = 1, 2, 3; \tag{3.30}$$

where

$$\boldsymbol{\mathcal{U}} = \begin{pmatrix} p_1 \\ p_2 \\ p_3 \\ F_{11} \\ F_{12} \\ F_{13} \\ F_{21} \\ F_{22} \\ F_{23} \\ F_{31} \\ F_{32} \\ F_{33} \\ E_T \end{pmatrix}, \quad \boldsymbol{\mathcal{F}}_I = \begin{pmatrix} -P_{1I} \\ -P_{2I} \\ -P_{3I} \\ -\delta_{I1} v_1 \\ -\delta_{I2} v_1 \\ -\delta_{I3} v_1 \\ -\delta_{I1} v_2 \\ -\delta_{I2} v_2 \\ -\delta_{I3} v_2 \\ -\delta_{I1} v_3 \\ -\delta_{I2} v_3 \\ -\delta_{I3} v_3 \\ Q_I - P_{iI} v_i \end{pmatrix}, \quad \boldsymbol{\mathcal{S}} = \begin{pmatrix} \rho_0 b_1 \\ \rho_0 b_2 \\ \rho_0 b_3 \\ 0 \\ 0 \\ 0 \\ 0 \\ 0 \\ 0 \\ 0 \\ 0 \\ 0 \\ 0 \end{pmatrix}. \tag{3.31}$$

3.5 Rankine-Hugoniot Relations

One of the most striking features in computational problems is the presence of shock waves in the solution. The conservation laws described above accept solutions with discontinuity travelling at certain propagation speed through the medium. In order to derive the jump conditions across such discontinuity surfaces, it is worth noting that the discontinuity in the problem variables $[\![\boldsymbol{\mathcal{U}}]\!]$ (across a surface Γ defined by the material outward unit normal vector $\boldsymbol{N}$) travelling with speed U takes the following form:

$$\frac{d}{dt} \int_V \boldsymbol{\mathcal{U}} \, dV = \int_V \frac{\partial \boldsymbol{\mathcal{U}}}{\partial t} \, dV - \int_\Gamma U \, [\![\boldsymbol{\mathcal{U}}]\!] \, dA. \tag{3.32}$$

Similarly, the flux term in the presence of discontinuity yields

$$\int_V \frac{\partial \boldsymbol{\mathcal{F}}_I}{\partial X_I}\, dV = \int_{\partial V} \boldsymbol{\mathcal{F}}_N\, dA - \int_\Gamma [\![\, \boldsymbol{\mathcal{F}}_N \,]\!]\, dA. \tag{3.33}$$

Note that the notation

$$[\![\, \boldsymbol{\mathcal{A}} \,]\!] = \boldsymbol{\mathcal{A}}^+ - \boldsymbol{\mathcal{A}}^-$$

denotes jump in variable $\boldsymbol{\mathcal{A}}$ when crossing the discontinuity. Combining (3.32) and (3.33) into a general integral conservation law, that is

$$\frac{d}{dt}\int_V \boldsymbol{\mathcal{U}}\, dV + \int_{\partial V} \boldsymbol{\mathcal{F}}_N\, dA = \mathbf{0},$$

leads to a local differential law in V as

$$\frac{\partial \boldsymbol{\mathcal{U}}}{\partial t} + \frac{\partial \boldsymbol{\mathcal{F}}_I}{\partial X_I} = \mathbf{0}, \quad \forall\, I = 1, 2, 3; \tag{3.34}$$

coupled with discontinuity (or jump) conditions

$$U\, [\![\, \boldsymbol{\mathcal{U}} \,]\!] = [\![\, \boldsymbol{\mathcal{F}}_N \,]\!] \quad \text{in} \quad \Gamma. \tag{3.35}$$

This is generally known as Rankine-Hugoniot relations, which in turn can be particularised for the cases of linear momentum $\boldsymbol{p}$, deformation gradient tensor $\boldsymbol{F}$ and total energy E_T:

$$U\, [\![\, \boldsymbol{p} \,]\!] = -[\![\, \boldsymbol{P} \,]\!] \boldsymbol{N} \tag{3.36a}$$

$$U\, [\![\, \boldsymbol{F} \,]\!] = -\frac{1}{\rho_0} [\![\, \boldsymbol{p} \,]\!] \otimes \boldsymbol{N} \tag{3.36b}$$

$$U\, [\![\, E_T \,]\!] = -\frac{1}{\rho_0} [\![\, \boldsymbol{P}^T \boldsymbol{p} \,]\!] \cdot \boldsymbol{N} \tag{3.36c}$$

where heat flux $\boldsymbol{Q}$ is neglected. The jump condition of linear momentum variable will be used to derive a general Riemann solver for nonlinear cases (see Chapter 5).

Part III

Numerical Technique

Chapter 4

Finite Volume Discretisation and Time Integration Scheme

"Everything should be made as simple as possible, but not simpler".

Albert Einstein (1879 – 1955)

4.1 Introductory Remarks

There are numerous numerical methods available for solving a first order hyperbolic system of conservation laws. Finite Volume Method (FVM) is one of the most widely used numerical techniques in the area of computational mechanics and will be employed herein.

However, the computational tool based on Finite Element Method (FEM) has evolved to become the most popular numerical method in modern Computational Solid Mechanics (CSM). FEM has firmly established itself as a pioneering approach for linear and nonlinear problems in CSM (see [10,137]). In [41,138], both standard spatial semi-discretisations, namely FVM and FEM, are described by integrating the governing equation over any predefined control volume where they only differ with regard to the type of weighting functions used. As a matter of fact, a standard FVM is a particular case of FEM where a non-Galerkin approach is employed.[1] A comprehensive review of this subject is detailed in [27].

In recent years, a number of researchers have applied FVM to problems within the context of Computational Structural Dynamics (CSD); for instance, plate bending analysis has been performed in [139–141]. Furthermore, dynamic analysis of solid mechanics was also investigated in [32,37]. Surge of interest in further developing the FVM is not surprising since it posesses some very interesting properties: 1) FVM, as well as FEM, are formulated in an integral (or weak) form and are suitable to deal with complex geometries in multi-dimensional problems, as the integral formulations do not rely in any special mesh structure.[2] 2) FVM allows for the strict conservation of physical properties in the control volume [27, 30, 31, 35]. 3) FVM shows a clear advantage in problems where shocks (or discontinuities) are present [142]. An excellent ability for capturing shock discontinuities is demonstrated by allowing great flexibility in defining local interpolation functions, where problem variables vary discontinuously between elements. This procedure leads to a Riemann problem and is very well explained in [60, 84]. 4) FVM, like FEM, can also be applied in other areas of physics and sciences (i.e. Maxwell's and Magnetohydrodynamic (MHD) equations have been studied [104, 143]).

A finite volume method for the numerical solution of a new mixed formulation based upon a first order hyperbolic system of conservation laws is presented. First, a general monotone upstream scheme for conservation law (MUSCL) technique associated with a first order cell-centred[3] finite volume spatial discretisation is briefly introduced in Section 4.2. A more detailed discussion can be found in [33–36,42,139,140]. In Section 4.3, the extension to second order spatial approximation using a monoslope MUSCL method is then derived. The main idea is to construct (or predict)

[1] FVM is alternatively known as subdomain collocation FEM.

[2] Finite Difference Method (FDM) is the oldest method (which based upon the application of a local Taylor series expansion) to approximate a system of differential equations. It encounters difficulties when dealings with complex geometry in multiple dimensions.

[3] General discussion on vertex-centred finite volume scheme can be found in [27, 29, 30, 32, 33].

a local piecewise linear reconstruction of the solution by a minimisation procedure. The predicted slope is then corrected by employing a slope limiter so as to respect the stability condition [93–95, 144]. Subsequently, the resulting semi-discrete non-linear evolution equation will be advanced forward in time by adopting a Total Variation Diminishing (TVD) Runge-Kutta time stepping scheme (see Section 4.5). The roadmap for this chapter is summarised in Figure 4.1.

4.2 Cell-Centred Based Discretisation

A system of nonlinear conservative equations takes a general form of

$$\frac{\partial \boldsymbol{\mathcal{U}}}{\partial t} + \frac{\partial \boldsymbol{\mathcal{F}}_I}{\partial X_I} = \boldsymbol{\mathcal{S}}, \qquad \forall I = 1, 2, 3, \tag{4.1}$$

where $\boldsymbol{\mathcal{U}}$ denotes the vector of conserved variables, $\{\boldsymbol{\mathcal{F}}_1, \boldsymbol{\mathcal{F}}_2, \boldsymbol{\mathcal{F}}_3\}$ is a set of conservative flux vectors and $\boldsymbol{\mathcal{S}}$ describes the source term. These variables are defined explicitly for a new mixed formulation in Section 2.5.

Integrating (4.1) over any arbitrary material control volume V_e and applying the divergence theorem to the flux integral results in[4]

$$\frac{d}{dt}\int_{V_e} \boldsymbol{\mathcal{U}}\, dV = -\int_{\partial V_e} \hat{\boldsymbol{\mathcal{F}}} \cdot \boldsymbol{N}\, dA = -\int_{\partial V_e} \boldsymbol{\mathcal{F}}_N\, dA, \tag{4.2}$$

where the source term $\boldsymbol{\mathcal{S}}$ is neglected for simplicity. $\boldsymbol{N} = (N_1, N_2, N_3)^T$ represents the outward pointing unit vector normal to the material boundary ∂V_e and the notation $\hat{\boldsymbol{\mathcal{F}}} = (\boldsymbol{\mathcal{F}}_1, \boldsymbol{\mathcal{F}}_2, \boldsymbol{\mathcal{F}}_3)$ is used for the sake of a compact presentation. By defining $\boldsymbol{\mathcal{U}}_e$ to be an average value of $\boldsymbol{\mathcal{U}}$ over a control volume V_e and also approximating the boundary integral with the aid of quadrature rule[5], equation above thus leads to a general spatial discretisation

$$\frac{d\boldsymbol{\mathcal{U}}_e}{dt} = -\frac{1}{V_e}\sum_{\substack{k=1 \\ k\in e}}^{N_f} \left(\sum_{\substack{g=1 \\ g\in k}}^{N_{gp}} (\hat{\boldsymbol{\mathcal{F}}}_g \cdot \boldsymbol{N}_g) \mathcal{W}_g \right), \tag{4.3}$$

where $\hat{\boldsymbol{\mathcal{F}}}_g$ represents the numerical flux functions at g^{th} Gauss point, V_e indicates the volume of grid cell e, N_f denotes the number of surfaces of the control volume V_e, N_{gp} is the number of Gauss quadrature points of k^{th} surface, $\boldsymbol{N}_g$ denotes the outward pointing unit vector normal to k^{th} surface at g^{th} flux integration point, and $\mathcal{W}_g$ represents the g^{th} quadrature weight. In equation (4.3), it is evident that a lumped mass is implied due to the presence of V_e [27, 32].

[4]The main idea of using FVM is to discretise a computational domain into a set of non-overlapping cells in which the conservative equations are enforced locally.

[5]Gaussian quadrature rule is a numerical integration technique which evaluates an integral as the weighted sum of function values at selected locations. Further explanation can be found in [38, 69, 114, 145].

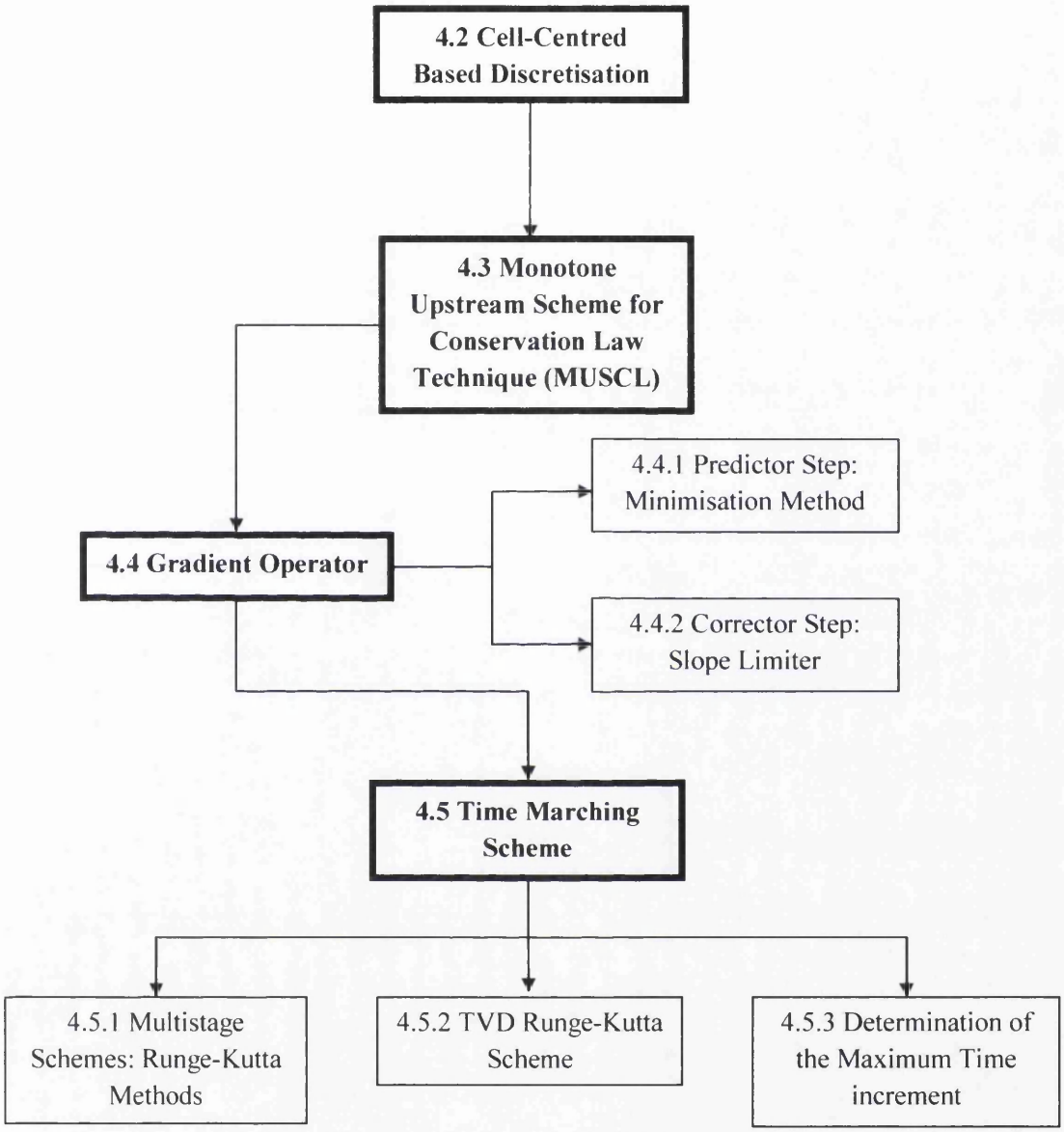

Figure 4.1: Structure of this chapter.

In particular, a general semi-discrete formulation, viz. (4.3), can be reduced to a two-dimensional finite volume discretisation:[6]

$$\frac{d\boldsymbol{\mathcal{U}}_e}{dt} = -\frac{1}{A_e}\sum_{\substack{k=1\\k\in e}}^{N_{ed}}(\hat{\boldsymbol{\mathcal{F}}}_k \cdot \boldsymbol{N}_k)\, l_k \tag{4.4a}$$

$$= -\frac{1}{A_e}\sum_{\substack{k=1\\k\in e}}^{N_{ed}}[\boldsymbol{\mathcal{F}}_N^C]_k\, l_k \tag{4.4b}$$

$$= -\boldsymbol{R}_e. \tag{4.4c}$$

Here, A_e is the area of cell e, N_{ed} denotes the number of edges belongs to cell e and l_k indicates k^{th} edge length. It is worth noting that a single Gauss quadrature point (that is $N_{gp} = 1$), which is located at the mid-edge, is sufficient for obtaining the spatial accuracy up to second order. Perhaps more importantly, its quadrature weight $\mathcal{W}_g$ at k^{th} mid-edge is equal to the edge length l_k. Insofar as the control volumes coincide with the grid cells, the numerical contact flux function $[\boldsymbol{\mathcal{F}}_N^C]_k$ is an approximation to the flux at k^{th} mid-edge (or contact point).

First it is assumed that the approximation to $\boldsymbol{\mathcal{U}}$ is constant within each cell. This will lead to discontinuities at cell edges which motivate the use of a Riemann solver by introducing an upwind bias into the evaluation of the numerical flux function $\boldsymbol{\mathcal{F}}_N^C$. In the case of linear elasticity (or nonlinear elasticity at the origin), that is $\boldsymbol{n} = \boldsymbol{N}$, the upwinding flux evaluation is given by[7]

$$[\boldsymbol{\mathcal{F}}_N^C]_k = \boldsymbol{\mathcal{F}}_N^C(\boldsymbol{\mathcal{U}}_e, \boldsymbol{\mathcal{U}}_\alpha)_k = \frac{1}{2}(\hat{\boldsymbol{\mathcal{F}}}_e + \hat{\boldsymbol{\mathcal{F}}}_\alpha)\cdot \boldsymbol{N}_k - \frac{1}{2}|\hat{\boldsymbol{\mathcal{A}}}\cdot \boldsymbol{N}_k|(\boldsymbol{\mathcal{U}}_\alpha - \boldsymbol{\mathcal{U}}_e), \quad \alpha = 1,\ldots,m, \tag{4.5}$$

where the Flux Jacobian matrix in two dimensions is denoted as $\hat{\boldsymbol{\mathcal{A}}} = (\boldsymbol{\mathcal{A}}_1, \boldsymbol{\mathcal{A}}_2)$ and $\boldsymbol{\mathcal{U}}_\alpha$ describes the vector of conserved variables in the adjacent grid cell α (see Figure 4.2a). m represents the number of adjacent cells (for structured grids); $m = 3$ and $m = 4$ for triangular and quadrilateral cells, respectively. In addition, the nonlinear upwinding flux evaluation will be fully discussed in Chapter 5. A first order scheme will be introduced so long as $\boldsymbol{\mathcal{U}}_e$ and $\boldsymbol{\mathcal{U}}_\alpha$ are treated as cell averaged values to the left and right states of k^{th} edge. Unfortunately, the accuracy is severely undermined by an excess of numerical dissipation. In order to alleviate this, it is vital to introduce a reconstruction procedure for choosing better values to the left and right states.

[6] In two dimensions, the flux $\hat{\boldsymbol{\mathcal{F}}}$ and the material unit normal vector $\boldsymbol{N}$ can be simplified to $\hat{\boldsymbol{\mathcal{F}}} = (\boldsymbol{\mathcal{F}}_1, \boldsymbol{\mathcal{F}}_2)$ and $\boldsymbol{N} = (N_1, N_2)^T$.

[7] A general nonlinear contact flux will be fully explored in Section 5.2. Nevertheless, this nonlinear flux can be linearised as the one shown in Section 2.7, which is only applicable to linear elasticity.

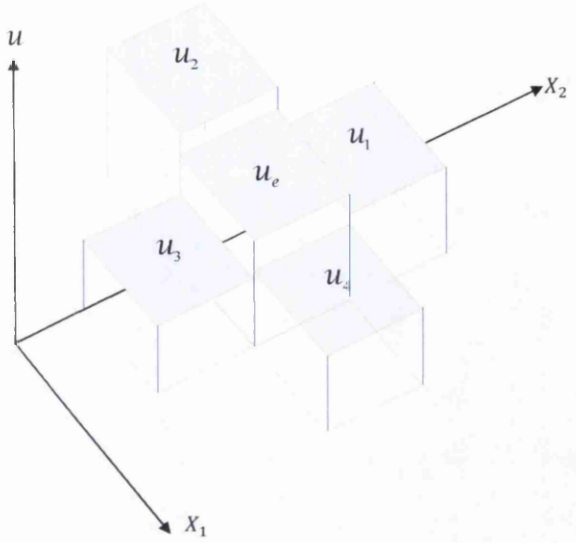

(a)

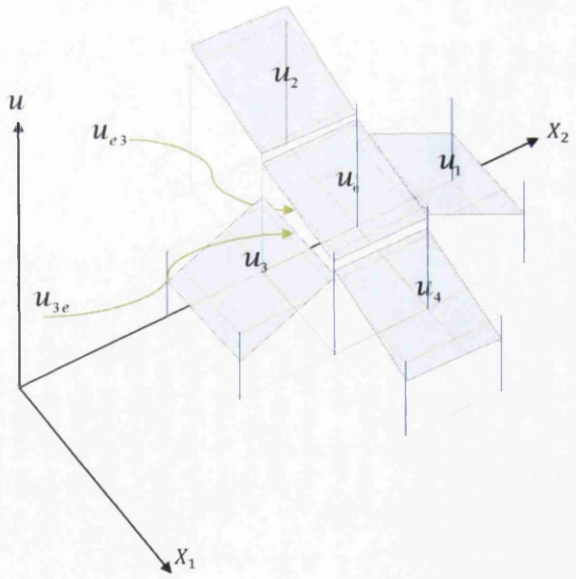

(b)

Figure 4.2: Reconstruction of the solution for quadrilateral control volumes: (a) Piecewise constant reconstruction; and (b) Piecewise linear reconstruction.

4.3 Monotone Upstream Scheme for Conservation Law Technique (MUSCL)

Higher order spatial accuracy is achieved by introducing a suitable reconstruction procedure for variables within each cell [60, 84, 93–95]. In particular, a piecewise linear approximation to the solution leads to a method which is of second order accuracy in space due to the fact that this approximation is exact for linear initial data (see Figure 4.2b).

First note that an initial averaged solution value $\mathcal{U}_e$ is given within an arbitrary cell e. In order to achieve second order spatial accuracy, a local linear reconstruction procedure is then carried out, which can be expressed mathematically as

$$\mathcal{U}_e(\boldsymbol{X}) = \mathcal{U}_e + \boldsymbol{G}_e \cdot (\boldsymbol{X} - \boldsymbol{X}_e), \tag{4.6}$$

where $\boldsymbol{X} \in$ cell e. $\boldsymbol{X} - \boldsymbol{X}_e$ denotes a position vector relative to the centroid of cell e, $\boldsymbol{G}_e$ represents a gradient operator at cell e and yet to be defined. It is easy to show that such a reconstruction is conservative [60] since

$$\frac{1}{A_e} \int_{A_e} \mathcal{U}_e(\boldsymbol{X})\, dA = \mathcal{U}_e.$$

The numerical flux function, viz. (4.5), at k^{th} mid-edge is now written in terms of the reconstructed solution values on either side of the edge, that is

$$[\mathcal{F}_N^C]_k = \mathcal{F}_N^C(\mathcal{U}_{e\alpha}, \mathcal{U}_{\alpha e})_k, \tag{4.7}$$

where

$$\mathcal{U}_{e\alpha} = \mathcal{U}_e + \boldsymbol{G}_e \cdot (\boldsymbol{X}_{e\alpha} - \boldsymbol{X}_e). \tag{4.8}$$

Here, $\boldsymbol{X}_{e\alpha} - \boldsymbol{X}_e$ is the position vector from the centroid of cell e to the mid-edge between cells e and α. An appropriate gradient operator $\boldsymbol{G}_e$ will be presented in the following section.

4.4 Gradient Operator

In general, the MUSCL technique consists of two steps. First, a local vectorial slope is predicted based upon the neighbouring values and information from the current cell itself. The predicted slope is then corrected in order to respect the maximum principle (or total variation diminishing constraints) [146, 147]. This predictor-corrector technique is collectively known as monoslope method since the reconstructed values are obtained using the same vectorial slope on each grid cell.[8]

[8] Recently, a new class of MUSCL method (namely multislope method) has been proposed but will not be considered herein. Its general discussion is detailed in [94, 95].

4.4.1 Predictor Step: Minimisation Method

Given a set of $m+1$ cell averaged values (i.e. $\{\mathcal{U}_e, \mathcal{U}_1, \mathcal{U}_2, \ldots, \mathcal{U}_m\}$) the slope within a cell e, $\boldsymbol{G}_e$, can be approximated in a coherent way such that

$$\Delta\mathcal{U} = \mathcal{U}_\alpha - (\mathcal{U}_e + \boldsymbol{G}_e \cdot \Delta\boldsymbol{X}) \approx 0; \qquad \Delta\boldsymbol{X} = \boldsymbol{X}_\alpha - \boldsymbol{X}_e, \tag{4.9}$$

where $\boldsymbol{X}_\alpha$ and $\boldsymbol{X}_e$ denote the centroids of the cells α and e, respectively. The expression $\Delta\mathcal{U}$ represents the difference between the centroid value $\mathcal{U}_\alpha$ and the value obtained by extrapolating the function $\mathcal{U}_e$ from cell e to α.

Firstly, the functional $\mathcal{D}$ is defined by

$$\mathcal{D}(\boldsymbol{G}_e) = \frac{1}{2}\sum_{\alpha=1}^{m} W_{e\alpha}\left[\mathcal{U}_\alpha^n - (\mathcal{U}_e^n + \boldsymbol{G}_e^n \cdot \Delta\boldsymbol{X})\right]^2, \qquad W_{e\alpha} = \frac{1}{d_{e\alpha}^2}. \tag{4.10}$$

A scalar value, $d_{e\alpha}$, is a material distance from the centroid of cell e to α. In order to determine a local vectorial slope $\boldsymbol{G}_e$ at cell e, the above functional has to be minimised with respect to $\boldsymbol{G}_e$ which, after some simple algebraic manipulations, yields

$$\boldsymbol{G}_e^n = \left[\sum_{\alpha=1}^{m} \boldsymbol{\nu}_{e\alpha} \otimes \boldsymbol{\nu}_{e\alpha}\right]^{-1} \sum_{\alpha=1}^{m} \left(\frac{\mathcal{U}_\alpha^n - \mathcal{U}_e^n}{d_{e\alpha}}\right) \boldsymbol{\nu}_{e\alpha}, \tag{4.11}$$

where the unit vector $\boldsymbol{\nu}$ is expressed as

$$\boldsymbol{\nu}_{e\alpha} = \frac{\boldsymbol{X}_\alpha - \boldsymbol{X}_e}{d_{e\alpha}}. \tag{4.12}$$

In two dimensions, $\boldsymbol{G}_e^n = \boldsymbol{0}$ if and only if a single neighbouring information ($m = 1$) is available. Substituting $\boldsymbol{G}_e$ from (4.11) into (4.8) leads to second order accuracy in space but does not prohibit overshoots and undershoots at flux integration points.[9] In order to rectify this, the predicted gradient operator $\boldsymbol{G}_e$ has to be corrected by employing a slope limiter [26, 60, 86].

4.4.2 Corrector Step: Slope Limiter

By including a slope limiter during reconstruction, no new local extrema can be formed. Barth and Jespersen [86] introduced the very first limiter for unstructured grids. In essence, the proposed scheme is to find a limiter value ϕ_e of the form

$$\mathcal{U}_{e\alpha} = \mathcal{U}_e + \phi_e \boldsymbol{G}_e \cdot (\boldsymbol{X}_{e\alpha} - \boldsymbol{X}_e); \qquad \phi_e = [0, 1]. \tag{4.13}$$

By virtue of the equation above, it is essential to obtain the largest ϕ_e which still prevents the formation of local extrema at flux integration point. In order to achieve this, the following standard procedure is used:

[9] Or equivalently, the spatial semi-discretisation scheme does not satisfy the local maximum principle [147].

1. Find the smallest and largest averaged values among adjacent cells α and the current cell e:

$$\mathcal{U}^{\min} = \min(\mathcal{U}_e, \mathcal{U}_\alpha) \qquad \text{and} \qquad \mathcal{U}^{\max} = \max(\mathcal{U}_e, \mathcal{U}_\alpha)$$

$\forall \alpha = 1, \ldots, m$.

2. Compute an unlimited reconstructed value at each flux integration point; for instance, $\mathcal{U}_{e\alpha}$ with $\phi_e = 1$.

3. Obtain a maximum allowable value of $\phi_{e\alpha}$ for each cell edge k.

$$\phi_{e\alpha} = \begin{cases} \min\left(1, \frac{\mathcal{U}^{\max} - \mathcal{U}_e}{\mathcal{U}_{e\alpha} - \mathcal{U}_e}\right), & \text{if} \quad \mathcal{U}_{e\alpha} - \mathcal{U}_e > 0 \\ \min\left(1, \frac{\mathcal{U}^{\min} - \mathcal{U}_e}{\mathcal{U}_{e\alpha} - \mathcal{U}_e}\right), & \text{if} \quad \mathcal{U}_{e\alpha} - \mathcal{U}_e < 0 \\ 1, & \text{if} \quad \mathcal{U}_{e\alpha} - \mathcal{U}_e = 0 \end{cases}$$

4. Select $\phi_e = \min_{\alpha \in V_e}(\phi_{e\alpha})$.

5. Evaluate the correct reconstructed value $\mathcal{U}_{e\alpha}$ at each flux integration point; using (4.13) together with ϕ_e obtained from step 4.

In practice, the non-differentiability of step 3 causes the greatest degradation in convergence performance [148]. For this reason, Venkatakrishnan (1993) [87] introduced an alternative smooth function by replacing the $\min(1, y)$ with $\min(1, P(y))$ where

$$P(y) = \frac{y^2 + 2y}{y^2 + y + 2}.$$

Note that Venkatakrishnan limiter is slightly more dissipative than the standard Barth-Jespersen limiter [149].

4.5 Time Marching Scheme

The application of the method of lines[10] leads to a system of ordinary coupled differential equations:

$$\frac{d\boldsymbol{\mathcal{U}}_e}{dt} = -\boldsymbol{R}_e. \tag{4.14}$$

This approach offers a great deal of flexibility since different levels of approximation can be easily selected for the fluxes, as well as the temporal scheme. A system of equations (4.14) has to be integrated in time so as to obtain either a steady-state solution ($\boldsymbol{R}_e = \boldsymbol{0}$) or a time history of an unsteady flow. The most popular and widespread explicit time integrator, namely Runge-Kutta time stepping scheme, will be adopted.

[10]The method of lines is a technique to semi-discretise first the spatial term of a governing equation into a system of Ordinary Differential Equations (ODEs), which in turn can be integrated using any temporal scheme that exists in literature.

4.5.1 Multistage Schemes: Runge-Kutta Methods

In numerical analysis, a family of Runge-Kutta methods is one of the most important explicit time integration techniques. Jameson *et al.*(1981) [150] have reported that the advantage of using Runge-Kutta schemes is such that no any special starting procedure is required, in contrast to LeapFrog and Adams-Bashforth methods. Crucially, they have been successfully applied in the numerical solutions for Euler equations [151–153].

The multistage schemes advance the solution in a number of steps, which is called Runge-Kutta stages. In order to achieve a sequence of updates from $\boldsymbol{\mathcal{U}}_e^n$ to $\boldsymbol{\mathcal{U}}_e^{n+1}$, it is essential to re-evaluate the residual $\boldsymbol{R}_e$ at points intermediate between $\boldsymbol{\mathcal{U}}_e^n$ and $\boldsymbol{\mathcal{U}}_e^{n+1}$. A basic general form of j^{th}-stage Runge-Kutta method is denoted as follows:

$$\begin{aligned}
\boldsymbol{\mathcal{U}}_e^{(1)} &= \boldsymbol{\mathcal{U}}_e^n \\
\boldsymbol{\mathcal{U}}_e^{(2)} &= \boldsymbol{\mathcal{U}}_e^n - \alpha_{12}\Delta t \boldsymbol{R}_e^{(1)} \\
\boldsymbol{\mathcal{U}}_e^{(3)} &= \boldsymbol{\mathcal{U}}_e^n - \alpha_{13}\Delta t \boldsymbol{R}_e^{(1)} - \alpha_{23}\Delta t \boldsymbol{R}_e^{(2)} \\
&\vdots \\
\boldsymbol{\mathcal{U}}_e^{(j)} &= \boldsymbol{\mathcal{U}}_e^n - \Delta t \sum_{k=1}^{j-1} \alpha_{kj} \boldsymbol{R}_e^{(k)} \\
\boldsymbol{\mathcal{U}}_e^{n+1} &= \boldsymbol{\mathcal{U}}_e^n - \Delta t \sum_{k=1}^{j} \beta_k \boldsymbol{R}_e^{(k)}
\end{aligned} \tag{4.15}$$

The notation $\boldsymbol{R}_e^{(k)}$ implies that

$$\boldsymbol{R}_e^{(k)} = \boldsymbol{R}\left(\boldsymbol{\mathcal{U}}_e^{(k)}\right). \tag{4.16}$$

Note that the order of temporal accuracy is defined by the values of α and β. These coefficients are shown as follows [154]:

- **Euler Method (First Order Accuracy)**. Defined by $j = \beta_1 = 1$.
- **The Improved Euler Method (Second Order Accuracy)**. Suppose that $j = 2$ and their coefficients are $\alpha_{12} = 1$, $\beta_1 = \beta_2 = 1/2$.

Low-storage Explicit Runge-Kutta Schemes

Unfortunately, the family of classical Runge-Kutta schemes described above requires a large memory storage; at stage j, all intermediate residuals of previous j^{th} stage, $\boldsymbol{R}_e^{(k)} \forall\, k = 1, \ldots, j-1$, need to be stored. In order to rectify this, a family of

low-storage Runge-Kutta schemes, which is demonstrated as

$$\begin{aligned}
\boldsymbol{U}_e^{(1)} &= \boldsymbol{U}_e^n \\
\boldsymbol{U}_e^{(2)} &= \boldsymbol{U}_e^n - \alpha_1 \Delta t \boldsymbol{R}_e^{(1)} \\
\boldsymbol{U}_e^{(3)} &= \boldsymbol{U}_e^n - \alpha_2 \Delta t \boldsymbol{R}_e^{(2)} \\
&\vdots \\
\boldsymbol{U}_e^{(j)} &= \boldsymbol{U}_e^n - \alpha_{(j-1)} \Delta t \boldsymbol{R}_e^{(j-1)} \\
\boldsymbol{U}_e^{n+1} &= \boldsymbol{U}_e^n - \Delta t \sum_{k=1}^{j} \beta_k \boldsymbol{R}_e^{(k)},
\end{aligned} \tag{4.17}$$

is usually applied. For consistency,

$$\sum_{k=1}^{j} \beta_k = 1. \tag{4.18}$$

A particular choice of

$$\beta_k = 0, \quad \forall \quad k = 1, \ldots, j-1; \qquad \beta_j = 1, \tag{4.19}$$

is adopted which eventually yields

$$\boldsymbol{U}_e^{n+1} = \boldsymbol{U}_e^n - \Delta t \boldsymbol{R}_e^{(j)}. \tag{4.20}$$

Table (4.1) shows a list of coefficients for a low-storage j^{th} stage first order

Table 4.1: Multistage schemes: optimised stage coefficients (α)

Stages	Three	Four	Five
α_1	0.1481	0.0833	0.0533
α_2	0.4	0.2069	0.1263
α_3	1	0.4265	0.2375
α_4		1	0.4414
α_5			1

scheme [98]. These selected coefficients are chosen to extend the stability of a scheme. A larger stability region can be achieved if higher Runge-Kutta stages is used.[11] Furthermore, a family of second order schemes will be introduced if and only if $\alpha_{j-1} = 1/2$. See [146] for detailed discussion. Shu and Osher(1988) [88] proved that non-TVD stable Runge-Kutta time stepping schemes can produce unphysical oscillations even for spatial discretisation satisfying maximum principle (or total variation diminishing constraints). Therefore, a family of TVD Runge-Kutta methods (TVD-RK) is crucial in practical applications and will be explored in the next section.

[11]The stage coefficients can be tuned to extend the stability region, which in turn increase the maximum time increment (see references [155,156]).

4.5.2 Total Variation Diminishing Runge-Kutta Scheme

Time integration schemes pose a threat in respect to the monotonic solution. Although any slope limiter ensures that no new local extrema can be created during spatial reconstruction process, however, it does not automatically guarantee that monotonicity will still be satisfied when evolves to the next time step. In order to achieve this, [88] proposed the second order TVD Runge-Kutta time integration scheme[12] satisfying the monotonicity criteria. This integrator has been successfully used in [96,97]. At the outset, the conserved variables $\boldsymbol{\mathcal{U}}_e^n$ are given at time step n, the time scheme then proceeds in two stages in order to obtain the updated field variables $\boldsymbol{\mathcal{U}}_e^{n+1}$ as

$$\boldsymbol{\mathcal{U}}_e^{(1)} = \boldsymbol{\mathcal{U}}_e^n \tag{4.21a}$$

$$\boldsymbol{\mathcal{U}}_e^{(2)} = \boldsymbol{\mathcal{U}}_e^n - \Delta t\, \boldsymbol{R}_e(\boldsymbol{\mathcal{U}}_e^{(1)}, t^n) \tag{4.21b}$$

$$\boldsymbol{\mathcal{U}}_e^{n+1} = \frac{1}{2}\boldsymbol{\mathcal{U}}_e^n + \frac{1}{2}\boldsymbol{\mathcal{U}}_e^{(2)} - \frac{1}{2}\Delta t\, \boldsymbol{R}_e(\boldsymbol{\mathcal{U}}_e^{(2)}, t^n + \Delta t), \tag{4.21c}$$

where $\boldsymbol{R}_e$ represents the residual of a conservative formula (see Section 4.2). In [88], Shu and Osher also identified that the first order Euler's method fulfills TVD constraint. For any given computational examples, the order of time accuracy should be matched if possible with the spatial accuracy. A clear disadvantage of using any explicit scheme is such that the time increment, Δt, is severely restricted by the grid geometry as well as the characteristics of a governing equation.

4.5.3 Determination of the Maximum Time increment

Evaluation of the time increment Δt is of particular importance since it is closely related to the stability of any explicit time marching scheme. The maximum allowable time increment is defined by making use of the Courant-Friedrichs-Lewy number[13], α_{CFL} [157]:

$$\Delta t = \alpha_{CFL} \frac{h_{min}}{U_{max}^n}, \tag{4.22}$$

where h_{min} is the minimum grid size and U_{max}^n describes the maximum wave speed presents at time level n. The maximum wave speed can then be found as

$$U_{max}^n = \max_e \left(U_p^n\right), \tag{4.23}$$

where $\{e\}$ includes a set of data arising from the physical domain and U_p^n is the local volumetric speed at time step n. Note that inappropriate choice of U_{max}^n in

[12]The second order TVD-RK method coincides with the Improved Euler method discussed in the previous section.

[13]It is a necessary stability condition that required by any type of explicit time integration schemes. This condition states that the domain of dependence of the numerical method should include the domain of dependence of the PDE. An excellent discussion can be found in [81].

(4.22) might lead to an unstable scheme. In the context of homogeneous linear elasticity, the time increment becomes constant ($\Delta t \equiv const$) due to the fact that the volumetric speed U_p solely depends on material properties (see equation (2.48a)). The CFL number α_{CFL} is yet to be specified and will be investigated in Chapter 8.

Chapter 5

Lagrangian Contact Algorithm

"If people do not believe that mathematics is simple, it is only because they do not realize how complicated life is".

John Louis Von Neumann (1903 – 1957)

5.1 Introductory Remarks

A new computational methodology comprising of a MUSCL cell-centred finite volume method and a TVD Runge-Kutta time integrator was presented in the previous chapter. However, the highly nonlinear numerical interface flux function $\mathcal{F}_N^C$ is yet to be defined (see Section 4.2). In order to achieve this, a generalised Riemann solver (also known as contact flux) will be introduced.

Interface fluxes including contact fluxes can be generally treated as a Riemann problem. Section 5.2 presents an overview of a generalised Riemann solver. This Riemann solver will be used to derive the specific boundary flux by specifying the boundary conditions without resorting to ghost method[1]. Section 5.3 provides detailed descriptions for various boundary fluxes. An improper implementation of these fluxes yields inaccurate result, therefore the numerical treatment at the boundary requires particular care. Otherwise, the stability and convergence rate of a numerical scheme can be adversely affected [98].

Figure 5.1 summarises the guide through this chapter.

5.2 Generalised Riemann Solver: Contact Flux

In Lagrangian dynamic problems, it is often the case that two surfaces, which lie on the reference configuration with the unique outward normal vector $\boldsymbol{N}$ at initial time $t = 0$, become in contact with each other after some time t in current configuration (see Figure 5.2). Physically, this is the result of an impact between two bodies or two parts of the same body. Numerically, contacts may arise from the use of discontinuous interpolations for problem variables at a given point. For instance, the interface flux $\mathcal{F}_N^C(\mathcal{U}^-, \mathcal{U}^+)$, which depends on the left and right states, will emerge in the numerical solutions of a Godunov-type finite volume scheme.

In order to derive a contact flux, it is necessary to evaluate the linear momentum and traction vectors at contact point immediately following the impact. Note first that the impact will generate two types of shock waves travelling from the contact point into each of the two bodies. In the case of frictionless contact, the generated shock waves will travel with volumetric speed U_p. Perhaps most importantly, the normal components of the momentum and traction vectors after contact must be identical for both surfaces. From (3.36a), equation for the linear momentum jump across the left and right shock waves can be deduced:

$$U_P^-(p_n^- - p_n^C) = t_n^- - t_n^C, \tag{5.1a}$$

$$U_p^+(p_n^+ - p_n^C) = -(t_n^+ - t_n^C), \tag{5.1b}$$

[1]Another approach is to extend the computational domain to include a few dummy (or ghost) cells, whose values depend on the the boundary conditions and interior solutions. For this purpose, a general ghost method will be discussed in Appendix F.

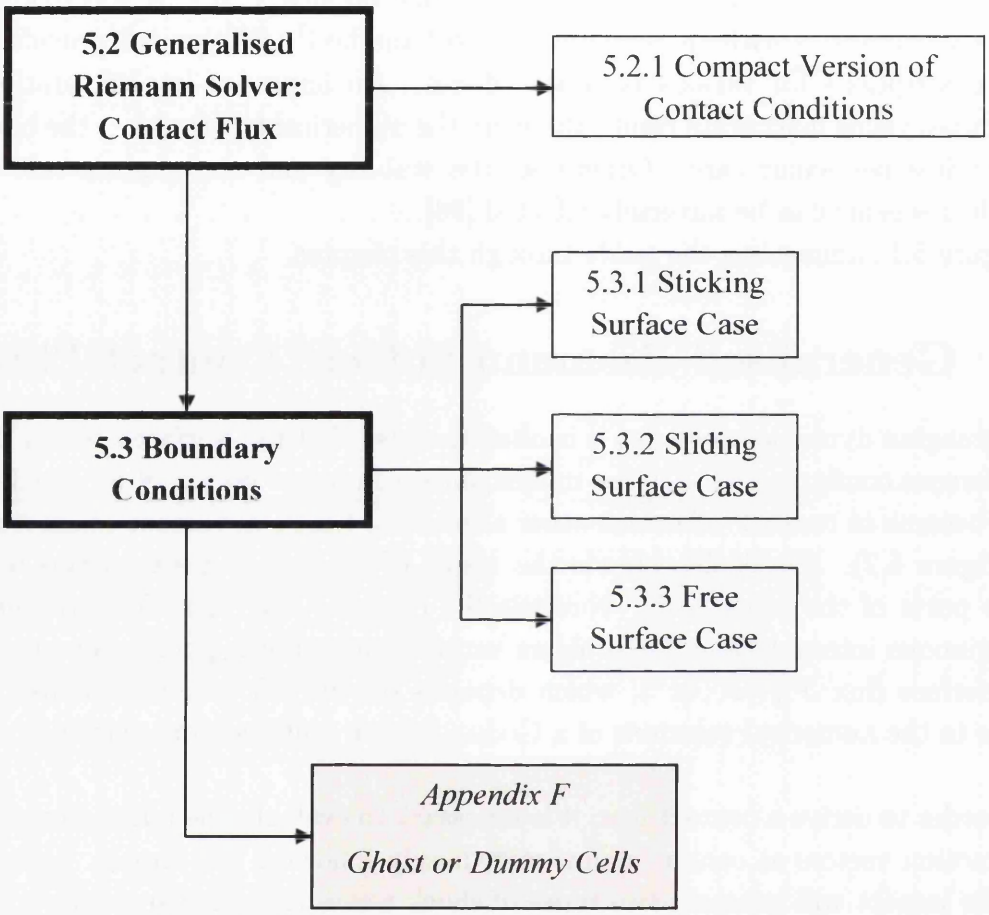

Figure 5.1: Content and guide of this chapter.

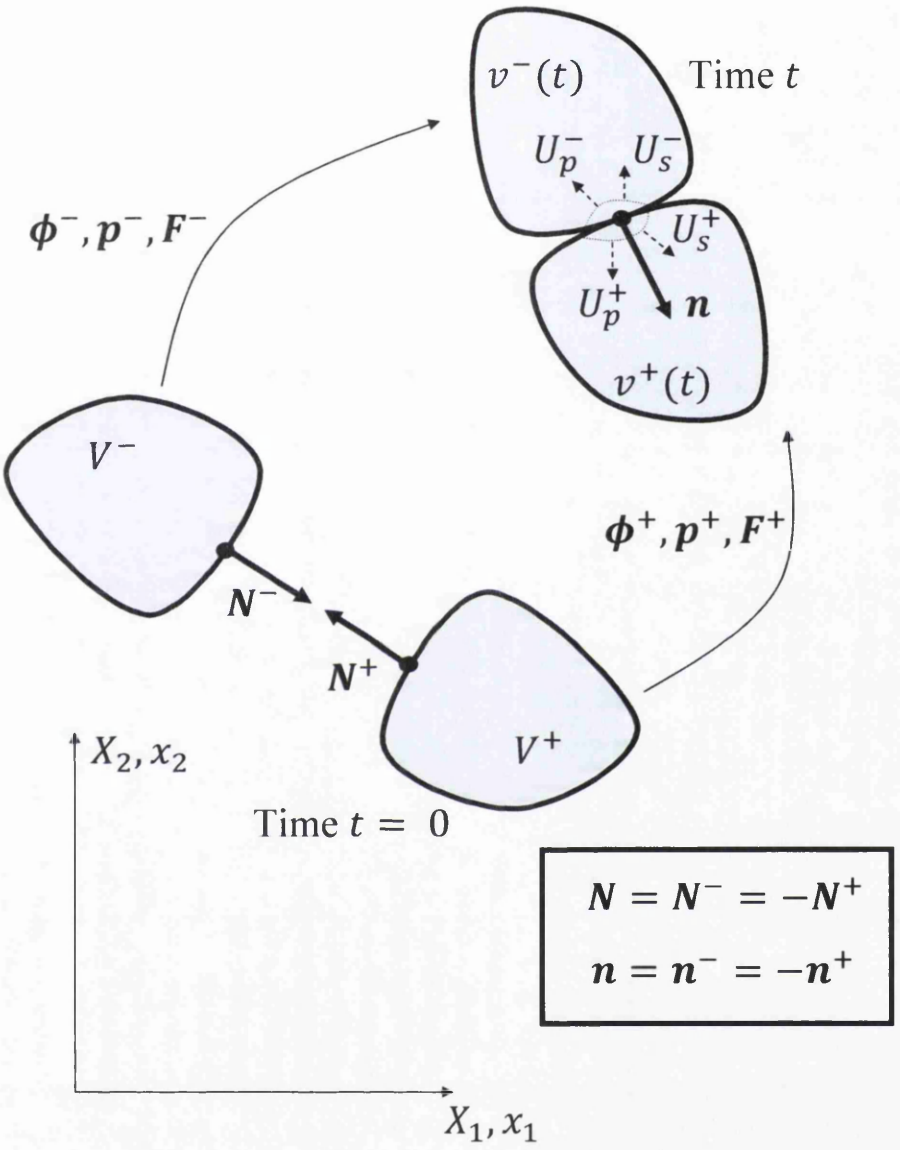

Figure 5.2: Contact generated shock waves.

where p_n^- and p_n^+ denote the left and right normal components of the momentum vector before contact, that is $p_n^{-,+} = \boldsymbol{p}^{-,+} \cdot \boldsymbol{n}$. Analogously, $t_n^{-,+}$ describe the normal components of the traction vector before contact such as $t_n^{-,+} = \boldsymbol{n} \cdot (\boldsymbol{P}^{-,+}\boldsymbol{N})$. Note that the surface normal is defined outwards for the left body and inwards, on the contrary, for the right body so as to define a unique traction vector after contact $\boldsymbol{t}^C$ (i.e. $\boldsymbol{N} = \boldsymbol{N}^- = -\boldsymbol{N}^+$ and $\boldsymbol{n} = \boldsymbol{n}^- = -\boldsymbol{n}^+$). Furthermore, (5.1) can be expanded which leads to the expressions of the momentum and traction vectors following the contact:

$$p_n^C = \frac{U_p^- p_n^- + U_p^+ p_n^+}{U_p^- + U_p^+} + \frac{t_n^+ - t_n^-}{U_p^- + U_p^+} \tag{5.2a}$$

$$t_n^C = \frac{U_p^- U_p^+}{U_p^- + U_p^+}\left(\frac{t_n^-}{U_p^-} + \frac{t_n^+}{U_p^+}\right) + \frac{U_p^- U_p^+}{U_p^- + U_p^+}(p_n^+ - p_n^-). \tag{5.2b}$$

An additional pair of shock waves will propagate with shear speed U_s under the infinite friction contact. The derivation performed above can now be followed for the tangential components of the momentum and traction vectors such as

$$\boldsymbol{p}_t^C = \frac{U_s^- \boldsymbol{p}_t^- + U_s^+ \boldsymbol{p}_t^+}{U_s^- + U_s^+} + \frac{\boldsymbol{t}_t^+ - \boldsymbol{t}_t^-}{U_s^- + U_s^+} \tag{5.3a}$$

$$\boldsymbol{t}_t^C = \frac{U_s^- U_s^+}{U_s^- + U_s^+}\left(\frac{\boldsymbol{t}_t^-}{U_s^-} + \frac{\boldsymbol{t}_t^+}{U_s^+}\right) + \frac{U_s^- U_s^+}{U_s^- + U_s^+}(\boldsymbol{p}_t^+ - \boldsymbol{p}_t^-). \tag{5.3b}$$

With the help of above expressions, the complete contact momentum and traction vectors are defined by

$$\boldsymbol{p}^C = \boldsymbol{p}_t^C + p_n^C \boldsymbol{n}\,; \quad \boldsymbol{t}^C = \boldsymbol{t}_t^C + t_n^C \boldsymbol{n}. \tag{5.4}$$

This enables the contact flux to be evaluated as

$$\boldsymbol{\mathcal{F}}_N^C = \begin{bmatrix} -\boldsymbol{t}^C \\ -\frac{1}{\rho_0}\boldsymbol{p}^C \otimes \boldsymbol{N} \\ -\frac{1}{\rho_0}\boldsymbol{t}^C \cdot \boldsymbol{p}^C \end{bmatrix} \tag{5.5}$$

where the heat flux term $\boldsymbol{Q}$ has been ignored for simplicity. The above expression generalises the linearised Riemann solver (derived from the eigenstructure of a flux Jacobian matrix) to the case where the energy balance principle is considered and also the wave speeds are different across the contact surface (see Section 2.7). It is easy to show that the solution obtained from the contact flux is identical to that of linearised Riemann solver if $U_p^- = U_p^+$ and $U_s^- = U_s^+$.

5.2.1 Compact Version of Contact Conditions

An alternative form of contact fluxes, in principle, is conveniently decomposed into [13]

$$\boldsymbol{p}^C = (\boldsymbol{n}\otimes\boldsymbol{n})\boldsymbol{p}^C + (\boldsymbol{I}-\boldsymbol{n}\otimes\boldsymbol{n})\boldsymbol{p}^C \tag{5.6a}$$
$$\boldsymbol{t}^C = (\boldsymbol{n}\otimes\boldsymbol{n})\boldsymbol{t}^C + (\boldsymbol{I}-\boldsymbol{n}\otimes\boldsymbol{n})\boldsymbol{t}^C. \tag{5.6b}$$

Note here that $\boldsymbol{n}\otimes\boldsymbol{n}$ is the projection of $\boldsymbol{p}^C$ and $\boldsymbol{t}^C$ in the direction of $\boldsymbol{n}$, whereas $\boldsymbol{I}-\boldsymbol{n}\otimes\boldsymbol{n}$ projects them onto the plane perpendicular to $\boldsymbol{n}$. With the aid of (5.2), (5.3) and (5.4), the above expressions are expanded to become

$$\begin{aligned}
\boldsymbol{p}^C =&(\boldsymbol{n}\otimes\boldsymbol{n})\frac{U_p^-\boldsymbol{p}^- + U_p^+\boldsymbol{p}^+}{U_p^- + U_p^+} + (\boldsymbol{I}-\boldsymbol{n}\otimes\boldsymbol{n})\frac{U_s^-\boldsymbol{p}^- + U_s^+\boldsymbol{p}^+}{U_s^- + U_s^+}\\
&+(\boldsymbol{n}\otimes\boldsymbol{n})\frac{(\boldsymbol{P}^+ - \boldsymbol{P}^-)}{U_p^- + U_p^+}\boldsymbol{N} + (\boldsymbol{I}-\boldsymbol{n}\otimes\boldsymbol{n})\frac{(\boldsymbol{P}^+ - \boldsymbol{P}^-)}{U_s^- + U_s^+}\boldsymbol{N},\\
\boldsymbol{t}^C =&(\boldsymbol{n}\otimes\boldsymbol{n})\frac{U_p^-U_p^+}{U_p^- + U_p^+}(\boldsymbol{p}^+ - \boldsymbol{p}^-) + (\boldsymbol{I}-\boldsymbol{n}\otimes\boldsymbol{n})\frac{U_s^-U_s^+}{U_s^- + U_s^+}(\boldsymbol{p}^+ - \boldsymbol{p}^-)\\
&+(\boldsymbol{n}\otimes\boldsymbol{n})\frac{(U_p^+\boldsymbol{P}^- + U_p^-\boldsymbol{P}^+)}{U_p^- + U_p^+}\boldsymbol{N} + (\boldsymbol{I}-\boldsymbol{n}\otimes\boldsymbol{n})\frac{(U_s^+\boldsymbol{P}^- + U_s^-\boldsymbol{P}^+)}{U_s^- + U_s^+}\boldsymbol{N}.
\end{aligned} \tag{5.7}$$

As discussed in Section D.2, $\boldsymbol{n}$ is simply a push forward mapping for $\boldsymbol{N}$ to spatial configuration, that is

$$\boldsymbol{n} = \frac{\boldsymbol{F}^{-T}\boldsymbol{N}}{\|\boldsymbol{F}^{-T}\boldsymbol{N}\|}.$$

Additionally, (5.7) can be further reduced to

$$\begin{aligned}
\boldsymbol{p}^C &= \frac{1}{2}(\boldsymbol{p}^- + \boldsymbol{p}^+) + \frac{1}{2}\left[\frac{1}{U_p}(\boldsymbol{n}\otimes\boldsymbol{n})(\boldsymbol{P}^+ - \boldsymbol{P}^-)\boldsymbol{N} + \frac{1}{U_s}(\boldsymbol{I}-\boldsymbol{n}\otimes\boldsymbol{n})(\boldsymbol{P}^+ - \boldsymbol{P}^-)\boldsymbol{N}\right],\\
\boldsymbol{t}^C &= \frac{1}{2}(\boldsymbol{P}^- + \boldsymbol{P}^+)\boldsymbol{N} + \frac{1}{2}\left[U_p(\boldsymbol{n}\otimes\boldsymbol{n})(\boldsymbol{p}^+ - \boldsymbol{p}^-) + U_s(\boldsymbol{I}-\boldsymbol{n}\otimes\boldsymbol{n})(\boldsymbol{p}^+ - \boldsymbol{p}^-)\right],
\end{aligned} \tag{5.8}$$

within the context of homogeneous linear elasticity (i.e. $U_p = U_p^- = U_p^+$ and $U_s = U_s^- = U_s^+$).

5.3 Boundary Conditions

Making use of contact flux derived above, it is now convenient to develop special formulas for use near the boundaries. In general, there are three types of boundary conditions that commonly encountered:

5.3.1 Sticking Surface Case

Under this circumstance, it imposes a no-slip condition[2] where the velocity vector $\boldsymbol{v}^+$ at outer domain (+) becomes

$$\boldsymbol{v}^+ = \boldsymbol{p}^+ = \mathbf{0}. \tag{5.9}$$

Due to the fact that no deformation is allowed in this particular case, the wave speeds are then denoted by

$$U_p^+ = U_s^+ \to \infty. \tag{5.10}$$

By substituting the conditions described above into (5.2) and (5.3), the velocity and traction vectors at contact point are easily derived:

$$\begin{aligned} &\boldsymbol{p}^C = \mathbf{0} \\ &t_n^C = t_n^- - U_p^- p_n^-, \qquad \boldsymbol{t}_t^C = \boldsymbol{t}_t^- - U_s^- \boldsymbol{p}_t^-. \end{aligned} \tag{5.11}$$

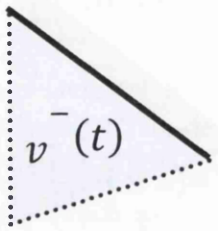

Figure 5.3: Sticking Case

Or alternatively, the above expression can be represented as

$$\begin{aligned} &\boldsymbol{p}^C = \mathbf{0} \\ &\boldsymbol{t}^C = \boldsymbol{t}^- - U_p^-(\boldsymbol{n}\otimes\boldsymbol{n})\boldsymbol{p}^- - U_s^-(\boldsymbol{I} - \boldsymbol{n}\otimes\boldsymbol{n})\boldsymbol{p}^-. \end{aligned} \tag{5.12}$$

Here, $\boldsymbol{n} = \boldsymbol{N}$ denotes the outward unit normal vector to the boundary face.

5.3.2 Sliding Surface Case

For sliding surface boundary condition, the velocity only slips over the tangent plane. It is equivalent to the condition such that there is no flow normal to the surface:

$$\boldsymbol{v}^+ \cdot \boldsymbol{n} = v_n^+ = p_n^+ = 0.$$

With the help of the above equation together with

$$U_p^+ \to \infty, \qquad U_s^+ = 0 \qquad \text{and} \qquad \boldsymbol{t}_t^+ = \boldsymbol{t}_t^B,$$

the contact fluxes are obtained as

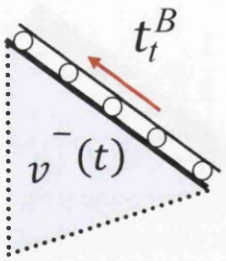

Figure 5.4: Sliding Case

$$p_n^C = 0, \qquad \boldsymbol{p}_t^C = \boldsymbol{p}_t^- + \frac{1}{U_s^-}(\boldsymbol{t}_t^B - \boldsymbol{t}_t^-) \tag{5.13}$$

and

$$t_n^C = t_n^- - U_p^- p_n^-, \qquad \boldsymbol{t}_t^C = \boldsymbol{t}_t^B. \tag{5.14}$$

[2] In fluid dynamics, velocity at the surface vanishes when viscous fluid passes a solid wall [25, 81, 83].

These fluxes can also be written in an alternative form:

$$\begin{aligned} \boldsymbol{p}^C &= (\boldsymbol{I} - \boldsymbol{n} \otimes \boldsymbol{n})\boldsymbol{p}^- + \frac{1}{U_s^-}(\boldsymbol{I} - \boldsymbol{n} \otimes \boldsymbol{n})(\boldsymbol{t}^B - \boldsymbol{t}^-) \\ \boldsymbol{t}^C &= (\boldsymbol{n} \otimes \boldsymbol{n})\boldsymbol{t}^- + (\boldsymbol{I} - \boldsymbol{n} \otimes \boldsymbol{n})\boldsymbol{t}^B - U_p^-(\boldsymbol{n} \otimes \boldsymbol{n})\boldsymbol{p}^-. \end{aligned} \tag{5.15}$$

The definition of $\boldsymbol{n}$ is identical to the sticking surface case; that is, $\boldsymbol{n} = \boldsymbol{N}$ defined at the boundary face.

5.3.3 Free Surface Case

This type of boundary condition concludes that

$$U_p^+ = U_s^+ = 0 \qquad \text{and} \qquad \boldsymbol{t}^+ = \boldsymbol{t}^B.$$

The normal and tangential components of contact velocity are thus

$$p_n^C = p_n^- + \frac{1}{U_p^-}(t_n^B - t_n^-) \qquad \text{and} \qquad \boldsymbol{p}_t^C = \boldsymbol{p}_t^- + \frac{1}{U_s^-}(\boldsymbol{t}_t^B - \boldsymbol{t}_t^-), \tag{5.16}$$

respectively. The traction vector at contact point, on the other hand, is described as

$$\boldsymbol{t}^C = \boldsymbol{t}^B. \tag{5.17}$$

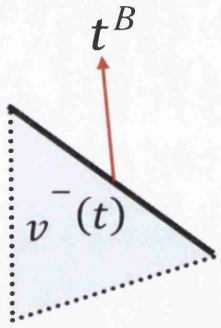

Figure 5.5: Free Case

For the sake of a compact representation, equations above can be conveniently re-expressed as

$$\begin{aligned} \boldsymbol{t}^C &= \boldsymbol{t}^B \\ \boldsymbol{p}^C &= \boldsymbol{p}^- + \frac{1}{U_p^-}(\boldsymbol{n} \otimes \boldsymbol{n})(\boldsymbol{t}^B - \boldsymbol{t}^-) + \frac{1}{U_s^-}(\boldsymbol{I} - \boldsymbol{n} \otimes \boldsymbol{n})(\boldsymbol{t}^B - \boldsymbol{t}^-). \end{aligned} \tag{5.18}$$

In contrast to the previous boundary cases, $\boldsymbol{n}$ is defined by the spatial outward unit normal vector to the interface of $v^-(t)$.

Chapter 6

Discrete Angular Momentum Conserving Algorithm

"No knowledge can be certain, if it is not based upon mathematics or upon some other knowledge which is itself based upon the mathematical sciences".

Leondardo da Vinci (1452 – 1519)

6.1 Introductory Remarks

The numerical technique that has been developed so far does not ensure the conservation of angular momentum of a system, which then induces energy loss under long-term analysis. In order to rectify this, an exact angular momentum conserving time stepping algorithm for Lagrangian rapid dynamic analysis will be introduced.

Energy-momentum conserving schemes for integration of the momentum balance principle in nonlinear elastodynamics were a matter of intense research over the past few decades. In the early 1990s, an exact energy-momentum conserving algorithm for nonlinear dynamics was first proposed by Simo *et al.*(1992) [99]. This class of schemes was successfully further extended to nonlinear shells in [101], as well as to nonlinear rods [100]. Unfortunately, the proposed conserving algorithm can only be applied in hyperelastic material with quadratic potentials, namely Saint-Venant Kirchhoff material, as pointed out by Laursen and Meng (2001) [103]. Some modifications were made to allow for any hyperelastic materials [102, 103] .

This chapter begins by establishing the condition that has to be satisfied for preserving angular momentum of a system. Section 6.2 presents a generic constraint derived from the above condition where the conservation property is inherent in the time integrator. In Section 6.3, a correction procedure based on a minimisation method will then be presented. This procedure does not involve any extra variables (or equations).

Figure 6.1 summarises the roadmap of this chapter.

6.2 A Generic Constraint

In general, the total angular momentum of a system is given as

$$\boldsymbol{A} = \int_V \boldsymbol{x} \times \boldsymbol{p}\, dV; \qquad \boldsymbol{p} = \rho_0 \boldsymbol{v}. \tag{6.1}$$

Alternatively, the equation above can also be represented in a discrete form:

$$\boldsymbol{A} = \sum_{e=1}^{N_{elem}} \boldsymbol{x}_e \times m_e \boldsymbol{v}_e. \tag{6.2}$$

Note here that $\boldsymbol{x}_e$ denotes the centroid coordinate of cell e, N_{elem} indicates the total number of elements in the computational domain, m_e and $\boldsymbol{v}_e$ describe the mass and velocity vector at cell e. In essence, the total angular momentum of a system of particles should stay conserved unless an external torque acts on it. Mathematically, this principle is given by

$$\boldsymbol{A}^{n+1} - \boldsymbol{A}^n = \boldsymbol{0}. \tag{6.3}$$

By inserting (6.2) into the above expression gives

$$\sum_{e=1}^{N_{elem}} \boldsymbol{x}_e^{n+1} \times m_e \boldsymbol{v}_e^{n+1} - \sum_{e=1}^{N_{elem}} \boldsymbol{x}_e^{n} \times m_e \boldsymbol{v}_e^{n} = \boldsymbol{0} \tag{6.4}$$

with the aid of mass conservation law, that is $m_e^{n+1} = m_e^n = m_e$. Making use of the second order TVD Runge-Kutta time integrator for $d\boldsymbol{x}/dt = \boldsymbol{v}$, the trapezoidal numerical approximation rule of $\boldsymbol{x}_e^{n+1}$ is given as

$$\boldsymbol{x}_e^{n+1} = \boldsymbol{x}_e^n + \frac{\Delta t}{2}(\boldsymbol{v}_e^n + \boldsymbol{v}_e^{n+1}). \tag{6.5}$$

Expression (6.4) then yields

$$\sum_{e=1}^{N_{elem}} \boldsymbol{x}_e^{n+1/2} \times m_e(\boldsymbol{v}_e^{n+1} - \boldsymbol{v}_e^n) = \boldsymbol{0}; \qquad \boldsymbol{x}_e^{n+1/2} = \boldsymbol{x}_e^n + \frac{\Delta t}{2}\boldsymbol{v}_e^n, \tag{6.6}$$

by using $\boldsymbol{v}_e^{n+1} \times \boldsymbol{v}_e^{n+1} = \boldsymbol{v}_e^n \times \boldsymbol{v}_e^n = \boldsymbol{0}$. The updated coordinate of $\boldsymbol{x}_e^{n+1}$ at time step $n+1$ is expressed as

$$\boldsymbol{x}_e^{n+1} = \boldsymbol{x}_e^{n+1/2} + \frac{\Delta t}{2}\boldsymbol{v}_e^{n+1}. \tag{6.7}$$

By virtue of (6.6b) and (6.7), (6.5) is simply recovered.

Alternatively, the derivation performed above can now be followed for the first order TVD Runge-Kutta time stepping scheme:

$$\sum_{e=1}^{N_{elem}} \boldsymbol{x}_e^{n+1} \times m_e(\boldsymbol{v}_e^{n+1} - \boldsymbol{v}_e^n) = \boldsymbol{0}; \qquad \boldsymbol{x}_e^{n+1} = \boldsymbol{x}_e^n + \Delta t \boldsymbol{v}_e^n. \tag{6.8}$$

Noting that the only unknown left in (6.6a) or (6.8a) is $\boldsymbol{v}_e^{n+1}$, it is essential to relate this term to the time integration for the momentum balance principle [88]:

1. **First order Euler temporal scheme**: This is usually expressed as

$$\Delta \boldsymbol{v}_e = -\frac{1}{\rho_0^e}\Delta t \boldsymbol{R}_{\boldsymbol{p},e}^n, \tag{6.9}$$

where

$$\boldsymbol{R}_{\boldsymbol{p},e}^n = \boldsymbol{R}_{\boldsymbol{p}}(\boldsymbol{t}_k^{C,n}, l_k, A_e) = -\frac{1}{A_e}\sum_{\substack{k=1 \\ k\in e}}^{N_{ed}} \boldsymbol{t}_k^{C,n} l_k. \tag{6.10}$$

Inserting above equation into (6.8a) yields

$$\sum_{e=1}^{N_{elem}} \left(\boldsymbol{x}_e^{n+1} \times \Delta t \sum_{\substack{k=1 \\ k\in e}}^{N_{ed}} \boldsymbol{t}_k^{C,n} l_k \right) = \boldsymbol{0}. \tag{6.11}$$

$\Delta t \equiv const$ is neglected for simplicity. Furthermore, the above expression is rearranged to be a summation over all the interior edges $N_{ed_{int}}$:

$$\sum_{\substack{k=1 \\ e,\alpha\in k}}^{N_{ed_{int}}} (\boldsymbol{x}_\alpha^{n+1} - \boldsymbol{x}_e^{n+1}) \times \boldsymbol{t}_k^{C,n} l_k = \boldsymbol{0}. \tag{6.12}$$

This implies that the total moment of the traction vectors at the interior edges of the cells vanishes. By virtue of (6.12), the boundary edges are not considered as they will contribute towards an external torque. Note that α is the neighbouring cell which shares a particular interior k^{th}-edge with cell e and $\boldsymbol{x}_{\beta}^{n+1}$ denotes the centroid coordinate of cell β at time step $n+1$, where $\beta = \{e, \alpha\}$ (see Figure 6.2).

2. **Second order Improved Euler temporal scheme**: The general framework is shown as

$$\begin{aligned}
\boldsymbol{v}_e^{(1)} &= \boldsymbol{v}_e^n \\
\boldsymbol{v}_e^{(2)} &= \boldsymbol{v}_e^n - \frac{1}{\rho_0^e}\Delta t \boldsymbol{R}_{\boldsymbol{p},e}^{(1)} \\
\boldsymbol{v}_e^{n+1} &= \frac{1}{2}\boldsymbol{v}_e^n + \frac{1}{2}\boldsymbol{v}_e^{(2)} - \frac{\Delta t}{2}\frac{1}{\rho_0^e}\boldsymbol{R}_{\boldsymbol{p},e}^{(2)}.
\end{aligned}$$

More specifically, the above expression reduces to

$$\Delta \boldsymbol{v}_e = -\frac{\Delta t}{2}\frac{1}{\rho_0^e}\left(\boldsymbol{R}_{\boldsymbol{p},e}^{(1)} + \boldsymbol{R}_{\boldsymbol{p},e}^{(2)}\right), \tag{6.13}$$

where

$$\begin{aligned}
\boldsymbol{R}_{\boldsymbol{p},e}^{(1)} &= \boldsymbol{R}_{\boldsymbol{p}}(\boldsymbol{t}_k^{C,(1)}, l_k, A_e) = -\frac{1}{A_e}\sum_{\substack{k=1 \\ k\in e}}^{N_{ed}} \boldsymbol{t}_k^{C,(1)} l_k, \\
\boldsymbol{R}_{\boldsymbol{p},e}^{(2)} &= \boldsymbol{R}_{\boldsymbol{p}}(\boldsymbol{t}_k^{C,(2)}, l_k, A_e) = -\frac{1}{A_e}\sum_{\substack{k=1 \\ k\in e}}^{N_{ed}} \boldsymbol{t}_k^{C,(2)} l_k.
\end{aligned} \tag{6.14}$$

By substituting (6.13) into (6.6a) for $\Delta \boldsymbol{v}_e = \boldsymbol{v}_e^{n+1} - \boldsymbol{v}_e^n$ yields

$$\sum_{e=1}^{N_{elem}} \boldsymbol{x}_e^{n+1/2} \times \left[-\frac{\Delta t}{2} A_e \left(\boldsymbol{\mathcal{R}}_{\boldsymbol{p},e}^{(1)} + \boldsymbol{\mathcal{R}}_{\boldsymbol{p},e}^{(2)}\right)\right] = \boldsymbol{0}. \tag{6.15}$$

By virtue of the equation above, it is easy to demonstrate that these conditions

$$\sum_{e=1}^{N_{elem}} \left(\boldsymbol{x}_e^{n+1/2} \times \sum_{\substack{k=1 \\ k\in e}}^{N_{ed}} \boldsymbol{t}_k^{C,(1)} l_k \right) = \boldsymbol{0}; \qquad \sum_{e=1}^{N_{elem}} \left(\boldsymbol{x}_e^{n+1/2} \times \sum_{\substack{k=1 \\ k\in e}}^{N_{ed}} \boldsymbol{t}_k^{C,(2)} l_k \right) = \boldsymbol{0}, \tag{6.16}$$

have to be strongly satisfied. Nevertheless, (6.16) are equivalently restructured into a summation over all interior edges, $N_{ted_{int}}$, as

- First stage:

$$\sum_{\substack{k=1 \\ e,\alpha\in k}}^{N_{ed_{int}}} (\boldsymbol{x}_{\alpha}^{n+1/2} - \boldsymbol{x}_e^{n+1/2}) \times \boldsymbol{t}_k^{C,(1)} l_k = \boldsymbol{0}. \tag{6.17}$$

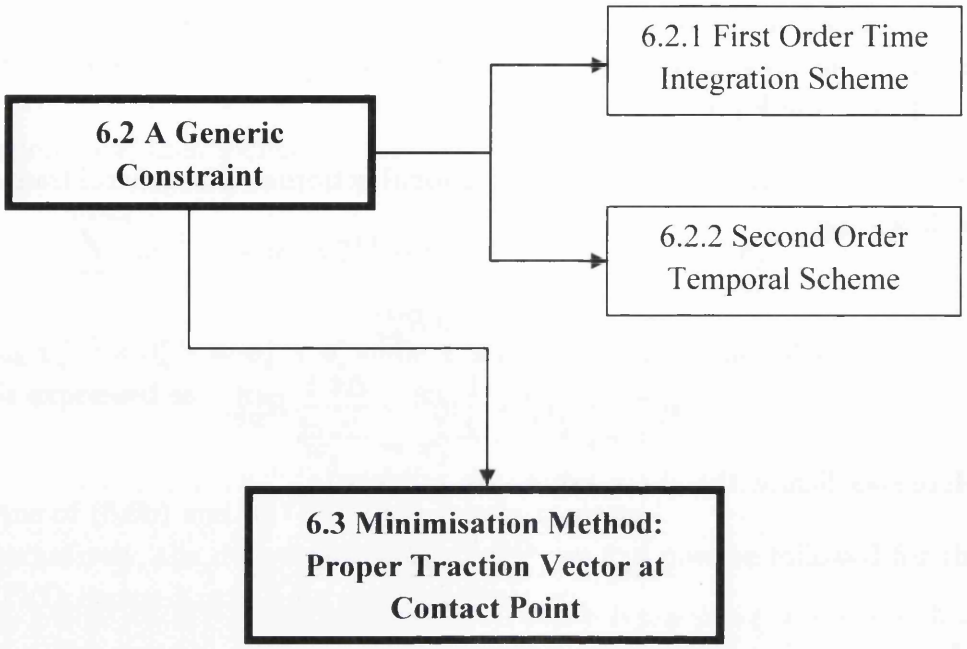

Figure 6.1: Roadmap of this chapter.

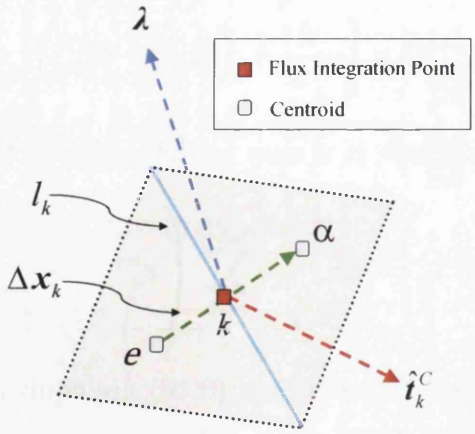

Figure 6.2: Constraint for preserving the total angular momentum of a system.

- Second stage:

$$\sum_{\substack{k=1 \\ e,\alpha\in k}}^{N_{ed_{int}}} (\boldsymbol{x}_\alpha^{n+1/2} - \boldsymbol{x}_e^{n+1/2}) \times \boldsymbol{t}_k^{C,(2)} l_k = \mathbf{0}. \tag{6.18}$$

Here, $\Delta \boldsymbol{v}_e = \boldsymbol{v}_e^{n+1} - \boldsymbol{v}_e^n$. A_e represents the area of cell e, l_k describes the length of contact k^{th}-edge, $\boldsymbol{t}_k^C$ indicates the traction vector at a contact k^{th}-point which is computed based upon Riemann solver, Δt is the time increment, ρ_0^e stands for the local material density and N_{ed} describes the number of edges belong to cell e. These constraints, viz. (6.12), (6.17) and (6.18), will be used to correct the traction vector at contact point through minimisation procedure, which shall be discussed in the next section.

6.3 Minimisation Method: Proper Traction Vector at Contact Point

In order that the total angular momentum of a system stays constant under long-term response analysis, it is essential to satisfy the constraint of the form

$$\sum_{\substack{k=1 \\ e,\alpha\in k}}^{N_{ed_{int}}} (\boldsymbol{x}_\alpha^{n+\eta} - \boldsymbol{x}_e^{n+\eta}) \times \boldsymbol{t}_k^{C,(\beta)} l_k = \mathbf{0}. \tag{6.19}$$

Here, β describes Runge-Kutta stages, $\eta = 1$ and $\eta = 1/2$ for first and second order overall numerical accuracy, respectively. For the sake of convenience, the time argument will be ignored in the development below. The constraint (6.19) is therefore re-expressed as

$$\sum_{k=1}^{N_{ed_{int}}} \boldsymbol{t}_k^C l_k \times \Delta \boldsymbol{x}_k = \mathbf{0}; \qquad \Delta \boldsymbol{x}_k|_{e,\alpha\in k} = \boldsymbol{x}_\alpha - \boldsymbol{x}_e. \tag{6.20}$$

It is now convenient to introduce a functional Π defined by

$$\Pi(\hat{\boldsymbol{t}}_k^C, \boldsymbol{\lambda}) = \left(\frac{1}{2} \sum_{k=1}^{N_{ed_{int}}} l_k^2 (\hat{\boldsymbol{t}}_k^C - \boldsymbol{t}_k^C) \cdot (\hat{\boldsymbol{t}}_k^C - \boldsymbol{t}_k^C) \right) + \boldsymbol{\lambda} \cdot \sum_{k=1}^{N_{ed_{int}}} l_k \hat{\boldsymbol{t}}_k^C \times \Delta \boldsymbol{x}_k, \tag{6.21}$$

where $\hat{\boldsymbol{t}}_k^C$ indicates the corrected traction vector at contact point and $\boldsymbol{\lambda}$ describes the Lagrange multiplier vector perpendicular to the plane in which $\hat{\boldsymbol{t}}^C$ and $\Delta \boldsymbol{x}$ lie (see Figure 6.2). The stationary condition of the above functional (6.21) with respect to $\boldsymbol{\lambda}$ and $\hat{\boldsymbol{t}}_k^C$ will be considered separately.

To this effect, note firstly that the derivative of Π with respect to $\boldsymbol{\lambda}$ is

$$\frac{\partial \Pi}{\partial \boldsymbol{\lambda}} = \sum_{k=1}^{N_{ed_{int}}} l_k \hat{\boldsymbol{t}}_k^C \times \Delta \boldsymbol{x}_k = \mathbf{0}. \tag{6.22}$$

Equation above implies that the total angular momentum of a system remains constant if and only if the corrected traction vector $\hat{\boldsymbol{t}}_k^C$ satisfies above condition. Additionally, the derivative of (6.21) with respect to $\hat{\boldsymbol{t}}_k^C$ is given as

$$\frac{\partial \Pi}{\partial \hat{\boldsymbol{t}}_k^C} = \sum_{k=1}^{N_{ed_{int}}} l_k^2 (\hat{\boldsymbol{t}}_k^C - \boldsymbol{t}_k^C) + \sum_{k=1}^{N_{ed_{int}}} l_k \Delta \boldsymbol{x}_k \times \boldsymbol{\lambda} = \boldsymbol{0}. \tag{6.23}$$

By using $\Delta \boldsymbol{x}_k \times \boldsymbol{\lambda} = -\boldsymbol{\lambda} \times \Delta \boldsymbol{x}_k$, the corrected traction vector $\hat{\boldsymbol{t}}_k^C$ is eventually obtained as

$$\hat{\boldsymbol{t}}_k^C = \boldsymbol{t}_k^C + \underbrace{\frac{1}{l_k} \boldsymbol{\lambda} \times \Delta \boldsymbol{x}_k}_{\text{correction term}}. \tag{6.24}$$

Once $\boldsymbol{\lambda}$ is determined, the traction vector $\boldsymbol{t}_k^C$ can now be corrected by substituting $\boldsymbol{\lambda}$ into (6.24). In order to achieve this, it is vital to insert (6.24) into (6.22) for $\hat{\boldsymbol{t}}_k^C$ which then yields

$$\sum_{k=1}^{N_{ed_{int}}} l_k (\boldsymbol{t}_k^C + \frac{1}{l_k} \boldsymbol{\lambda} \times \Delta \boldsymbol{x}_k) \times \Delta \boldsymbol{x}_k = \boldsymbol{0}. \tag{6.25}$$

To this end, $\boldsymbol{\lambda}$ is derived as follows:

$$\sum_{k=1}^{N_{ed_{int}}} \Delta \boldsymbol{x}_k \times (\boldsymbol{\lambda} \times \Delta \boldsymbol{x}_k) = \sum_{k=1}^{N_{ed_{int}}} l_k \boldsymbol{t}_k^C \times \Delta \boldsymbol{x}_k$$

$$\boldsymbol{\lambda} \sum_{k=1}^{N_{ed_{int}}} (\Delta \boldsymbol{x}_k \cdot \Delta \boldsymbol{x}_k) = \sum_{k=1}^{N_{ed_{int}}} l_k \boldsymbol{t}_k^C \times \Delta \boldsymbol{x}_k$$

$$\boldsymbol{\lambda} = \frac{\sum_{k=1}^{N_{ed_{int}}} l_k \boldsymbol{t}_k^C \times \Delta \boldsymbol{x}_k}{\sum_{k=1}^{N_{ed_{int}}} \Delta \boldsymbol{x}_k \cdot \Delta \boldsymbol{x}_k}. \tag{6.26}$$

Note that $(\Delta \boldsymbol{x}_k \cdot \boldsymbol{\lambda})$ vanishes due to the fact that their directions are orthogonal to each other, that is $\Delta \boldsymbol{x}_k \perp \boldsymbol{\lambda}$.

Chapter 7

Involution: Compatibility Condition

"Numerical precision is the very soul of science".

Sir D'Arcy Wentworth Thompson (1860 – 1948)

7.1 Introductory Remarks

Many evolution equations in engineering and science come with intrinsic constraints. The evolution of $\boldsymbol{F}$ considered in this work is

$$\frac{\partial \boldsymbol{F}}{\partial t} = \boldsymbol{\nabla}_0 \boldsymbol{v} = \boldsymbol{\nabla}_0 \cdot (\boldsymbol{v} \otimes \boldsymbol{I}) .$$

It is clear that the components of $\boldsymbol{F}$ must satisfy some compatibility conditions (i.e. $\operatorname{curl} \boldsymbol{F} = \boldsymbol{0}$) in order to guarantee the existence of a single-valued continuous displacement field. These conditions (also known as involutions[1]) are such that they are satisfied under exact integration provided they are satisfied by the initial condition, which implies that the curl preservation is an inherent analytical property of the evolution operator. The most challenging aspect of designing a reliable and robust numerical method is the ability to control curl errors (modes) under long-term response analysis. These errors usually accummulate and lead to a breakdown of classical numerical schemes. Two approaches have been used for constructing a curl-free method. The first one is based upon the local projection, at every step of the time integration process, of the deformation gradient tensor onto the space of curl free tensors [59, 64]. The second approach, introduced by Miller and Colella (2001) [118], is to formulate a modified system of equations based on the assumption that $\operatorname{curl} \boldsymbol{F} \neq \boldsymbol{0}$. This new system contains additional terms which advect the errors out of the computational domain. More recently, a general framework for a locally curl-preserving finite volume method on two-dimensional structured quadrilateral grids has been proposed in [104]. This latter approach, based on the introduction of a set of special curl-preserving flux distributions, will be explored and expanded in this chapter for the curl preservation of the deformation gradient tensor $\boldsymbol{F}$ for two-dimensional structured (i.e. quadrilateral and triangular) grids.

The roadmap of this chapter is depicted in Figure 7.1.

7.2 Curl-preserving Updated Scheme

A locally constraint-preserving finite volume method has been successfully employed in shallow water equations [105]. This section will extend its use by exploring a more physically meaningful alternative framework. In Jeltsch and Torrilhon (2006) [105], the evolution equation is given by

$$\frac{\partial \boldsymbol{m}}{\partial t} + \boldsymbol{\nabla}_{\boldsymbol{x}} \cdot (p\boldsymbol{I}) = \boldsymbol{0}. \tag{7.1}$$

This is equivalent to

$$\dot{\boldsymbol{m}} = -\boldsymbol{\nabla}_{\boldsymbol{x}} p, \tag{7.2}$$

[1]Involution (as opposed to a classical constraint) is not necessary to close the system of conservation laws, but must be an inherent property of the evolution operator.

where $\boldsymbol{m}$ describes the momentum variable, p represents the pressure and $\boldsymbol{\nabla}_{\boldsymbol{x}}$ denotes the gradient operator in deformed configuration. The evolution equation (7.2) reveals the constraint curl $\boldsymbol{m} = const$ and notably, the expression above shows an interesting structural similarity with $\dot{\boldsymbol{F}}$, given as

$$\frac{\partial \boldsymbol{F}^i}{\partial t} = \boldsymbol{\nabla}_0 v_i, \qquad \forall i = 1, 2, 3. \tag{7.3}$$

Note that $\boldsymbol{F}^i$ is the i^{th}-row of deformation gradient tensor and v_i denotes the velocity in respective i^{th} direction of cartesian axes. Consequently, curl $\boldsymbol{F}^i = const$ at all times.

In order to preserve this constraint in a discrete formulation, $\dot{\boldsymbol{m}}$ can be expressed as a linear combination of curl-preserving functions $\boldsymbol{\Phi}^{e,\text{curl-free}}$ [105]. In the case of quadrilateral grid cells, the adjacent elements of a given node a are demonstrated as

$$\begin{aligned} \boldsymbol{\Phi}_a^{NE,\text{curl-free}} &= (\Delta y, \Delta x)^T, & \boldsymbol{\Phi}_a^{NW,\text{curl-free}} &= (-\Delta y, \Delta x)^T, \\ \boldsymbol{\Phi}_a^{SE,\text{curl-free}} &= (\Delta y, -\Delta x)^T, & \boldsymbol{\Phi}_a^{SW,\text{curl-free}} &= (-\Delta y, -\Delta x)^T, \end{aligned} \tag{7.4}$$

(see Figure 7.2a). These curl-preserving functions enable the evolution of $\boldsymbol{m}$ to be expressed as

$$\dot{\boldsymbol{m}}^e = \sum_{\substack{a=1 \\ e \in a}}^{Nn} f(p) \boldsymbol{\Phi}_a^{e,\text{curl-free}}. \tag{7.5}$$

$f(p)$ denotes an arbitrary function of element pressures and Nn describes the number of nodes. It is useful to notice that the functions $\boldsymbol{\Phi}_a^{e,\text{curl-free}}$ are proportional to the gradients of standard bilinear shape function $\hat{N}_a$, that is

$$\boldsymbol{\Phi}_a^{e,\text{curl-free}} = -2A_e \boldsymbol{\nabla}_{\boldsymbol{x}} \hat{N}_a^e; \qquad A_e = \Delta x \Delta y, \tag{7.6}$$

where the gradient is evaluated at the centroid of the cell e. Expression (7.5) is thus equivalent to

$$\dot{\boldsymbol{m}}^e = -\sum_{\substack{a=1 \\ e \in a}}^{Nn} p_a \boldsymbol{\nabla}_{\boldsymbol{x}} \hat{N}_a^e, \qquad p_a = 2A_e f(p). \tag{7.7}$$

Here, p_a are some nodal values of p obtained from element pressures that are yet to be defined. Expression (7.7) is obviously curl-preserving as the evolution of $\boldsymbol{m}$ is formulated by the gradient of an artificially constructed pressure field. In addition, equation above can be further extended to triangular mesh by simply changing the shape function $\hat{N}_a$ to that of linear triangle. The real challenging questions are two-fold:

- How to relate (7.7) to a finite volume formulation and,
- how to obtain the nodal pressure p_a.

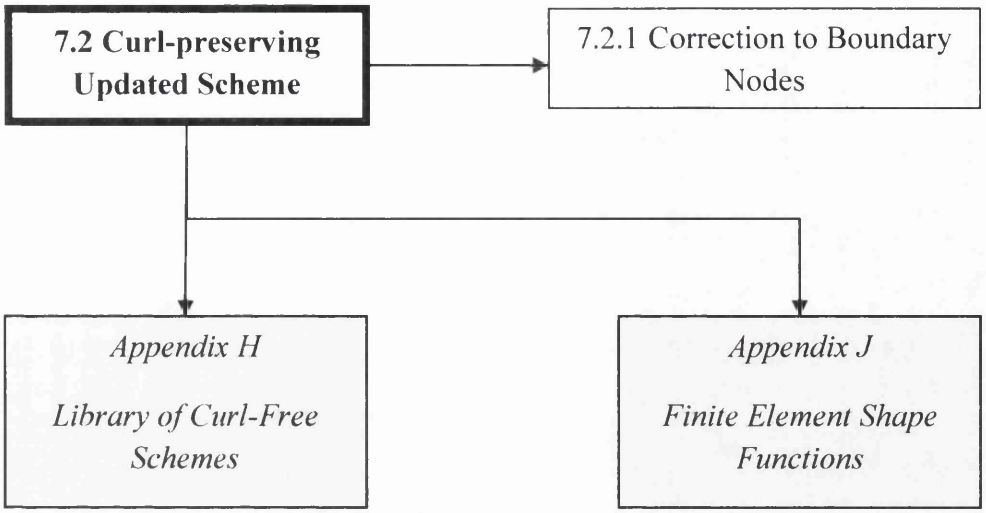

Figure 7.1: Structure of this chapter.

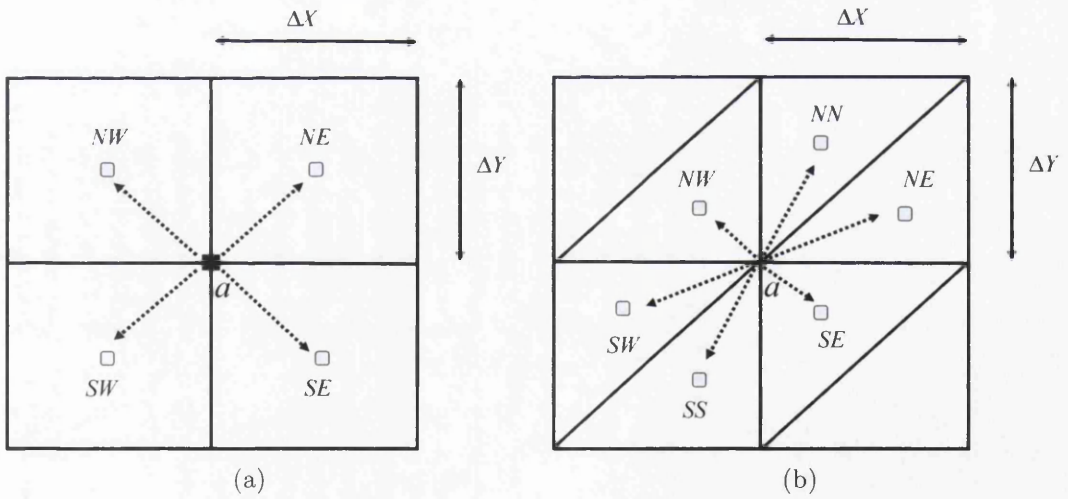

Figure 7.2: A set of adjacent elements for a given node a: (a) Quadrilateral; and (b) Triangular meshes.

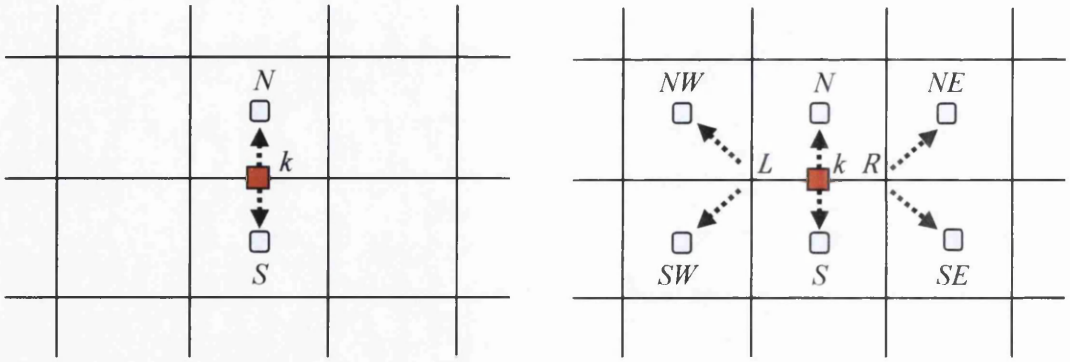

(a) (b)

Figure 7.3: Flux distributions of a given k^{th}-edge: (a) A classical finite volume method; and (b) Curl-free updated scheme.

The standard finite volume spatial discretisation for (7.1) is denoted as

$$\dot{\boldsymbol{m}}^e = -\frac{1}{A_e}\sum_{\substack{k=1\\ e\in k}}^{N_{ted}} p_k \boldsymbol{n}_k l_k \tag{7.8a}$$

$$= \frac{1}{A_e}\sum_{\substack{k=1\\ e\in k}}^{N_{ted}} p_k \boldsymbol{\Phi}_k^{e,\text{class}} \tag{7.8b}$$

Note that p_k is evaluated at contact point, $\boldsymbol{n}_k$ stands for the spatial unit outward normal vector, A_e denotes the area of cell e, l_k represents the length of boundary face and N_{ted} describes the total number of edges in the physical domain including boundary edges. The classical edge distribution functions for an arbitrary k^{th}-edge are defined as follows (see Figure 7.3a),

$$\boldsymbol{\Phi}_k^{N,\text{class}} = (0, \Delta x)^T, \qquad \boldsymbol{\Phi}_k^{S,\text{class}} = (0, -\Delta x)^T. \tag{7.9}$$

In order to make this update compatible with (7.5), $\boldsymbol{\Phi}_k^{e,\text{class}}$ is replaced by a linear combination of curl-preserving $\boldsymbol{\Phi}^{e,\text{curl-free}}$ defined as

$$\boldsymbol{\Phi}_k^{e,\text{class}} = \alpha(\boldsymbol{\Phi}_L^{e,\text{curl-free}} + \boldsymbol{\Phi}_R^{e,\text{curl-free}}), \qquad L, R \in k, \tag{7.10}$$

where α is a coefficient that ensures the consistency of this new approach and L, R are the two nodes connected to edge k (see Figure 7.3b). In this approach, an arbitrary k^{th}-edge contributes to a set of the surrounding elements e, namely $\{NW, SW, N, S, NE, SE\}$ (see Figure 7.3b) whereas, only two adjacent elements $\{N, S\}$ are updated in the classical finite volume scheme (see Figure 7.3a). It is now possible to evaluate the coefficient α by inserting (7.10) into (7.8b) for $\dot{\boldsymbol{m}}$, and relate it back to (7.5). By rearranging the sum, it gives

$$\dot{\boldsymbol{m}}^e = \sum_{\substack{k=1\\ e,L,R\in k}}^{N_{ted}} \frac{\alpha}{A_e} p_k(\boldsymbol{\Phi}_L^{e,\text{curl-free}} + \boldsymbol{\Phi}_R^{e,\text{curl-free}}) = \sum_{\substack{a=1\\ e\in a}}^{N_n} \frac{\alpha}{A_e}\left(\sum_{\substack{k=1\\ k\in a}}^{4} p_k\right) \boldsymbol{\Phi}_a^{e,\text{curl-free}}. \tag{7.11}$$

Substituting (7.6) into above one yields

$$\dot{\boldsymbol{m}}^e = -\sum_{\substack{a=1\\ e\in a}}^{N_n} \left[2\alpha \sum_{\substack{k=1\\ k\in a}}^{4} p_k \right] \boldsymbol{\nabla}_{\boldsymbol{x}} \hat{N}_a^e = -\sum_{\substack{a=1\\ e\in a}}^{N_n} p_a \boldsymbol{\nabla}_{\boldsymbol{x}} \hat{N}_a^e. \tag{7.12}$$

The expression in square bracket denotes an averaged evaluation of nodal pressure obtained from Riemann values at contact points. For consistency, the coefficient α has to be $\alpha = 1/8$.

An extension to $\dot{\boldsymbol{F}}$ is trivial such that[2]

$$\dot{\boldsymbol{F}}^e = \sum_{\substack{a=1\\ e\in a}}^{N_n} \boldsymbol{v}_a \otimes \boldsymbol{\nabla}_0 \hat{N}_a^e. \tag{7.13}$$

Note that change in sign convention is required (see equation (7.2)). More generally, the nodal velocity $\boldsymbol{v}_a$ can be computed based upon area-weighted averaging technique:

$$\boldsymbol{v}_a = \frac{1}{A_a} \sum_{\substack{k=1\\ k\in a}}^{4} \boldsymbol{v}_k A_k. \tag{7.14}$$

For a regular quadrilateral mesh, a simple averaging process will be recovered, that is

$$\boldsymbol{v}_a = \frac{1}{4} \sum_{\substack{k=1\\ k\in a}}^{4} \boldsymbol{v}_k,$$

where A_k and $\boldsymbol{v}_k$ denote the area and contact velocity at k^{th}-edge.

7.2.1 Correction to Boundary Nodes

The area-weighted averaging procedure described above, viz. (7.14), produces good results at interior nodes but leave something to be desired at boundary nodes. In order to improve this, it is essential to introduce a correction at each boundary node [69]. Two types of boundary node corrections, specifically for quadrilateral grid cells (see Figure 7.4a), are carried out in the following two steps:

Step 1: Non-corner boundary nodes. A typical situation is depicted in Figure 7.4b. For a uniform mesh, the weighted averaged nodal velocity at non-corner boundary node a, $\boldsymbol{v}_a$, has to be corrected by a linear extrapolation from interior node b and velocity at contact point k, that is

$$\boldsymbol{v}_a \longleftarrow \frac{1}{2}(\boldsymbol{v}_a + 2\boldsymbol{v}_k - \boldsymbol{v}_b). \tag{7.15}$$

[2]The gradient of a shape function will be discussed in Appendix J.

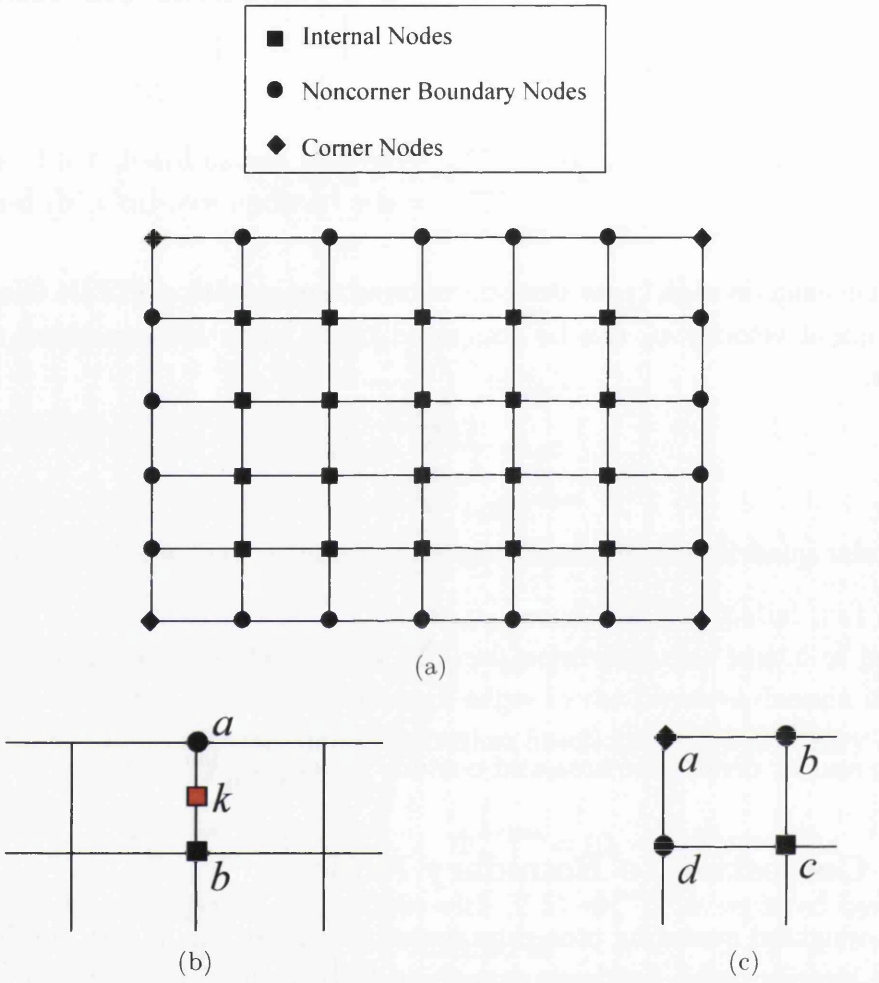

Figure 7.4: Four-noded quadrilateral cell: (a) Mesh; (b) Non-corner boundary node; and (c) Corner node.

Step 2: Corner nodes. A linear extrapolation is employed through corrected non-corner boundary nodes b, d and interior node c (see Figure 7.4c):

$$\boldsymbol{v}_a \longleftarrow \frac{\hat{L}_b \boldsymbol{v}_b + \hat{L}_c \boldsymbol{v}_c + \hat{L}_d \boldsymbol{v}_d}{L} \tag{7.16}$$

where

$$\begin{aligned}
L &= L_b + L_c + L_d \\
L_b &= X_c Y_d - X_d Y_c \\
L_c &= X_d Y_b - X_b Y_d \\
L_d &= X_b Y_c - X_c Y_b \\
\hat{L}_b &= L_b + (Y_c - Y_d) X_a + (X_d - X_c) Y_a \\
\hat{L}_c &= L_c + (Y_d - Y_b) X_a + (X_b - X_d) Y_a \\
\hat{L}_d &= L_d + (Y_b - Y_c) X_a + (X_c - X_b) Y_a.
\end{aligned}$$

Here, X and Y are cartesian coordinates. Expression (7.16) can be further reduced to

$$\boldsymbol{v}_a \longleftarrow \boldsymbol{v}_b + \boldsymbol{v}_d - \boldsymbol{v}_c \tag{7.17}$$

for a uniform mesh.

Chapter 8

Analysis of Numerical Scheme

"This definitive source on the accuracy and stability of numerical algorithms is quite a bargain and a worthwhile addition to the library of any statistician heavily involved in computing".

Robert L. Strawderman, Journal of the American Statistical Association 1999

8.1 Introductory Remarks

The overall numerical strategy has now to be analysed for its validity and accuracy. In order to investigate this, it is essential to introduce a certain number of concepts such as consistency, stability and convergence. These fundamental concepts are of paramount importance in ensuring that the result obtained from computer simulation represents a valid approximation of reality. More detailed numerical analysis of any numerical method can be found in [25, 60, 92, 98, 158].

The chapter is organised as follows. Firstly, the numerical scheme has to be consistent with the mathematical model by introducing a small error in a single time step (see Section 8.2). This truncation error leads to an important source of information on the expected accuracy of the particular scheme. Section 8.3 is focusing on the Von Neumann stability analysis[1] so as to avoid errors grow catastrophically. Once the method is proven to be consistent and stable, it shall automatically satisfy the convergence requirement [106]. This fundamental theorem will be discussed in Section 8.4.

Interrelations between consistency, stability and convergence are illustrated in Figure 8.1. The consistency establishes a relation between the differential equation and its discrete formulation counterpart; stability condition defines a relation between the computed solution and exact solution of discrete formulation; convergence relates the computed solution to the exact solution of differential equation.

Figure 8.2 illustrates the structure of this chapter.

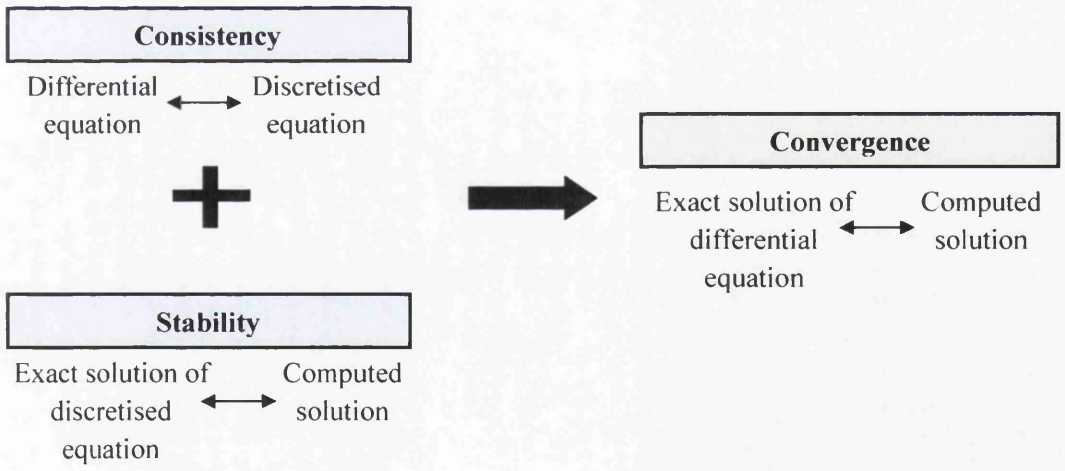

Figure 8.1: Relations between consistency, stability and convergence.

[1] In numerical analysis, Von Neumann stability analysis is also known as Fourier stability analysis.

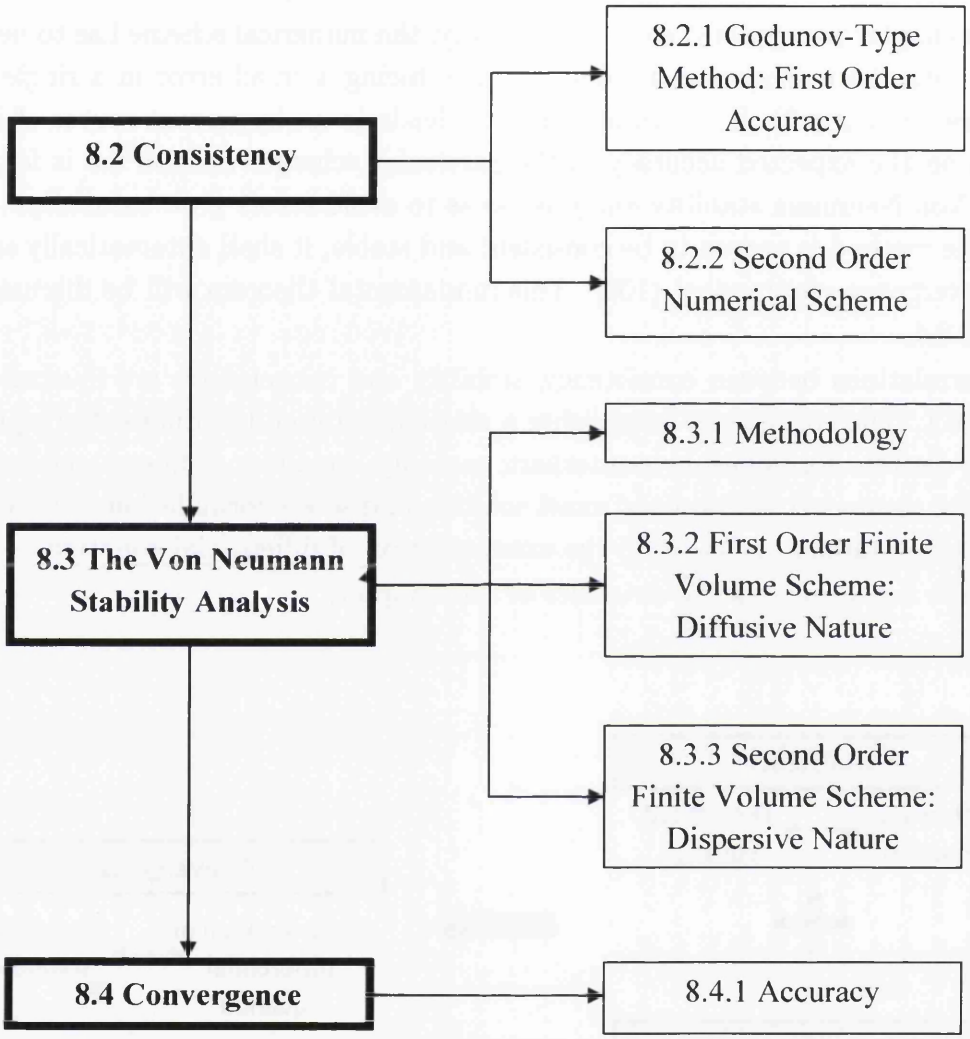

Figure 8.2: Structure of this chapter.

8.2 Consistency

Consistency implies that the numerical scheme tends to the original differential equation (or mathematical model) when the mesh size Δx is refined. This condition leads to a very important property of numerical discretisation, namely truncation error, which expresses a new vision of the relationship between the numerical scheme and the original differential equation. The major conclusion of this study is that the numerical solution does not satisfy a given differential equation but instead, a solution to an equivalent differential equation (or modified equation). See [25, 60] for some further discussions. For simplicity, a one dimensional linear constant convection equation, that is

$$q_t + aq_x = 0, \tag{8.1}$$

will be considered. Here, $a \equiv const$ describes the constant wave speed flows in a positive direction, q represents an unknown variable and $(\cdot)_k = \partial(\cdot)/\partial k$.

In general, an explicit numerical method can be written in the form

$$u_i^{n+1} = \mathcal{N}(u_\alpha^n). \tag{8.2}$$

Note that $\mathcal{N}(\cdot)$ is a numerical operator for mapping the approximate solution, u, at time step n to the following time step $n+1$. Perhaps most importantly, the local truncation error, τ^n, is defined by comparing the solution obtained from applying the numerical operator to the analytical solution q at time step n with the analytical solution at time step $n+1$ and then dividing this by Δt, from which gives

$$\tau^n = \frac{1}{\Delta t}[\mathcal{N}(q^n) - q^{n+1}]. \tag{8.3}$$

The method is said to be consistent with the original differential equation if the local truncation error vanishes as Δx (or Δt) $\longrightarrow 0$. To this end, a numerical analysis of (8.1) will be carried out.

Firstly, it merits noting that (8.1) is integrated over the length $\Delta x = X_{i+1/2} - X_{i-1/2}$. By employing the divergence theorem[2], the integral equation then yields

$$\frac{d}{dt}\int_{X_{i-1/2}}^{X_{i+1/2}} q\, dX = -a\int_{\partial A} qN_X\, dA, \tag{8.4}$$

where N_X is the material outward unit normal vector in X direction. Subsequently, (8.4) can be approximated as

$$\frac{du_i}{dt} = -\frac{a}{\Delta x}(u_{i+1/2}^C - u_{i-1/2}^C) \tag{8.5a}$$

$$= -\frac{a}{\Delta x}(u_i^+ - u_{i-1}^+). \tag{8.5b}$$

[2]Divergence theorem is alternatively known as Gauss' theorem. This fundamental theorem is discussed in any Calculus textbook.

Due to the fact that only a single wave is travelling towards the right at speed a, unknowns at contact points are easily reduced to $u^C_{i+1/2} = u^+_i$ and $u^C_{i-1/2} = u^+_{i-1}$ [25, 26, 60–62, 84]. The expression above leaves a wide range of choices for time integration schemes. The definitions of u^+_i and u^+_{i-1} will be clearly presented as follows (see Figure 8.3).

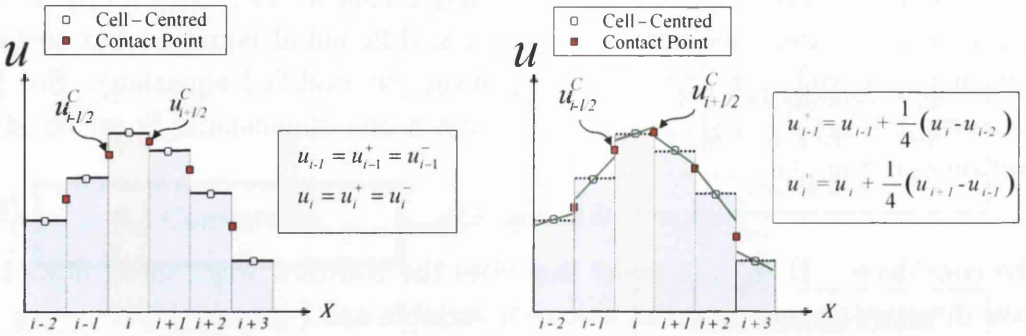

(a) (b)

Figure 8.3: Definitions of u^+_{i-1} and u^+_i: (a) Piecewise constant reconstruction; and (b) Piecewise linear reconstruction.

8.2.1 Godunov-Type Method: First Order Accuracy

In the Godunov-type method, the problem (or unknown) variable, u, is reconstructed as a piecewise constant over the grid cells at each time step. This constant reconstruction process is mathematically expressed by

$$u_{i-1} = u^+_{i-1} = u^-_{i-1}, \qquad u_i = u^+_i = u^-_i \tag{8.6}$$

With the aid of above conditions, an upwind method based on (8.5) is reduced to

$$\frac{du_i}{dt} = -R; \qquad R = \frac{a}{\Delta x}(u_i - u_{i-1}). \tag{8.7}$$

Furthermore, the first-order explicit Euler time scheme is chosen to advance forward in time

$$\frac{u^{n+1}_i - u^n_i}{\Delta t} = -R^n; \qquad R^n = \frac{a}{\Delta x}(u^n_i - u^n_{i-1}). \tag{8.8}$$

Equation above can be rearranged to

$$u^{n+1}_i = u^n_i - \alpha_{CFL}(u^n_i - u^n_{i-1}), \tag{8.9}$$

where $\alpha_{CFL} = a\Delta t/\Delta x$. This expression represents a two-point stencil method by means of only two grid points are needed for updating u^{n+1}_i, which can be generally expressed as

$$u^{n+1}_i = \mathcal{N}(u^n_{i-1}, u^n_i). \tag{8.10}$$

With the numerical operator $\mathcal{N}$ defined above, it is possible to determine the local truncation error τ^n . By substituting the analytical solution into (8.9), the truncation error (8.3) yields

$$\tau^n = \frac{1}{\Delta t}\left[q_i^n - q_i^{n+1} + \alpha_{CFL}(q_{i-1}^n - q_i^n)\right]. \tag{8.11}$$

Here, $(\cdot)_a^b = (\cdot)(a,b)$. Using Taylor series expansion techniques, the above terms involving $(\cdot)_a^b$ (where $a \neq i$ and $b \neq n$) are expanded about (x_i, t^n):

$$\tau^n = \underbrace{-\left[q_t + aq_x\right]_i^n}_{\text{equal to 0}} + \frac{1}{2}\left[a\Delta x q_{xx} - \Delta t q_{tt} + \mathcal{O}(\Delta x)^2\right]_i^n. \tag{8.12}$$

Note here that the terms in $[\cdot]$ are computed at (x_i, t^n). The first term in the expression above vanishes due to the fact that analytical solution satisfies the corresponding differential equation; that is, $q_t + aq_x = 0$. Based upon the definition of $q_{tt} = a^2 q_{xx}$, (8.12) reduces to

$$\tau^n = \frac{a\Delta x}{2}(1 - \alpha_{CFL})[q_{xx}]_i^n + \mathcal{O}(\Delta x)^2. \tag{8.13}$$

It is obvious that the local truncation error, τ^n, is dominated by $\mathcal{O}(\Delta x)$, which clearly depends upon diffusive term q_{xx}. Therefore, the numerical scheme is of first order accuracy in space and time.

8.2.2 Second Order Numerical Scheme

This section demonstrates the local truncation error, τ, of a second-order finite volume spatial discretisation together with an Improved Euler time integrator. The gradient operators (as discussed in Section 4.4) are represented as

$$G_{i-1} = \frac{u_i - u_{i-2}}{2\Delta x}; \qquad G_i = \frac{u_{i+1} - u_{i-1}}{2\Delta x}. \tag{8.14}$$

Thus, the reconstructed values at contact points are shown as

$$u_{i-1}^+ = u_{i-1} + \frac{1}{4}(u_i - u_{i-2}), \tag{8.15a}$$

$$u_i^+ = u_i + \frac{1}{4}(u_{i+1} - u_{i-1}). \tag{8.15b}$$

By substituting them into (8.5b), after some simple algebraic manipulations, it gives

$$\frac{du_i}{dt} = -R; \qquad R = \frac{a}{4\Delta x}(u_{i+1} + 3u_i - 5u_{i-1} + u_{i-2}). \tag{8.16}$$

It is now convenient to evolve the ordinary differential equation (8.16) by the second order Improved Euler time integrator [88]:

$$u_i^{(1)} = u_i^n \tag{8.17a}$$

$$u_i^{(2)} = u_i^n - \Delta t\, R(u^{(1)}) \tag{8.17b}$$

$$u_i^{n+1} = \frac{1}{2}u_i^n + \frac{1}{2}u_i^{(2)} - \frac{1}{2}\Delta t\, R(u^{(2)}), \tag{8.17c}$$

where the residual terms are

$$R(u^{(1)}) = \frac{a}{4\Delta x}(u_{i+1}^n + 3u_i^n - 5u_{i-1}^n + u_{i-2}^n), \tag{8.18a}$$

$$R(u^{(2)}) = \frac{a}{4\Delta x}(u_{i+1}^{(2)} + 3u_i^{(2)} - 5u_{i-1}^{(2)} + u_{i-2}^{(2)}). \tag{8.18b}$$

By simple inspection, it transpires that the variables to be determined are $u_\alpha^{(2)}$ where $\alpha = \{i-2, i-1, i, i+1\}$. Based on (8.17b), $u_i^{(2)}$ is stated as

$$u_i^{(2)} = u_i^n - \frac{1}{4}\alpha_{CFL}(u_{i+1}^n + 3u_i^n - 5u_{i-1}^n + u_{i-2}^n); \qquad \alpha_{CFL} = \frac{a\Delta t}{\Delta x}. \tag{8.19}$$

Furthermore, the rest of the unknowns can be evaluated in a similar manner as

$$u_{i+\beta}^{(2)} = u_{i+\beta}^n - \frac{1}{4}\alpha_{CFL}(u_{i+1+\beta}^n + 3u_{i+\beta}^n - 5u_{i-1+\beta}^n + u_{i-2+\beta}^n); \qquad \forall\, \beta = \{-2, -1, 1\} \tag{8.20}$$

Substituting (8.20) into (8.18b), the residual term yields

$$\begin{aligned} R(u^{(2)}) =& \frac{a}{4\Delta x}(u_{i+1}^n + 3u_i^n - 5u_{i-1}^n + u_{i-2}^n) \\ &- \frac{a^2\Delta t}{16\Delta x^2}(u_{i+2}^n + 6u_{i+1}^n - u_i^n - 28u_{i-1}^n + 31u_{i-2}^n - 10u_{i-3}^n + u_{i-4}^n), \end{aligned} \tag{8.21}$$

and in turn the updated u_i^{n+1} is obtained as

$$\begin{aligned} u_i^{n+1} =& u_i^n - \frac{1}{4}\alpha_{CFL}(u_{i+1}^n + 3u_i^n - 5u_{i-1}^n + u_{i-2}^n) \\ &+ \frac{1}{32}\alpha_{CFL}^2(u_{i+2}^n + 6u_{i+1}^n - u_i^n - 28u_{i-1}^n + 31u_{i-2}^n - 10u_{i-3}^n + u_{i-4}^n). \end{aligned} \tag{8.22}$$

Alternatively, (8.22) is explicitly stated as

$$u_i^{n+1} = \mathcal{N}(u_\alpha^n); \qquad \forall \alpha = i-4, i-3, \ldots, i+2. \tag{8.23}$$

Here, a larger stencil is needed for updating the unknown u_i^{n+1} than was the case in (8.10).

In order to achieve the local truncation error, τ^n, a Taylor series expansion about (x_i, t^n) will be performed which eventually gives

$$\tau^n = \frac{a\Delta x^2}{6}\left(\alpha_{CFL}^2 + \frac{1}{2}\right)[q_{xxx}]_i^n + \mathcal{O}(\Delta x)^3. \tag{8.24}$$

The error τ^n is dominated by $\mathcal{O}(\Delta x)^2$, where its leading error term depends on the dispersive nature of q_{xxx} [25, 60, 81, 83]. The expression above confirms that the overall numerical method is of second order accuracy.

8.3 The Von Neumann Stability Analysis

Once consistency has been verified, it is necessary to establish the stability behaviour of a numerical scheme. The Von Neumann method[3] offers an easy and simple way of assessing the stability properties of linear schemes with constant coefficients, where the boundary conditions are assummed periodic. The key innovation of this analysis is to introduce an arbitrary harmonic function into the numerical scheme such that its amplitude, V, should not grow indefinitely in time. Excellent discussion can be found in [25, 60].

8.3.1 Methodology

In order to study the Von Neumann stability analysis, the following procedure will be used [25]:

1. Replace the unknown variable u_{i+p}^{n+q} by

$$u_{i+p}^{n+q} = V^{n+q} e^{I(i+p)\phi}; \qquad I = \sqrt{-1}. \tag{8.25}$$

2. Since all the terms of the subsequent expansion contain $e^{Ii\phi}$, the resulting equation can be simplified by this factor.

3. Derive an explicit form for the amplification factor $G = V^{n+1}/V^n$.

4. Ensure that the Von Neumann stability condition is satisfied as follows:

$$|G| \leq 1 \qquad \forall \phi \in [-\pi, \pi]. \tag{8.26}$$

Apply this methodology to the numerical schemes derived previously, viz. (8.9) and (8.22), for the linear constant convection equation $q_t + aq_x = 0$.

8.3.2 First Order Finite Volume Scheme: Diffusive Nature

The stability analysis of the first order numerical scheme, which depends upon piecewise constant reconstruction together with an explicit Euler time integrator (see equation (8.9)), will be studied. For clarity, the discretised equation[4] is shown again below:

$$u_i^{n+1} = u_i^n - \alpha_{CFL}(u_i^n - u_{i-1}^n); \qquad \alpha_{CFL} = \frac{a\Delta t}{\Delta x}. \tag{8.27}$$

[3] Von Neumann technique, developed by John Von Neumann, has emerged as the most widely applied method in stability analysis.

[4] In the usual terminology of finite differences, the discretised equation (8.9) is widely regarded as first order upwind scheme (FOU) in which the first order backward discretisation in space with an explicit first order difference in time have been adopted.

Firstly, replace the above terms using (8.25) to give:

$$V^{n+1}e^{Ii\phi} = V^n e^{Ii\phi}\left(1 - \alpha_{CFL} + \alpha_{CFL}e^{-I\phi}\right). \tag{8.28}$$

Next, cancel the common factor $e^{Ii\phi}$ and the amplitude G is then obtained in terms of any arbitrary harmonic function as[5]

$$\begin{aligned} G = \frac{V^{n+1}}{V^n} &= 1 - \alpha_{CFL} + \alpha_{CFL}e^{-I\phi} \\ &= \underbrace{1 - \alpha_{CFL} + \alpha_{CFL}\cos\phi}_{\mathrm{Re}(G)} + \underbrace{(-\alpha_{CFL}\sin\phi)}_{\mathrm{Im}(G)}I. \end{aligned} \tag{8.30}$$

In order to satisfy the Von Neumann stability condition (8.26), a certain range of CFL number, α_{CFL},

$$0 \leq \alpha_{CFL} \leq 1, \qquad \forall\phi \in [-\pi, \pi] \tag{8.31}$$

has to be fulfilled.

8.3.3 Second Order Finite Volume Scheme: Dispersive Nature

In order to obtain a higher order finite volume scheme, it is essential to introduce an appropriate reconstruction procedure for choosing better values for the left and the right states. By applying a piecewise linear reconstruction, the updated variable u_i^{n+1}, viz. (8.22), is shown as:

$$\begin{aligned} \Delta u_i = &-\frac{\alpha_{CFL}}{4}(u_{i+1}^n + 3u_i^n - 5u_{i-1}^n + u_{i-2}^n) \\ &+ \frac{\alpha_{CFL}^2}{32}(u_{i+2}^n + 6u_{i+1}^n - u_i^n - 28u_{i-1}^n + 31u_{i-2}^n - 10u_{i-3}^n + u_{i-4}^n), \end{aligned} \tag{8.32}$$

where $\Delta u_i = u_i^{n+1} - u_i^n$. With the aid of (8.25), the amplification factor is reduced to

$$G = \frac{V^{n+1}}{V^n} = 1 - \frac{1}{4}\alpha_{CFL}\eta + \frac{1}{32}\alpha_{CFL}^2\beta, \tag{8.33}$$

where

$$\eta = e^{I\phi} + 3 - 5e^{-I\phi} + e^{-2I\phi}, \tag{8.34a}$$

$$\beta = e^{2I\phi} + 6e^{I\phi} - 1 - 28e^{-I\phi} + 31e^{-2I\phi} - 10e^{-3I\phi} + e^{-4I\phi}. \tag{8.34b}$$

By substituting the exponential property ($e^{I\theta} = \cos\theta + I\sin\theta$) into the equation above, after some simple but tedious algebra, yields

$$G = \mathrm{Re}(G) + \mathrm{Im}(G)I, \tag{8.35}$$

[5]The modulus of G can be achieved by

$$|G| = \sqrt{\mathrm{Re}(G)^2 + \mathrm{Im}(G)^2}. \tag{8.29}$$

where

$$\begin{aligned}\mathrm{Re}(G) =& 1 - \frac{3}{4}\alpha_{CFL} - \frac{1}{32}\alpha_{CFL}^2 + \frac{1}{4}\alpha_{CFL}\left(4\cos\phi - \cos 2\phi\right) \\ &+ \frac{1}{32}\alpha_{CFL}^2\left(-22\cos\phi + 32\cos 2\phi - 10\cos 3\phi + \cos 4\phi\right),\end{aligned} \tag{8.36}$$

and

$$\mathrm{Im}(G) = \frac{1}{4}\alpha_{CFL}\left(\sin 2\phi - 6\sin\phi\right) + \frac{1}{32}\alpha_{CFL}^2\left(34\sin\phi - 30\sin 2\phi + 10\sin 3\phi - \sin 4\phi\right). \tag{8.37}$$

By virtue of (8.35), (8.36) and (8.37), $|G|$ seems to be very complex but doable[6]. Its modulus $|G| \leq 1$ if and only if

$$0 \leq \alpha_{CFL} \leq 1, \qquad \forall\, \phi \in [-\pi, \pi] \tag{8.38}$$

is satisfied.

8.4 Convergence

Convergence is defined by the numerical solution should approach the exact solution of the original differential equation when Δx (or Δt) tends to zero. The fundamental Equivalence Theorem of Lax states that for a well-posed linear initial value problem, stability is the only necessary condition for convergence provided that the numerical method is consistent [106] (see Figure 8.1).

8.4.1 Accuracy

The quality of a numerical scheme is often summarised by a single parameter s, namely order of accuracy. Firstly by noting that the error is expected to behave like[7]

$$E_i^n = C(\Delta x)^s + H.O.T \tag{8.39}$$

as the grid is refined (or $\Delta x \to 0$). Here, C is the constant that depends upon the particular solution being computed and also time t. Mesh refinement analysis will be performed in the forthcoming chapters by means of the analytic and computed pointwise solutions will be compared on a sequence of grids at a certain time instant. The error is plotted as a function of grid size (Δx) in a log-log scale. From (8.39), a linear behavior is anticipated in the plot as

[6] Commerical programming software (such as Matlab) can be used to obtain the result efficiently.

[7] E_i^n describes the pointwise error at time step n. This error can be denoted by

$$E_i^n = \frac{|q_i^n - u_i^n|}{|q_i^n|},$$

where u_i^n denotes the computed solution and q_i^n represents an analytical pointwise value.

$$\log E_i^n \approx \log C + s \log \Delta x \tag{8.40}$$

with a slope given by the order of accuracy s. Note that a higher order method is not inevitably more accurate on a certain grid size [60] (depend upon constant C in the above equation).

Part IV

Numerical Examples

Chapter 9

One Dimensional Problems

"The essence of mathematics is not to make simple things complicated, but to make complicated things simple".

Stanley Gudder, mathematician

9.1 Governing Equations

Under a reversible process, the one dimensional mixed formulation easily reduces to[1]

$$\frac{\partial \boldsymbol{\mathcal{U}}}{\partial t} + \frac{\partial \boldsymbol{\mathcal{F}}_1}{\partial X} = \mathbf{0}, \tag{9.1}$$

where their components are illustrated as

$$\boldsymbol{\mathcal{U}} = \begin{pmatrix} p_1 \\ F_{11} \end{pmatrix}; \qquad \boldsymbol{\mathcal{F}}_1 = \begin{pmatrix} -P_{11} \\ -p_1/\rho_0 \end{pmatrix}. \tag{9.2}$$

Note that the unknowns are linear momentum $p_1(X,t)$ and deformation gradient $F_{11}(X,t)$, ρ_0 denotes a constant material density. These conservation laws (viz. (9.1) and (9.2)) have to be supplemented by a constitutive law so as to close the coupled system; that is, $P_{11} = \partial\psi/\partial F_{11}$. In the small strain linear regime, the (engineering) stress is expressed by (see equation 2.19)

$$P_{11} = \sigma_{11} = (\lambda + 2\mu)(F_{11} - 1). \tag{9.3}$$

With the aid of above relationship, (9.1) and (9.2) can be further expanded as

$$\begin{aligned} \frac{\partial p_1}{\partial t} - (\lambda + 2\mu)\frac{\partial F_{11}}{\partial X} &= 0, \\ \frac{\partial F_{11}}{\partial t} - \frac{1}{\rho_0}\frac{\partial p_1}{\partial X} &= 0. \end{aligned} \tag{9.4}$$

When written in a matrix form, this system reads[2]

$$\boldsymbol{\mathcal{U}}_t + \boldsymbol{\mathcal{A}}_1 \boldsymbol{\mathcal{U}}_X = \mathbf{0} \tag{9.5}$$

with

$$\boldsymbol{\mathcal{U}} = \begin{pmatrix} p_1 \\ F_{11} \end{pmatrix}, \qquad \boldsymbol{\mathcal{A}}_1 = \begin{pmatrix} 0 & -(\lambda + 2\mu) \\ -1/\rho_0 & 0 \end{pmatrix}. \tag{9.6}$$

More specifically, the imposition of a null Poisson's ratio ($\nu = 0$) leads to[3]

$$\lambda = \frac{\nu E}{(1+\nu)(1-2\nu)} = 0 \qquad \text{and} \qquad E = 2\mu(1+\nu) = 2\mu.$$

Consequently, the Jacobian matrix, $\boldsymbol{\mathcal{A}}_1$, can be alternatively denoted as

$$\boldsymbol{\mathcal{A}}_1 = \begin{pmatrix} 0 & -E \\ -1/\rho_0 & 0 \end{pmatrix}. \tag{9.7}$$

[1] General discussion on the conservation-law formulation has been presented in Section 2.5.
[2] Notation $[\cdot]_a = \partial[\cdot]/\partial a$.
[3] In general, a non-zero value of ν could have been chosen.

9.2 Eigenstructure

The eigenvalues of a system are defined by zeros of the characteristic polynomial:

$$|\boldsymbol{\mathcal{A}}_1 - U_\alpha \boldsymbol{I}| = \det \begin{pmatrix} -U_\alpha & -(\lambda + 2\mu) \\ -1/\rho_0 & -U_\alpha \end{pmatrix} = 0. \tag{9.8}$$

By virtue of the equation above, the system has two real and distinct solutions, namely

$$U_1 = U_p, \qquad U_2 = -U_p, \tag{9.9}$$

where

$$U_p = \sqrt{\frac{\lambda + 2\mu}{\rho_0}}. \tag{9.10}$$

It is now possible to find the eigenvectors $\boldsymbol{\mathcal{R}}_1$, $\boldsymbol{\mathcal{R}}_2$ corresponding to their eigenvalues U_1 and U_2 counterparts. The eigenvector $\boldsymbol{\mathcal{R}}_1$ for $U_1 = U_p$ is found as follows such that $\boldsymbol{\mathcal{R}}_1$ is a right eigenvector of $\boldsymbol{\mathcal{A}}_1$; that is, $\boldsymbol{\mathcal{A}}_1 \boldsymbol{\mathcal{R}}_1 = U_1 \boldsymbol{\mathcal{R}}_1$. Writing this in full gives

$$\begin{pmatrix} 0 & -(\lambda + 2\mu) \\ -1/\rho_0 & 0 \end{pmatrix} \begin{pmatrix} \mathcal{R}_1^{(1)} \\ \mathcal{R}_1^{(2)} \end{pmatrix} = U_1 \begin{pmatrix} \mathcal{R}_1^{(1)} \\ \mathcal{R}_1^{(2)} \end{pmatrix}, \tag{9.11}$$

which produces two linear algebraic equations for the unknowns $\mathcal{R}_1^{(1)}$ and $\mathcal{R}_1^{(2)}$. Due to the fact that these two equations are equivalent, only a single linear algebraic equation has to be considered and then yields a one-parameter family of solutions. By selecting an arbitrary non-zero scaling factor β_1 and set $\mathcal{R}_1^{(1)} = \beta_1$, the first right eigenvector becomes

$$\boldsymbol{\mathcal{R}}_1 = \beta_1 \begin{pmatrix} 1 \\ -1/\rho_0 U_p \end{pmatrix}. \tag{9.12}$$

On the other hand, the eigenvector $\boldsymbol{\mathcal{R}}_2$ of $U_2 = -U_p$ is derived in a similar manner:

$$\boldsymbol{\mathcal{R}}_2 = \beta_2 \begin{pmatrix} 1 \\ 1/\rho_0 U_p \end{pmatrix} \tag{9.13}$$

where β_2 is a scaling factor. The complete right eigenvector matrix is presented as follows:

$$\boldsymbol{\mathcal{R}} = (\boldsymbol{\mathcal{R}}_1 | \boldsymbol{\mathcal{R}}_2) = \begin{pmatrix} \beta_1 & \beta_2 \\ -\beta_1/\rho_0 U_p & \beta_2/\rho_0 U_p \end{pmatrix}. \tag{9.14}$$

By noting that $\boldsymbol{\mathcal{L}}_\alpha^T \boldsymbol{\mathcal{A}}_1 = U_\alpha \boldsymbol{\mathcal{L}}_\alpha^T$, the left eigenvectors of matrix $\boldsymbol{\mathcal{A}}_1$ can be obtained as

$$\boldsymbol{\mathcal{L}}^T = \boldsymbol{\mathcal{R}}^{-1} = \begin{pmatrix} \boldsymbol{\mathcal{L}}_1^T \\ \boldsymbol{\mathcal{L}}_2^T \end{pmatrix} = \frac{1}{2} \begin{pmatrix} 1/\beta_1 & -\rho_0 U_p/\beta_1 \\ 1/\beta_2 & \rho_0 U_p/\beta_2 \end{pmatrix}. \tag{9.15}$$

Set the scaling factors to unity (i.e. $\beta_1 = \beta_2 = 1$), the right eigenvectors

$$\boldsymbol{\mathcal{R}}_1 = \begin{pmatrix} 1 \\ -1/\rho_0 U_p \end{pmatrix}, \qquad \boldsymbol{\mathcal{R}}_2 = \begin{pmatrix} 1 \\ 1/\rho_0 U_p \end{pmatrix}, \tag{9.16}$$

and the left eigenvectors

$$\boldsymbol{\mathcal{L}}_1 = \frac{1}{2}\begin{pmatrix} 1 \\ -\rho_0 U_p \end{pmatrix}, \qquad \boldsymbol{\mathcal{L}}_2 = \frac{1}{2}\begin{pmatrix} 1 \\ \rho_0 U_p \end{pmatrix}, \tag{9.17}$$

can be easily achieved. These eigenvectors satisfy the well-known orthogonality condition.

The linearised solid dynamics system of equations (viz. (9.5) and (9.6)) is strictly hyperbolic since U_1 and U_2 are real and distinct. This ensures the existence of a set of linearly independent eigenvectors (see Appendix C).

9.3 Linearised Riemann Solver

A variety of different approaches have been used to derive the linearised Riemann solver for a one-dimensional rapid dynamics system of equations:

1. Expanding the initial data $\boldsymbol{\mathcal{U}}^-$ and $\boldsymbol{\mathcal{U}}^+$ in terms of eigenvectors.
2. Expanding the total jump $[\![\boldsymbol{\mathcal{U}}]\!]$ in terms of waves.
3. Using the Rankine-Hugoniot conditions across each wave.
4. Applying the Generalised Riemann Invariants (GRI).

A complete and thorough description of this subject is provided in [60, 62, 82, 84].

9.3.1 Expanding the Initial Data in terms of Eigenvectors

Firstly, the left state $\boldsymbol{\mathcal{U}}^-$ is decomposed into a summation of their linearly independent eigenvectors, namely

$$\boldsymbol{\mathcal{U}}^- \equiv \begin{pmatrix} p_1^- \\ F_{11}^- \end{pmatrix} = \gamma_1 \boldsymbol{\mathcal{R}}_1 + \gamma_2 \boldsymbol{\mathcal{R}}_2 \equiv \gamma_1 \begin{pmatrix} 1 \\ -1/\rho_0 U_p \end{pmatrix} + \gamma_2 \begin{pmatrix} 1 \\ 1/\rho_0 U_p \end{pmatrix}.$$

From expression above, the coefficients γ_1 and γ_2 are solved as

$$\gamma_1 = \frac{1}{2}\left(p_1^- - \rho_0 U_p F_{11}^-\right), \qquad \gamma_2 = \frac{1}{2}\left(p_1^- + \rho_0 U_p F_{11}^-\right), \tag{9.18}$$

respectively. Analogously, the unknowns ζ_1 and ζ_2 of the right state $\boldsymbol{\mathcal{U}}^+$ can also be achieved:

$$\zeta_1 = \frac{1}{2}\left(p_1^+ - \rho_0 U_p F_{11}^+\right), \qquad \zeta_2 = \frac{1}{2}\left(p_1^+ + \rho_0 U_p F_{11}^+\right). \tag{9.19}$$

By noting that the unknown variable at contact point is

$$\boldsymbol{\mathcal{U}}^C \equiv \begin{pmatrix} p_1^C \\ F_{11}^C \end{pmatrix} = \gamma_1 \boldsymbol{\mathcal{R}}_1 + \zeta_2 \boldsymbol{\mathcal{R}}_2 \equiv \gamma_1 \begin{pmatrix} 1 \\ -1/\rho_0 U_p \end{pmatrix} + \zeta_2 \begin{pmatrix} 1 \\ 1/\rho_0 U_p \end{pmatrix}, \tag{9.20}$$

the above equation can be further extended to

$$p_1^C = \frac{1}{2}(p_1^- + p_1^+) + \frac{\rho_0 U_p}{2}(F_{11}^+ - F_{11}^-), \tag{9.21a}$$

$$F_{11}^C = \frac{1}{2\rho_0 U_p}(p_1^+ - p_1^-) + \frac{1}{2}(F_{11}^- + F_{11}^+), \tag{9.21b}$$

with the aid of γ_1 and ζ_2.

9.3.2 Expanding the Total Jump in terms of Waves

The total jump $[\![\boldsymbol{\mathcal{U}}]\!]$ [4] consists of a series of waves, that is

$$[\![\boldsymbol{\mathcal{U}}]\!] = \eta_1 \boldsymbol{\mathcal{R}}_1 + \eta_2 \boldsymbol{\mathcal{R}}_2 = \eta_1 \begin{pmatrix} 1 \\ -1/\rho_0 U_p \end{pmatrix} + \eta_2 \begin{pmatrix} 1 \\ 1/\rho_0 U_p \end{pmatrix}. \tag{9.22}$$

It is trivial to evaluate the coefficients of η_1 and η_2:

$$\eta_1 = \frac{1}{2}\left([\![p_1]\!] - \rho_0 U_p [\![F_{11}]\!]\right), \qquad \eta_2 = \frac{1}{2}([\![p_1]\!] + \rho_0 U_p [\![F_{11}]\!]). \tag{9.23}$$

Insofar as the unknown variable at contact point is represented as

$$\begin{aligned} \boldsymbol{\mathcal{U}}^C \equiv \begin{pmatrix} p_1^C \\ F_{11}^C \end{pmatrix} &= \boldsymbol{\mathcal{U}}^- + \eta_2 \begin{pmatrix} 1 \\ 1/\rho_0 U_p \end{pmatrix} \\ &= \boldsymbol{\mathcal{U}}^+ - \eta_1 \begin{pmatrix} 1 \\ -1/\rho_0 U_p \end{pmatrix}, \end{aligned} \tag{9.24}$$

the expression above can then be concluded, after some simple algebraic manipulations, as

$$p_1^C = \frac{1}{2}(p_1^- + p_1^+) + \frac{\rho_0 U_p}{2}(F_{11}^+ - F_{11}^-), \tag{9.25a}$$

$$F_{11}^C = \frac{1}{2\rho_0 U_p}(p_1^+ - p_1^-) + \frac{1}{2}(F_{11}^- + F_{11}^+). \tag{9.25b}$$

9.3.3 Rankine-Hugoniot Relations

Applying the Rankine-Hugoniot conditions[5] across the U_1-wave gives

$$U_p \begin{pmatrix} p_1^+ - p_1^C \\ F_{11}^+ - F_{11}^C \end{pmatrix} = \begin{pmatrix} -(\lambda + 2\mu)(F_{11}^+ - F_{11}^C) \\ -\frac{1}{\rho_0}(p_1^+ - p_1^C) \end{pmatrix}. \tag{9.26}$$

[4] Discontinuity of a variable is denoted as $[\![\cdot]\!] = (\cdot)^+ - (\cdot)^-$.

[5] For a linear system with constant coefficients, the Rankine-Hugoniot relations across the wave speed U_α read

$$U_\alpha [\![\boldsymbol{\mathcal{U}}]\!] = [\![\boldsymbol{\mathcal{F}}_1]\!].$$

Expanding and solving for p_1^C yields

$$p_1^C = p_1^+ + \rho_0 U_p (F_{11}^+ - F_{11}^C). \tag{9.27}$$

Likewise, for the U_2-wave, the contact linear momentum is derived as

$$p_1^C = p_1^- + \rho_0 U_p (F_{11}^C - F_{11}^-). \tag{9.28}$$

The solutions to the simultaneous linear algebraic equations are

$$p_1^C = \frac{1}{2}(p_1^- + p_1^+) + \frac{\rho_0 U_p}{2}(F_{11}^+ - F_{11}^-), \tag{9.29a}$$

$$F_{11}^C = \frac{1}{2\rho_0 U_p}(p_1^+ - p_1^-) + \frac{1}{2}(F_{11}^- + F_{11}^+), \tag{9.29b}$$

respectively. A basic introduction to this underlying technique was presented in Section 5.2.

9.3.4 Generalised Riemann Invariants (GRI)

A linearised Riemann solver based upon Generalised Riemann Invariants technique[6] is demonstrated in this section. Across the U_1-right wave, dp_1 is defined as

$$dp_1 = \frac{dF_{11}}{-1/\rho_0 U_p}, \tag{9.30}$$

which, after some simple rearrangements, gives

$$dF_{11} + \frac{1}{\rho_0 U_p} dp_1 = 0. \tag{9.31}$$

By integrating the equation above, this produces

$$I_R = F_{11} + \frac{1}{\rho_0 U_p} p_1 = const. \tag{9.32}$$

Similarly, the U_2-left wave leads to

$$I_L = F_{11} - \frac{1}{\rho_0 U_p} p_1 = const. \tag{9.33}$$

Applying I_L across the left wave connecting $\boldsymbol{\mathcal{U}}^-$ and $\boldsymbol{\mathcal{U}}^C$ yields

$$F_{11}^C - \frac{1}{\rho_0 U_p} p_1^C = F_{11}^- - \frac{1}{\rho_0 U_p} p_1^-. \tag{9.34}$$

[6]For a certain α-wave, the Generalised Riemann Invariants are relations that hold true across the wave structure:

$$\frac{d\mathcal{U}_1}{\mathcal{R}_\alpha^{(1)}} = \frac{d\mathcal{U}_2}{\mathcal{R}_\alpha^{(2)}}; \quad \boldsymbol{\mathcal{U}} = \begin{pmatrix} \mathcal{U}_1 \\ \mathcal{U}_2 \end{pmatrix}; \quad \boldsymbol{\mathcal{R}}_\alpha = \begin{pmatrix} \mathcal{R}_\alpha^{(1)} \\ \mathcal{R}_\alpha^{(2)} \end{pmatrix}.$$

Further discussion can be found in [91].

On the other hand, the application of I_R across the right wave gives

$$F_{11}^C + \frac{1}{\rho_0 U_p} p_1^C = F_{11}^+ + \frac{1}{\rho_0 U_p} p_1^+. \tag{9.35}$$

The simultaneous equations for unknowns p_1^C and F_{11}^C can then be computed as[7]

$$p_1^C = \frac{1}{2}(p_1^- + p_1^+) + \frac{\rho_0 U_p}{2}(F_{11}^+ - F_{11}^-), \tag{9.36a}$$

$$F_{11}^C = \frac{1}{2\rho_0 U_p}(p_1^+ - p_1^-) + \frac{1}{2}(F_{11}^- + F_{11}^+). \tag{9.36b}$$

Note that the above solutions are identical to those obtained from other techniques (see (9.21), (9.25) and (9.29)).

9.4 Notation of Cell-Centred Scheme

The spatial semi-discretisation is performed on a cell-centred cartesian grid, where the primary variables are defined at the centroids of the cells. Under this circumstance, any control volume can be identified with the existing grid; for instance, $i = (X_{i-1/2}, X_{i+1/2})$ (see Figure 9.1). In order to be compatible with the definitions discussed in Section 9.3, for any arbitrary contact point (such as $(\cdot)^C = (\cdot)_{i-1/2}$), $(\cdot)^+$ and $(\cdot)^-$ represent $(\cdot)_i$ and $(\cdot)_{i-1}$ in the case of first-order Godunov scheme.

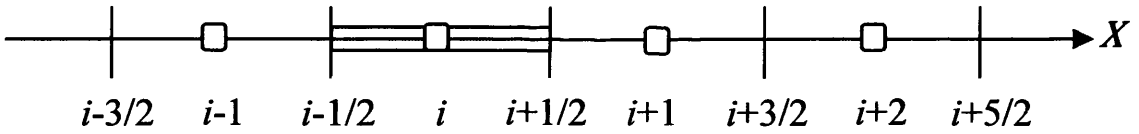

Figure 9.1: The position of a control volume with respect to the grid cell. Integer indexes, $\ldots, i-1, i, i+1, \ldots$, are the centroids of grid cells whereas non-integer indexes, $\ldots, i-3/2, i-1/2, i+1/2, \ldots$, are the grid (or contact) points correspondingly.

9.5 Godunov's and Explicit Euler Time Scheme

As discussed previously, the differential law of a system of conservation equations is

$$\frac{\partial \boldsymbol{\mathcal{U}}}{\partial t} + \frac{\partial \boldsymbol{\mathcal{F}}_1}{\partial X} = \mathbf{0}, \tag{9.37}$$

[7]The contact variables (i.e. p_1^C and P_{11}^C) can be alternatively stated as

$$p_1^C = \frac{1}{2}(p_1^- + p_1^+) + \frac{1}{2U_p}(P_{11}^+ - P_{11}^-),$$

$$P_{11}^C = \frac{U_p}{2}(p_1^+ - p_1^-) + \frac{1}{2}(P_{11}^- + P_{11}^+),$$

with the aid of linear constitutive relation; that is, $F_{11} = P_{11}/(\lambda + 2\mu) + 1$.

and their components are illustrated in (9.2). In order to yield a physically consistent solution where discontinuities are present, it is essential to introduce the weak form of its corresponding differential law:

$$\frac{d}{dt}\int_{V_i} \boldsymbol{\mathcal{U}}(X,t)\,dX = \boldsymbol{\mathcal{F}}_1(\boldsymbol{\mathcal{U}}(X_{i-1/2},t)) - \boldsymbol{\mathcal{F}}_1(\boldsymbol{\mathcal{U}}(X_{i+1/2},t)). \tag{9.38}$$

Note that the volume of *i-th* grid cell is described as $V_i = \Delta x = X_{i+1/2} - X_{i-1/2}$. The above equation is then divided by Δx which gives

$$\frac{d}{dt}\left(\frac{1}{\Delta x}\int_{V_i} \boldsymbol{\mathcal{U}}(X,t)\,dX\right) = \frac{1}{\Delta x}\left(\boldsymbol{\mathcal{F}}_{1,i-1/2} - \boldsymbol{\mathcal{F}}_{1,i+1/2}\right), \tag{9.39}$$

where

$$\boldsymbol{\mathcal{F}}_{1,i-1/2} \equiv \boldsymbol{\mathcal{F}}_1(\boldsymbol{\mathcal{U}}(X_{i-1/2},t)); \qquad \boldsymbol{\mathcal{F}}_{1,i+1/2} \equiv \boldsymbol{\mathcal{F}}_1(\boldsymbol{\mathcal{U}}(X_{i+1/2},t)).$$

By giving an approximation of the averaged value over *i-th* cell

$$\boldsymbol{\mathcal{U}}_i \approx \frac{1}{\Delta x}\int_{V_i} \boldsymbol{\mathcal{U}}(X,t)\,dX, \tag{9.40}$$

and the use of explicit Euler time integration scheme, (9.39) yields

$$\boldsymbol{\mathcal{U}}_i^{n+1} = \boldsymbol{\mathcal{U}}_i^n - \frac{\Delta t}{\Delta x}\left(\boldsymbol{\mathcal{F}}_{1,i+1/2}^n - \boldsymbol{\mathcal{F}}_{1,i-1/2}^n\right). \tag{9.41}$$

The expression above (widely known as flux differencing formula) offers a great variety of different possibilities to update the cell averaged $\boldsymbol{\mathcal{U}}_i$ at one time step, which clearly depends on the flux computation. The simplest form of interface flux evaluation, $\boldsymbol{\mathcal{F}}_{1,i-1/2}^n$, can be obtained by choosing the cell averaged values as the left and right states, that is

$$\boldsymbol{\mathcal{F}}_{1,i-1/2}^n = \boldsymbol{\mathcal{F}}_1(\boldsymbol{\mathcal{U}}_{i-1}^n, \boldsymbol{\mathcal{U}}_i^n). \tag{9.42}$$

Any method of this type is an explicit numerical scheme with three-point spatial stencil, where its resulting solution is of first order accuracy in both space and time. In short, Godunov's method is implemented in two-folds:

- Solve the Riemann problem at cell interface (refer to contact algorithm introduced in Chapter 5).
- Apply the flux differencing formula (9.41).

An alternative wave propagation framework allowing for application on more general hyperbolic systems is described in [60]. It is worth noting that the first-order accurate numerical schemes are becoming less acceptable to the CFD community due to their poor performance in predicting advection-dominated flows (see [25, 26, 60, 81–84]). In order to rectify this, it is vital to introduce a linear reconstruction procedure for selecting better values for the left and the right states (which will be presented in Section 9.6).

9.6 Linear Reconstruction Procedure

It is well known that Godunov's method achieves only first order accuracy in space, which therefore introduces a great deal of numerical diffusion into the solution (see [25, 26, 60–62, 81–84, 98]). A second-order spatial accuracy can be obtained by introducing a suitably linear reconstruction procedure, as already generally discussed in Section 4.4. Nevertheless, a simplified one-dimensional reconstruction framework is provided in this section.

A local piecewise linear reconstruction[8] at cell i is represented as:

$$\mathcal{U}(X)|_i = \mathcal{U}_i + \left.\frac{\partial \mathcal{U}}{\partial X}\right|_i (X - X_i), \tag{9.43}$$

where $\mathcal{U}(X)|_i$ varies linearly within cell i and the slope $\partial\mathcal{U}/\partial X|_i$ is yet to be specified. Here, $\mathcal{U}_i$ describes an averaged value over cell i and $X \in [X_{i-1/2}, X_{i+1/2}]$ (see Figure 9.1). There are various techniques available to solve for the slope [60, 84]. The standard second-order centred finite difference approximation, that is

$$\left.\frac{\partial \mathcal{U}}{\partial X}\right|_i \approx \frac{1}{2\Delta x}(\mathcal{U}_{i+1} - \mathcal{U}_{i-1}), \tag{9.44}$$

is employed. Note that the slope at cell i is approximated by adjacent information $(i-1, i+1)$ relative to the particular cell under consideration. By substituting (9.44) into (9.43), the explicit formulas for cell interfaces at cell i can be obtained as

$$\mathcal{U}_{i,i+1} = \mathcal{U}_i + \frac{1}{4}(\mathcal{U}_{i+1} - \mathcal{U}_{i-1}); \quad \mathcal{U}_{i,i-1} = \mathcal{U}_i - \frac{1}{4}(\mathcal{U}_{i+1} - \mathcal{U}_{i-1}). \tag{9.45}$$

The relation of $\mathcal{U}_{i,i-1} = \mathcal{U}_{i,i+1} = \mathcal{U}_i$ is recovered in Godunov's method (see Section 9.5).

Since at least two neighbouring information are required, (9.45) is not applicable to cells near the physical boundary points.[9] However, slopes near both ends can be reconstructed based upon a single neighbouring information and the end cell itself:

$$\left.\frac{\partial \mathcal{U}}{\partial X}\right|_{i_L} \approx \underbrace{\frac{1}{\Delta x}(\mathcal{U}_{i_L+1} - \mathcal{U}_{i_L})}_{\text{central difference approximation}} \quad ; \quad \left.\frac{\partial \mathcal{U}}{\partial X}\right|_{i_R} \approx \underbrace{\frac{1}{\Delta x}(\mathcal{U}_{i_R} - \mathcal{U}_{i_R-1})}_{\text{central difference approximation}} \quad , \tag{9.46}$$

With the aid of equations above, the reconstructed unknown variables at two boundary points can be represented by

$$\mathcal{U}_{LB} = \mathcal{U}_{i_L} - \frac{1}{2}(\mathcal{U}_{i_L+1} - \mathcal{U}_{i_L}); \quad \mathcal{U}_{RB} = \mathcal{U}_{i_R} + \frac{1}{2}(\mathcal{U}_{i_R} - \mathcal{U}_{i_R-1}), \tag{9.47}$$

where LB and RB describe left and right boundary points, respectively. Graphical representation is depicted in Figure 9.2.

[8] Consistency is satisfied since the origin is located at the centroid of cell i.

[9] Otherwise, it is essential to extend the computational domain to include a few additional dummy cells, whose values depend on the boundary conditions and interior solutions. A general framework for assigning ghost values is developed in Appendix F.

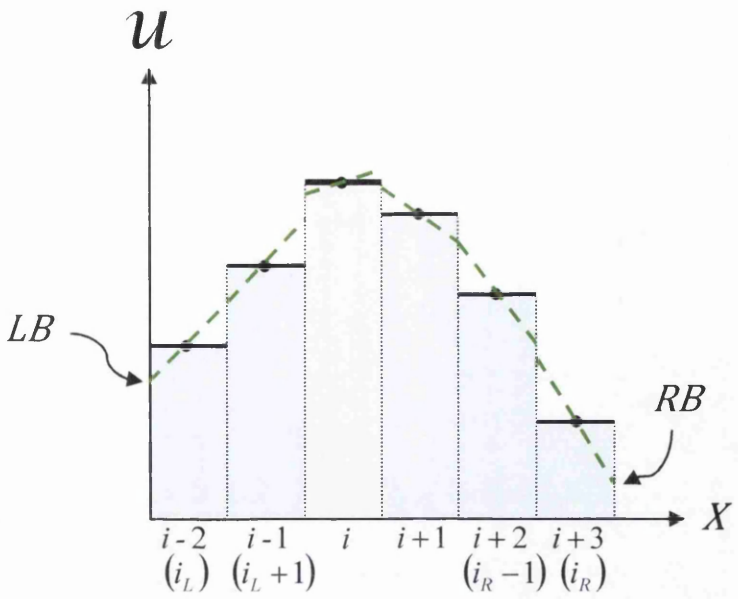

Figure 9.2: Depiction of piecewise linear reconstruction.

9.7 Slope Limiter

Godunov (1969) [85] concluded that only first-order linear schemes are monotonicity-preserving. High order spatial discretisation schemes exhibit unphysical oscillatory behaviour in the vicinity of discontinuities. For this reason, a nonlinear slope limiter will be introduced so as to control the spurious oscillations, where the limiting function depends upon the solution values (see [60,84,86,87,93]). The use of slope limiter ϕ_i (aims at correcting the solution gradient) enables the polynomial reconstruction over cell i to be expressed as

$$\mathcal{U}(X)|_i = \mathcal{U}_i + \phi_i \left.\frac{\partial \mathcal{U}}{\partial X}\right|_i (X - X_i). \tag{9.48}$$

Note that $\phi_i = 0$ corresponds to piecewise constant representation, whereas $\phi_i = 1$ represents unlimited piecewise linear reconstruction (see equation (9.43)). The evaluation of ϕ_i has been fully discussed in Section 4.4.2.

9.8 Initial Value Problem: Characteristic Theory

The general Initial Value Problem (IVP) of the new conservation law formulation is presented where its system of equations are shown in (9.5) and (9.6). Note that the initial conditions and characteristic variable are defined as

$$\begin{pmatrix} p_1(X,0) \\ F_{11}(X,0) \end{pmatrix} = \begin{pmatrix} \mathring{p}_1(X) \\ \mathring{F}_{11}(X) \end{pmatrix} \quad \text{and} \quad \boldsymbol{\mathcal{W}} = \boldsymbol{\mathcal{R}}^{-1}\boldsymbol{\mathcal{U}}, \tag{9.49}$$

respectively.[10] In order to gain a better understanding of an initial value part of the Cauchy problem, it is advisable to review Appendix C.4 in advance.

Since $U_1 = U_p$ and $U_2 = -U_p$, the characteristic variables can be written as

$$\begin{pmatrix} w_1 \\ w_2 \end{pmatrix}_t + \begin{pmatrix} U_p & 0 \\ 0 & -U_p \end{pmatrix} \begin{pmatrix} w_1 \\ w_2 \end{pmatrix}_X = 0, \tag{9.50}$$

or in full

$$\frac{\partial w_1}{\partial t} + U_p \frac{\partial w_1}{\partial X} = 0, \qquad \frac{\partial w_2}{\partial t} - U_p \frac{\partial w_2}{\partial X} = 0, \tag{9.51}$$

where their initial conditions satisfy

$$\begin{pmatrix} \mathring{w}_1(X) \\ \mathring{w}_2(X) \end{pmatrix} = \boldsymbol{\mathcal{R}}^{-1} \begin{pmatrix} \mathring{p}_1(X) \\ \mathring{F}_{11}(X) \end{pmatrix} = \begin{pmatrix} \frac{1}{2}\left[\mathring{p}_1(X) - \rho_0 U_p \mathring{F}_{11}(X)\right] \\ \frac{1}{2}\left[\mathring{p}_1(X) + \rho_0 U_p \mathring{F}_{11}(X)\right] \end{pmatrix}. \tag{9.52}$$

Expressions in (9.51) are typically known as linear advection equations. The solutions for characteristic variables (i.e. w_1 and w_2) are displayed as

$$w_1(X,t) = \mathring{w}_1(X - U_p t), \qquad w_2(X,t) = \mathring{w}_2(X + U_p t), \tag{9.53}$$

with

$$\begin{aligned} \mathring{w}_1(X - U_p t) &= \frac{1}{2}\left(\mathring{p}_1(X - U_p t) - \rho_0 U_p \mathring{F}_{11}(X - U_p t)\right), \\ \mathring{w}_2(X + U_p t) &= \frac{1}{2}\left(\mathring{p}_1(X + U_p t) + \rho_0 U_p \mathring{F}_{11}(X + U_p t)\right). \end{aligned} \tag{9.54}$$

Transformation (such as $\boldsymbol{\mathcal{U}} = \boldsymbol{\mathcal{R}}\boldsymbol{\mathcal{W}}$) is then performed, which in turn yields the final solutions as

$$\begin{aligned} p_1(X,t) &= \frac{1}{2}\left(\mathring{p}_1(X - U_p t) + \mathring{p}_1(X + U_p t)\right) + \frac{\rho_0 U_p}{2}\left(\mathring{F}_{11}(X + U_p t) - \mathring{F}_{11}(X - U_p t)\right), \\ F_{11}(X,t) &= \frac{1}{2\rho_0 U_p}\left(\mathring{p}_1(X + U_p t) - \mathring{p}_1(X - U_p t)\right) + \frac{1}{2}\left(\mathring{F}_{11}(X + U_p t) + \mathring{F}_{11}(X - U_p t)\right). \end{aligned} \tag{9.55}$$

An analytical example (extracted from [60]) is demonstrated with an initial data such as $v_1 = 0$ and $F_{11} = 1$ everywhere except v_1 in some small region near the origin:

$$v_1(X,0) = \frac{1}{2}\exp(-80X^2) + \mathcal{G}(Z); \qquad F_{11}(X,0) = 1, \qquad \forall X \in [-1.5, 1.5]$$

where

$$\mathcal{G}(Z) = \begin{cases} 1 & \text{if } -0.3 < Z < -0.1, \\ 0 & \text{Otherwise.} \end{cases}$$

Figure 9.3 and Figure 9.4 illustrate the time evolution of unknown variables (i.e. v_1 and F_{11}) with the initial conditions desribed above. In this example, Young's modulus E and density ρ_0 are treated as unity, Poisson's ratio $\nu = 0$. For small

[10] The right eigenvector matrix $\boldsymbol{\mathcal{R}}$ and its inverse $\boldsymbol{\mathcal{R}}^{-1}$ have been introduced in Section 9.2.

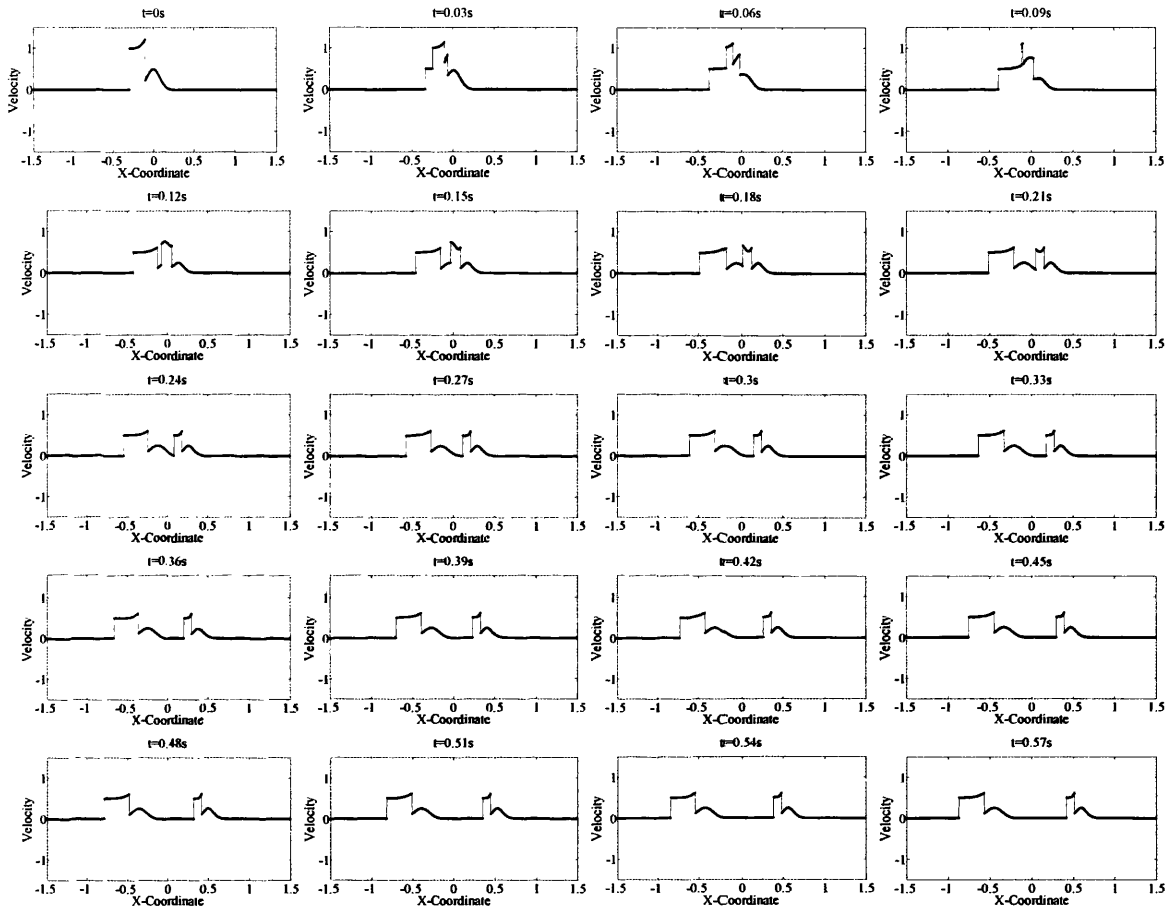

Figure 9.3: Characteristic Theory: Evolution of v_1 waves travel with two different propagation speeds $-U_p$ and U_p with their shapes unchanged. Poisson's ratio $\nu = 0$, Young's modulus E and density ρ_0 are unity.

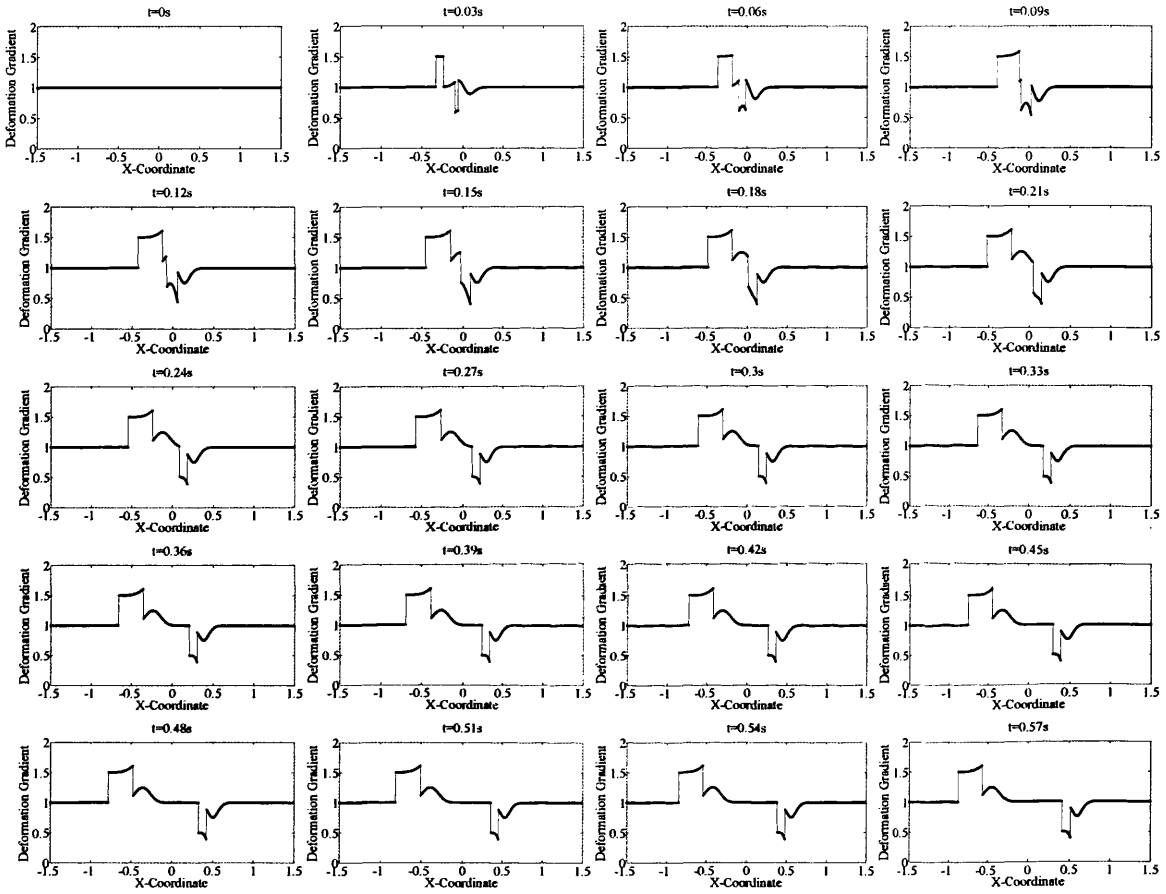

Figure 9.4: Characteristic Theory: Evolution of F_{11} waves travel with two different propagation speeds $-U_p$ and U_p with their shapes unchanged. Poisson's ratio $\nu = 0$, Young's modulus E and density ρ_0 are unity.

time the solutions change in a seemingly haphazard way as the left-going and right-going waves superpose. Nevertheless, it is essential to observe that two separate waves, as time advances, travel at constant propagation speeds with their shapes unchanged. In the next section, numerical example will be presented to examine both the accuracy and computational capabilities of the proposed algorithm.

9.9 Shock Dominated Case: Pile Driving Example

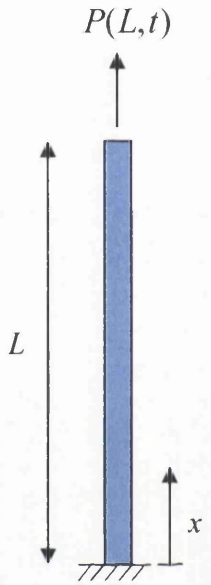

Figure 9.5: Pile driving example: configuration.

The first example which will be considered is that of the wave propagation on a one-dimensional linear elastic steel pile. This example is taken from Clough and Penzien (1993) [44]. The bottom end of the pile is fixed and a forcing function is applied at its free top end. The configuration (see Figure 9.5) consists of a structural element of length $L = 10\,\mathrm{m}$ and unit cross sectional area; the material properties are Young's modulus $E = 200\,\mathrm{GPa}$, density $\rho_0 = 8\,\mathrm{Mg/m^3}$ and Poisson's ratio $\nu = 0$. This implies that the wave speed of this elastic material is given by $U_p = \sqrt{E/\rho_0} = 5 \times 10^3\,\mathrm{m/s}$. The example is first discretised with 100 cells (or grid size $h = 0.1\,\mathrm{m}$) and the time step has been chosen as $\Delta t = 1 \times 10^{-5}\,s$, which results in a Courant-Friedrichs-Lewy number [157] α_{CFL}[11] $= U_p \Delta t/h = 0.5$. The applied step function force is described as (see Figure 9.6a)

$$P(L,t) = \begin{cases} 0 & \mathrm{t} < 0 \\ -P_0 & \mathrm{t} \geq 0 \end{cases}, \qquad P_0 = 5 \times 10^7 \mathrm{N}. \tag{9.56}$$

[11]The effect of various CFL number on the accuracy of the numerical solutions will be assessed in the following chapter (see Section 10.3.2).

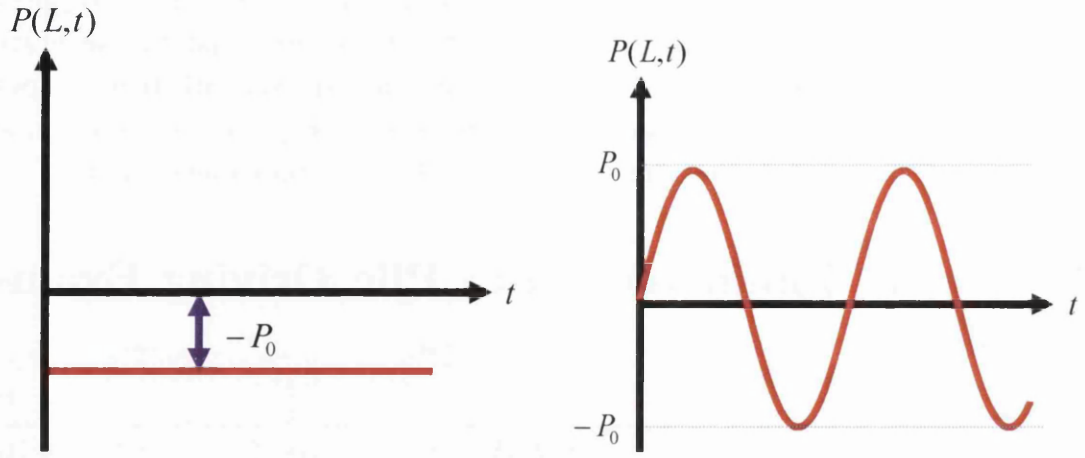

(a) (b)

Figure 9.6: Forcing function: (a) Step function loading; and (b) Sinusoidal loading.

A stress shock of -5×10^7Pa propagates down the pile due to a suddenly applied load P_0. This shock wave reflects at the fixed end (or $x = 0$) and the amplitude of the stress shock is then doubled at $t = 2 \times 10^{-3}$s. Both the classical FEM[12] and the new proposed methodology predict the correct arrival time of the stress shock. However, the first order FVM introduces considerable numerical diffusion and then leads to inaccurate solution in the long term, as depicted in Figure 9.7a. To enhance the accuracy, it is essential to introduce a piecewise linear reconstruction within each cell. The second order FVM (see Figure 9.7b) gives much better accuracy but fails near discontinuities, where oscillations are generated due to its dispersive nature. In order to control these spurious oscillations, slope limiter is implemented. A great improvement is observed in Figure 9.7c. As it is well known, the standard displacement based FEM formulation produces non-physical oscillations in the vicinity of sharp solution gradients, as observed in Figure 9.7d.

In addition, a convergence analysis by means of the L1-norm and L2-norm has been carried out on a sequence of grids. To achieve a smooth solution, a sinusoidal forcing function is employed by

$$P(L,t) = K\left(\sin\left(\frac{\pi}{20}t - \frac{\pi}{2}\right) + 1\right); \qquad t \geq 0, \tag{9.57}$$

where the constant $K = 1 \times 10^{-3}$ (see Figure 9.6b). In this particular case, Young's modulus E and density ρ_0 are taken to be unity and the Poisson's ratio is chosen as $\nu = 0.3$. Figure 9.8 demonstrates the expected accuracy of the scheme (with and without slope limiters) for different variables. As can be observed, the inclusion of slope limiters is expected to be less accurate (than those without it) as limiters generate diffusion into the solution. It can be concluded that FVM-limiter scheme achieves second order of accuracy in stress (only first order precision for displacement

[12]See Appendix G for detailed explanation of standard finite element computational methodology.

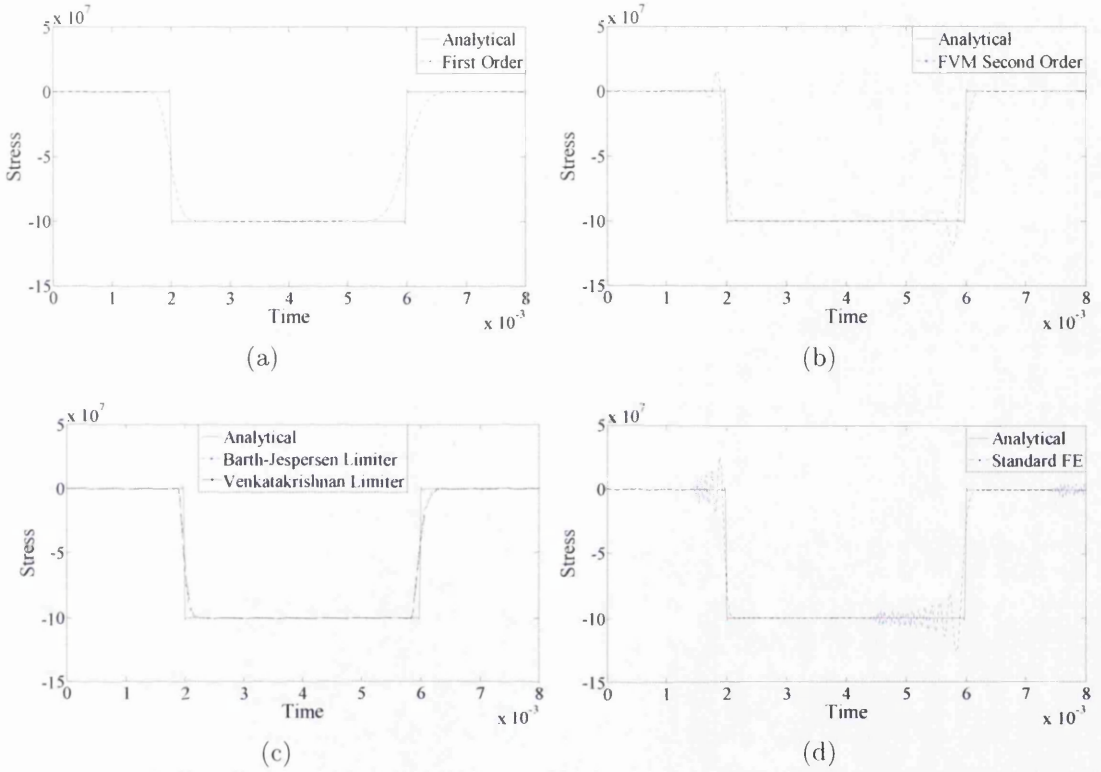

Figure 9.7: Pile Driving Example (Step Function Loading): Stress history at fixed end, $x = 0$, in the elastic case: (a) Piecewise constant reconstruction; (b) Piecewise linear reconstruction; (c) With limiters; and (d) Standard finite element methodology (Newmark trapezoidal rule). This test case is run with the linear elastic model and material properties are such that Poisson's ratio $\nu = 0$, Young's modulus $E = 200\text{GPa}$, density $\rho_0 = 8\text{Mg/m}^3$ and $\alpha_{CFL} = 0.5$. Discretisation of 100 cells. Time step $\Delta t = 1 \times 10^{-5}\text{s}$.

based formulation) and performs well in the vicinity of sharp gradients.

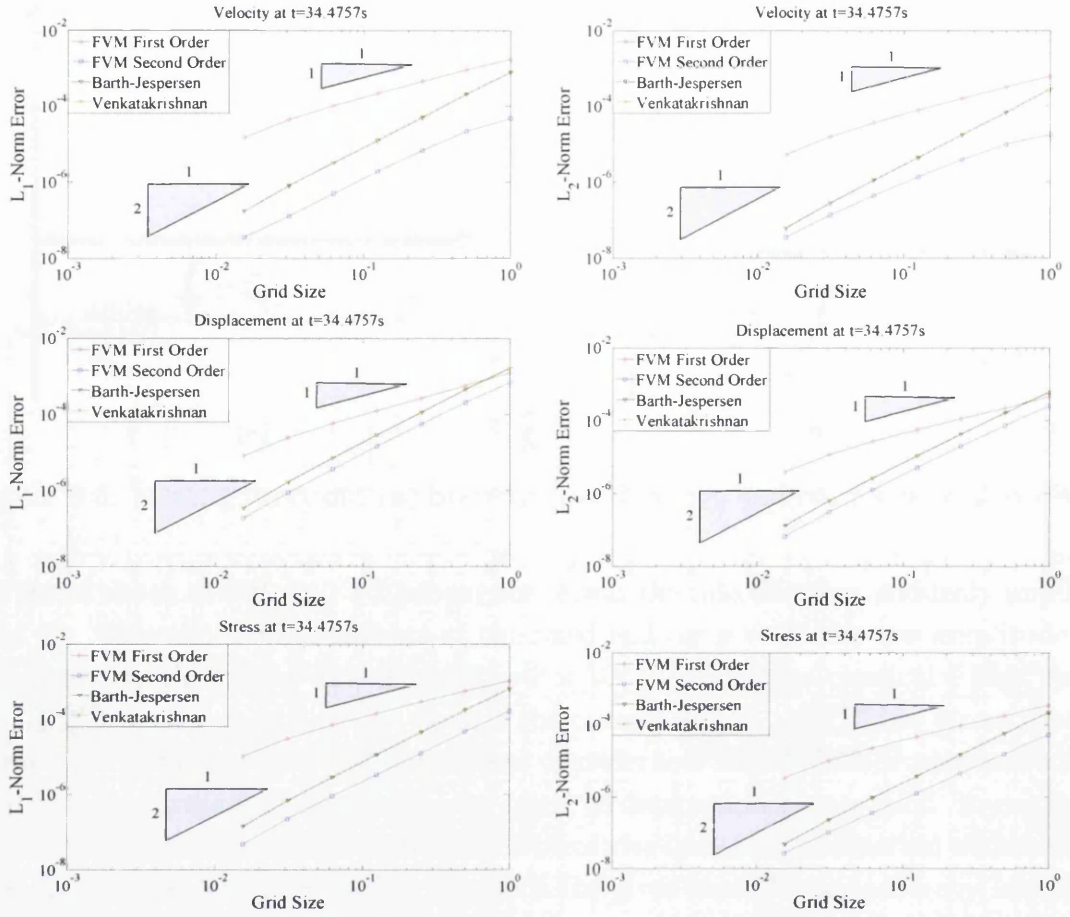

Figure 9.8: Pile Driving Example (Sinusoidal Loading): Results obtained with $P(L,t) = K\left(\sin\left(\pi t/20 - \pi/2\right) + 1\right)$. First column shows the L1-norm convergence and second column shows the L2-norm convergence. First and second rows show the velocity and displacement errors. Last row illustrates the stress error. The linear elastic model is used and material properties are Poisson's ratio $\nu = 0.3$, Young's modulus $E = 1\text{Pa}$, density $\rho_0 = 1\text{kg/m}^3$ and $\alpha_{CFL} = 0.5$.

Chapter 10

Multi-Dimensional Problems

"Example is the best precept".

Aesop (620 – 564 BCE)

d

10.1 The Plane Strain Equations for 2D Elasticity

The generic form of the new mixed system of equations, viz. (2.21) and (2.22), reduces to two space dimensions by assuming that there is no variation in X_3 direction. Under this circumstance, the small strain ε_{33} must vanish[1], which thus implies that deformation gradient in X_3 direction has to be $F_{33} = 1$. The stress P_{33} (or widely known as σ_{33}[2]), however, will not generally be zero and can be determined in terms of F_{11} and F_{22}:

$$P_{33} = \sigma_{33} = \lambda \left[\underbrace{(F_{11} - 1)}_{\varepsilon_{11}} + \underbrace{(F_{22} - 1)}_{\varepsilon_{22}} \right]. \tag{10.1}$$

Dropping all the components involved in X_3 space dimension of (2.21-2.22), the remaining six equations are

$$\frac{\partial \boldsymbol{\mathcal{U}}}{\partial t} + \frac{\partial \boldsymbol{\mathcal{F}}_1}{\partial X_1} + \frac{\partial \boldsymbol{\mathcal{F}}_2}{\partial X_2} = \mathbf{0}, \tag{10.2}$$

where

$$\boldsymbol{\mathcal{U}} = \begin{pmatrix} p_1 \\ p_2 \\ F_{11} \\ F_{12} \\ F_{21} \\ F_{22} \end{pmatrix}; \quad \boldsymbol{\mathcal{F}}_1 = \begin{pmatrix} -P_{11} \\ -P_{21} \\ -p_1/\rho_0 \\ 0 \\ -p_2/\rho_0 \\ 0 \end{pmatrix}; \quad \boldsymbol{\mathcal{F}}_2 = \begin{pmatrix} -P_{12} \\ -P_{22} \\ 0 \\ -p_1/\rho_0 \\ 0 \\ -p_2/\rho_0 \end{pmatrix}. \tag{10.3}$$

The expression above is often called the two-dimensional plane strain equations. The system (10.2) models P-wave and S-wave for which the motion is confined in X_1-X_2 plane. The S-wave modeled by this system has material motion orthogonal to the direction of wave propagation, but still remained in the X_1-X_2 plane. This is a reasonable model for plane waves propagating through a three-dimensional elastic body in the case where there is no variation in X_3 direction. For instance, the body will try to expand in X_3 direction if it is compressed in the X_1 or X_2 direction. However, this will be prevented by the adjacent material, which is trying equally hard to expand in other direction. It is important to note that (10.2) will not be able to model the elastic waves in thin plate [38].

10.2 Eigenstructure

Eigenstructure of the system above is discussed as follows. Rather than displaying the matrices $\boldsymbol{\mathcal{A}}_1$ and $\boldsymbol{\mathcal{A}}_2$ separately, it is essential to perform the linear combination

[1]Plane strain is defined to be a state of strain where the strain normal to X_1-X_2 plane, ε_{33}, and the shear strains, ε_{13} and ε_{23}, are assumed to be zero [8, 114, 159].

[2]The difference between $\boldsymbol{P}$ and $\boldsymbol{\sigma}$ disappears in small strain theory.

of $\boldsymbol{\mathcal{A}}_N$ such that $\boldsymbol{\mathcal{A}}_N = \boldsymbol{\mathcal{A}}_1 N_1 + \boldsymbol{\mathcal{A}}_2 N_2$, where $\boldsymbol{N} = (N_1, N_2)^T$ describes the material outward unit normal vector to the interface. Consequently, the matrix $\boldsymbol{\mathcal{A}}_N$ is given by

$$\boldsymbol{\mathcal{A}}_N = \begin{pmatrix} 0 & 0 & -(\lambda+2\mu)N_1 & -\mu N_2 & -\mu N_2 & -\lambda N_1 \\ 0 & 0 & -\lambda N_2 & -\mu N_1 & -\mu N_1 & -(\lambda+2\mu)N_2 \\ -N_1/\rho_0 & 0 & 0 & 0 & 0 & 0 \\ -N_2/\rho_0 & 0 & 0 & 0 & 0 & 0 \\ 0 & -N_1/\rho_0 & 0 & 0 & 0 & 0 \\ 0 & -N_2/\rho_0 & 0 & 0 & 0 & 0 \end{pmatrix} \tag{10.4}$$

By setting $\boldsymbol{N} = (1,0)^T$ or $(0,1)^T$, the matrices $\boldsymbol{\mathcal{A}}_1$ and $\boldsymbol{\mathcal{A}}_2$ are easily recovered. The eigenvalues of $\boldsymbol{\mathcal{A}}_N$ are

$$U_{1,2} = \pm U_p; \qquad U_{3,4} = \pm U_s; \qquad U_{5,6} = 0. \tag{10.5}$$

Their corresponding P-wave and S-wave eigenvectors are

$$\boldsymbol{\mathcal{R}}_1 = \begin{pmatrix} N_1 \\ N_2 \\ -N_1^2/\rho_0 U_p \\ -N_1 N_2/\rho_0 U_p \\ -N_1 N_2/\rho_0 U_p \\ -N_2^2/\rho_0 U_p \end{pmatrix}; \qquad \boldsymbol{\mathcal{R}}_2 = \begin{pmatrix} N_1 \\ N_2 \\ N_1^2/\rho_0 U_p \\ N_1 N_2/\rho_0 U_p \\ N_1 N_2/\rho_0 U_p \\ N_2^2/\rho_0 U_p \end{pmatrix} \tag{10.6}$$

and

$$\boldsymbol{\mathcal{R}}_3 = \begin{pmatrix} N_2 \\ -N_1 \\ -N_1 N_2/\rho_0 U_s \\ -N_2^2/\rho_0 U_s \\ N_1^2/\rho_0 U_s \\ N_1 N_2/\rho_0 U_s \end{pmatrix}; \qquad \boldsymbol{\mathcal{R}}_4 = \begin{pmatrix} N_2 \\ -N_1 \\ N_1 N_2/\rho_0 U_s \\ N_2^2/\rho_0 U_s \\ -N_1^2/\rho_0 U_s \\ -N_1 N_2/\rho_0 U_s \end{pmatrix} \tag{10.7}$$

respectively. Observe that P-wave has velocity components directed in $\boldsymbol{N}$ direction. The S-wave, on the contrary, has motion in the orthogonal direction $\boldsymbol{T} = (N_2, -N_1)^T$ where $\boldsymbol{T} \perp \boldsymbol{N}$ (or $\boldsymbol{T} \cdot \boldsymbol{N} = 0$).

10.3 Numerical Examples

A series of examples will be examined in order to illustrate the performance of the proposed method. In all instances, numerical results will be compared with either the analytical solution or finite element simulations to assess the validity and quality of this new computational methodology.

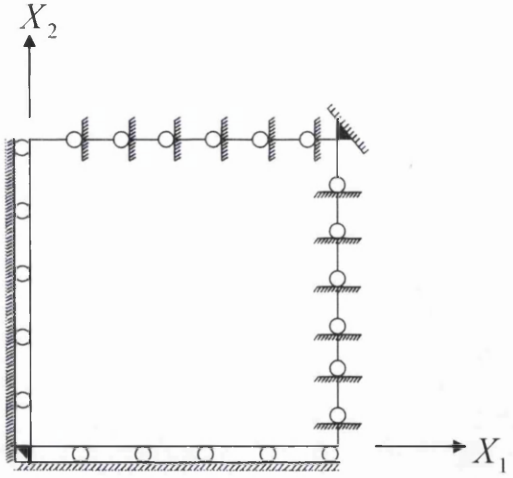

Figure 10.1: Plane strain test case.

10.3.1 A Plane Strain Case: Low Dispersion Wave Propagation

This first example has been extracted from Peraire *et al.* (2006) [58]. A square flat plate of unit side length under plane strain is considered. The west and south boundaries are allowed to move only tangentially, whereas the north and east boundaries are restricted to move normally (see Figure 10.1). In the small deformation case, this problem has an analytical solution (displacement) of the form

$$\boldsymbol{u}(t) = \begin{bmatrix} u_1(t) \\ u_2(t) \end{bmatrix} = U_0 \cos\left(\frac{c_d \pi t}{\sqrt{2}}\right) \begin{bmatrix} \sin\left(\frac{\pi X_1}{2}\right)\cos\left(\frac{\pi X_2}{2}\right) \\ -\cos\left(\frac{\pi X_1}{2}\right)\sin\left(\frac{\pi X_2}{2}\right) \end{bmatrix}; \qquad c_d = \sqrt{\frac{\mu}{\rho_0}}. \tag{10.8}$$

With the aid of equation above, the deformation gradient can also be expressed as (by using the definition of $\boldsymbol{F} = \boldsymbol{I} + \partial \boldsymbol{u}/\partial \boldsymbol{X}$)

$$\boldsymbol{F} = \alpha \begin{bmatrix} \cos\left(\frac{\pi X_1}{2}\right)\cos\left(\frac{\pi X_2}{2}\right) + \alpha^{-1} & -\sin\left(\frac{\pi X_1}{2}\right)\sin\left(\frac{\pi X_2}{2}\right) \\ \sin\left(\frac{\pi X_1}{2}\right)\sin\left(\frac{\pi X_2}{2}\right) & -\cos\left(\frac{\pi X_1}{2}\right)\cos\left(\frac{\pi X_2}{2}\right) + \alpha^{-1} \end{bmatrix} \tag{10.9}$$

where

$$\alpha = \frac{U_0 \pi}{2} \cos\left(\frac{c_d \pi t}{\sqrt{2}}\right).$$

For values of U_0 below 0.001, the solution can be considered to be linear. This plate is initially loaded with deformation gradient at time $t = 0$ (by substituting $t = 0$ into (10.9)) without any initial velocity. The purpose of this example is to show conservation property (dominated by low dispersion wave propagation) and pointwise convergence order of the proposed methodology.

The square domain is discretised into 20×20 equal quadrilateral cells per edge and run for a large number of cycles with $U_0 = 5 \times 10^{-4}$, where the small deformation behaviour is observed. The simulation is performed by assuming near incompressibility for a value of $\kappa/\mu = 2(1+\nu)/3(1-2\nu) = 9.67$, which corresponds

to a Poisson's ratio of $\nu = (1 - \mu/\kappa)/2 = 0.45$, Young's modulus $E = 1.7 \times 10^7$Pa and density $\rho_0 = 1.1 \times 10^3$kg/m^3. The velocity and displacement in X_1 direction at point $(1, 0)$ are monitored and compared in Figure 10.2. The time histories of stress at point $(0, 0)$, linear momentum $\boldsymbol{L}$, angular momentum A, kinetic energy K, elastic potential energy ψ and total energy $(K + \psi)$ are also illustrated. It can be observed that first order FVM (piecewise constant representation) produces unreliable solutions over long-term responses due to diffusion. To eliminate this, a second order FVM (piecewise linear reconstruction) has to be employed and the agreement with the analytical solutions (i.e. displacement, velocity and stresses) is excellent. For completeness, the incorporation of slope limiters (i.e. Barth-Jespersen and Venkatakrishnan) into second order FVM is also illustrated (there is no advantage of introducing slope limiters since shocks do not form in this particular case). It is clear that the total energy should stay conserved since no forces applied externally to the system. As expected, higher order FVM (with and without slope limiters) improve significantly the energy conservation. Figure 10.3 shows the numerical dissipations for various mesh sizes. Here, less dissipative results (regardless of the order of FVM) can be obtained as the discretisation is refined. Grid convergence error analysis is also performed in Figure 10.4. Note that the numerical solution converges to the analytical solution by increasing the mesh resolution. The inclusion of slope limiter produces less accurate results (translational difference) than those without it whilst maintaing the expected order of convergence.

10.3.2 Spinning Plate

This example was considered in Laursen and Meng (2001) [103]. A unit thickness square plate (without any constraints) is released without any initial deformation but with an initial angular velocity of $\Omega = 105\,\text{rad/s}$ (see Figure 10.5). In this case, the initial velocity field (classical rigid-body dynamics) relative to the origin is denoted as

$$\boldsymbol{v}(\boldsymbol{X}) = \boldsymbol{\omega} \times \boldsymbol{X}; \qquad \boldsymbol{\omega} = (0, 0, \Omega)^T; \qquad \boldsymbol{X} = (X_1, X_2, 0)^T. \tag{10.10}$$

The angular momentum dominated example is chosen to illustrate the conservation properties of Total Variation Diminishing Runge-Kutta (TVD-RK) time stepping algorithm. Since TVD-RK is not a time-reversible integrator[3] (unlike Leapfrog time scheme) the conservation of angular momentum has to be incorporated as part of the space-time integrator, in the form of a geometric marching scheme (see Chapter 6). Moreover, the effect of different Courant-Friedrichs-Lewy (CFL) number on the accuracy of the numerical solutions is also examined. The plate is made of a nearly incompressible rubber material with Young's modulus $E = 1.7 \times 10^7$Pa, density $\rho_0 = 1.1 \times 10^3$ kg/m^3 and Poisson's ratio $\nu = (1 - \mu/k)/2 = 0.45$. Note that the

[3]Time reversibility is important because it guaranteess conservation properties (i.e. angular momentum and energy).

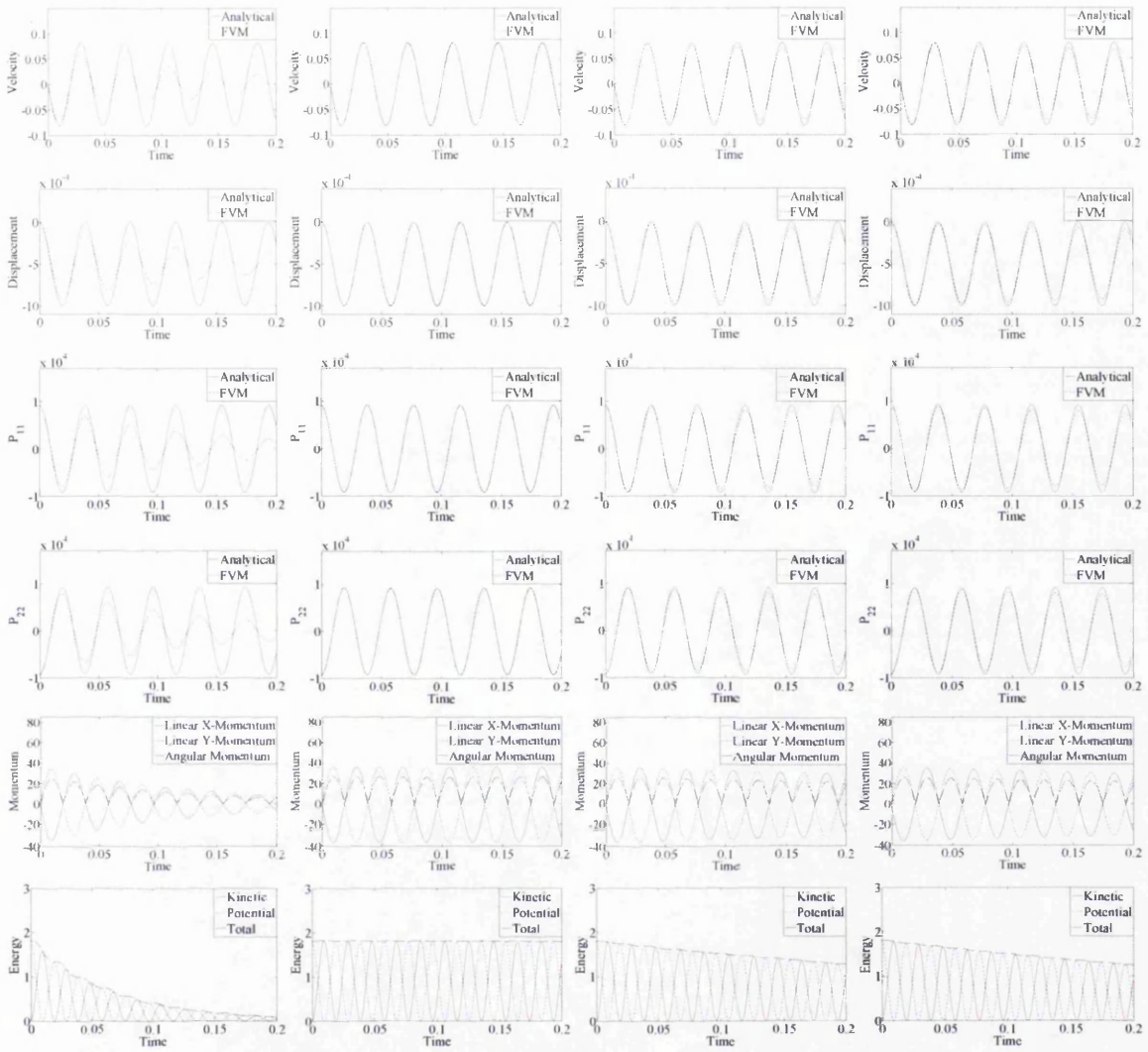

Figure 10.2: Plane Strain Test Case: Results obtained with $U_0 = 5 \times 10^{-4}$ where analytical solution is available. First column shows the results based upon piecewise constant reconstruction, second column for piecewise linear reconstruction, third for Barth-Jespersen limiter and last for Venkatakrishnan limiter. First and second rows show the time history of horizontal velocity and horizontal displacement at point $(1, 0)$ compared to analytical solution. Third and fourth rows demonstrate the P_{11} and P_{22} at point $(0, 0)$. Fifth row shows linear and angular momentum. Last row illustrates the kinetic, potential and total energy. The linear elastic constitutive model is used and material properties are such that Poisson's ratio $\nu = 0.45$, Young's modulus $E = 1.7 \times 10^7$Pa, density $\rho_0 = 1.1 \times 10^3$kg/m^3 and $\alpha_{CFL} = 0.5$. Discretisation of 20×20 cells per edge. Time step $\Delta t \approx 1 \times 10^{-4}$s.

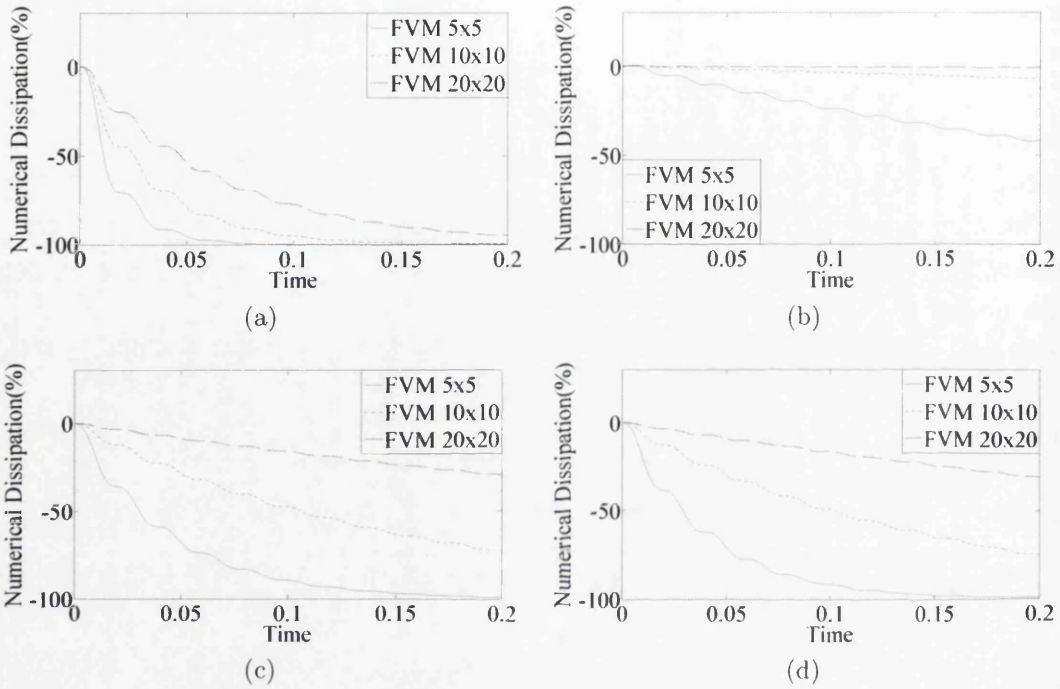

Figure 10.3: Plane Strain Test Case: Results obtained with $U_0 = 5\times10^{-4}$. Numerical dissipations of various mesh sizes are illustrated: (a) FVM First order; (b) FVM second order; (c) Barth-Jespersen limiter; and (d) Venkatakrishnan limiter. This example is run with the linear elastic constitutive model and material properties are such that Poisson's ratio $\nu = 0.45$, Young's modulus $E = 1.7 \times 10^7$Pa, density $\rho_0 = 1.1 \times 10^3$kg/m^3 and $\alpha_{CFL} = 0.5$. Time steps for three different mesh sizes: $\Delta t|_{5\times5} \approx 4 \times 10^{-4}$s, $\Delta t|_{10\times10} \approx 2 \times 10^{-4}$s and $\Delta t|_{20\times20} \approx 1 \times 10^{-4}$s.

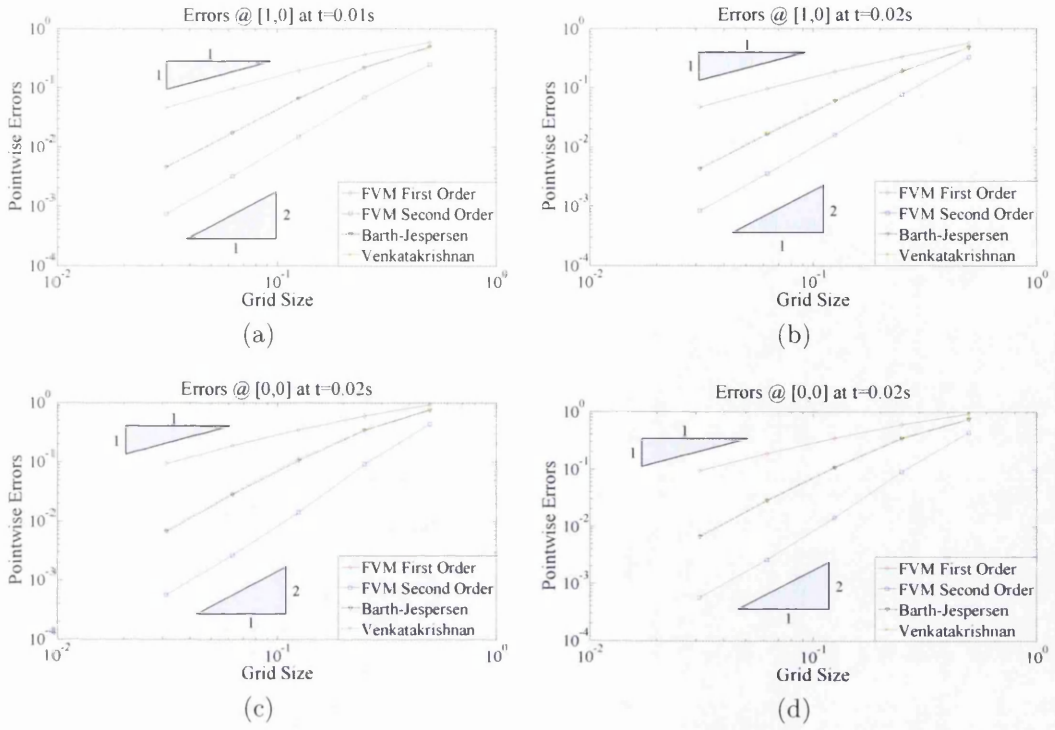

Figure 10.4: Plane Strain Test Case: Mesh convergence errors of (a) Velocity; (b) Displacement; (c) P_{11}; and (d) P_{22} stresses. Results obtained with $U_0 = 5 \times 10^{-4}$ where analytical solution is available. The linear elastic model is used and material properties are such that Poisson's ratio $\nu = 0.45$, Young's modulus $E = 1.7 \times 10^7$Pa, density $\rho_0 = 1.1 \times 10^3 \text{kg/m}^3$ and $\alpha_{CFL} = 0.5$.

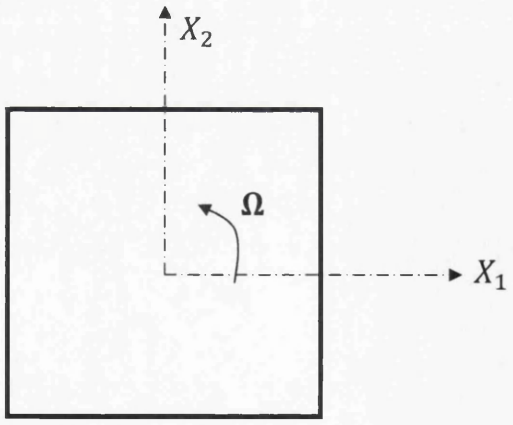

Figure 10.5: Spinning plate.

initial conditions used here are such that there is no steady-state solution, even in a rotating reference frame. Figure 10.6 presents the results using a discretisation of 20×20 equal quadrilateral cells per edge. First by noting that the linear momentum, $\boldsymbol{L} = \int_V \boldsymbol{p}\, dV$, is very small (nearly zero) at all times as no movement of the centre of mass is appreciated. Both the angular momentum ($A = \int_V \|\boldsymbol{x} \times \boldsymbol{p}\|\, dV$) and total energy ($K + \psi$) are expected to be conserved at its initial value during time integration (see Figure 10.6). The numerical dissipation for different mesh sizes is also studied in Figure 10.7. Note that the second order FVM (piecewise linear reconstruction) with a discretisation of 20×20 cells is low-dissipative and therefore very well suited for long-term responses. Figure 10.8 shows the pressure distribution of the deformed shape at various time instants. It is seen that the plate experiences deformations due to centrifugal (radially outward) force tending to stretch the plate.

A comparison of different Courant-Friedrichs-Lewy (CFL) number for a fixed number of mesh elements (10×10 quadrilateral cells per edge) is also performed in this particular case (see Figure 10.9). It can be shown that small CFL number implies relatively large numerical dissipation (compared to large CFL number), as a large number of time steps are required (which in turn introduces undesirable dissipation through evaluation of contact flux).

10.3.3 Uniform Cantilever Thick Beam in Bending Application

This example (extracted from Izian *et al.* 2011 [64]) represents the large deformation (dynamic) response of an end-loaded cantilever thick beam of length $L = 10\text{m}$ with a unit section ($H = 1\text{m}$). The forcing function is prescribed as $P_{app}(t) = 5 \times 10^3\text{N}$ where $t \geq 0$ (see Figure 10.10). A nearly incompressible rubber beam is chosen with material properties stated as belows: Young's modulus $E = 1.7 \times 10^7\text{Pa}$, density $\rho_0 = 1.1 \times 10^3\text{kg/m}^3$ and Poisson's ratio $\nu = 0.45$. The purpose of this example is to illustrate the performance of the proposed methodology in bending application. For validation purposes, the standard FEM simulations will be used to assess the quality of the proposed methodology. A qualitative comparison of the difference between various numerical techniques is illustrated in Figure 10.11 (where the deformation patterns at four identical times are shown). It is clear that the finite element solution with standard four-noded quadrilateral elements is far stiffer than proposed formulation. The deformed shapes (locking free) obtained with proposed algorithm compare extremely well with those of mean dilatation technique (a particular case of Selective Reduced Integration (SRI)).

10.3.4 Large Deformation of a Short Column: Highly Nonlinear Behaviour

The same problem was originally analysed by Bonet *et al.* (2001) [24]. A large strain vibration of a short column, which is given by a uniform initial velocity $V_0 = 10\text{m/s}$

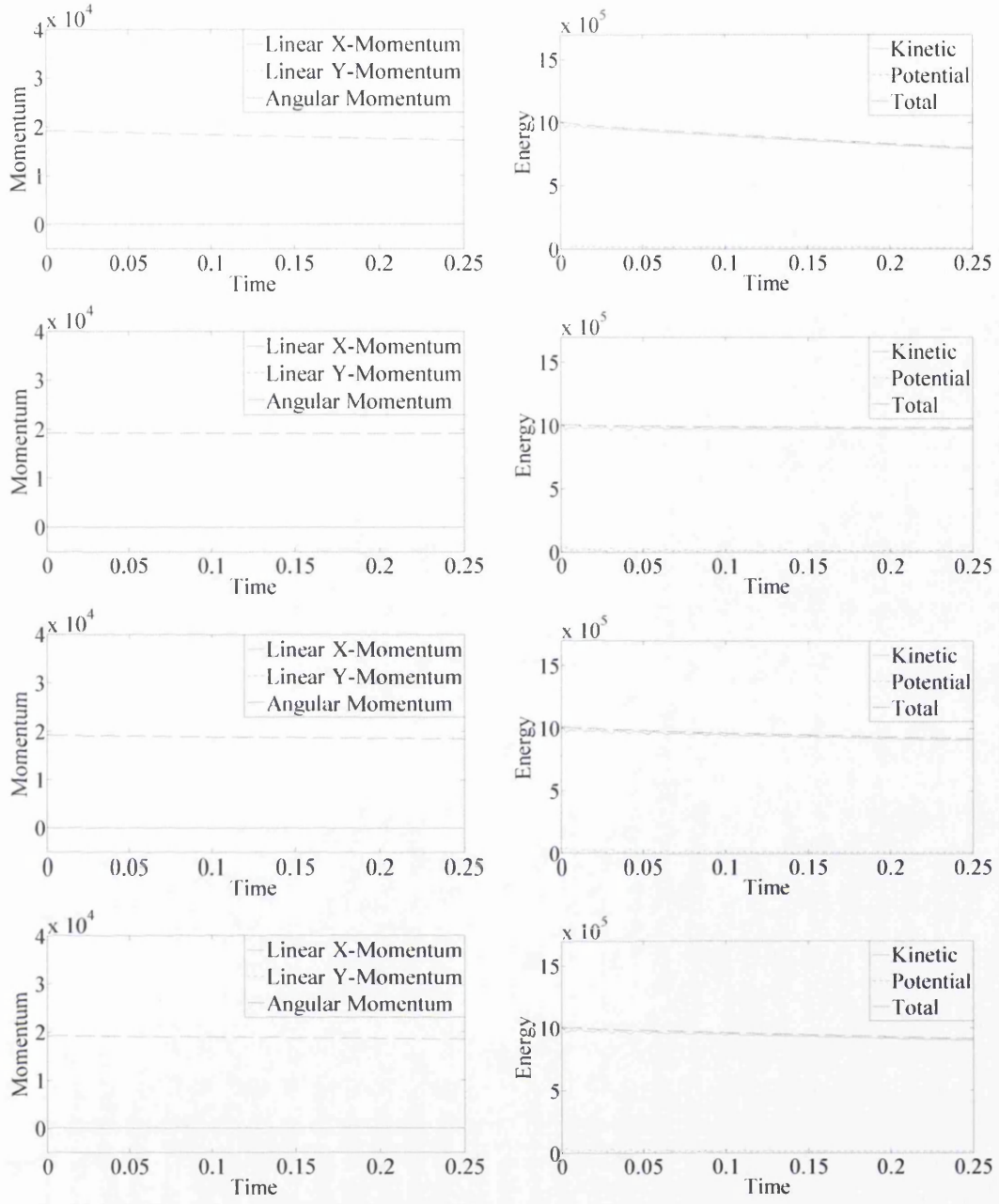

Figure 10.6: Spinning Plate: Results obtained with angular velocity $\Omega = 105\,\mathrm{rad/s}$. First row shows the results based upon piecewise constant reconstruction, second row for piecewise linear reconstruction, third for Barth-Jespersen limiter and last for Venkatakrishnan limiter. First column shows linear and angular momentum. Second column illustrates the kinetic, potential and total energy. The nearly incompressible Neo-Hookean (NH) constitutive model is used and material properties are such that Poisson's ratio $\nu = 0.45$, Young's modulus $E = 1.7 \times 10^7\mathrm{Pa}$, density $\rho_0 = 1.1 \times 10^3\mathrm{kg/m^3}$ and $\alpha_{CFL} = 0.5$. Discretisation of 20×20 cells per edge. Time step $\Delta t \approx 1 \times 10^{-4}\mathrm{s}$.

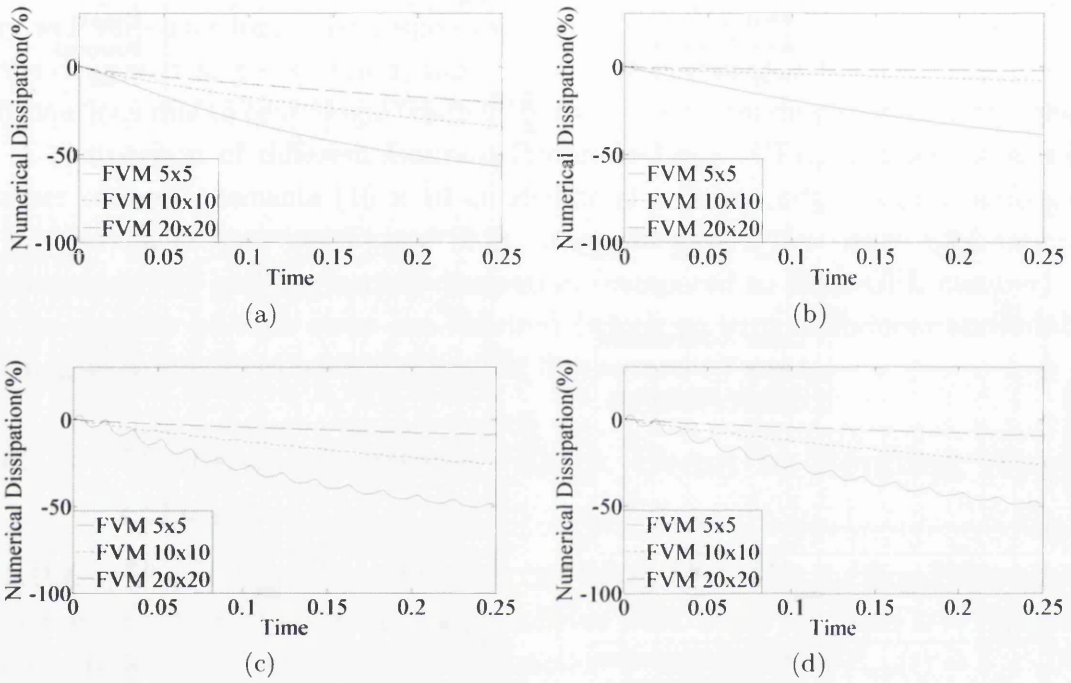

Figure 10.7: Spinning Plate: Results obtained with angular velocity $\Omega = 105\,\text{rad/s}$. Numerical dissipations of various mesh sizes are illustrated: (a) FVM First order; (b) FVM second order; (c) Barth-Jespersen limiter; and (d) Venkatakrishnan limiter. This example is run with the nearly incompressible Neo-Hookean (NH) constitutive model and material properties are such that Poisson's ratio $\nu = 0.45$, Young's modulus $E = 1.7 \times 10^7\text{Pa}$, density $\rho_0 = 1.1 \times 10^3\text{kg/m}^3$ and $\alpha_{CFL} = 0.5$. Time steps for three different mesh sizes: $\Delta t|_{5\times5} \approx 4 \times 10^{-4}\text{s}$, $\Delta t|_{10\times10} \approx 2 \times 10^{-4}\text{s}$ and $\Delta t|_{20\times20} \approx 1 \times 10^{-4}\text{s}$.

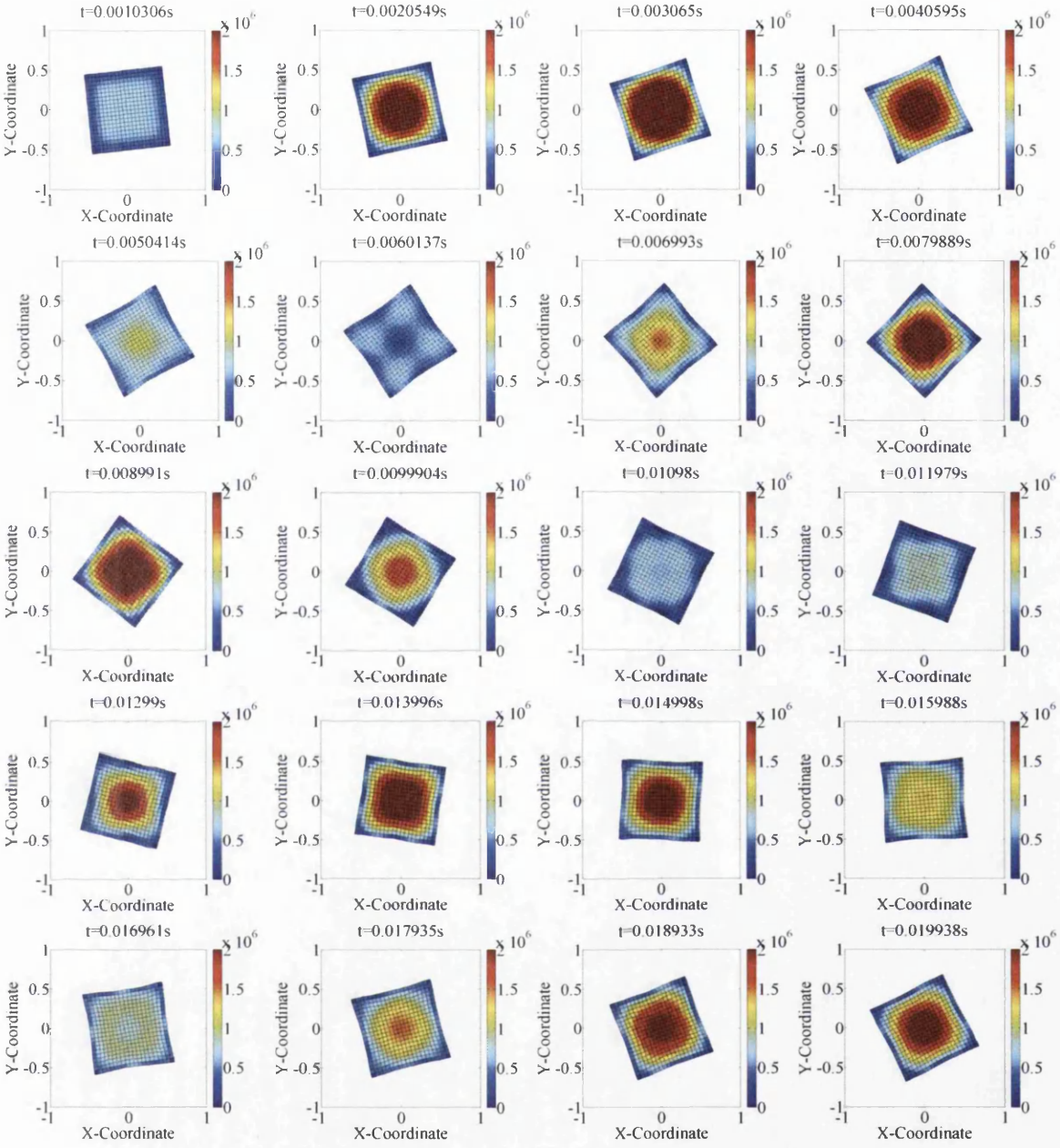

Figure 10.8: Spinning Plate: Evolution of pressure distribution at different time instants. Results obtained imposing a piecewise linear reconstruction and $\Omega = 105\text{rad/s}$. This test case is run with the nearly incompressible Neo-Hookean (NH) constitutive model such that Poisson's ratio $\nu = 0.45$, Young's modulus $E = 1.7 \times 10^7\text{Pa}$, density $\rho_0 = 1.1 \times 10^3\text{kg/m}^3$ and $\alpha_{CFL} = 0.5$. Discretisation of 20×20 cells per edge. Time step $\Delta t \approx 1 \times 10^{-4}\text{s}$.

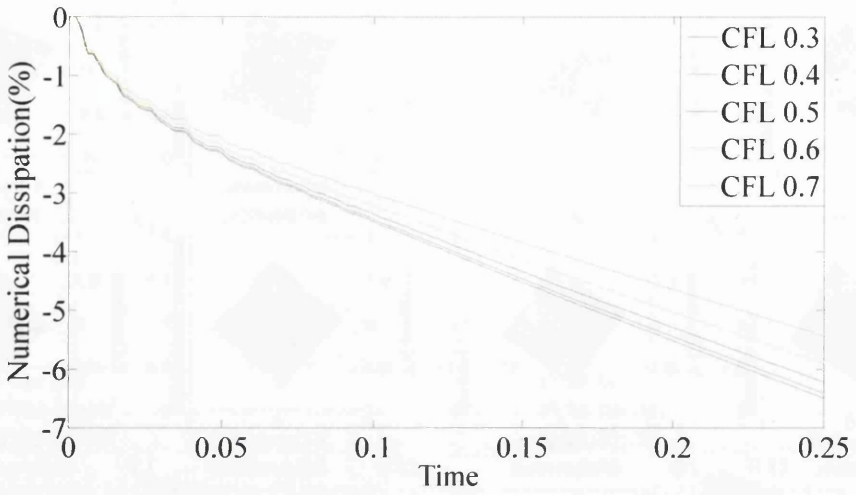

Figure 10.9: Spinning Plate: Results obtained with angular velocity $\Omega = 105\,\text{rad/s}$. Numerical dissipation (second order FVM) of various CFL numbers with a fixed number of elements is illustrated. This example is run with the nearly incompressible Neo-Hookean (NH) constitutive model and material properties are such that Poisson's ratio $\nu = 0.45$, Young's modulus $E = 1.7 \times 10^7\text{Pa}$ and density $\rho_0 = 1.1 \times 10^3\text{kg/m}^3$. Discretisation of 10×10 cells per edge.

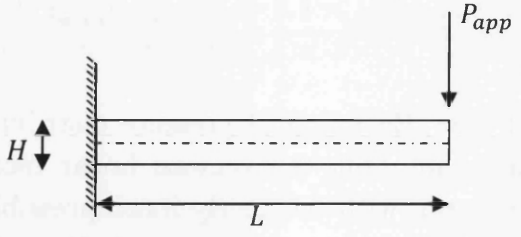

Figure 10.10: Cantilever beam configuration.

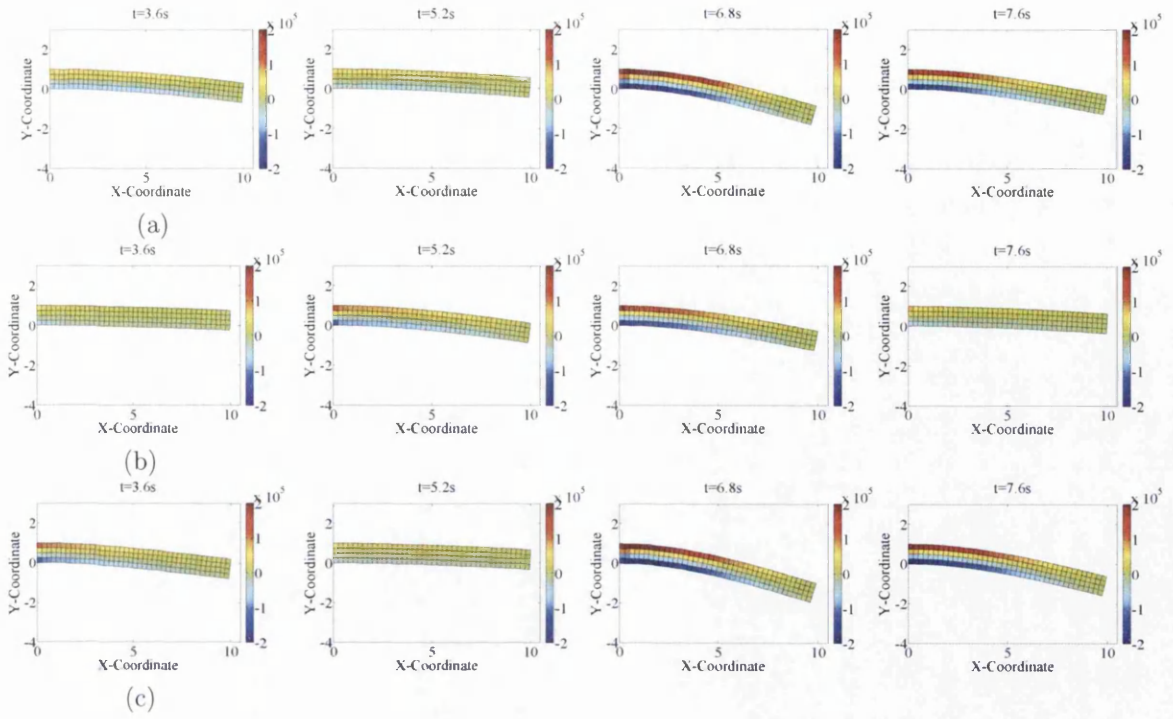

Figure 10.11: Cantilever Thick Beam: Sequence of deformed shapes for the cantilever beam using: (a) Mean dilatation approach; (b) Standard FEM procedure; and (c) Proposed methodology imposing a piecewise linear reconstruction. The nearly incompressible Neo-Hookean (NH) constitutive model is used such that Poisson's ratio $\nu = 0.45$, Young's modulus $E = 1.7 \times 10^7$Pa and density $\rho_0 = 1.1 \times 10^3$kg/m^3. Discretisation of 40×4 cells per edge. Time step $\Delta t = 5 \times 10^{-4}$s.

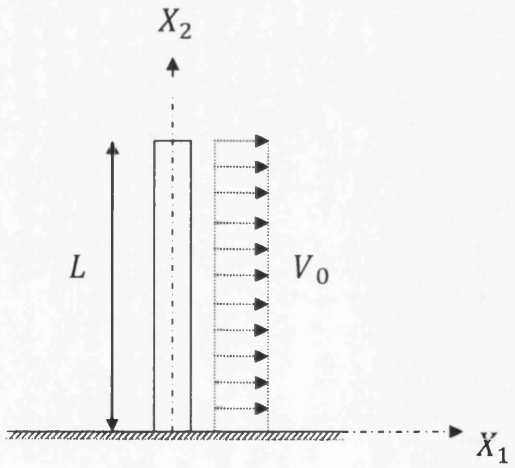

Figure 10.12: Short column definition.

whilst the unit width base is kept fixed, is considered (see Figure 10.12). This problem is highly nonlinear and involves large deformations. The main objective is to illustrate the performance of the proposed algorithm in bending dominated scenario. The properties of the material being used are described as belows: Young's modulus $E = 1.7 \times 10^7$Pa, density $\rho_0 = 1.1 \times 10^3$kg/m^3 and Poisson's ratio $\nu = 0.45$. Length L of the column is taken to be 6m. For comparison purposes, the same problem is also discretised using a standard FEM procedure and mean dilatation technique. Figure 10.13 depicts the positions of the column at various times for three cases: mean dilatation approach, standard FEM and proposed methodology. It is clear that the proposed formulation can be used without bending difficulty. The deformed shapes obtained from new methodology are found to be in good agreement with the conventional mean dilatation approach, whereas the standard formulation experiences the well-known locking phenomena. By making use of the proposed method, a series of deformed states are shown in Figure 10.14, where the colour contour plot indicates the pressure distribution.

The same example is now solved with the introduction of Von-Mises plasticity model (isochoric plastic flow) where yield stress is given by $\bar{\tau}_y^0 = 1.5$MPa and the hardening modulus $H = 0.25$MPa. Linear variation of velocity distribution is given in this case; that is, $v_{\text{linear}} = \bar{V} X_2 / L$ where $X_2 \in [0, L]$ and $\bar{V} = 15$m/s. This problem is first analysed using two-tep Taylor-Galerkin approach[4] (curl-projection and $\bar{\alpha} = 0.2$) and then with the new proposed methodology. See [64] for detailed discussion on choosing the value $\bar{\alpha}$ (problem-dependent parameter). Deformed shapes for both cases are shown in Figure 10.15. It can be clearly seen that the new proposed approach performs well in the case of near incompressibility.

10.3.5 A Punch Test

A punching test case is considered [160]. A flat square rubber plate of unit side length is constrained with rollers at the bottom and on the left and right hand sides. The right half of the domain experiences a prescribed punch velocity, $v_{\text{punch}} = 100$m/s (see Figure 10.16). The nearly incompressible rubber material is chosen where the Young's modulus $E = 1.7 \times 10^7$Pa, Poisson's ratio $\nu = 0.45$ and material density $\rho_0 = 1.1 \times 10^3$kg/m^3. The objective of this example is to show that the proposed algorithm eliminates both the locking effect and the appearance of spurious (checkerboard) pressure modes in the case of near incompressibility. It is well-known that volumetric locking is commonly encountered in standard FEM analysis for nearly incompressible rubber material. To alleviate this, the mean dilatation approach is usually employed but unfortunately, the results obtained containing spurious pressure modes caused of the resolution of stress. This can be corrected by the use of new proposed methodology (see Figure 10.17). Figure 10.18 shows the numerical result obtained by proposed method compares well with the two-step Taylor-Galerkin solution of $\bar{\alpha} = 0.1$. It is observed that the existence of curl errors ($\bar{\alpha} = 0$) in the solution

[4]Two-step Taylor-Galerkin computational methodology is briefly discussed in Appendix I.

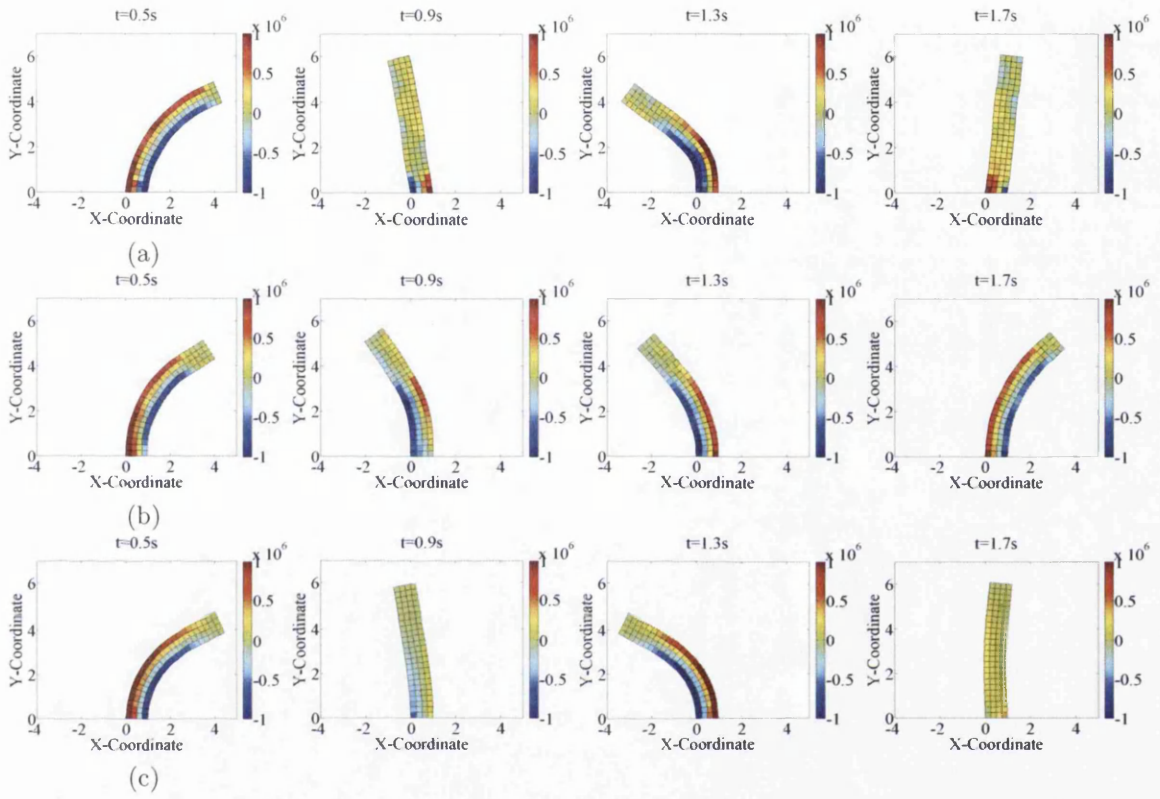

Figure 10.13: Short Column: Sequence of deformed shapes for the short column using: (a) Mean dilatation approach; (b) Standard FEM procedure; and (c) Proposed methodology imposing a piecewise linear reconstruction. The nearly incompressible Neo-Hookean (NH) constitutive model is used such that Poisson's ratio $\nu = 0.45$, Young's modulus $E = 1.7 \times 10^7$Pa and density $\rho_0 = 1.1 \times 10^3$kg/m^3. Discretisation of 4×24 cells per edge. Time step $\Delta t = 5 \times 10^{-4}$s.

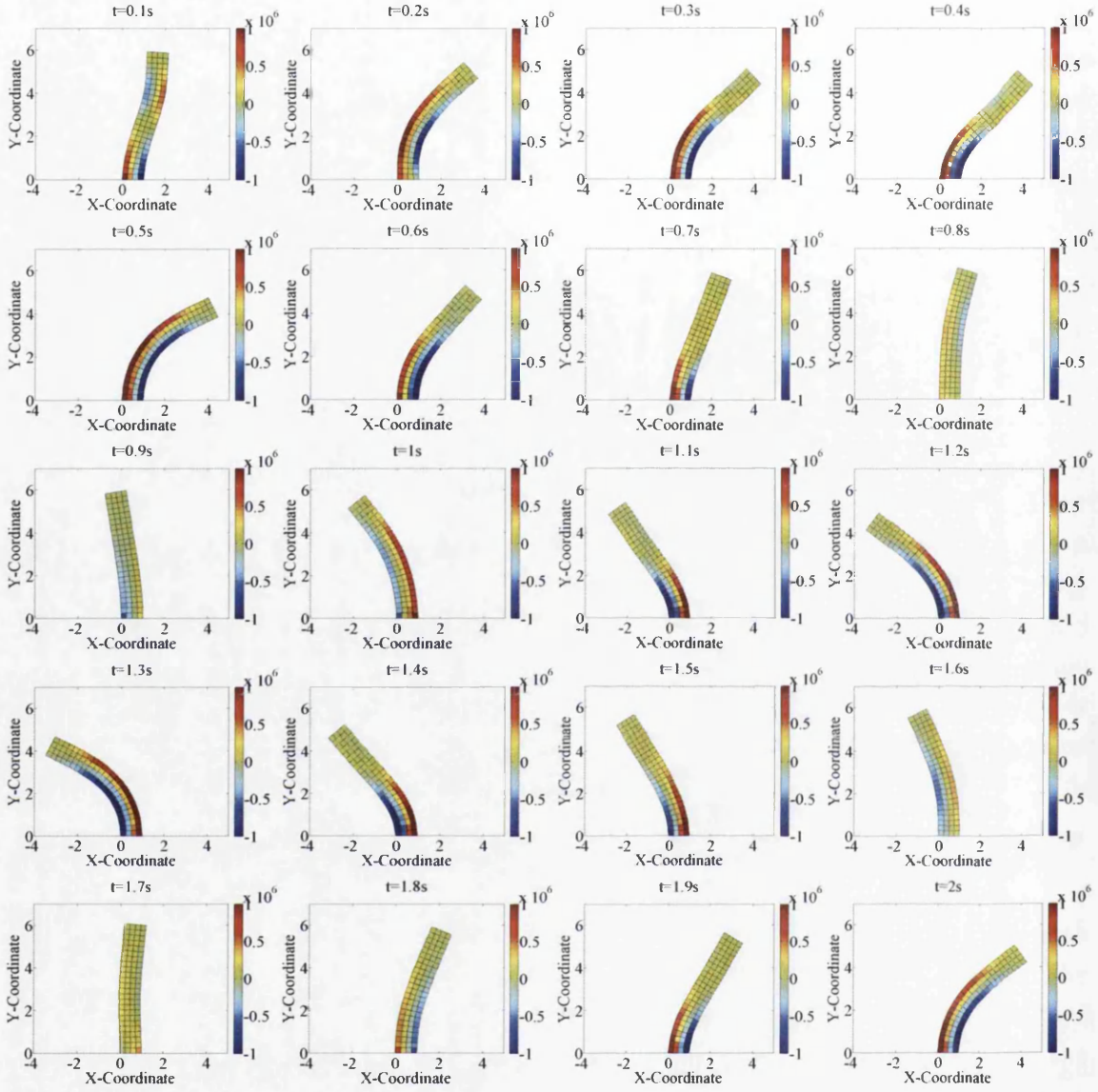

Figure 10.14: Short Column: Evolution of pressure distribution at different time instants. Results obtained with proposed methodology imposing a piecewise linear reconstruction and $V_0 = 10\text{m/s}$. The nearly incompressible Neo-Hookean (NH) constitutive model is used and its material properties are such that Poisson's ratio $\nu = 0.45$, Young's modulus $E = 1.7 \times 10^7\text{Pa}$, density $\rho_0 = 1.1 \times 10^3\text{kg/m}^3$ and $\alpha_{CFL} \approx 0.5$. Discretisation of 4×24 cells per edge. Time step $\Delta t = 5 \times 10^{-4}\text{s}$.

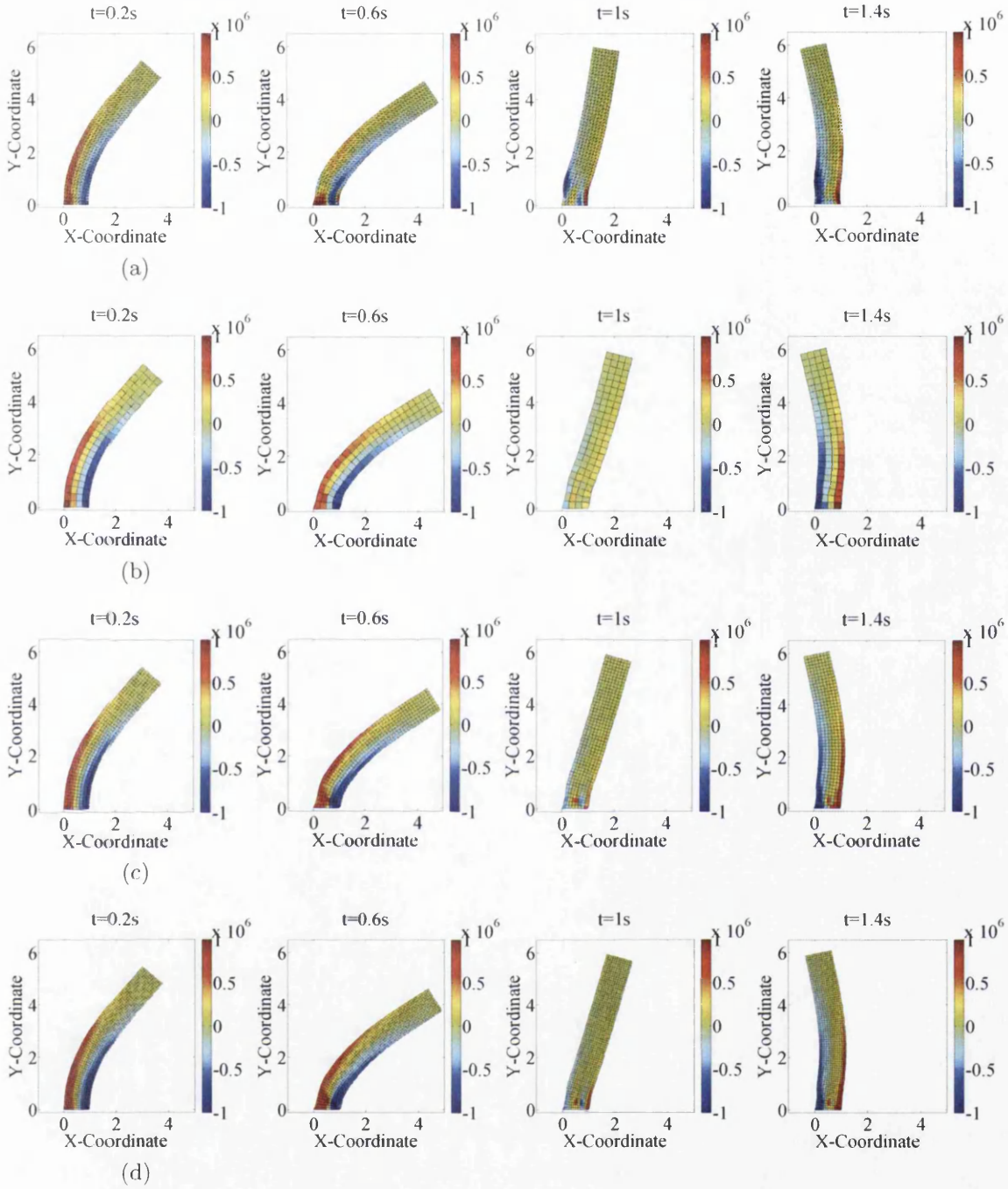

Figure 10.15: Short Column: Sequence of deformed shapes for short column with plasticity: (a) Two step Taylor-Galerkin technique (curl-projection and $\bar{\alpha} = 0.2$) of $8 \times 48 \times 2$; and (b-d) Proposed methodology imposing a piecewise linear reconstruction with discretisation of 4×24, 8×48 and 12×72, respectively. The Von-Mises plasticity model is used such that Poisson's ratio $\nu = 0.45$, Young's modulus $E = 1.7 \times 10^7$Pa, density $\rho_0 = 1.1 \times 10^3$kg/m^3, yield stress $\bar{\tau}_y^0 = 1.5$MPa and hardening modulus $H = 0.25$MPa. Time steps for four different meshes: $\Delta t|_{4\times24} = 4 \times 10^{-4}$s, $\Delta t|_{8\times48\,\text{or}\,8\times48\times2} = 2 \times 10^{-4}$s and $\Delta t|_{12\times72} = 1 \times 10^{-4}$s.

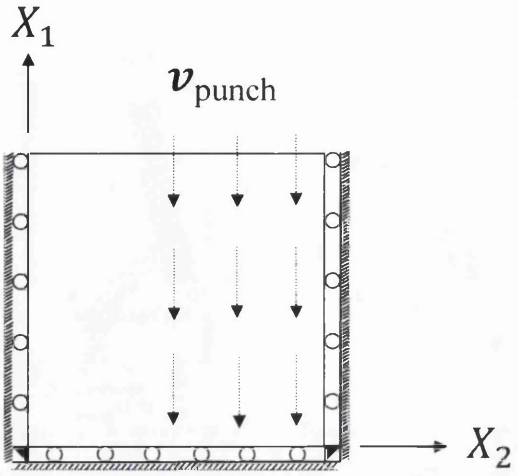

Figure 10.16: A punch test case.

leads to a breakdown of the numerical scheme. Numerical dissipation and pressure distribution are depicted in Figure 10.19 and Figure 10.20, respectively. Reliable solution over long time integration can be obtained by refining the mesh elements. This problem is also analysed by making use of Von-Mises plasticity model with yield stress $\bar{\tau}_y^0 = 10\text{MPa}$ and hardening parameter $H = 2.5\text{MPa}$. A comparison between the proposed methodology and two-step Taylor-Galerkin method is presented in Figure 10.21. It shows that both algorithms produce similar deformation behaviours.

10.3.6 Tensile Case

Similar to the punching problem, a tensile test case is considered [160]. A square steel plate, with material properties defined as Young's modulus $E = 2.1 \times 10^{10}\text{Pa}$, density $\rho_0 = 7 \times 10^3 \text{kg/m}^3$ and Poisson's ratio $\nu = 0.3$, is pulled rapidly by $v_{\text{pull}} = 500\text{m/s}$, as shown in Figure 10.22. In this particular example, the incompressibility limit, given by $\kappa/\mu = 2.1667$, is used. In these circumstances, the standard FEM procedure should be able to produce convincing results, which can be treated as reference solutions for comparison purposes (see Figure 10.23). The numerical predictions obtained by the new methodology and a two-step Taylor-Galerkin approach qualitatively agree quite well with those of convectional standard FEM analysis. Pressure evolution is also depicted in Figure 10.24. Moreover, the same problem is further analysed by employing Von-Mises plasticity model with yield stress $\bar{\tau}_y^0 = 5\text{GPa}$ and hardening modulus $H = 1\text{GPa}$. In Figure 10.25, the deformed shapes of proposed methodology are found to be in good agreement with the existing two-step Taylor-Galerkin solutions. Figure 10.27 illustrates the evolution of pressure distribution for the tensile test case with plasticity model implemented. Irrecoverable (permanent) behaviour has taken place near the bottom fixed end, as the plate is stretched vertically.

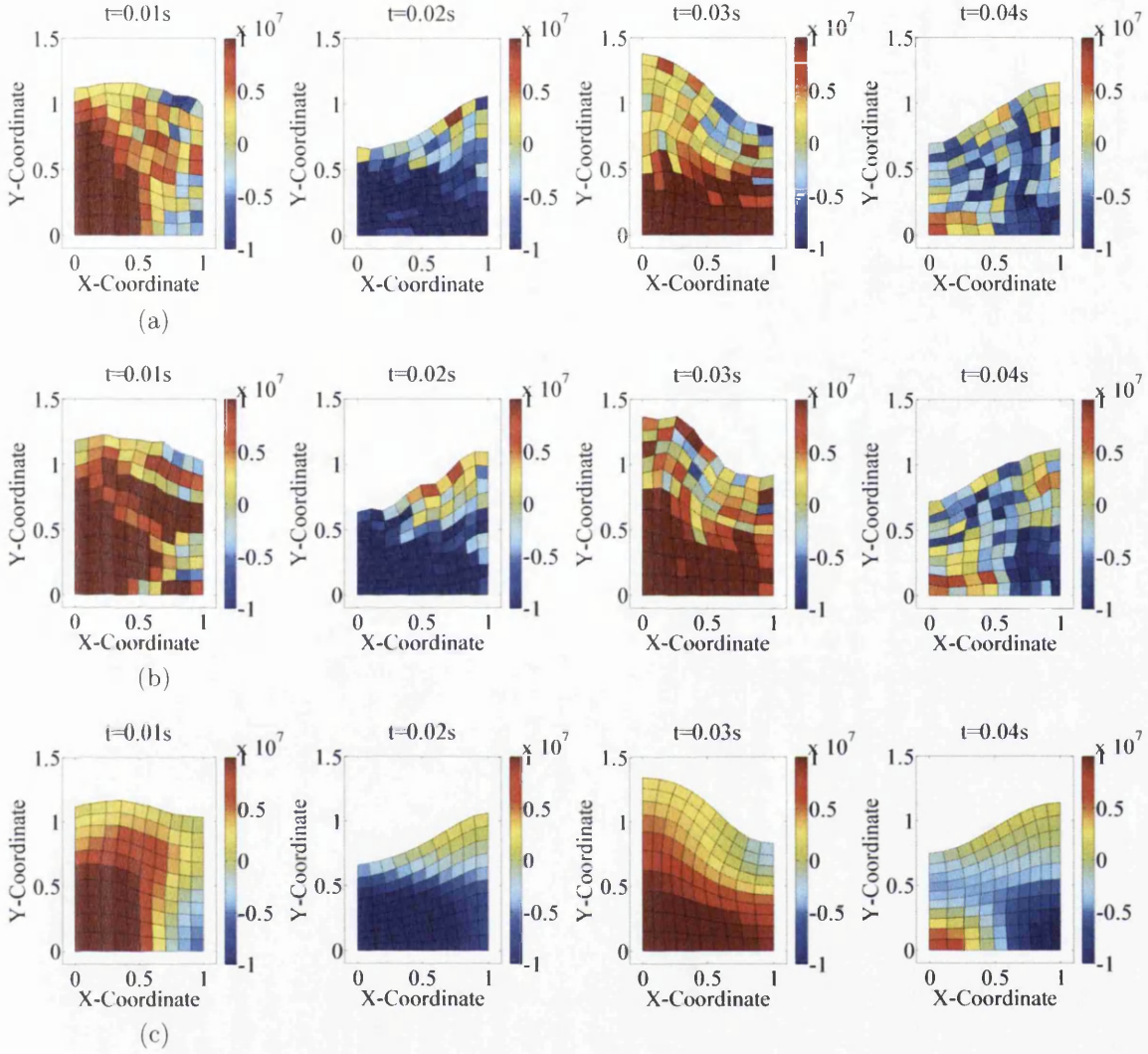

Figure 10.17: Punch Test Case: Sequence of pressure distribution of deformed shapes using: (a) Mean dilatation technique; (b) Standard FEM procedure; and (c) Proposed methodology imposing a piecewise linear reconstruction. Initial compressive velocity $v_{\text{punch}} = 100\text{m/s}$ is applied. A rubber plate is used and its material properties are such that Poisson's ratio $\nu = 0.45$, Young's modulus $E = 1.7 \times 10^7\text{Pa}$ and density $\rho_0 = 1.1 \times 10^3\text{kg/m}^3$. Discretisation of 10×10 cells per edge. Time step $\Delta t = 2 \times 10^{-4}\text{s}$.

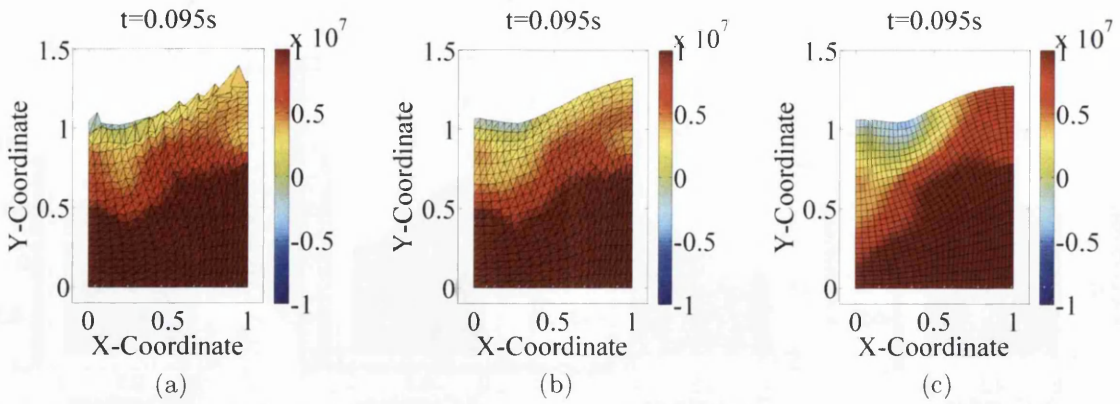

Figure 10.18: Punch Test Case: Deformed shapes at a particular time instant with $v_{\text{punch}} = 100\text{m/s}$. (a-b) Two step Taylor-Galerkin technique (curl-projection and discretisation of $20 \times 20 \times 2$) with $\bar{\alpha} = 0$ and $\bar{\alpha} = 0.1$, respectively. (c) Proposed methodology imposing a piecewise linear reconstruction with discretisation of 28×28. The nearly incompressible Neo-Hookean (NH) model is used and its material properties are such that Poisson's ratio $\nu = 0.45$, Young's modulus $E = 1.7 \times 10^7\text{Pa}$, density $\rho_0 = 1.1 \times 10^3\text{kg/m}^3$. Time step $\Delta t = 5 \times 10^{-5}\text{s}$.

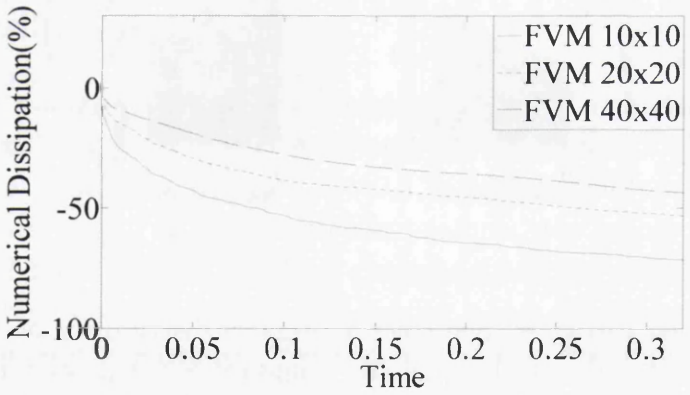

Figure 10.19: Punch Test Case: Results obtained imposing a piecewise linear reconstruction with an initial compressive velocity $v_{\text{punch}} = 100\,\text{m/s}$. Numerical dissipation of various mesh sizes are illustrated. The nearly incompressible Neo-Hookean (NH) constitutive model is used where properties are such that Poisson's ratio $\nu = 0.45$, Young's modulus $E = 1.7 \times 10^7\text{Pa}$, density $\rho_0 = 1.1 \times 10^3\text{kg/m}^3$ and $\alpha_{CFL} = 0.5$. Time steps for three different mesh sizes: $\Delta t|_{10\times10} \approx 2 \times 10^{-4}\text{s}$, $\Delta t|_{20\times20} \approx 1 \times 10^{-4}\text{s}$ and $\Delta t|_{40\times40} \approx 5 \times 10^{-5}\text{s}$.

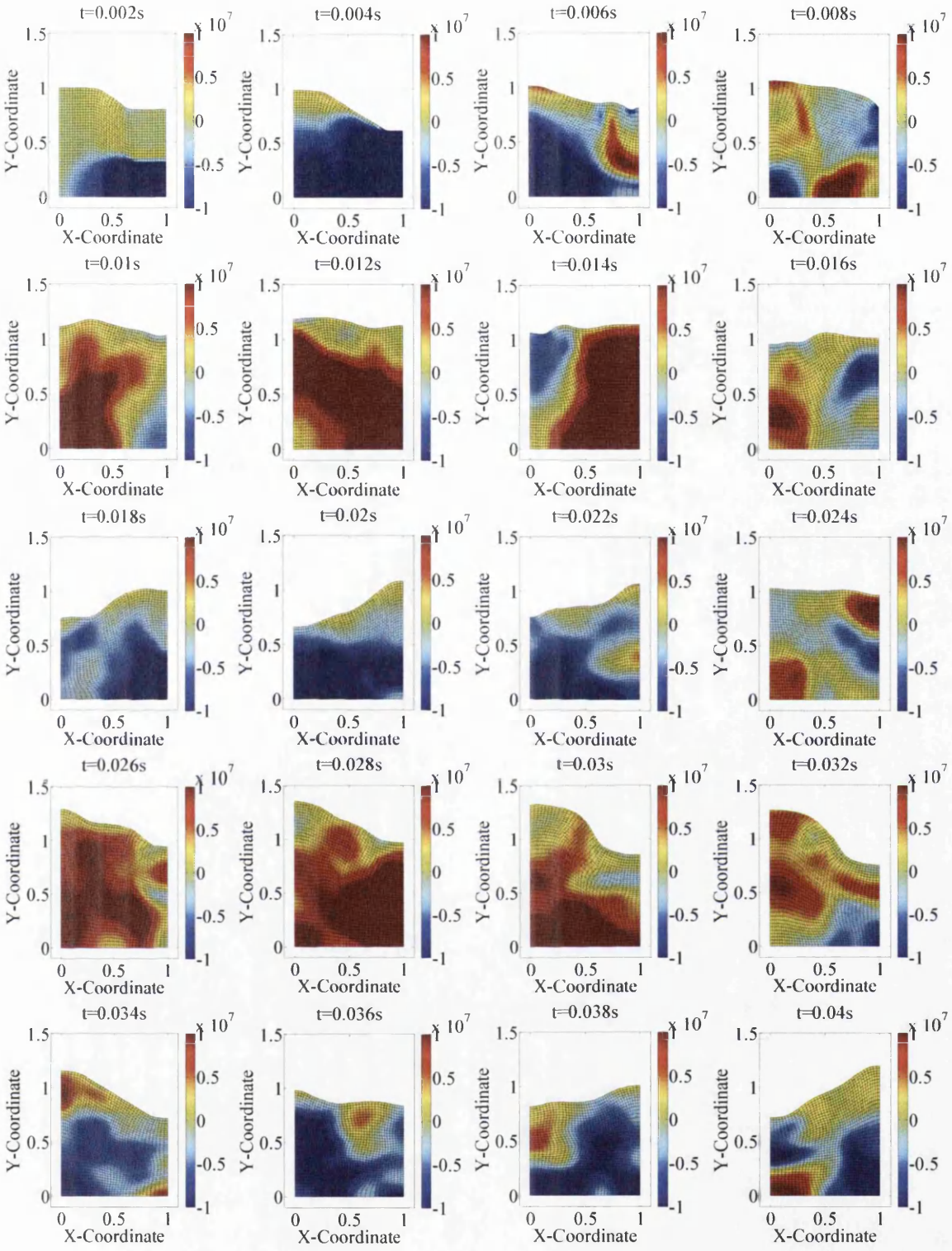

Figure 10.20: Punch Test Case: Evolution of pressure distribution at different time instants. Results obtained imposing a piecewise linear reconstruction and $v_{\text{punch}} = 100\text{m/s}$. The nearly incompressible Neo-Hookean (NH) constitutive model is used and its material properties are such that Poisson's ratio $\nu = 0.45$, Young's modulus $E = 1.7 \times 10^7\text{Pa}$ and density $\rho_0 = 1.1 \times 10^3\text{kg/m}^3$. Discretisation of 40×40 cells per edge. Time step $\Delta t = 2 \times 10^{-5}\text{s}$.

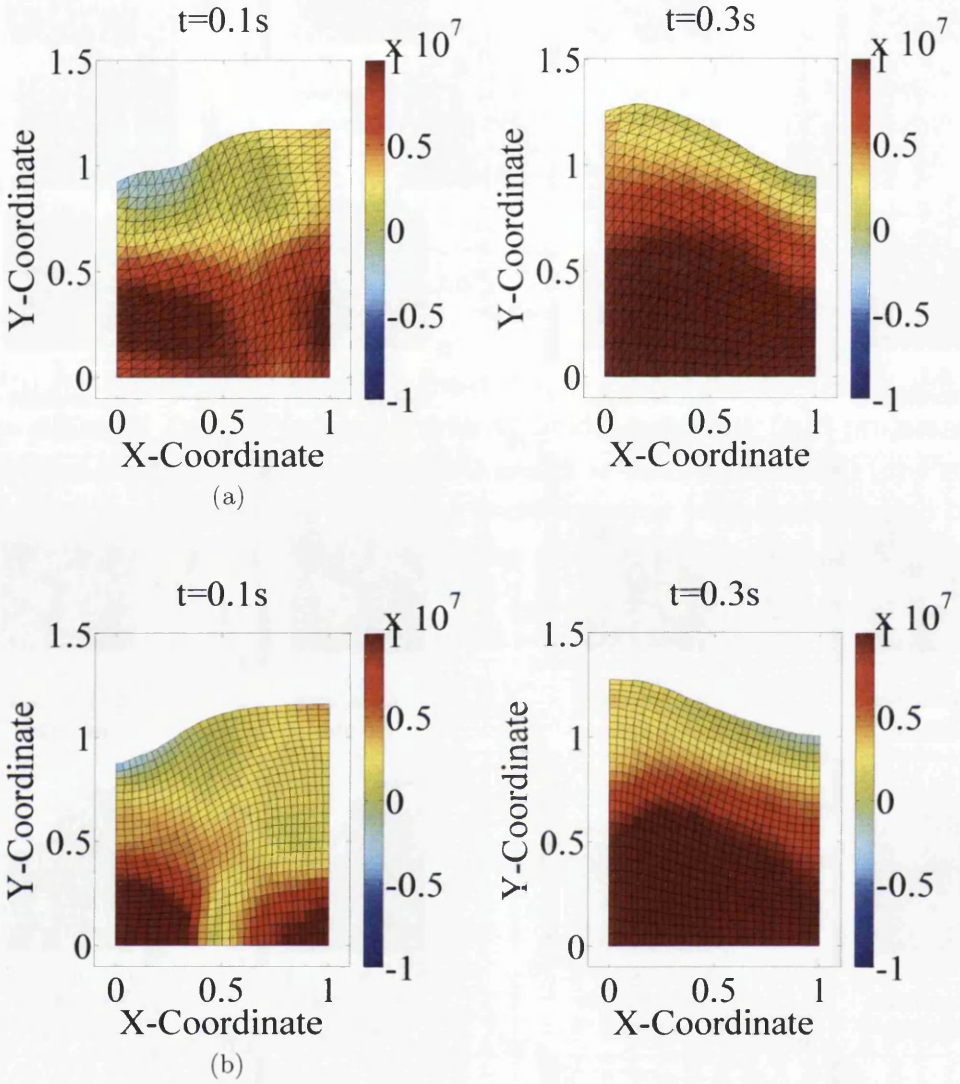

Figure 10.21: Punch Test Case: Deformed shapes for punch case with plasticity and $v_{\text{punch}} = 100\text{m/s}$. (a) Two-step Taylor-Galerkin technique (curl-projection and $\bar{\alpha} = 0.2$) of $20 \times 20 \times 2$; and (b) Proposed methodology imposing a piecewise linear reconstruction with discretisation of 28×28. The Von-Mises plasticity model is used and its material properties are such that Poisson's ratio $\nu = 0.45$, Young's modulus $E = 1.7 \times 10^7\text{Pa}$, density $\rho_0 = 1.1 \times 10^3\text{kg/m}^3$, yield stress $\bar{\tau}_y^0 = 10\text{MPa}$ and hardening modulus $H = 2.5\text{MPa}$. Time step $\Delta t = 5 \times 10^{-5}\text{s}$.

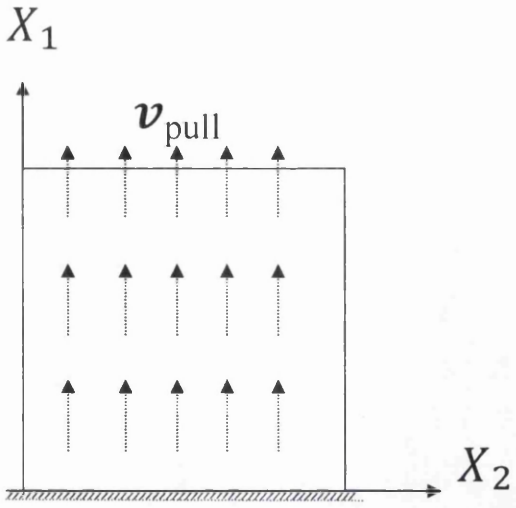

Figure 10.22: Tensile test case.

10.3.7 Beam Bending Case: Buckling

Another bending-dominated example is demonstrated [161]. A vertical cantilever beam of length $L = 10\text{m}$ with a unit width base is considered (see Figure 10.26). The beam is fixed at the bottom and a vertical velocity, $v_0 = 5\text{m/s}$, is prescribed at right half of the beam. The material properties of the beam are Young's modulus $E = 1.17 \times 10^7\text{Pa}$, Poisson's ratio $\nu = 0.35$ and density $\rho_0 = 1.1 \times 10^3\text{kg/m}^3$. As discussed previously, the standard FEM procedure encountered problems near incompressibility where it exhibits volumetric locking and bending difficulty. This can be resolved by using the averaged nodal finite element [23, 24]. However, the nodal averaging process develops artificial mechanisms similar to hourglassing in some 2D plane strain cases [22]. To remedy this problem, Lahiri (2006) [161] proposed a stabilised internal potential energy comprising of linear combinations of standard and averaged nodal element. With the new conservation-law formulation, the proposed methodology can be simulated without encountering any non-physical behaviours (or spurious energy modes); see Figure 10.28.

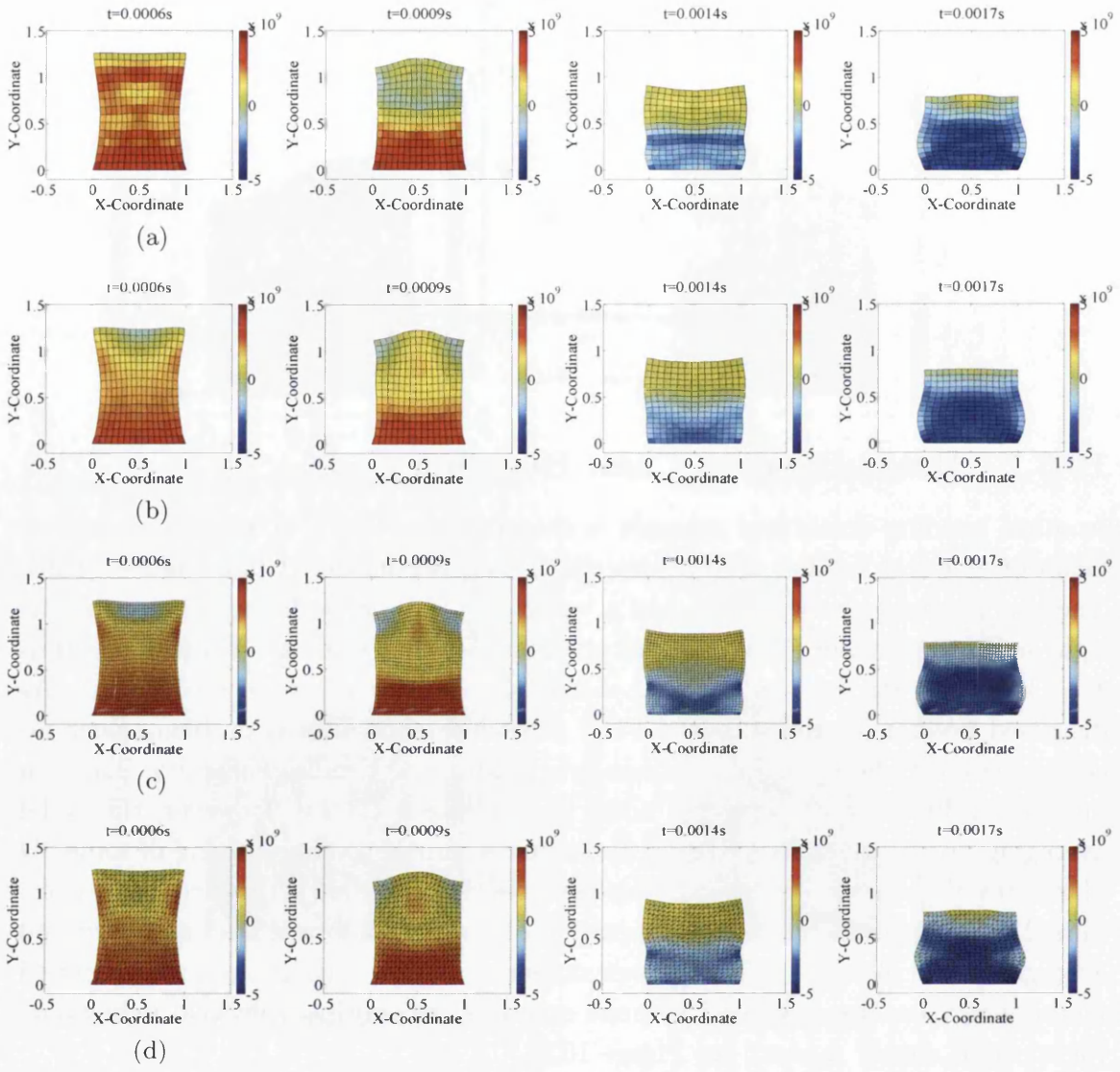

Figure 10.23: Tensile Test Case: Sequence of pressure distribution of deformed shapes using: (a) Standard FEM procedure (15×15); (b-c) Proposed methodology imposing a piecewise linear reconstruction with meshes of 15×15 and 30×30; and (d) Two-step Taylor-Galerkin technique (curl-projection and $\bar{\alpha} = 0.2$) with $20 \times 20 \times 2$. Initial tensile velocity $v_{\text{pull}} = 500\text{m/s}$ is applied. A steel plate is used and its material properties are such that Poisson's ratio $\nu = 0.3$, Young's modulus $E = 2.1 \times 10^{10}\text{Pa}$ and density $\rho_0 = 7 \times 10^3\text{kg/m}^3$. Time steps for various mesh sizes: $\Delta t|_{15\times15} = 1 \times 10^{-5}\text{s}$ and $\Delta t|_{30\times30\text{ or }20\times20\times2} = 5 \times 10^{-6}\text{s}$.

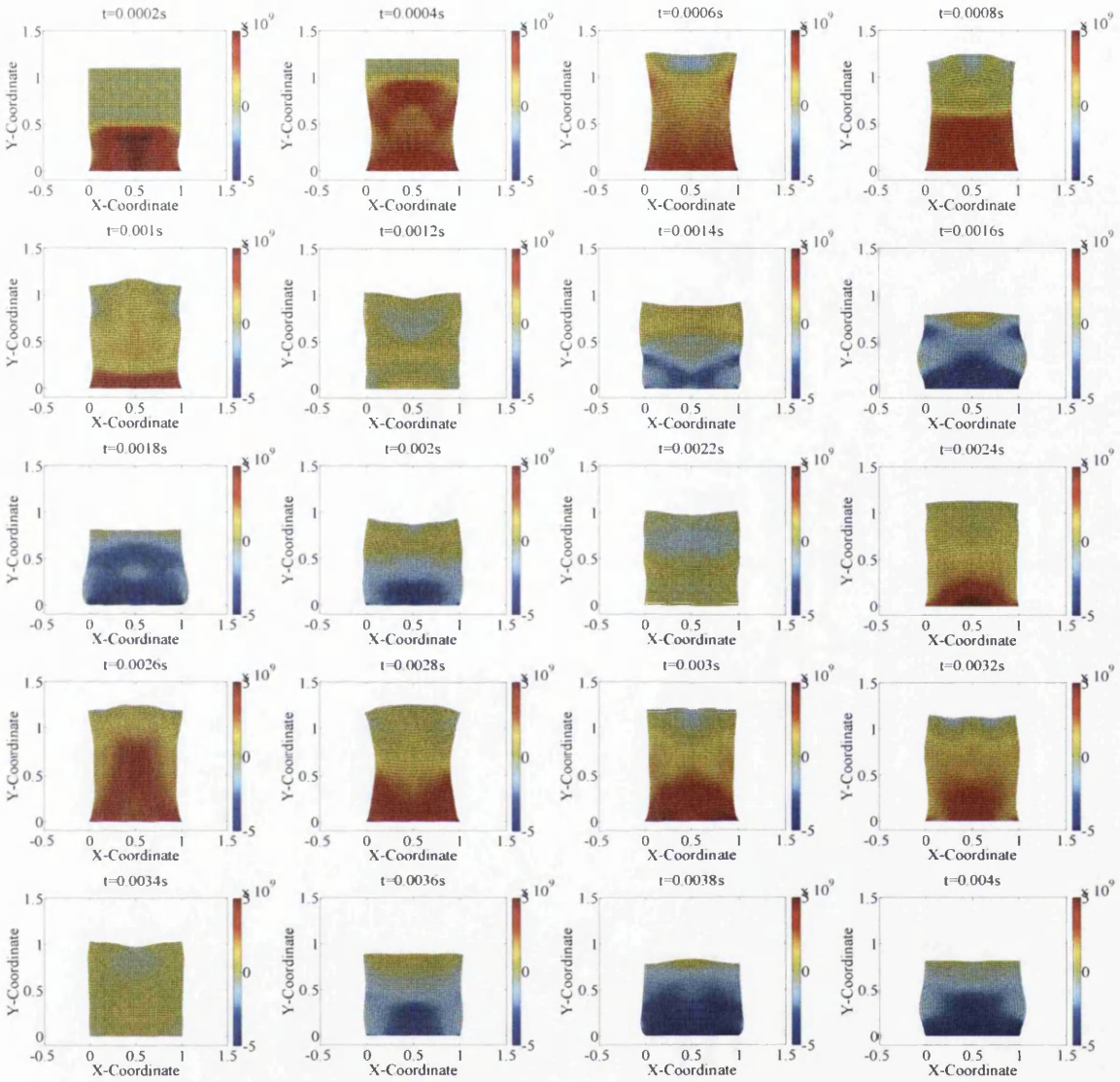

Figure 10.24: Tensile Test Case: Evolution of pressure distribution at different time instants. Results obtained based upon proposed methodology imposing a piecewise linear reconstruction with an initial vertical tensile velocity $v_{\text{pull}} = 500\,\text{m/s}$. A nearly incompressible Neo-Hookean (NH) constitutive model is used and its material properties are such that Poisson's ratio $\nu = 0.3$, Young's modulus $E = 2.1 \times 10^{10}\text{Pa}$ and density $\rho_0 = 7 \times 10^3 \text{kg/m}^3$. Discretisation of 40×40 cells per edge. Time step $\Delta t = 5 \times 10^{-6}\text{s}$.

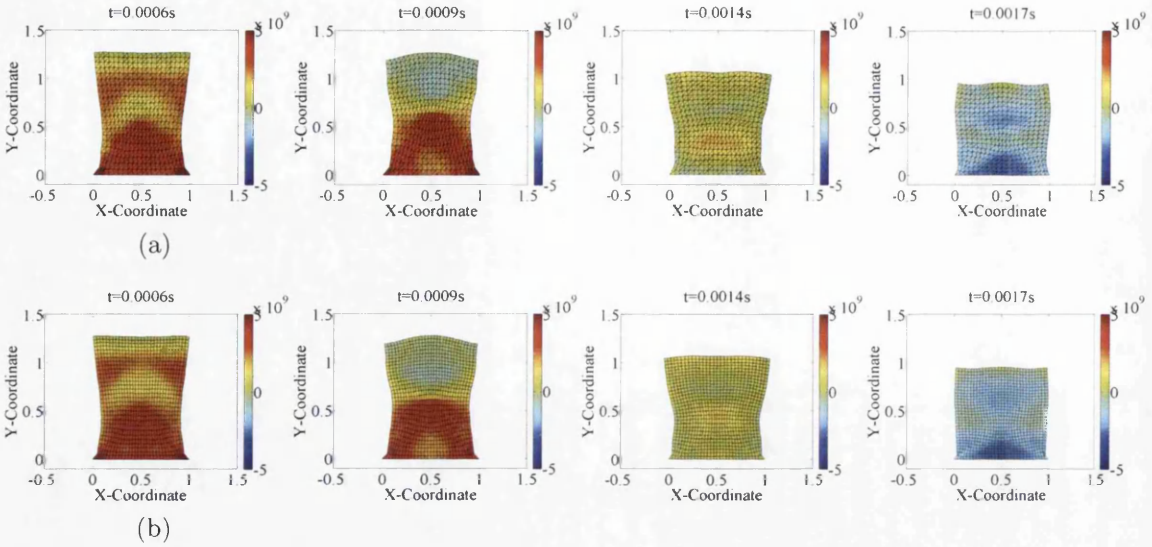

Figure 10.25: Tensile Test Case: Sequence of pressure distribution of deformed shapes with plasticity implemented using: (a) Two step Taylor-Galerkin technique (curl-projection, $\bar{\alpha} = 0.2$ and $20 \times 20 \times 2$); (b) Proposed methodology imposing a piecewise linear reconstruction with meshes of 30×30. Initial tensile velocity $v_{\text{pull}} = 500\text{m/s}$ is applied. The Von-Mises plasticity model is used such that Poisson's ratio $\nu = 0.3$, Young's modulus $E = 2.1 \times 10^{10}\text{Pa}$, density $\rho_0 = 7 \times 10^3\text{kg/m}^3$, yield stress $\bar{\tau}_y^0 = 5\text{GPa}$ and hardening modulus $H = 1\text{GPa}$. Same time step is used for two different approaches: $\Delta t = 5 \times 10^{-6}\text{s}$.

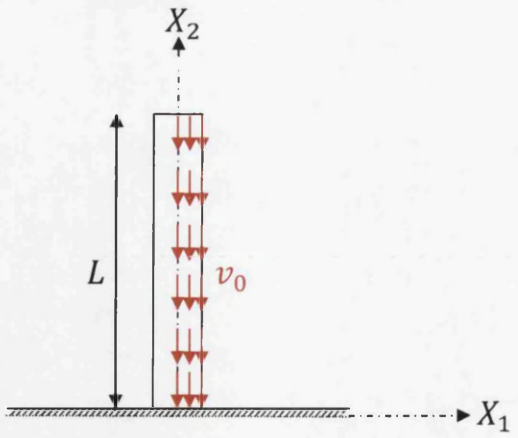

Figure 10.26: Beam buckling test case.

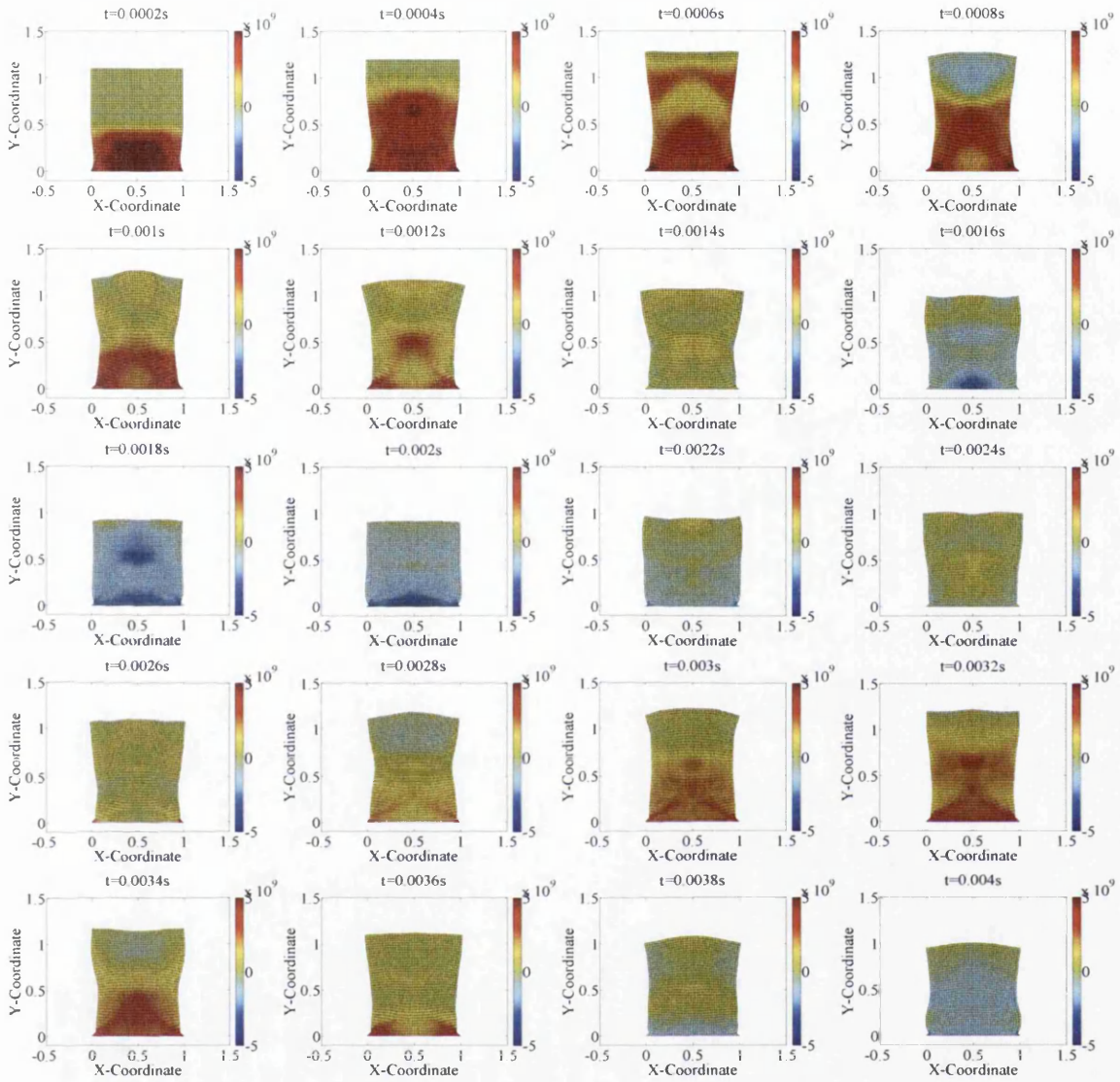

Figure 10.27: Tensile Test Case: Evolution of pressure distribution at different time instants. Results obtained based upon proposed methodology imposing a piecewise linear reconstruction with an initial vertical tensile velocity $v_{\text{pull}} = 500\,\text{m/s}$. The Von-Mises plasticity constitutive model is used and its material properties are such that Poisson's ratio $\nu = 0.3$, Young's modulus $E = 2.1 \times 10^{10}\text{Pa}$, density $\rho_0 = 7 \times 10^3\text{kg/m}^3$, yield stress $\bar{\tau}_y^0 = 5\text{GPa}$ and hardening modulus $H = 1\text{GPa}$. Discretisation of 40×40 cells per edge. Time step $\Delta t = 5 \times 10^{-6}\text{s}$.

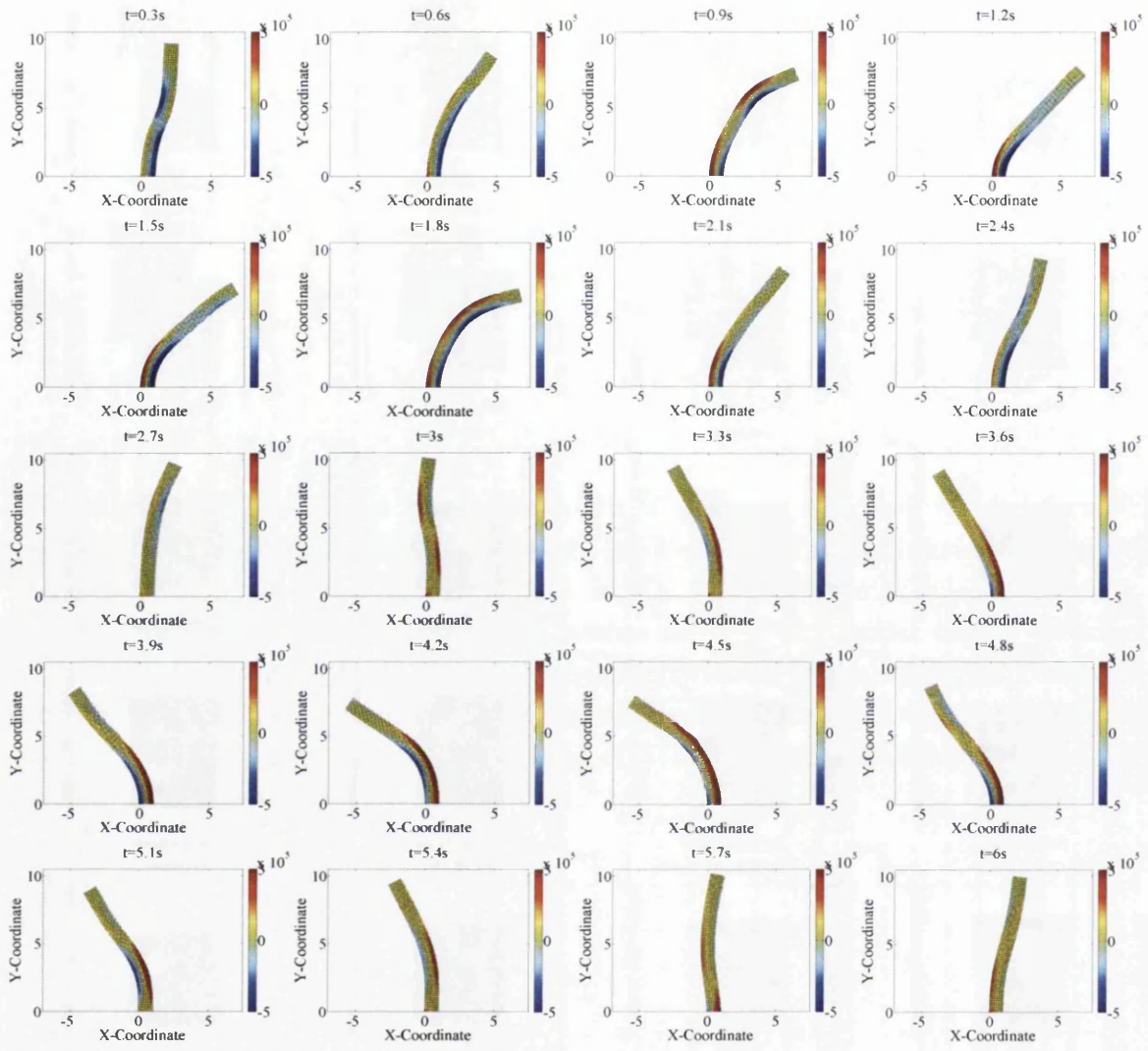

Figure 10.28: Beam Buckling: Evolution of pressure distribution at different time instants. Results obtained imposing a piecewise linear reconstruction with an initial vertical velocity, v_0, applied at right half of the beam. The nearly incompressible Neo-Hookean (NH) constitutive model is used and its material properties are such that Poisson's ratio $\nu = 0.35$, Young's modulus $E = 1.17 \times 10^7$Pa, density $\rho_0 = 1.1 \times 10^3$kg/m^3 and $\alpha_{CFL} \approx 0.5$. Discretisation of 6×60 cells per edge. Time step $\Delta t = 6 \times 10^{-4}$s.

Part V

Conclusions

Chapter 11

Concluding Remarks

"The engineer has been, and is, a maker of history".

James Kip Finch (1883 – 1967)

11.1 Conclusions

This thesis deals with the physical responses of structures with small and/or large deformations for nearly incompressible applications without bending and locking difficulties. For this purpose, a new mixed formulation based on a first order hyperbolic system of conservation laws has been developed and implemented in the context of cell centred finite volume method. The guideline to the overall organisation of this thesis is summarised on the following chart (See Figure 11.1).

11.1.1 The New Mixed Formulation

Solid dynamics explicit finite element codes are oftenly used for the simulation of finite (large) deformation dynamics problems by aerospace, automotive and military industries [162]. In these codes, the traditional solid dynamics formulation for displacement field is employed. This second-order dynamics equilibrium equation is discretised by standard Galerkin finite element procedure in conjunction with a family of classical Newmark time integration schemes.

Many practical applications of engineering interest involve the analysis of rubber hyperelastic behaviour, as well as elastoplastic simulations under the assumption of isochoric plastic flow (such as metal plasticity model [2, 6]). In such situations, spurious volumetric locking and overly stiff solutions are frequently encountered in standard Galerkin FEM with low-order elements, due to the fact that the low-order interpolation polynomials are unable to adequately represent the volume-preserving displacement field [80]. For this reason, a rich variety of different approaches have been proposed for low-order finite elements based on four-noded quadrilaterals (or eight-noded hexahedra). Among others, mixed u/p formulation, F-bar, B-bar, Enhanced Assummed Strain method (EAS) and Selective Reduced Integration scheme (SRI) are possible alternatives that allow the use of these elements near the incompressibility limit [6, 69–74, 76–79].

Unfortunately, some applications involving complex geometries are sometimes preferred to be meshed using triangles (or tetrahedra) [161]. The presence of large strains may lead to poorly shaped elements even for simple initial geometry. Mesh adaptation is then required but can only be achieved at a reasonable cost with simple triangular (or tetrahedra) element [160]. Efforts to develop locking-free tetrahedral elements based on simple averaging process that are effective in nearly incompressible and bending-dominated situations have only been partially successful. The resulting formulation suffers from artificial mechanisms similar to hourglassing [6, 22–24].

Another limitation of using linear elements in traditional displacement-based formulation is that it leads to second-order convergence for displacement field but one order less for strains and stresses [58, 59, 63, 64]. This is not sufficiently accurate for problems where stress analysis is of primary interest [163].

With the purpose of targeting these shortcomings, a new mixed solid dynam-

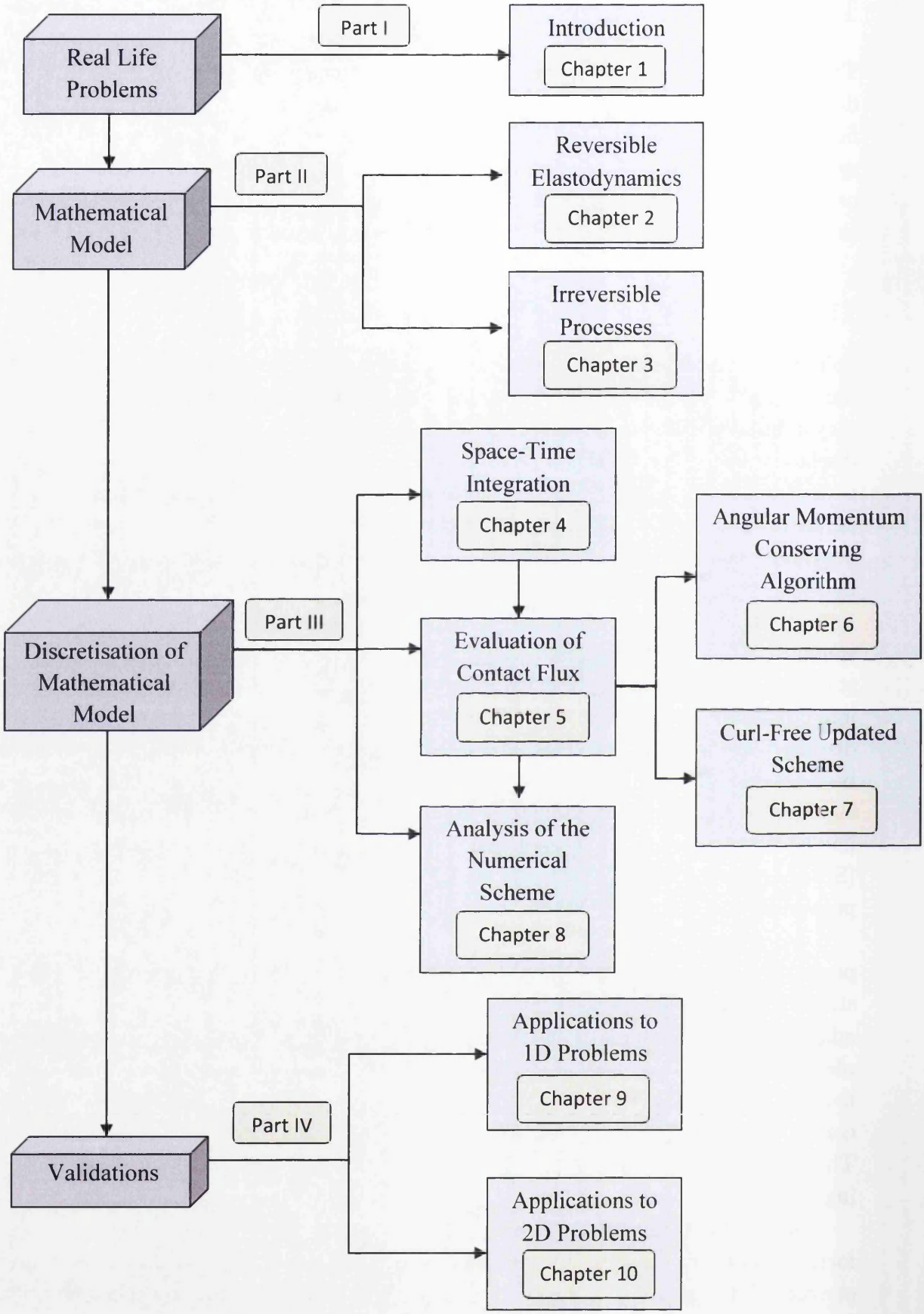

Figure 11.1: Structure and content of this thesis.

ics formulation as a first-order system of hyperbolic Partial Differential Equations (PDE) was proposed (a modification of that used in [117, 118]). The new formulation is derived from balance laws describing the conservation of linear momentum, deformation gradient and total energy, which consists of a set of thirteen conservation equations in three dimensions [58]. There are three equations for conservation of linear momentum, nine equations for deformation gradient and one equation for conservation of total energy. However, these equations involve twenty-three unknowns: linear momentum $\boldsymbol{p}$, deformation gradient $\boldsymbol{F}$, First Piola-Kirchhoff stress tensor $\boldsymbol{P}$, total energy E and temperature θ. In order to close the system, ten additional relationships among these unknowns must be specified. Two different types of constitutive equations are required to complete the system. The first type consists of constitutive laws that characterise the material [7]; for instance, the stress tensor is related to the deformation gradient by a kinetic equation of state for elastic material. Another type of constitutive equation (known as thermo-mechanical constitutive law) allows the stress to be dependent upon temperature with the aid of Laws of Thermodynamics [3].

More crucially, the curl-free constraint has to be fully satisfied by the evolution of deformation gradient [117]. If the constraint is satisfied initially, it will then be satisfied for all later times [104, 105]. An unphysical wave propagation property (spurious curl modes) arises without imposing this constraint properly, as it plays an essential role in analysis of the characteristic structure of the system [58].

The proposed formulation (a mixed linear momentum-deformation gradient-total energy) enables stresses to converge at the same rate as velocities and displacements [63, 64]. With this sort of framework, it is convenient to apply a state-of-the-art shock capturing technique for problems where discontinuities are present [26, 60, 84, 86, 87]. Such conservation-law formulation also permits the use of low-order elements without volumetric locking and bending difficulty [59, 63]. This will lead to a cheap and easy-to-implement code [69].

11.1.2 Computational Methodology

Some key conclusions can be summarised as follows:

- The proposed computational methodology is developed based on the philosophy of the Method of Lines (MOL). In the method of lines, the space and time discretisations of a Partial Differential Equations (PDE) are decoupled and analysed independently [98]. First, a spatial method is selected to discretise the differential equation in space and incorporates the suitable boundary conditions. An arbitrary time integrator is then used for integrating the semi-discrete equations in time.

- The dissipative effects of a numerical method are crucial for constructing reliable schemes of conservation laws [82, 83]. This is particularly important when the solution is discontinuous in the vicinity of sharp gradients. Making use of

a numerical scheme with appropriate dissipation helps building up the success of the numerical calculation.

- The projection-evolution approach for space discretisation is employed and consists of two key steps [84]: (1) a reconstruction (or projection) step where the data are approximated by polynomials within each cell; (2) upwind (or contact flux) step where the fluxes at each interface are evaluated by a procedure that takes into account the wave directions. In particular, the classical Godunov scheme (1959) [85] employs the simplest reconstruction; that is, the piecewise constant reconstruction. This classical scheme is only first-order accurate in space which then introduces a great deal of numerical diffusion into the solution [25]. Consequently, it is essential to enhance accuracy by using higher-order polynomials in the reconstruction step [26]. Accurate interpolations (i.e. linear and higher orders) are derived by assuming that the data are smooth [93]. These interpolations create unwanted oscillatory behaviours in the vicinity of shocks. To prevent such oscillations, it is vital to introduce a monotonicity constraint (also known as nonlinear slope limiter) into the scheme [86, 87].

- A family of Total Variation Diminishing (TVD) Runge-Kutta time integration explicit schemes is used to integrate the evolutionary system of equations. This type of temporal schemes shows a clear advantage over a family of non-TVD Runge-Kutta time integration schemes, where the latter can generate oscillations even for TVD spatial discretisation [88].

- The standard finite volume algorithm loses the desirable angular momentum conservation property (especially in the angular momentum dominated scenario) and thus induces energy dissipation under long-term response analysis [99–103]. One purpose of this thesis is to propose an algorithm that conserves the total angular momentum of a system, which requires a predictor-corrector strategy (incorporates the conservation of angular momentum as part of the space-time integrator).

- The new mixed hyperbolic system of equations has added complexity of possessing involutions, where the components of deformation gradient $\boldsymbol{F}$ must satisfy some compatibility conditions [117]. An involution is an additional equation that has to be satisfied for all time, provided that this equation is satisfied at some initial time [118] (inherent property of the evolution operator). Such involutions introduce difficulties into the development of any numerical scheme since discrete preservation properties are not easily established [104]. The numerical method that obeys involutions on a discrete level is designed so as to avoid spurious modes (curl errors) for long-term analysis [63].

- Mesh convergence analysis [60] has been performed on a sequence of mesh sizes for various numerical examples. This analysis measures the numerical

(i.e. pointwise and global) errors at a particular time and an optimal convergence $\mathcal{O}(h^{p+1})$ can be obtained where p denotes the polynomial orders. Finite volume schemes equipped with piecewise linear reconstruction (with and without limiters), in conjunction with TVD Runge-Kutta time stepping scheme, achieved second order accuracy in overall numerical scheme. Of course those schemes with limiters are expected to be less accurate since they introduce numerical dissipation into the solution.

- A series of numerical examples involving the analysis of infinitesimal (small) and/or finite (large) deformations for nearly incompressible rubber material and/or plastic-dominant deformations (isochoric plastic flow) were demonstrated. As expected, the locking behaviour was clearly observed in the standard FEM procedure. The locking-free responses obtained by proposed methodology compared extremely well with those of mean dilatation technique.

- Both the standard FEM procedure and mean dilatation technique produced spurious pressure modes (checkerboard) in the case of near incompressibility [114]. However, this can be eliminated by introducing of the new mixed conservation law formulation (high order of precision for stress variable).

- The proposed numerical algorithm provides a good balance between accuracy and speed of computation.

11.2 Recommendations for Further Research

Future research lines have been open-up after the developments presented in this thesis. A few directions are pointed out:

- **Non-Cartesian Geometries.** All physical domains presented are Cartesian by means of their boundaries been perfectly aligned with the Cartesian coordinate directions. Unfortunately, most domains are not Cartesian in practice. The well known approach for dealing with general domain is that of mapping the irregular domain in physical space to a regular domain in computational space [84, 145].

- **Extension to Triangular Mesh.** Some operations like curl-preserving updated scheme and discrete angular momentum conserving algorithm are generally applicable to any arbitrary (i.e. structured and unstructured) meshes in 2D problems. High order spatial discretisation (i.e. gradient operator and slope limiter) has to be modified for computational efficiency in 2D unstructured mesh, preferably Jameson-Schmidt-Turkel (JST) scheme.

- **Thermo-Mechanical Process.** Many applications in engineering and science have to consider irreversible process where thermal effects are of practical importance (see Appendix E). Realistic problems involving thermo-elastodynamic analysis are of great interest.

- **Complex Constitutive Models.** The consideration of viscoelastic model [4], as well as some other basic plasticity models[1] [6], could be implemented in source code library.

- **Vertex-Based Finite Volume Method** [27]. It should be noted that when a solid body undergoes deformation, the application of mechanical boundary conditions is best modelled if they can be assigned at physical boundary. For a cell centred approach, the displacements at boundary have to be projected from the nearest node of discretisation.

- **Mesh Adaptation Algorithm.** Lagrangian mesh often suffers from issues related to mesh tangling in cases of large deformations for dynamic simulations. Several types of mesh adaptive updates can be used to reduce mesh distortions: (a) h-adaptation which reduces the element size in a specified region to improve the solution accuracy [164]; (b) r-adaptation in which an initial mesh is modified by changing the position of nodes [165]; and (c) p-adaptation which increases the polynomial order of the shape function without changing the initial mesh configuration [166]. Special care has to be exercised since such updates introduce advection error to the solution [160].

- **Parallelisation.** The use of parallel algorithm is becoming increasingly vital for large-scale analysis due to the requirement of large memory size and computational time.

[1] Other plasticity models: (1) Tresca model; (2) Mohr-Coulomb model; and (3) Drucker-Prager model.

Part VI

Appendices

Appendix A

Vector and Tensor Algebra

A.1 Introductory Remarks

This appendix reviews some fundamentals of linear algebra which are extensively employed in this thesis. The use of a Cartesian coordinate system is sufficient for applications considered. A more in-depth explanation can be found in [6, 7, 13, 119, 121, 167–169].

A.2 Vectors

Let $\mathscr{E}$ be an n-dimensional Euclidean space and $\mathscr{U}$ be the space of n-dimensional vectors associated with $\mathscr{E}$. A set of vectors $\{\boldsymbol{u}, \boldsymbol{v}, \boldsymbol{w}\} \in \mathscr{U}$ will be used in the following section.

A.2.1 Inner Product, Norm and Orthogonality

Inner product of two arbitrary vectors is defined by

$$\boldsymbol{u} \cdot \boldsymbol{v}. \tag{A.1}$$

Let

$$\|\boldsymbol{u}\| = \sqrt{\boldsymbol{u} \cdot \boldsymbol{u}}. \tag{A.2}$$

describes the Euclidean norm of a vector $\boldsymbol{u}$ and $\boldsymbol{u}$ is said to be a unit vector if

$$\|\boldsymbol{u}\| = 1. \tag{A.3}$$

A vector $\boldsymbol{u}$ is said to be orthogonal with respect to a vector $\boldsymbol{v}$ if

$$\boldsymbol{u} \cdot \boldsymbol{v} = 0. \tag{A.4}$$

A.3 Second Order Tensors

Any second order tensor is a linear transformation from $\mathscr{U}$ into $\mathscr{U}$; that is, $\boldsymbol{L} : \mathscr{U} \longrightarrow \mathscr{U}$. It maps a vector $\boldsymbol{u}$ into another vector $\boldsymbol{v}$ such as

$$\boldsymbol{v} = \boldsymbol{L}\boldsymbol{u}. \tag{A.5}$$

In particular,

$$\mathbf{0}\boldsymbol{u} = \mathbf{0}; \qquad \boldsymbol{I}\boldsymbol{u} = \boldsymbol{u}, \tag{A.6}$$

where $\mathbf{0}$ represents the zero tensor and $\boldsymbol{I}$ denotes the identity tensor.

A.3.1 Symmetric and Skew Tensors

An arbitrary second order tensor $\boldsymbol{L}$ can be conveniently decomposed into

$$\boldsymbol{L} = \text{sym}(\boldsymbol{L}) + \text{skew}(\boldsymbol{L}). \tag{A.7}$$

Their symmetric and skew parts are denoted as

$$\text{sym}(\boldsymbol{L}) = \frac{1}{2}(\boldsymbol{L} + \boldsymbol{L}^T); \qquad \text{skew}(\boldsymbol{L}) = \frac{1}{2}(\boldsymbol{L} - \boldsymbol{L}^T). \tag{A.8}$$

A.3.2 Tensor Product

The tensor product of two vectors $\boldsymbol{u}$ and $\boldsymbol{v}$ is dictated by $\boldsymbol{u} \otimes \boldsymbol{v}$. Such resulting product maps an arbitrary vector $\boldsymbol{w}$ into the vector $(\boldsymbol{w} \cdot \boldsymbol{v})\boldsymbol{u}$:

$$(\boldsymbol{u} \otimes \boldsymbol{v})\boldsymbol{w} = (\boldsymbol{w} \cdot \boldsymbol{v})\boldsymbol{u}. \tag{A.9}$$

This is also known as a dyadic process.

A.3.3 Trace, Inner Product and Euclidean Norm

The trace of the tensor $(\boldsymbol{u} \otimes \boldsymbol{v})$ is a linear map defined by

$$\text{tr}(\boldsymbol{u} \otimes \boldsymbol{v}) = \boldsymbol{u} \cdot \boldsymbol{v}. \tag{A.10}$$

For a generic tensor $\boldsymbol{L}$, its trace is the summation of the diagonal terms of its matrix representation, that is

$$\text{tr}\boldsymbol{L} = \sum_{i=1}^{3} L_{ii}. \tag{A.11}$$

The inner product of two tensors, $\boldsymbol{T}\colon \boldsymbol{L}$, is described as

$$\boldsymbol{T}\colon \boldsymbol{L} = \text{tr}(\boldsymbol{T}^T\boldsymbol{L}) = \text{tr}(\boldsymbol{T}\boldsymbol{L}^T) = \sum_{i,j=1}^{3} T_{ij}L_{ij}. \tag{A.12}$$

Euclidean norm of a tensor $\boldsymbol{L}$ is then dictated by

$$\|\boldsymbol{L}\| = \sqrt{\boldsymbol{L}\colon \boldsymbol{L}} = \left(\sum_{i,j=1}^{3} L_{ij}^2\right)^{1/2}. \tag{A.13}$$

A.3.4 Invariants

In general, the Cartesian components of vectors and second order tensors will vary when the axes are rotated. However, certain intrinsic magnitudes associated with them will remain invariant under such transformations. The first of these magnitudes, $I_{\boldsymbol{L}}$, is given by

$$I_{\boldsymbol{L}} = \text{tr}(\boldsymbol{L}) = \sum_{i=1}^{3} L_{ii}. \tag{A.14}$$

Analogous to the scalar product of vectors, the second independent invariant for any second-order tensor $\boldsymbol{L}$ can be defined as

$$II_{\boldsymbol{L}} = \boldsymbol{L} : \boldsymbol{L} = \sum_{i,j=1}^{3} L_{ij}^2. \tag{A.15}$$

The last invariant is provided by its determinant represented by

$$III_{\boldsymbol{L}} = \det(\boldsymbol{L}). \tag{A.16}$$

A.3.5 Spectral Decomposition

Given a tensor $\boldsymbol{L}$, a non-zero vector $\boldsymbol{n}$ is said to be an eigenvector of $\boldsymbol{L}$ associated with the eigenvalue ω if

$$\boldsymbol{L}\boldsymbol{n} = \omega \boldsymbol{n}. \tag{A.17}$$

The expression above represents the characteristic space of $\boldsymbol{L}$ corresponding to ω and the following properties hold:

1. The eigenvalues of a positive definite tensor are strictly positive.
2. The characteristic spaces of a symmetric tensor are mutually orthogonal.

Let $\boldsymbol{L}$ be a symmetric tensor, then admits the representation of

$$\boldsymbol{L} = \sum_{\alpha=1}^{3} \omega_\alpha \, \boldsymbol{n}_\alpha \otimes \boldsymbol{n}_\alpha. \tag{A.18}$$

Here, $\{\boldsymbol{n}_1, \boldsymbol{n}_2, \boldsymbol{n}_3\}$ are eigenvectors of $\boldsymbol{L}$, which can also be used as an alternative Cartesian base. $\{\omega_1, \omega_2, \omega_3\}$ denote the set of corresponding eigenvalues. The above expression is called the spectral decomposition of $\boldsymbol{L}$.

A.4 Isotropic Tensors

A tensor is said to be isotropic if its components are invariant under an orthogonal change of basis (or rotation).

A.4.1 Isotropic Second Order Tensors

A second order tensor $\boldsymbol{L}$ is isotropic if

$$\boldsymbol{L} = \boldsymbol{R}^T \boldsymbol{L} \boldsymbol{R}; \qquad L_{ij} = R_{mi} R_{nj} L_{mn} \tag{A.19}$$

for any rotation tensor $\boldsymbol{R}$. Spherical tensors, $\alpha \boldsymbol{I}$, with any scalar α are the only second order isotropic tensors.

A.4.2 Isotropic Fourth Order Tensors

A fourth-order tensor, $\boldsymbol{\mathcal{L}}$, is isotropic if

$$\mathcal{L}_{ijkl} = R_{mi}R_{nj}R_{ok}R_{pl}\mathcal{L}_{mnop} \tag{A.20}$$

for any rotation $\boldsymbol{R}$. Any isotropic fourth-order tensor, $\boldsymbol{\mathcal{C}}$, can be represented as a linear combination of three basic isotropic tensors:

$$\boldsymbol{\mathcal{C}} = \alpha\boldsymbol{\mathcal{I}} + \beta\hat{\boldsymbol{\mathcal{I}}} + \gamma(\boldsymbol{I}\otimes\boldsymbol{I}), \tag{A.21}$$

where α, β and γ are scalars. These three isotropic tensors are described as follows. The fourth-order identity tensor, $\boldsymbol{\mathcal{I}}$, is given by

$$\mathcal{I}_{ijkl} = \delta_{ik}\delta_{jl}. \tag{A.22}$$

For any second-order tensor $\boldsymbol{L}$, the fourth-order identity tensor satisfies

$$\boldsymbol{\mathcal{I}}\colon\boldsymbol{L} = \boldsymbol{L}\colon\boldsymbol{\mathcal{I}} = \boldsymbol{L}. \tag{A.23}$$

Furthermore, this tensor gives

$$\boldsymbol{\mathcal{I}}\colon\boldsymbol{\mathcal{L}} = \boldsymbol{\mathcal{L}}\colon\boldsymbol{\mathcal{I}} = \boldsymbol{\mathcal{L}}, \tag{A.24}$$

for any fourth-order tensor $\boldsymbol{\mathcal{L}}$. The tensor $\hat{\boldsymbol{\mathcal{I}}}$ is the transposition tensor which maps any second-order tensor $\boldsymbol{L}$ onto its transpose:

$$\hat{\boldsymbol{\mathcal{I}}}\colon\boldsymbol{L} = \boldsymbol{L}\colon\hat{\boldsymbol{\mathcal{I}}} = \boldsymbol{L}^T; \qquad \hat{\mathcal{I}}_{ijkl} = \delta_{il}\delta_{jk}. \tag{A.25}$$

Multiplying any tensor $\boldsymbol{L}$ with $(\boldsymbol{I}\otimes\boldsymbol{I})$ yields

$$(\boldsymbol{I}\otimes\boldsymbol{I})\colon\boldsymbol{L} = (\mathrm{tr}\boldsymbol{L})\boldsymbol{I}. \tag{A.26}$$

Another important isotropic tensor (symmetric projection or symmetric identity) that frequently used in continuum mechanics is defined by

$$\boldsymbol{\mathcal{S}}\colon\boldsymbol{L} = \boldsymbol{L}\colon\boldsymbol{\mathcal{S}} = \mathrm{sym}(\boldsymbol{L}), \tag{A.27}$$

where $\boldsymbol{\mathcal{S}} = (\boldsymbol{\mathcal{I}} + \hat{\boldsymbol{\mathcal{I}}})/2$.

Appendix B

Fundamentals of Nonlinear Continuum Mechanics

B.1 Introductory Remarks

This appendix summarises some kinematic aspects regarding the deformation for a continuous medium without considering the applied loads and the constitutive behaviour of the material. See [1,3,6,7,13,15,89,115,121,170] for detailed explanation on this subject.

B.2 Motion

Let $\mathscr{B}$ be a body which occupies an open region V of the three-dimensional Euclidean space $\mathscr{E}$ with a boundary ∂V in its reference configuration. The motion (or time-dependent deformation) of a continuum body $\mathscr{B}$ is defined by a mapping from a reference or material volume V to a current or spatial volume $v(t)$ as

$$\phi : V \times \mathbb{R}^+ \longrightarrow v(t) \quad \text{in} \quad \mathscr{E}. \tag{B.1}$$

For each time t, the mapping function, $\phi(\cdot, t)$, is a deformation of $\mathscr{B}$. Material domain, $V \subset \mathbb{R}^{n_{sd}}$, consists of material particles $\boldsymbol{X}$, whereas the spatial domain is made up of spatial points $\boldsymbol{x}$, $v(t) \subset \mathbb{R}^{n_{sd}}$. Here, n_{sd} denotes spatial dimensions.

B.3 The Deformation Gradient

The deformation gradient tensor is defined by

$$\boldsymbol{F}(\boldsymbol{X}, t) = \frac{\partial \phi(\boldsymbol{X}, t)}{\partial \boldsymbol{X}} = \frac{\partial \boldsymbol{x}}{\partial \boldsymbol{X}}. \tag{B.2}$$

This can be conveniently decomposed into a purely volumetric deformation followed by a deviatoric (or isochoric) deformation or vice-versa:

$$\boldsymbol{F} = \boldsymbol{F}_{dev}\boldsymbol{F}_{vol} = \boldsymbol{F}_{vol}\boldsymbol{F}_{dev}, \tag{B.3}$$

where the deviatoric and volumetric components are, respectively, described as

$$\boldsymbol{F}_{dev} = (\det \boldsymbol{F})^{-\frac{1}{3}}\boldsymbol{F}; \qquad \boldsymbol{F}_{vol} = (\det \boldsymbol{F})^{\frac{1}{3}}\boldsymbol{I}. \tag{B.4}$$

B.3.1 Volume Changes

The Jacobian J relates the volume element in both reference and current configurations. For this reason, consider an infinitesimal volume element in material configuration with all edges parallel to Cartesian axes such as $d\boldsymbol{X}_1 = dX_1\boldsymbol{E}_1$, $d\boldsymbol{X}_2 = dX_2\boldsymbol{E}_2$ and $d\boldsymbol{X}_3 = dX_3\boldsymbol{E}_3$, where $\{\boldsymbol{E}_1, \boldsymbol{E}_2, \boldsymbol{E}_3\}$ is a set of orthonormal vectors. The elemental material volume dV is clearly given as $dV = (d\boldsymbol{X}_1 \times d\boldsymbol{X}_2) \cdot d\boldsymbol{X}_3$.[1] To obtain the

[1] In mathematics, the scalar triple product of three vectors represents the volume of the parallelepiped defined by these three vectors.

corresponding deformed volume, dv, material vectors have to undergo push forward operation such as $dv = (\boldsymbol{F}d\boldsymbol{X}_1 \times \boldsymbol{F}d\boldsymbol{X}_2) \cdot \boldsymbol{F}d\boldsymbol{X}_3$, which concludes that

$$dv = JdV; \qquad J = \det\boldsymbol{F}. \tag{B.5}$$

B.3.2 Polar Decomposition

Polar decomposition of the deformation gradient is of the form

$$\boldsymbol{F} = \boldsymbol{R}\boldsymbol{U} = \boldsymbol{V}\boldsymbol{R},^{2} \tag{B.6}$$

where $\boldsymbol{U}$ and $\boldsymbol{V}$ denote the right and left stretch tensors. $\boldsymbol{R}$ describes the local rotation tensor[3]. From equation above, the right and left stretch tensors are related as

$$\boldsymbol{V} = \boldsymbol{R}\boldsymbol{U}\boldsymbol{R}^{T}. \tag{B.7}$$

Alternatively, $\boldsymbol{U}$ and $\boldsymbol{V}$ can also be expressed as

$$\boldsymbol{U} = \sqrt{\boldsymbol{C}}, \quad \boldsymbol{V} = \sqrt{\boldsymbol{b}}. \tag{B.8}$$

where $\boldsymbol{C}$ and $\boldsymbol{b}$ are the right and left Cauchy-Green strain tensors.

Spectral Decomposition of the Stretch Tensors

Since $\boldsymbol{U}$ and $\boldsymbol{V}$ are symmetric tensors, they follow from the spectral theorem that

$$\boldsymbol{U} = \sum_{\alpha=1}^{3} \lambda_\alpha \boldsymbol{N}_\alpha \otimes \boldsymbol{N}_\alpha, \quad \boldsymbol{V} = \sum_{\alpha=1}^{3} \bar{\lambda}_\alpha \boldsymbol{n}_\alpha \otimes \boldsymbol{n}_\alpha. \tag{B.9}$$

Note that $\{\lambda_1, \lambda_2, \lambda_3\}$ and $\{\bar{\lambda}_1, \bar{\lambda}_2, \bar{\lambda}_3\}$ are the principal stretches of $\boldsymbol{U}$ and $\boldsymbol{V}$. $\boldsymbol{N}_\alpha$ and $\boldsymbol{n}_\alpha$ are represented as the Lagrangian and Eulerian principal directions. By substituting (B.9) into (B.7), some interesting relationships can be derived:

$$\lambda_\alpha = \bar{\lambda}_\alpha, \quad \boldsymbol{n}_\alpha = \boldsymbol{R}\boldsymbol{N}_\alpha \quad \forall\alpha = 1, 2, 3. \tag{B.10}$$

This expression implies that the two point tensor, $\boldsymbol{R}$, rotates the material vector triad $\{\boldsymbol{N}_1, \boldsymbol{N}_2, \boldsymbol{N}_3\}$ into the corresponding set of spatial vector triad $\{\boldsymbol{n}_1, \boldsymbol{n}_2, \boldsymbol{n}_3\}$.

B.4 Strain Measures

As discussed previously, pure rotation within an infinitesimal neighbourhood of a material particle $\boldsymbol{X}$ can be distinguished from pure stretching by means of polar decomposition. Strain measures have to be performed under stretching. In general, the Green-Lagrange strain tensor is defined by

[2] $\boldsymbol{U}$ and $\boldsymbol{V}$ are symmetric positive definite tensors.

[3] Determinant of the rotation tensor $\boldsymbol{R}$ must be equal to 1.

$$\boldsymbol{E}^{(2)} = \frac{1}{2}(\boldsymbol{C} - \boldsymbol{I}) = \frac{1}{2}\left(\boldsymbol{H} + \boldsymbol{H}^T + \boldsymbol{H}^T\boldsymbol{H}\right); \qquad \boldsymbol{F} = \boldsymbol{I} + \boldsymbol{H}. \tag{B.11}$$

Here, $\boldsymbol{C}$ is the right Cauchy-Green tensor and the meaning of the superscript on $\boldsymbol{E}^{(2)}$ will become clearer below. If no straining occurs, that is $\boldsymbol{H} = \boldsymbol{0}$, the expression above thus implies that $\boldsymbol{E}^{(2)} = \boldsymbol{0}$ (or $\boldsymbol{C} = \boldsymbol{I}$).

With the aid of spectral decomposition theorem, $\boldsymbol{E}^{(2)}$ can be re-expressed as

$$\boldsymbol{E}^{(2)} = \sum_{\alpha=1}^{3} \frac{1}{2}(\lambda_\alpha^2 - 1)\boldsymbol{N}_\alpha \otimes \boldsymbol{N}_\alpha, \tag{B.12}$$

by using

$$\boldsymbol{C} = \boldsymbol{U}^2 = \sum_{\alpha=1}^{3} \lambda_\alpha^2 \boldsymbol{N}_\alpha \otimes \boldsymbol{N}_\alpha. \tag{B.13}$$

Note that if the set of principal stretches $\{\lambda_1, \lambda_2, \lambda_3\}$ is of particular interest, it is considerably easy to obtain by taking a square root of the eigenvalues of $\boldsymbol{C}$.

B.4.1 Family of Strain Measures

An important family of material strain tensors is defined as

$$\boldsymbol{E}^{(m)} = \begin{cases} \frac{1}{m}(\boldsymbol{U}^m - \boldsymbol{I}) & m \neq 0 \\ \ln(\boldsymbol{U}) & m = 0 \end{cases} \tag{B.14}$$

where $m \in \mathbb{R}$. Equivalently, the equation above can be re-expressed in terms of principle values by

$$\boldsymbol{E}^{(m)} = \sum_{\alpha=1}^{3} \mathcal{G}(\lambda_\alpha)\boldsymbol{N}_\alpha \otimes \boldsymbol{N}_\alpha, \tag{B.15}$$

where

$$\mathcal{G}(\lambda_\alpha) = \begin{cases} \frac{1}{m}(\lambda_\alpha^m - 1) & m \neq 0 \\ \ln\lambda_\alpha & m = 0 \end{cases} \tag{B.16}$$

Analogously, the family of Eulerian strain measures is represented as

$$\boldsymbol{e}^{(m)} = \begin{cases} \frac{1}{m}(\boldsymbol{I} - \boldsymbol{V}^{-m}) & m \neq 0 \\ \ln(\boldsymbol{V}) & m = 0 \end{cases} \tag{B.17}$$

or, alternatively

$$\boldsymbol{e}^{(m)} = \sum_{\alpha=1}^{3} \mathcal{H}(\lambda_\alpha)\boldsymbol{n}_\alpha \otimes \boldsymbol{n}_\alpha; \qquad \mathcal{H}(\lambda_\alpha) = \begin{cases} \frac{1}{m}(1 - \lambda_\alpha^{-m}) & m \neq 0 \\ \ln\lambda_\alpha & m = 0 \end{cases} \tag{B.18}$$

Consequently, the Lagrangian and Eulerian strain tensors are related by

$$\boldsymbol{e}^{(-m)} = \boldsymbol{R}\boldsymbol{E}^{(m)}\boldsymbol{R}^T. \tag{B.19}$$

Commonly used strain measures are Green-Lagrange ($m = 2$), Biot ($m = 1$) and Hencky ($m = 0$) tensors.

B.5 Directional Derivative

To introduce the infinitesimal kinematic descriptions in small strain regime, it is essential to linearise some of the nonlinear kinematic magnitudes described above. The directional derivative concept is introduced for that purpose [6, 7].

Consider a small displacement $\boldsymbol{u}(\boldsymbol{x},t)$ imposed in the spatial configuration $\boldsymbol{x} = \boldsymbol{\phi}(\boldsymbol{X},t)$. With the the aid of $D\boldsymbol{F}[\boldsymbol{u}] = \boldsymbol{\nabla}_0\boldsymbol{u} = (\boldsymbol{\nabla}_{\boldsymbol{x}}\boldsymbol{u})\,\boldsymbol{F}$ [4], the right and left Cauchy-Green deformation tensors can then be linearised in the direction of $\boldsymbol{u}(\boldsymbol{x},t)$:

$$
\begin{aligned}
D\boldsymbol{C}[\boldsymbol{u}] &= \boldsymbol{F}^T D\boldsymbol{F}[\boldsymbol{u}] + D\boldsymbol{F}^T[\boldsymbol{u}]\,\boldsymbol{F} && \text{(B.21a)}\\
&= \boldsymbol{F}^T\left[\boldsymbol{\nabla}_{\boldsymbol{x}}\boldsymbol{u} + (\boldsymbol{\nabla}_{\boldsymbol{x}}\boldsymbol{u})^T\right]\boldsymbol{F} && \text{(B.21b)}\\
&= 2\boldsymbol{F}^T\left[\frac{1}{2}\left(\boldsymbol{\nabla}_{\boldsymbol{x}}\boldsymbol{u} + (\boldsymbol{\nabla}_{\boldsymbol{x}}\boldsymbol{u})^T\right)\right]\boldsymbol{F} && \text{(B.21c)}\\
&= 2\boldsymbol{F}^T\boldsymbol{\varepsilon}\boldsymbol{F} && \text{(B.21d)}
\end{aligned}
$$

and

$$
\begin{aligned}
D\boldsymbol{b}[\boldsymbol{u}] &= \boldsymbol{F}D\boldsymbol{F}^T[\boldsymbol{u}] + D\boldsymbol{F}[\boldsymbol{u}]\,\boldsymbol{F}^T && \text{(B.22a)}\\
&= \boldsymbol{F}\boldsymbol{F}^T(\boldsymbol{\nabla}_{\boldsymbol{x}}\boldsymbol{u})^T + (\boldsymbol{\nabla}_{\boldsymbol{x}}\boldsymbol{u})\,\boldsymbol{F}\boldsymbol{F}^T && \text{(B.22b)}\\
&= \boldsymbol{b}(\boldsymbol{\nabla}_{\boldsymbol{x}}\boldsymbol{u})^T + (\boldsymbol{\nabla}_{\boldsymbol{x}}\boldsymbol{u})\,\boldsymbol{b} && \text{(B.22c)}
\end{aligned}
$$

respectively. Note that the term inside [ ], viz. (B.21c), is known as small strain tensor $\boldsymbol{\varepsilon}$. Making use of (B.21d), the Green-Lagrange strain tensor (B.11) can be linearised as follows:

$$
\begin{aligned}
D\boldsymbol{E}^{(2)}[\boldsymbol{u}] &= \frac{1}{2}D\boldsymbol{C}[\boldsymbol{u}] && \text{(B.23a)}\\
&= \boldsymbol{F}^T\boldsymbol{\varepsilon}\boldsymbol{F}. && \text{(B.23b)}
\end{aligned}
$$

Similarly , the linearised Eulerian-Almansi finite strain tensor $\boldsymbol{e}^{(2)}$ can be expressed

[4] Show that $D\boldsymbol{F}[\boldsymbol{u}] = \boldsymbol{\nabla}_0\boldsymbol{u} = (\boldsymbol{\nabla}_{\boldsymbol{x}}\boldsymbol{u})\,\boldsymbol{F}$:

$$
\begin{aligned}
D\boldsymbol{F}(\boldsymbol{\phi}(\boldsymbol{X},t))[\boldsymbol{u}(\boldsymbol{x})] &= \frac{d}{d\varepsilon}\Big|_{\varepsilon=0}\frac{\partial(\boldsymbol{\phi}(\boldsymbol{X},t)+\varepsilon\boldsymbol{u})}{\partial\boldsymbol{X}} && \text{(B.20a)}\\
&= \frac{\partial\boldsymbol{u}(\boldsymbol{x})}{\partial\boldsymbol{X}} && \text{(B.20b)}\\
&= \boldsymbol{\nabla}_0\boldsymbol{u} && \text{(B.20c)}\\
&= (\boldsymbol{\nabla}_{\boldsymbol{x}}\boldsymbol{u})\,\boldsymbol{F}. && \text{(B.20d)}
\end{aligned}
$$

Note that $\boldsymbol{\nabla}_0$ indicates the material gradient with respect to undeformed space whereas, $\boldsymbol{\nabla}_{\boldsymbol{x}}$ denotes spatial gradient in deformed space.

as

$$D\boldsymbol{e}^{(2)}[\boldsymbol{u}] = -\frac{1}{2} D\boldsymbol{b}^{-1}[\boldsymbol{u}] \tag{B.24a}$$

$$= \frac{1}{2}\left[\boldsymbol{b}^{-1} D\boldsymbol{b}[\boldsymbol{u}]\, \boldsymbol{b}^{-1}\right] \tag{B.24b}$$

$$= \frac{1}{2}\left[\boldsymbol{b}^{-1}(\nabla_{\boldsymbol{x}}\boldsymbol{u}) + (\nabla_{\boldsymbol{x}}\boldsymbol{u})^T \boldsymbol{b}^{-1}\right]. \tag{B.24c}$$

In the case of linear elasticity, the linearisations of $\boldsymbol{E}^{(2)}$ and $\boldsymbol{e}^{(2)}$ should be performed at initial material configuration ($\boldsymbol{F} = \boldsymbol{I}$) and hence

$$D\boldsymbol{E}_0^{(2)}[\boldsymbol{u}] = D\boldsymbol{e}_0^{(2)}[\boldsymbol{u}] = \boldsymbol{\varepsilon}. \tag{B.25}$$

Indeed, the general expression for a family of linearised strain tensors is denoted as

$$D\boldsymbol{E}_0^{(m)}[\boldsymbol{u}] = D\boldsymbol{e}_0^{(m)}[\boldsymbol{u}] = \boldsymbol{\varepsilon}. \tag{B.26}$$

Appendix C

Notions of Hyperbolic System of Differential Equations

C.1 Introductory Remarks

Some elementary properties of the class of one-dimensional hyperbolic Partial Differential Equations (PDEs) are summarised in this section. The selected aspects are those thought to be essential for the development of the numerical procedure presented in the main body of the thesis. Section C.2 introduces a general representation of conservation laws. In order to study its eigenstructure, it is then necessary to obtain the Jacobian matrix $\boldsymbol{\mathcal{A}}_1$ (see Section C.3). In addition, characteristic theory is of paramount importance in hyperbolic system of equations. Section C.4 briefly explains the diagonalisation and characteristic variable in a general Initial Value Problem (IVP). Riemann problem, which is simply a given equation together with a special initial data, is further explored in Section C.5.

C.2 Conservation-Law

Conservation-law is a system of partial differential equations, which can be written as

$$\frac{\partial \boldsymbol{\mathcal{U}}}{\partial t} + \frac{\partial \boldsymbol{\mathcal{F}}_1}{\partial X} = \mathbf{0}, \tag{C.1}$$

where

$$\boldsymbol{\mathcal{U}} = \begin{pmatrix} u_1 \\ u_2 \\ \vdots \\ u_m \end{pmatrix}, \qquad \boldsymbol{\mathcal{F}}_1(\boldsymbol{\mathcal{U}}) = \begin{pmatrix} f_1 \\ f_2 \\ \vdots \\ f_m \end{pmatrix}. \tag{C.2}$$

Here, $\boldsymbol{\mathcal{U}}$ is defined as a vector of conserved (or problem) variable and $\boldsymbol{\mathcal{F}}_1 \equiv \boldsymbol{\mathcal{F}}_1(\boldsymbol{\mathcal{U}})$ describes the vector of conservative flux, in which each of the component f_α is a function of the components of $\boldsymbol{\mathcal{U}}$.

C.3 Quasi-Linear Equation

This section studies a system of first order partial differential equations in the form of

$$\frac{\partial u_\alpha}{\partial t} + \sum_{\beta=1}^{m} a_{\alpha\beta}(X, t, u_1, \ldots, u_m)\frac{\partial u_\beta}{\partial X} = s_\alpha(X, t, u_1, \ldots, u_m), \qquad \forall\, \alpha = 1, \ldots, m. \tag{C.3}$$

The expression above is a system of m equations in m unknowns which depend upon space X and time variable t. X and t are independent variables whereas, u_α denotes dependent variable. Here, $u_\alpha \equiv u_\alpha(X, t)$, $\partial u_\alpha/\partial t$ describes the partial derivative of $u_\alpha(X, t)$ with respect to t and $\partial u_\alpha/\partial X$ indicates the partial derivative of $u_\alpha(X, t)$ upon space X.

For the sake of compact representation, subscript is introduced to denote partial derivative; for instance, $(\cdot)_\eta \equiv \partial(\cdot)/\partial\eta$. System (C.3) can also be written in a matrix form

$$\boldsymbol{\mathcal{U}}_t + \boldsymbol{\mathcal{A}}_1 \boldsymbol{\mathcal{U}}_X = \boldsymbol{\mathcal{S}}, \tag{C.4}$$

with

$$\boldsymbol{\mathcal{U}} = \begin{pmatrix} u_1 \\ u_2 \\ \vdots \\ u_m \end{pmatrix}, \qquad \boldsymbol{\mathcal{A}}_1 = \begin{pmatrix} a_{11} & \dots & a_{1m} \\ a_{21} & \dots & a_{2m} \\ \vdots & \ddots & \vdots \\ a_{m1} & \dots & a_{mm} \end{pmatrix}, \qquad \boldsymbol{\mathcal{S}} = \begin{pmatrix} s_1 \\ s_2 \\ \vdots \\ s_m \end{pmatrix}. \tag{C.5}$$

By virtue of the equation above, it is worth mentioning that the system is linear with constant coefficients if the components of matrix $\boldsymbol{\mathcal{A}}_1$ and vector $\boldsymbol{\mathcal{S}}$ are constant. If $a_{\alpha\beta} = a_{\alpha\beta}(X,t)$ and $s_\alpha = s_\alpha(X,t)$, the system is called linear with variable coefficients. Expression (C.4) is also known as homogeneous equation if the source term $\boldsymbol{\mathcal{S}}$ vanishes.

In general, a PDE alone (without any initial and auxiliary boundary conditions) will either have no solution, or have an infinity of solutions. For this reason, one needs to specify the range of variation for independent variables X and t. X usually lies in a subinterval of the real line, $X \in [X_l, X_r]$. This subinterval is called the spatial domain of the PDEs. At boundary points of X_l and X_r, the boundary conditions (BCs) have to be imposed. As to variation of time t, some initial conditions (ICs) have to be specified at the initial time, which is typically chosen to be $t_0 = 0$.

C.3.1 Jacobian Matrix

The Jacobian matrix of a flux function $\boldsymbol{\mathcal{F}}_1$ in (C.1) is

$$\boldsymbol{\mathcal{A}}_1(\boldsymbol{\mathcal{U}}) = \frac{\partial \boldsymbol{\mathcal{F}}_1}{\partial \boldsymbol{\mathcal{U}}} = \begin{pmatrix} \partial f_1/\partial u_1 & \dots & \partial f_1/\partial u_m \\ \partial f_2/\partial u_1 & \dots & \partial f_2/\partial u_m \\ \vdots & \ddots & \vdots \\ \partial f_m/\partial u_1 & \dots & \partial f_m/\partial u_m \end{pmatrix}. \tag{C.6}$$

The component $a_{\alpha\beta}$ (of $\boldsymbol{\mathcal{A}}_1(\boldsymbol{\mathcal{U}})$) is defined by the partial derivative of component f_α of the vector $\boldsymbol{\mathcal{F}}_1$ with respect to the component u_β of problem variable $\boldsymbol{\mathcal{U}}$; that is, $a_{\alpha\beta} = \partial f_\alpha/\partial u_\beta$.

First by noting that the conservation law, viz. (C.1) and (C.2), can be expressed in a quasi-linear form (C.4) with the aid of chain rule such as

$$\frac{\partial \boldsymbol{\mathcal{F}}_1(\boldsymbol{\mathcal{U}})}{\partial X} = \frac{\partial \boldsymbol{\mathcal{F}}_1}{\partial \boldsymbol{\mathcal{U}}} \frac{\partial \boldsymbol{\mathcal{U}}}{\partial X}. \tag{C.7}$$

By assuming that, for simplicity, the source term vanishes, (C.1) then becomes

$$\boldsymbol{\mathcal{U}}_t + \boldsymbol{\mathcal{A}}_1(\boldsymbol{\mathcal{U}}) \boldsymbol{\mathcal{U}}_X = \mathbf{0}. \tag{C.8}$$

This is a special case of (C.4), widely regarded as a homogeneous equation.

C.3.2 Eigenvalues

The eigenvalues U_α of a matrix $\boldsymbol{\mathcal{A}}_1$ are solutions of the characteristic polynomial equation

$$\det(\boldsymbol{\mathcal{A}}_1 - U_\alpha \boldsymbol{I}) = |\boldsymbol{\mathcal{A}}_1 - U_\alpha \boldsymbol{I}| = 0, \tag{C.9}$$

where $\boldsymbol{I}$ is the identity matrix. Physically, eigenvalues represent the information propagation speeds.

C.3.3 Eigenvectors

The right eigenvector of a matrix $\boldsymbol{\mathcal{A}}_1$, which corresponds to its eigenvalue counterpart U_α, is denoted by $\boldsymbol{\mathcal{R}}_\alpha = (\mathcal{R}_\alpha^{(1)}, \mathcal{R}_\alpha^{(2)}, \ldots, \mathcal{R}_\alpha^{(m)})^T$ that satisfies $\boldsymbol{\mathcal{A}}_1 \boldsymbol{\mathcal{R}}_\alpha = U_\alpha \boldsymbol{\mathcal{R}}_\alpha$. Similarly, the left eigenvector of a matrix $\boldsymbol{\mathcal{A}}_1$ is a vector $\boldsymbol{\mathcal{L}}_\alpha^T = (\mathcal{L}_\alpha^{(1)}, \mathcal{L}_\alpha^{(2)}, \ldots, \mathcal{L}_\alpha^{(m)})$ such that $\boldsymbol{\mathcal{L}}_\alpha^T \boldsymbol{\mathcal{A}}_1 = U_\alpha \boldsymbol{\mathcal{L}}_\alpha^T$.

C.3.4 Orthogonality Condition

Making use of $\boldsymbol{\mathcal{R}}_\alpha$ and $\boldsymbol{\mathcal{L}}_\alpha$, it is now possible to define a condition, namely orthogonality, which defines

$$\boldsymbol{\mathcal{R}}_\alpha^T \boldsymbol{\mathcal{L}}_\beta = \begin{cases} 1 & \text{if } \alpha = \beta, \\ 0 & \text{Otherwise.} \end{cases} \tag{C.10}$$

C.4 Characteristic Theory: Constant Coefficient Linear System of Equations

A set of m hyperbolic PDEs is generally expressed as

$$\boldsymbol{\mathcal{U}}_t + \boldsymbol{\mathcal{A}}_1 \boldsymbol{\mathcal{U}}_X = \boldsymbol{0}, \tag{C.11}$$

where the coefficient matrix $\boldsymbol{\mathcal{A}}_1$ is constant. If $\boldsymbol{\mathcal{A}}_1$ has real eigenvalues U_α and linearly independent eigenvectors $\boldsymbol{\mathcal{R}}_\alpha$, the system is simply hyperbolic. If these eigenvalues are real and distinct, the system is called strictly hyperbolic.

C.4.1 Diagonalisation and Characteristic Variable

It is useful to introduce a variable transformation technique to transform the dependent variable $\boldsymbol{\mathcal{U}}(X,t)$ to a new set of variable $\boldsymbol{\mathcal{W}}(X,t)$. The definition is described as follows.

Diagonalisable System

The Jacobian matrix $\boldsymbol{\mathcal{A}}_1$ is said to be diagonalisable if it can be decomposed into

$$\boldsymbol{\mathcal{A}}_1 = \boldsymbol{\mathcal{R}}\boldsymbol{\Lambda}\boldsymbol{\mathcal{R}}^{-1} \quad \text{or} \quad \boldsymbol{\Lambda} = \boldsymbol{\mathcal{R}}^{-1}\boldsymbol{\mathcal{A}}_1\boldsymbol{\mathcal{R}}, \tag{C.12}$$

where the diagonal matrix $\boldsymbol{\Lambda}$ and $\boldsymbol{\mathcal{R}}$ are denoted as

$$\boldsymbol{\Lambda} = \begin{bmatrix} U_1 & \dots & 0 \\ \vdots & \ddots & \vdots \\ 0 & \dots & U_m \end{bmatrix}, \quad \boldsymbol{\mathcal{R}} = [\boldsymbol{\mathcal{R}}_1, \dots, \boldsymbol{\mathcal{R}}_m], \tag{C.13}$$

respectively. The column vector $\boldsymbol{\mathcal{R}}_\alpha$ of $\boldsymbol{\mathcal{R}}$ is the right eigenvector of $\boldsymbol{\mathcal{A}}_1$ corresponds to its real eigenvalue U_α; that is, $\boldsymbol{\mathcal{A}}_1\boldsymbol{\mathcal{R}}_\alpha = U_\alpha\boldsymbol{\mathcal{R}}_\alpha$.

Characteristic Variable

The existence of the inverse matrix $\boldsymbol{\mathcal{R}}^{-1}$ makes it possible to define a new set of dependent variable $\boldsymbol{\mathcal{W}} = (w_1, w_2, \dots, w_m)^T$ such that

$$\boldsymbol{\mathcal{W}} = \boldsymbol{\mathcal{R}}^{-1}\boldsymbol{\mathcal{U}} \qquad \text{or} \qquad \boldsymbol{\mathcal{U}} = \boldsymbol{\mathcal{R}}\boldsymbol{\mathcal{W}}, \tag{C.14}$$

where new variable $\boldsymbol{\mathcal{W}}$ is regarded as characteristic variable. Since $\boldsymbol{\mathcal{A}}_1$ and $\boldsymbol{\mathcal{R}}$ are constant, the linear system (C.11) can be decoupled as

$$\boldsymbol{\mathcal{W}}_t + \boldsymbol{\Lambda}\boldsymbol{\mathcal{W}}_X = \mathbf{0}. \tag{C.15}$$

This is known as canonical (or characteristic) form of (C.11). When written in full, (C.15) yields

$$\begin{pmatrix} w_1 \\ w_2 \\ \vdots \\ w_m \end{pmatrix}_t + \begin{pmatrix} U_1 & \dots & 0 \\ 0 & \dots & 0 \\ \vdots & \ddots & \vdots \\ 0 & \dots & U_m \end{pmatrix} \begin{pmatrix} w_1 \\ w_2 \\ \vdots \\ w_m \end{pmatrix}_X = \mathbf{0}. \tag{C.16}$$

The α-th PDE is

$$\frac{\partial w_\alpha}{\partial t} + U_\alpha \frac{\partial w_\alpha}{\partial X} = 0, \qquad \alpha = 1, \dots, m. \tag{C.17}$$

The above system is clearly decoupled, each of which can be treated as a linear advection equation.

C.4.2 Initial Value Problem (IVP)

The general solution of IVP (viz. (C.11)) can be achieved by first solving the corresponding canonical system (C.15). In order to achieve this, it is worth noting that the initial condition of characteristic variable can be obtained as

$$\mathring{\boldsymbol{\mathcal{W}}} = \boldsymbol{\mathcal{R}}^{-1}\mathring{\boldsymbol{\mathcal{U}}}; \qquad \mathring{\boldsymbol{\mathcal{U}}} = (\mathring{u}_1, \dots, \mathring{u}_m)^T. \tag{C.18}$$

By considering each unknown $w_\alpha(X, t)$ of (C.17), its solution is simply stated as

$$w_\alpha(X, t) = \mathring{w}_\alpha(X - U_\alpha t), \qquad \forall\, \alpha = 1, \dots, m. \tag{C.19}$$

Consequently, the solution of original variable $\boldsymbol{\mathcal{U}}$ is followed by variable transformation technique in accordance with (C.14b); that is, $\boldsymbol{\mathcal{U}} = \boldsymbol{\mathcal{R}}\boldsymbol{\mathcal{W}}$.

C.5 Riemann Problem for a Linear System

The Riemann problem consists of a hyperbolic system of equations together with a set of special initial conditions, each of which is defined by a piecewise constant with a single jump discontinuity at X:

$$\boldsymbol{\mathcal{U}}(X,0) = \mathring{\boldsymbol{\mathcal{U}}}(X) = \begin{cases} \boldsymbol{\mathcal{U}}^- & \text{if } X < 0, \\ \boldsymbol{\mathcal{U}}^+ & \text{if } X > 0. \end{cases} \tag{C.20}$$

The discontinuity $(\boldsymbol{\mathcal{U}}^+ - \boldsymbol{\mathcal{U}}^-)$ propagates only along the characteristic curve and therefore can be decomposed into the linear combination of the eigenvectors of $\boldsymbol{\mathcal{A}}_1$:

$$\boldsymbol{\mathcal{U}}^+ - \boldsymbol{\mathcal{U}}^- = \eta_1 \boldsymbol{\mathcal{R}}_1 + \ldots + \eta_m \boldsymbol{\mathcal{R}}_m = \boldsymbol{W}_1 + \ldots + \boldsymbol{W}_m. \tag{C.21}$$

Note that η_α is a scalar multiple (or α-th wave strength) and $\boldsymbol{W}_\alpha$ describes α-th wave. Thus, the solution of $\boldsymbol{\mathcal{U}}(X,t)$ is denoted as

$$\boldsymbol{\mathcal{U}}(X,t) = \boldsymbol{\mathcal{U}}^- + \sum_{\alpha=1}^{m} H(X - U_\alpha t)\boldsymbol{W}_\alpha, \tag{C.22}$$

where $H(\xi)$ is the Heaviside function

$$H(\xi) = \begin{cases} 0 & \text{if } \xi < 0, \\ 1 & \text{if } \xi > 0. \end{cases} \tag{C.23}$$

Appendix D

Wave Speeds

D.1 Wave Speeds: Linear Case

The standard linear isotropic elasticity tensor is typically represented by

$$\boldsymbol{\mathcal{C}} = \lambda \boldsymbol{I} \otimes \boldsymbol{I} + \mu(\boldsymbol{\mathcal{I}} + \bar{\boldsymbol{\mathcal{I}}}), \tag{D.1}$$

where μ and λ are Lamé constants. It is now convenient to perform indicial tensor manipulation for the derivation that will be demonstrated below. Firstly by noting that the indicial notation of the expression above is written as

$$\mathcal{C}_{iIjJ} = \lambda \delta_{iI}\delta_{jJ} + \mu\delta_{ij}\delta_{IJ} + \mu\delta_{iJ}\delta_{Ij}, \tag{D.2}$$

where

$$\boldsymbol{I} \otimes \boldsymbol{I} = \delta_{iI}\delta_{jJ}; \qquad \boldsymbol{\mathcal{I}} = \delta_{ij}\delta_{IJ}; \qquad \bar{\boldsymbol{\mathcal{I}}} = \delta_{iJ}\delta_{Ij}, \tag{D.3}$$

$\boldsymbol{\mathcal{C}}_{NN}$ can then be easily defined:

$$[\boldsymbol{\mathcal{C}}_{NN}]_{ij} = \mathcal{C}_{iIjJ}N_I N_J \tag{D.4a}$$

$$= \lambda N_i N_j + \mu\delta_{ij} + \mu N_i N_j. \tag{D.4b}$$

Or simply,

$$\boldsymbol{\mathcal{C}}_{NN} = \lambda \boldsymbol{N} \otimes \boldsymbol{N} + \mu \boldsymbol{I} + \mu \boldsymbol{N} \otimes \boldsymbol{N} \tag{D.5a}$$

$$= (\lambda + 2\mu)\boldsymbol{N} \otimes \boldsymbol{N} + \mu \boldsymbol{T}_1 \otimes \boldsymbol{T}_1 + \mu \boldsymbol{T}_2 \otimes \boldsymbol{T}_2, \tag{D.5b}$$

with the aid of $\boldsymbol{I} = \boldsymbol{N} \otimes \boldsymbol{N} + \boldsymbol{T}_1 \otimes \boldsymbol{T}_1 + \boldsymbol{T}_2 \otimes \boldsymbol{T}_2$. Here, $\{\boldsymbol{N}, \boldsymbol{T}_1, \boldsymbol{T}_2\}$ is a set of orthonormal vectors. Recall first that the eigenstructure is of the form

$$\boldsymbol{\mathcal{C}}_{NN}\boldsymbol{p}^R_\alpha = \rho_0 U^2_\alpha \boldsymbol{p}^R_\alpha, \tag{D.6}$$

substituting (D.5b) into the above expression leads to

$$\left[\frac{(\lambda + 2\mu)}{\rho_0}\boldsymbol{N} \otimes \boldsymbol{N} + \frac{\mu}{\rho_0}\boldsymbol{T}_1 \otimes \boldsymbol{T}_1 + \frac{\mu}{\rho_0}\boldsymbol{T}_2 \otimes \boldsymbol{T}_2\right] \boldsymbol{p}^R_\alpha = U^2_\alpha \boldsymbol{p}^R_\alpha. \tag{D.7}$$

By simple inspection, it transpires that 3 pairs of linear wave speeds can be obtained:

$$U_{1,2} = \pm U_p; \qquad U_{3,4} = U_{5,6} = \pm U_s, \tag{D.8}$$

where

$$U_p = \sqrt{\frac{(\lambda + 2\mu)}{\rho_0}}; \quad U_s = \sqrt{\frac{\mu}{\rho_0}}. \tag{D.9}$$

Note that U_p and U_s travel in the direction of $\boldsymbol{N}$ and $\{\boldsymbol{T}_1, \boldsymbol{T}_2\}$, respectively.

D.2 Wave Speeds: Nonlinear Case

In order to solve the eigenvalue problem (D.6) for nonlinear case, recall first that the first Piola-Kirchhoff stress tensor of the nearly incompressible Neo-Hookean material model, $\boldsymbol{P}$, is given by

$$\boldsymbol{P}(\boldsymbol{F}) = \mu J^{-2/3}\left[\boldsymbol{F} - \frac{1}{3}(\boldsymbol{F}:\boldsymbol{F})\boldsymbol{F}^{-T}\right] + \kappa(J-1)J\boldsymbol{F}^{-T}. \tag{D.10}$$

By taking in account that $\partial J/\partial \boldsymbol{F} = J\boldsymbol{F}^{-T}$, the nonlinear elasticity tensor can then be computed:

$$\begin{aligned}\boldsymbol{\mathcal{C}} = \frac{\partial \boldsymbol{P}}{\partial \boldsymbol{F}} =& -\frac{2}{3}\mu J^{-2/3}\left[\boldsymbol{F} - \frac{1}{3}(\boldsymbol{F}:\boldsymbol{F})\boldsymbol{F}^{-T}\right]\otimes \boldsymbol{F}^{-T} \\ &+ \mu J^{-2/3}\left[\boldsymbol{\mathcal{I}} - \frac{1}{3}(\boldsymbol{F}:\boldsymbol{F})\frac{\partial \boldsymbol{F}^{-T}}{\partial \boldsymbol{F}} - \frac{2}{3}\boldsymbol{F}^{-T}\otimes\boldsymbol{F}\right] \\ &+ \kappa J(2J-1)\boldsymbol{F}^{-T}\otimes\boldsymbol{F}^{-T} + \kappa J(J-1)\frac{\partial \boldsymbol{F}^{-T}}{\partial \boldsymbol{F}}.\end{aligned} \tag{D.11}$$

With the aid of $\mathcal{H}_{iIjJ} := \partial \boldsymbol{F}^{-T}/\partial \boldsymbol{F} = -F^{-T}_{iJ}F^{-T}_{jI}$, equation above can be written as

$$\begin{aligned}\boldsymbol{\mathcal{C}} = \frac{\partial \boldsymbol{P}}{\partial \boldsymbol{F}} =& -\frac{2}{3}\mu J^{-2/3}\boldsymbol{F}\otimes\boldsymbol{F}^{-T} + \frac{2}{9}\mu J^{-2/3}(\boldsymbol{F}:\boldsymbol{F})\boldsymbol{F}^{-T}\otimes\boldsymbol{F}^{-T} \\ &+ \mu J^{-2/3}\boldsymbol{\mathcal{I}} - \frac{1}{3}\mu J^{-2/3}(\boldsymbol{F}:\boldsymbol{F})\boldsymbol{\mathcal{H}} - \frac{2}{3}\mu J^{-2/3}\boldsymbol{F}^{-T}\otimes\boldsymbol{F} \\ &+ \kappa J(2J-1)\boldsymbol{F}^{-T}\otimes\boldsymbol{F}^{-T} + \kappa J(J-1)\boldsymbol{\mathcal{H}}.\end{aligned} \tag{D.12}$$

Multiplying the above expression by $N_I N_J$ and defining $\boldsymbol{F}^{-T}\boldsymbol{N} = \boldsymbol{m}$ and $\boldsymbol{F}\boldsymbol{N} = \boldsymbol{m}^\star$ yields

$$\begin{aligned}[\boldsymbol{\mathcal{C}}_{NN}]_{ij} = \mathcal{C}_{iIjI}N_I N_J =& -\frac{2}{3}\mu J^{-2/3}\boldsymbol{m}^\star\otimes\boldsymbol{m} + \frac{2}{9}\mu J^{-2/3}(\boldsymbol{F}:\boldsymbol{F})\boldsymbol{m}\otimes\boldsymbol{m} \\ &+ \mu J^{-2/3}\boldsymbol{I} + \frac{1}{3}\mu J^{-2/3}(\boldsymbol{F}:\boldsymbol{F})\boldsymbol{m}\otimes\boldsymbol{m} - \frac{2}{3}\mu J^{-2/3}\boldsymbol{m}\otimes\boldsymbol{m}^\star \\ &+ \kappa J(2J-1)\boldsymbol{m}\otimes\boldsymbol{m} - \kappa J(J-1)\boldsymbol{m}\otimes\boldsymbol{m}.\end{aligned} \tag{D.13}$$

The matrix $\boldsymbol{\mathcal{C}}_{NN}$ is rearranged and gives

$$\boldsymbol{\mathcal{C}}_{NN} = \alpha(\boldsymbol{m}\otimes\boldsymbol{m}) + \beta\boldsymbol{I} + \gamma(\boldsymbol{m}^\star\otimes\boldsymbol{m} + \boldsymbol{m}\otimes\boldsymbol{m}^\star), \tag{D.14}$$

where

$$\alpha = \kappa J^2 + \frac{5}{9}\mu J^{-2/3}(\boldsymbol{F}:\boldsymbol{F}) \tag{D.15a}$$

$$\beta = \mu J^{-2/3} \tag{D.15b}$$

$$\gamma = -\frac{2}{3}\mu J^{-2/3}. \tag{D.15c}$$

Assuming for simplicity that $\boldsymbol{N}$ is a principal direction of the deformation (which thus implies that $\boldsymbol{F}\boldsymbol{N} = \Lambda\boldsymbol{n} = \boldsymbol{m}^\star$ and $\boldsymbol{F}^{-T}\boldsymbol{N} = \boldsymbol{n}/\Lambda = \boldsymbol{m}$), (D.14) can be further reduced to

$$\boldsymbol{C}_{NN} = (\alpha + 2\gamma\Lambda^2)\boldsymbol{m} \otimes \boldsymbol{m} + \beta\boldsymbol{I}. \tag{D.16}$$

This expression is comprised of three eigenvectors: $\boldsymbol{n} = \Lambda\boldsymbol{m}$ and two arbitrary unit vectors orthogonal to $\boldsymbol{n}$ (where $\Lambda = 1/\|\boldsymbol{F}^{-T}\boldsymbol{N}\|$). The associated longitudinal and shear wave speeds are

$$U_p = \sqrt{\frac{\beta + \left(\frac{\alpha}{\Lambda^2} + 2\gamma\right)}{\rho_0}}; \qquad U_s = \sqrt{\frac{\beta}{\rho_0}}, \tag{D.17}$$

respectively.

Appendix E

Laws of Thermodynamics and Viscous Formulation

E.1 Entropy and Second Law of Thermodynamics: The Clausius-Duhem Inequality

The First Law of Thermodynamics governs the energy transfer within a thermodynamic process, but it places no restriction on the direction of the process. For this purpose, it is necessary to introduce a fundamental state variable, namely entropy, which satisfies an inequality known as the Second Law of Thermodynamics (responsible for the direction of energy transfer).

It is important to firstly note that the total production of entropy per unit time[1], $\mathcal{E}(t)$, is postulated to be a non-negative scalar-valued function and described as

$$\mathcal{E}(t) = \underbrace{\frac{d}{dt}\int_V \eta(\boldsymbol{X},t)\,dV}_{\text{rate of change of entropy}} - \underbrace{\left[-\int_{\partial V}\left(\frac{\boldsymbol{Q}}{\theta}\right)\cdot \boldsymbol{N}\,dA\right]}_{\text{rate of entropy input}} \geq 0, \tag{E.1}$$

where η denotes the entropy, $\boldsymbol{Q}$ indicates the heat flux vector and $\boldsymbol{N}$ is the material outward unit normal vector. By virtue of (E.1), negative sign is required in the entropy flux due to the fact that the heat flows from hot to cold and the heat source term is neglected for simplicity. This expression is widely known as the Lagrangian Clausius-Duhem inequality and its local counterpart becomes

$$\frac{\partial \eta}{\partial t} + \boldsymbol{\nabla}\cdot\left(\frac{\boldsymbol{Q}}{\theta}\right) \geq 0. \tag{E.2}$$

Equation above can then be expanded to

$$\frac{\partial \eta}{\partial t} + \frac{1}{\theta}\boldsymbol{\nabla}\cdot\boldsymbol{Q} - \frac{1}{\theta^2}\boldsymbol{Q}\cdot\boldsymbol{\nabla}\theta \geq 0. \tag{E.3}$$

By substituting the First Law (3.3) into (E.3) for $\boldsymbol{\nabla}\cdot\boldsymbol{Q}$, an alternative expression concludes as belows:

$$\dot{\eta} + \frac{1}{\theta}\left(\boldsymbol{P}\colon \dot{\boldsymbol{F}} - \dot{e}\right) - \frac{1}{\theta^2}\boldsymbol{Q}\cdot\boldsymbol{\nabla}\theta \geq 0. \tag{E.4}$$

The last term in the above equation $(-(\boldsymbol{Q}\cdot\boldsymbol{\nabla}\theta)/\theta^2)$ determines the entropy production due to heat conduction. This term must be a non-negative scalar value function which implies that the condition[2]

$$\boldsymbol{Q}\cdot\boldsymbol{\nabla}\theta \leq 0 \tag{E.5}$$

has to be satisfied.

A stronger form of the Clausius-Duhem inequality (often referred to as Clausius-Planck inequality) is established as

$$\mathcal{D}_{\text{int}} = \theta\dot{\eta} + \boldsymbol{P}\colon\dot{\boldsymbol{F}} - \dot{e} \geq 0, \tag{E.6}$$

[1]Total production of entropy is determined by the difference between the rate of change of entropy and the rate of entropy input.

[2]This condition is widely known as heat conduction inequality. For instance, $\boldsymbol{Q} = \boldsymbol{0}$ is implied if and only if there is no temperature gradient exists.

where $\mathcal{D}_{\text{int}}$ describes the internal dissipation (or local production of entropy). With the help of the Legendre transformation, that is

$$\psi(\boldsymbol{F}, \theta) = e(\boldsymbol{F}, \eta) - \theta\eta, \tag{E.7}$$

equation (E.6) can be expressed as

$$\mathcal{D}_{\text{int}} = \boldsymbol{P}\colon \dot{\boldsymbol{F}} - \dot{\psi} - \eta\dot{\theta} \geq 0. \tag{E.8}$$

Here, $\mathcal{D}_{\text{int}} = 0$ holds for all admissible thermoelastic processes. In an isothermal process (thermal effects such as η and θ are neglected), inequality (E.8) reduces to

$$\mathcal{D}_{\text{int}} = \boldsymbol{P}\colon \dot{\boldsymbol{F}} - \dot{\psi} \geq 0. \tag{E.9}$$

By considering the isothermal perfectly elastic material, the above inequality can be degenerated to

$$\mathcal{D}_{\text{int}} = \boldsymbol{P}\colon \dot{\boldsymbol{F}} - \dot{\psi} = 0 \tag{E.10}$$

This expression shows that the rate of change of internal mechanical work per unit of undeformed volume ($\boldsymbol{P}\colon \dot{\boldsymbol{F}}$ or equivalently known as stress power) equals to the rate of Helmholtz free energy functional, that is

$$\dot{\psi}(\boldsymbol{F}) = \boldsymbol{P}\colon \dot{\boldsymbol{F}}. \tag{E.11}$$

E.1.1 Thermo-mechanical Constitutive Equations

Many important stress analysis problems of engineering interest involve structures that are subjected to both mechanical and thermal loadings. Most solids exhibit a volumetric change with temperature variation, which in turn generally induce stresses. In the case where temperature variation is sufficiently high, these stresses can reach an ultimate level that lead to structural failure. More detailed information can be found in [171].

It is worth mentioning that the constitutive equations for irreversible thermodynamics are more complex than those of reversible elastodynamics. First it is necessary to provide a material relationship between the heat flux vector $\boldsymbol{Q}$ and the temperature θ[3]

$$\boldsymbol{Q} = -\boldsymbol{h}\boldsymbol{\nabla}\theta, \tag{E.12}$$

where $\boldsymbol{h}$ denotes the material thermal conductivity tensor. Inserting (E.12) into (E.5) leads to $(\boldsymbol{h}\boldsymbol{\nabla}\theta)\cdot\boldsymbol{\nabla}\theta \geq 0$. This clearly implies that $\boldsymbol{h}$ is a positive semidefinite matrix[4]. The conductivity tensor of a thermally isotropic material can be further simplified to $\boldsymbol{h} = h\boldsymbol{I}$, which yields

$$\boldsymbol{Q} = -h\boldsymbol{\nabla}\theta; \qquad \forall\, h \geq 0 \tag{E.13}$$

[3]This is generally known as Duhamel's law of heat conduction.

[4]A positive semidefinite matrix is defined for which all its eigenvalues are non-negative.

and is typically known as Fourier's law.

For all admissible thermoelastic processes, the expression for Clausius-Planck inequality degenerates to

$$\mathcal{D}_{\text{int}} = \boldsymbol{P}\colon \dot{\boldsymbol{F}} - \dot{\psi} - \eta\dot{\theta} = 0$$

and it can be further rearranged as

$$\frac{\partial\psi(\boldsymbol{F},\theta)}{\partial t} = \boldsymbol{P}\colon \frac{\partial \boldsymbol{F}}{\partial t} - \eta\frac{\partial\theta}{\partial t}. \tag{E.14}$$

By applying the chain rule, the time differentiation of Helmholtz free energy functional, ψ, is obtained as

$$\frac{\partial\psi(\boldsymbol{F},\theta)}{\partial t} = \left.\frac{\partial\psi(\boldsymbol{F},\theta)}{\partial \boldsymbol{F}}\right|_{\theta}\colon \frac{\partial \boldsymbol{F}}{\partial t} + \left.\frac{\partial\psi(\boldsymbol{F},\theta)}{\partial\theta}\right|_{\boldsymbol{F}}\frac{\partial\theta}{\partial t}. \tag{E.15}$$

The physical expressions can then be deduced by comparing terms in (E.14) and (E.15):

$$\boldsymbol{P} = \left.\frac{\partial\psi(\boldsymbol{F},\theta)}{\partial \boldsymbol{F}}\right|_{\theta}; \qquad \eta = -\left.\frac{\partial\psi(\boldsymbol{F},\theta)}{\partial\theta}\right|_{\boldsymbol{F}} \tag{E.16}$$

for any given $\boldsymbol{F}$ and θ. From equation above, it is necessary to define the free energy function $\psi(\boldsymbol{F},\theta)$ which expressed in terms of deformation gradient and temperature.

Note first that the relationship between the internal energy and temperature is usually denoted in terms of the specific heat coefficient at constant deformation $C_{\boldsymbol{F}}$ (defined by the amount of energy required to produce a unit increase in the temperature of a unit mass). In order to achieve this, the specific heat capacity, $\rho_0 C_{\boldsymbol{F}}$, is generally defined to be a positive function of the form

$$\rho_0 C_{\boldsymbol{F}}(\boldsymbol{F},\theta) = -\theta\frac{\partial}{\partial\theta}\left(\frac{\partial\psi(\boldsymbol{F},\theta)}{\partial\theta}\right) > 0. \tag{E.17}$$

Using (E.16b) and $\partial e/\partial\eta = \theta$, the above expression can be derived as

$$\begin{aligned}\rho_0 C_{\boldsymbol{F}}(\boldsymbol{F},\theta) &= \theta\left.\frac{\partial\eta(\boldsymbol{F},\theta)}{\partial\theta}\right|_{\boldsymbol{F}} \\ &= \left.\frac{\partial e(\boldsymbol{F},\eta)}{\partial\eta}\right|_{\boldsymbol{F}}\left.\frac{\partial\eta(\boldsymbol{F},\theta)}{\partial\theta}\right|_{\boldsymbol{F}} \\ &= \left.\frac{\partial e(\boldsymbol{F},\theta)}{\partial\theta}\right|_{\boldsymbol{F}}.\end{aligned} \tag{E.18}$$

By integrating (E.18c) with respect to temperature, it then leads to

$$\Delta e = e(\boldsymbol{F},\theta) - e_0(\boldsymbol{F}) = \int_{\theta_0}^{\theta}\rho_0 C_{\boldsymbol{F}}(\boldsymbol{F},\theta)\,\mathrm{d}\theta; \qquad e_0(\boldsymbol{F}) = e(\boldsymbol{F},\theta_0), \tag{E.19}$$

where θ_0 denotes a reference temperature. Hence, the change in the internal energy Δe can be determined. Analogously, the entropy change simply results from (E.18a) as

$$\Delta\eta = \eta(\boldsymbol{F},\theta) - \eta_0(\boldsymbol{F}) = \int_{\theta_0}^{\theta} \frac{\rho_0 C_{\boldsymbol{F}}(\boldsymbol{F},\theta)}{\theta}\,\mathrm{d}\theta, \tag{E.20}$$

where $\eta_0(\boldsymbol{F}) = \eta(\boldsymbol{F},\theta_0)$ denotes the entropy at a reference temperature.

With the aid of (E.19) and (E.20), a general Helmholtz free energy functional (note that the internal energy $e(\boldsymbol{F},\eta) \neq e(\boldsymbol{F},\theta)$) can be easily obtained as

$$\psi(\boldsymbol{F},\theta) = \psi_0(\boldsymbol{F}) - \eta_0(\boldsymbol{F})\Delta\theta + \rho_0 C_{\boldsymbol{F}}\left(\Delta\theta - \theta\ln\frac{\theta}{\theta_0}\right); \qquad \Delta\theta = \theta - \theta_0 \tag{E.21}$$

provided that $C_{\boldsymbol{F}}$ does not change with temperature and deformation gradient ($C_{\boldsymbol{F}} \equiv const$). Here, $\psi_0(\boldsymbol{F}) = \psi(\boldsymbol{F},\theta_0)$ and $\eta_0(\boldsymbol{F}) = \eta(\boldsymbol{F},\theta_0)$. The stress tensor is thus conveniently evaluated as

$$\boldsymbol{P} = \boldsymbol{P}_0 - \frac{\partial\eta_0(\boldsymbol{F})}{\partial\boldsymbol{F}}\Delta\theta; \qquad \boldsymbol{P}_0 = \frac{\partial\psi(\boldsymbol{F},\theta_0)}{\partial\boldsymbol{F}}, \tag{E.22}$$

where $\eta_0(\boldsymbol{F})$ couples the thermal and mechanical effects. Most solids experience volumetric change under temperature variation by means of $\eta_0(\boldsymbol{F})$ depends only on Jacobian J; that is, $\eta_0(\boldsymbol{F}) = \eta_0(J)$. Under this circumstance, the deviatoric component of the First Piola-Kirchhoff stress tensor is computed directly from $\psi_0(\boldsymbol{F})$ whereas, the pressure becomes

$$p(J,\theta) = p_0(J) - \eta_0'(J)\Delta\theta; \qquad \eta_0'(J) = \frac{\partial\eta_0(J)}{\partial J} \tag{E.23}$$

where

$$\Delta\theta = \frac{e - e_0(\boldsymbol{F})}{\rho_0 C_{\boldsymbol{F}}} = \theta - \theta_0. \tag{E.24}$$

A particular form of function $\eta_0(J)$ is shown in the next section.

E.1.2 Mie-Gruneisen Model

The Mie-Gruneisen equation of state is derived as

$$\Gamma(J) = -J\frac{\partial p(J,\theta)}{\partial e}\bigg|_J = -J\frac{\partial p(J,\theta)}{\partial\theta}\bigg|_J \frac{\partial\theta(J,e)}{\partial e}\bigg|_J = -\frac{J}{\rho_0 C_{\boldsymbol{F}}}\frac{\partial p(J,\theta)}{\partial\theta}\bigg|_J = \frac{J\eta_0'(J)}{\rho_0 C_{\boldsymbol{F}}},$$

where $\partial\theta/\partial e = 1/\rho_0 C_{\boldsymbol{F}}$ from which

$$\theta(J,e) = \theta_0 + \frac{e - e_0(J)}{\rho_0 C_{\boldsymbol{F}}}.$$

Assuming that Mie-Gruneisen coefficient Γ remains constant with respect to J (that is, $\Gamma = \Gamma(J)$), the entropy at reference temperature can be integrated as

$$\eta_0(J) = \rho_0 C_{\boldsymbol{F}}\Gamma\ln(J)$$

and hence the total entropy for Mie-Gruneisen equation of state is

$$\eta(J,\theta) = \rho_0 C_{\boldsymbol{F}} \ln\left(\frac{\theta J^{\Gamma}}{\theta_0}\right).$$

It is now possible to derive an explicit expression for pressure p as

$$p(J,\theta) = p_0(J) - \frac{\rho_0 C_{\boldsymbol{F}} \Gamma}{J}\Delta\theta. \tag{E.25}$$

The change in temperature emerges as

$$\Delta\theta = \frac{e - e_0(J)}{\rho_0 C_{\boldsymbol{F}}}, \tag{E.26}$$

where $e_0(J) = \psi_0(J) + \rho_0 C_{\boldsymbol{F}} \Gamma \theta_0 \ln(J)$.

E.2 Artificial Viscosity

In problems which are highly nonlinear, it is essential to introduce an artificial viscosity term which is aimed at eliminating the high frequencies in the solution. The amount of viscosity required for stability is determined by the resolution of the approximating space and therefore varies proportionally to the order of the approximating polynomial.

The artificial viscosity is initially applied in the whole computational domain, where no discontinuity sensor is implemented. A simple dissipative formulation can be derived based on

$$\boldsymbol{\sigma}_v = \boldsymbol{\mathcal{C}}_v : \boldsymbol{d}, \tag{E.27}$$

where $\boldsymbol{\sigma}_v$ describes the viscous component of symmetric Cauchy stress tensor and $\boldsymbol{d}$ represents the rate of deformation tensor. In addition, $\boldsymbol{\mathcal{C}}_v$ is a fourth-order constitutive tensor, which can be expressed in its simplest form, defined by

$$\boldsymbol{\mathcal{C}}_v = \lambda_v \boldsymbol{I} \otimes \boldsymbol{I} + \mu_v(\boldsymbol{\mathcal{I}} + \hat{\boldsymbol{\mathcal{I}}}), \tag{E.28}$$

where

$$\mathcal{I}_{iIjJ} = \delta_{ij}\delta_{IJ}; \qquad \hat{\mathcal{I}}_{iIjJ} = \delta_{iJ}\delta_{Ij}; \qquad \lambda_v = \kappa_v - \frac{2}{3}\mu_v. \tag{E.29}$$

Here, κ_v denotes the volumetric viscosity and μ_v indicates the shear viscosity. By substituting (E.28) into (E.27), the viscous stress can be obtained as

$$\boldsymbol{\sigma}_v = \lambda_v(\mathrm{tr}\boldsymbol{d})\boldsymbol{I} + 2\mu_v \boldsymbol{d}, \tag{E.30}$$

with the aid of symmetric fourth-order tensor, that is $\boldsymbol{\mathcal{S}} = 1/2(\boldsymbol{\mathcal{I}} + \hat{\boldsymbol{\mathcal{I}}})$. This symmetric tensor projects the rate of deformation tensor $\boldsymbol{d}$ onto its symmetric component:

$$\boldsymbol{\mathcal{S}} : \boldsymbol{d} = \frac{1}{2}\left(\boldsymbol{d} + \boldsymbol{d}^T\right). \tag{E.31}$$

In order to develop a viscous formulation such that the volumetric component is decoupled from shear one, it is necessary to decouple the rate of deformation tensor into the deviatoric distortional $\boldsymbol{d}_{dev}$ and volumetric parts $\boldsymbol{d}_{vol}$:

$$\begin{aligned}\boldsymbol{d} &= \boldsymbol{d}_{dev} + \boldsymbol{d}_{vol} \\ &= \boldsymbol{d}_{dev} + \frac{1}{3}(\mathrm{tr}\boldsymbol{d})\boldsymbol{I}.\end{aligned} \tag{E.32}$$

Consequently, the viscous stress can be easily reduced to

$$\boldsymbol{\sigma}_v = \kappa_v(\mathrm{tr}\boldsymbol{d})\boldsymbol{I} + 2\mu_v\boldsymbol{d}_{dev}. \tag{E.33}$$

This expression clearly depends on the spatial configuration due to the fact that the rate of deformation tensor $\boldsymbol{d}$ is fundamentally defined as the symmetric part of the velocity gradient $\boldsymbol{l}$ [6, 7, 38, 115, 125, 126]; that is $\boldsymbol{d} = (\boldsymbol{l} + \boldsymbol{l}^T)/2$.

To describe the viscous stress within the Total Lagrangian framework, it is vital to re-express the rate of deformation tensor in terms of Lagrangian velocity gradient as

$$\boldsymbol{d} = \frac{1}{2\rho_0}\left[(\boldsymbol{\nabla}_0\boldsymbol{p})\boldsymbol{F}^{-1} + \boldsymbol{F}^{-T}(\boldsymbol{\nabla}_0\boldsymbol{p})^T\right], \tag{E.34}$$

where $\boldsymbol{\nabla}_0$ denotes the gradient operator in undeformed configuration. Recall first that the stresses are related by $\boldsymbol{P}_v = J\boldsymbol{\sigma}_v\boldsymbol{F}^{-T}$, the viscous component of the stress tensor can be eventually found as

$$\begin{aligned}\boldsymbol{P}_v &= \frac{J\kappa_v}{\rho_0}\left(\boldsymbol{F}^{-T} : \boldsymbol{\nabla}_0\boldsymbol{p}\right)\boldsymbol{F}^{-T} + \frac{J\mu_v}{\rho_0}\boldsymbol{F}^{-T}(\boldsymbol{\nabla}_0\boldsymbol{p})^T\boldsymbol{F}^{-T} + \frac{J\mu_v}{\rho_0}(\boldsymbol{\nabla}_0\boldsymbol{p})\boldsymbol{C}^{-1} - \frac{2J\mu_v}{3\rho_0}\left(\boldsymbol{F}^{-T} : \boldsymbol{\nabla}_0\boldsymbol{p}\right)\boldsymbol{I} \\ &= \underbrace{\frac{J\kappa_v}{\rho_0}\left(\boldsymbol{F}^{-T} : \boldsymbol{\nabla}_0\boldsymbol{p}\right)\boldsymbol{F}^{-T}}_{\text{volumetric}} + \underbrace{\frac{J\mu_v}{\rho_0}\left(\boldsymbol{F}^{-T}(\boldsymbol{\nabla}_0\boldsymbol{p})^T\boldsymbol{F}^{-T} + (\boldsymbol{\nabla}_0\boldsymbol{p})\boldsymbol{C}^{-1} - \frac{2}{3}\left(\boldsymbol{F}^{-T} : \boldsymbol{\nabla}_0\boldsymbol{p}\right)\boldsymbol{F}^{-T}\right)}_{\text{shear}},\end{aligned} \tag{E.35}$$

where $\boldsymbol{C} = \boldsymbol{F}^T\boldsymbol{F}$.

Viscous Parameters

It is now necessary to compute the viscous material parameters (i.e. κ_v and μ_v) by first recalling that the maximum time increment of the convective nature, Δt_c, is defined by

$$\Delta t_c = \alpha_{CFL}\frac{h_{min}}{U^n_{max}}, \tag{E.36}$$

where h_{min} is the minimum grid size, U^n_{max} describes the maximum wave speed presents at time level n and α_{CFL} denotes the Courant-Friedrichs-Lewy number. See Section 4.5.3 for detailed explanation. However, this convective time increment needs to be modified by taking account of the artificial viscosity that described above. For this reason, the new time increment can be defined as

$$\Delta t = \frac{\alpha_{CFL}h^2_{min}}{2\nu\alpha_{CFL} + U^n_{max}h_{min}}; \qquad \nu = \frac{\alpha\mu}{\rho_0}\Delta t_c, \tag{E.37}$$

where α describes a set of constant parameters. In the absence of viscosity, ν, the convective time increment (E.36) is simply recovered. Consequently, the viscous material parameters are evaluated as

$$\lambda_v = \alpha\lambda\Delta t; \qquad \mu_v = \alpha\mu\Delta t; \qquad \kappa_v = \lambda_v + \frac{2}{3}\mu_v; \tag{E.38}$$

where $\alpha = [0, 1]$.

E.2.1 Internal Energy Dissipation Rate

In isothermal irreversible process, the Clausius-Planck inequality (E.9) is repeated here for convenience:

$$D_{\text{int}} = \boldsymbol{P} : \dot{\boldsymbol{F}} - \dot{\psi} \geq 0. \tag{E.39}$$

Recall first that the perfectly elastic strain energy functional can be described as $\psi = \psi(\boldsymbol{F})$, its time derivative then leads to

$$\begin{aligned} \frac{\partial \psi(\boldsymbol{F})}{\partial t} &= \frac{\partial \psi(\boldsymbol{F})}{\partial \boldsymbol{F}} : \frac{\partial \boldsymbol{F}}{\partial t} \\ &= \boldsymbol{P}_e : \dot{\boldsymbol{F}}, \end{aligned} \tag{E.40}$$

where $\boldsymbol{P}_e := \partial\psi(\boldsymbol{F})/\partial\boldsymbol{F}$ denotes the elastic contribution of First Piola-Kirchhoff stress tensor. Substituting $\dot{\psi}$ from above equation into (E.39) yields

$$\begin{aligned} D_{\text{int}} &= (\boldsymbol{P} - \boldsymbol{P}_e) : \dot{\boldsymbol{F}} \geq 0 \\ &= \boldsymbol{P}_v : \dot{\boldsymbol{F}} \geq 0 \\ &= \boldsymbol{P}_v : \boldsymbol{\nabla}_0 \boldsymbol{v} \geq 0 \\ &= J\boldsymbol{\sigma}_v \boldsymbol{F}^{-T} : \boldsymbol{\nabla}_0 \boldsymbol{v} \geq 0 \\ &= J(\boldsymbol{\mathcal{C}}_v : \boldsymbol{d}) : \left(\boldsymbol{\nabla}_0 \boldsymbol{v} \boldsymbol{F}^{-1}\right) \geq 0 \\ &= J(\boldsymbol{d} : \boldsymbol{\mathcal{C}}_v : \boldsymbol{d}) \geq 0. \end{aligned} \tag{E.41}$$

Note the dissipation rate will be positive provided that the viscosity tensor $\boldsymbol{\mathcal{C}}_v$ is positive semidefinite.

Appendix F

Ghost or Dummy Cells

F.1 Introductory Remarks

The concept of dummy cells is very popular on structured grids [60, 98]. First by noting that the dummy cells are additional layers of virtual cells outside the bounded domain and clearly, their geometrical arrangements depend upon topological meshes inside the physical domain. For this purpose, it is necessary to develop a general framework for assigning the appropriate values of conservative variables at ghost cells.

F.2 Velocity and Traction Vectors

It is convenient to establish the linear momentum vector $\boldsymbol{p}^+$ and traction vector $\boldsymbol{t}^+$ at dummy cells. With the aid of these ghost values, the special formulas derived for boundary fluxes (discussed in Section 5.3) will be recovered. Three types of boundary conditions are presented as follows:

1. **Sticking Surface Case**: By assuming $\boldsymbol{p}^+ = -\boldsymbol{p}^-$ and $\boldsymbol{t}^+ = \boldsymbol{t}^-$ leads to

   - $\boldsymbol{p}^C = \boldsymbol{0}$.
   - $\boldsymbol{t}^C = \boldsymbol{t}^- - U_p^-(\boldsymbol{n}\otimes\boldsymbol{n})\boldsymbol{p}^- - U_s^-(\boldsymbol{I}-\boldsymbol{n}\otimes\boldsymbol{n})\boldsymbol{p}^-$.

2. **Sliding Surface Case**: The normal component of the linear momentum vector and the tangential component of the traction vector should vanish at contact point, which are mathematically defined by $(\boldsymbol{n}\otimes\boldsymbol{n})\boldsymbol{p}^+ = -(\boldsymbol{n}\otimes\boldsymbol{n})\boldsymbol{p}^-$ and $(\boldsymbol{I}-\boldsymbol{n}\otimes\boldsymbol{n})\boldsymbol{t}^+ = -(\boldsymbol{I}-\boldsymbol{n}\otimes\boldsymbol{n})\boldsymbol{t}^-$. In contrast, the tangential linear momentum vector and normal traction vector are $(\boldsymbol{I}-\boldsymbol{n}\otimes\boldsymbol{n})\boldsymbol{p}^+ = (\boldsymbol{I}-\boldsymbol{n}\otimes\boldsymbol{n})\boldsymbol{p}^-$ and $(\boldsymbol{n}\otimes\boldsymbol{n})\boldsymbol{t}^+ = (\boldsymbol{n}\otimes\boldsymbol{n})\boldsymbol{t}^-$, respectively. Above conditions imply

   - $\boldsymbol{p}^C = (\boldsymbol{I}-\boldsymbol{n}\otimes\boldsymbol{n})\boldsymbol{p}^- + \frac{1}{U_s^-}(\boldsymbol{I}-\boldsymbol{n}\otimes\boldsymbol{n})(\boldsymbol{t}^B-\boldsymbol{t}^-)$.
   - $\boldsymbol{t}^C = (\boldsymbol{n}\otimes\boldsymbol{n})\boldsymbol{t}^- + (\boldsymbol{I}-\boldsymbol{n}\otimes\boldsymbol{n})\boldsymbol{t}^B - U_p^-(\boldsymbol{n}\otimes\boldsymbol{n})\boldsymbol{p}^-$.

3. **Free Surface Case**: The conditions of linear momentum and traction vectors at ghost cells are described as $\boldsymbol{p}^+ = \boldsymbol{p}^-$ and $\boldsymbol{t}^+ = 2\boldsymbol{t}^B - \boldsymbol{t}^-$, which then yield

   - $\boldsymbol{p}^C = \boldsymbol{p}^- + \frac{1}{U_p^-}(\boldsymbol{n}\otimes\boldsymbol{n})(\boldsymbol{t}^B-\boldsymbol{t}^-) + \frac{1}{U_s^-}(\boldsymbol{I}-\boldsymbol{n}\otimes\boldsymbol{n})(\boldsymbol{t}^B-\boldsymbol{t}^-)$.
   - $\boldsymbol{t}^C = \boldsymbol{t}^B$.

Here, $\boldsymbol{t}^B$ describes the applied traction vector. Note that the linear momentum ($\boldsymbol{p}^+$) and traction vector ($\boldsymbol{t}^+ = \boldsymbol{P}^+\boldsymbol{N}$) at ghost cells are introduced. However, a more general discussion on assigning the deformation gradient (which in turn leads to stresses) will be presented.

F.3 Deformation Gradient Tensor

This section demonstrates a general framework for which the deformation gradient tensor $\boldsymbol{F}$ can be assigned into dummy (or ghost) cells. For this purpose, two conditions have to be fulfilled:

1. $\boldsymbol{F}^{+}_{\perp \boldsymbol{N}} = \boldsymbol{F}^{-}_{\perp \boldsymbol{N}}$.
2. The traction vector $\boldsymbol{t}^{+} = \boldsymbol{P}(\boldsymbol{F}^{+})\boldsymbol{N}$, which is already known and discussed in Section F.2.

Here, $+$ and $-$ represent ghost and interior domains, respectively. The tangential component of deformation gradient, $\boldsymbol{F}_{\perp \boldsymbol{N}}$, plays a crucial role in the development below. In general, the deformation gradient $\boldsymbol{F}$ is conveniently decomposed into the combination of tangential and normal components:

$$\boldsymbol{F} = \boldsymbol{F}_{\perp \boldsymbol{N}} + \boldsymbol{a} \otimes \boldsymbol{N}, \tag{F.1}$$

where $\boldsymbol{a}$ is an arbitrary spatial vector. Note that $\boldsymbol{F}_{\perp \boldsymbol{N}}$ denotes the tangential part and $\boldsymbol{a} \otimes \boldsymbol{N}$ describes the normal component of deformation gradient. The above expression can be written as

$$\boldsymbol{F}_{\perp \boldsymbol{N}} = \boldsymbol{F}\,(\boldsymbol{I} - \boldsymbol{N} \otimes \boldsymbol{N}) \tag{F.2}$$

with the aid of $\boldsymbol{a} = \boldsymbol{F}\boldsymbol{N}$. Since there is no jump in the direction orthogonal to $\boldsymbol{N}$ across the boundary face, $\boldsymbol{F}_{\perp \boldsymbol{N}}$ must remain the same

$$\boldsymbol{F}^{+}_{\perp \boldsymbol{N}} = \boldsymbol{F}^{-}_{\perp \boldsymbol{N}} = \boldsymbol{F}_{\perp \boldsymbol{N}}. \tag{F.3}$$

Therefore, the deformation gradient at ghost cell is defined by

$$\boldsymbol{F}^{+} = \boldsymbol{F}_{\perp \boldsymbol{N}} + \boldsymbol{a} \otimes \boldsymbol{N} \tag{F.4}$$

where $\boldsymbol{a}$ is yet to be specified.

In order to achieve this, it is necessary to establish a Newton-Raphson algorithm [7] to linearise the traction relationship $\boldsymbol{t}^{+} = \boldsymbol{P}(\boldsymbol{F}_{\perp \boldsymbol{N}} + \boldsymbol{a} \otimes \boldsymbol{N})\boldsymbol{N}$, which is clearly a nonlinear equation in $\boldsymbol{a}$. First by noting that the solution of a set of nonlinear algebraic equations is considered

$$\boldsymbol{R}(\boldsymbol{a}) = \boldsymbol{0}; \quad \boldsymbol{R} = \boldsymbol{P}(\boldsymbol{F}_{\perp \boldsymbol{N}} + \boldsymbol{a} \otimes \boldsymbol{N})\boldsymbol{N} - \boldsymbol{t}^{+}. \tag{F.5}$$

This type of nonlinear behaviour equations is generally solved based on Newton-Raphson iterative process. By giving an estimate solution $\boldsymbol{a}_k$ at iteration k, a new value $\boldsymbol{a}_{k+1}$ is obtained through the increment $\Delta\boldsymbol{a}$ by establishing the linear approximation

$$\boldsymbol{R}(\boldsymbol{a}_{k+1}) \approx \boldsymbol{R}(\boldsymbol{a}_k) + D\boldsymbol{R}(\boldsymbol{a}_k)[\Delta\boldsymbol{a}] = \boldsymbol{0}; \quad D\boldsymbol{R}(\boldsymbol{a}_k)[\Delta\boldsymbol{a}] = \boldsymbol{K}(\boldsymbol{a}_k)\Delta\boldsymbol{a}, \tag{F.6}$$

where the tangent stiffness matrix is described by

$$\boldsymbol{K}(\boldsymbol{a}_k) = \left.\frac{d\boldsymbol{R}}{d\boldsymbol{a}}\right|_{\boldsymbol{a}_k}. \tag{F.7}$$

Substituting (F.7) for the directional derivative into (F.6a) leads to a linear set of equations for $\Delta\boldsymbol{a}$ to be solved at each iterative process as

$$\Delta\boldsymbol{a} = -\left[\left.\frac{d\boldsymbol{R}}{d\boldsymbol{a}}\right|_{\boldsymbol{a}_k}\right]^{-1} \boldsymbol{R}(\boldsymbol{a}_k); \quad \boldsymbol{a}_{k+1} = \boldsymbol{a}_k + \Delta\boldsymbol{a}. \tag{F.8}$$

The residual vector at iteration k is denoted by

$$\boldsymbol{R}(\boldsymbol{a}_k) = \boldsymbol{P}(\boldsymbol{F}_{\perp N} + \boldsymbol{a}_k \otimes \boldsymbol{N})\boldsymbol{N} - \boldsymbol{t}^+. \tag{F.9}$$

Note that $\boldsymbol{K} = d\boldsymbol{R}/d\boldsymbol{a} = \boldsymbol{\mathcal{C}}_{NN}$[1] is detailed in Appendix D. The resulting Newton-Raphson algorithm is summarised in Algorithm F.3.1.

Algorithm F.3.1: ASSIGNING GHOST VALUES($\boldsymbol{F}^+, \boldsymbol{P}^+$)

(1). Given $\boldsymbol{F}^-$ and $\boldsymbol{P}^-$ of interior domain.
(2). Initialize $\boldsymbol{a} = \boldsymbol{F}^-\boldsymbol{N}$ and set $\Delta\boldsymbol{a} = [1, 0]^T$ and tolerance.
(3). Find $\boldsymbol{F}_{\perp N}$ from (F.2).
while ($\|\Delta\boldsymbol{a}\|$ > tolerance)
do
(4). Find $\boldsymbol{F}^+ = \boldsymbol{F}_{\perp N} + \boldsymbol{a} \otimes \boldsymbol{N}$.
(5). Solve $\boldsymbol{P}^+ = \boldsymbol{P}(\boldsymbol{F}^+)$. (Depends on constitutive model)
(6). Evaluate $\boldsymbol{R} = \boldsymbol{P}^+\boldsymbol{N} - \boldsymbol{t}^+$. (See Section F.2 for $\boldsymbol{t}^+$)
(7). Find $\boldsymbol{\mathcal{C}}_{NN}$. (see Appendix D)
(8). Solve $\Delta\boldsymbol{a} = -[\boldsymbol{\mathcal{C}}_{NN}]^{-1}\boldsymbol{R}$.
(9). Update $\boldsymbol{a} = \boldsymbol{a} + \Delta\boldsymbol{a}$.
return ($\boldsymbol{F}^+, \boldsymbol{P}^+$)

[1]The derivation for obtaining $\boldsymbol{K} = d\boldsymbol{R}/d\boldsymbol{a} = \boldsymbol{\mathcal{C}}_{NN}$ is performed below:

$$K_{ik} = \frac{dR_i}{da_k} = \frac{dP_{iI}}{da_k}N_I \tag{F.10a}$$

$$= \frac{dP_{iI}}{dF_{jJ}}\frac{dF_{jJ}}{da_k}N_I \tag{F.10b}$$

$$= \mathcal{C}_{iIjJ}\frac{d(a_jN_J)}{da_k}N_I \tag{F.10c}$$

$$= \mathcal{C}_{iIkJ}N_IN_J. \tag{F.10d}$$

Appendix G

Classical Structural Dynamics Formulations

G.1 Introductory Remarks

A variety of different classical time integration schemes have been proposed for solving structural dynamic problems [69]. The general semi-discrete displacement-based system of equations is given by [43, 44]

$$\boldsymbol{M}\ddot{\boldsymbol{u}}_{n+1} + \boldsymbol{T}(\boldsymbol{u}_{n+1}, \dot{\boldsymbol{u}}_{n+1}) = \hat{\boldsymbol{F}}(\boldsymbol{u}_{n+1}), \tag{G.1}$$

where $\boldsymbol{M}$ denotes the mass matrix, $\boldsymbol{T}$ describes the internal force vector and $\hat{\boldsymbol{F}}$ indicates the external force vector[1]. To solve this algebraic system of equations, the acceleration vector $\ddot{\boldsymbol{u}}_{n+1}$ has to be integrated in time for displacement field $\boldsymbol{u}_{n+1}$. The most widely used time integrator in structural dynamics is the method developed by Newmark (1959) [172]. A major drawback of this scheme is the tendency for high frequency noise to persist in the solution. Some minor modifications have been made in order to dissipate the high frequencies numerically for problems involving short wavelength [18–21]. Rather than providing a general overview of a large number of different approaches, detailed description of only Newmark method will be presented.

G.2 Newmark Method

G.2.1 Methodology

Newmark developed a family of time-stepping methods based on the following equations [172]:

$$\dot{\boldsymbol{u}}_{n+1} = \dot{\boldsymbol{u}}_n + \Delta t\left[(1-\gamma)\ddot{\boldsymbol{u}}_n + \gamma\ddot{\boldsymbol{u}}_{n+1}\right] \tag{G.2a}$$

$$\boldsymbol{u}_{n+1} = \boldsymbol{u}_n + \Delta t\dot{\boldsymbol{u}}_n + \frac{(\Delta t)^2}{2}\left[(1-2\beta)\,\ddot{\boldsymbol{u}}_n + 2\beta\ddot{\boldsymbol{u}}_{n+1}\right] \tag{G.2b}$$

where Δt is the time increment. The parameters γ and β determine the stability and accuracy of the algorithm.[2] In general, the Newmark family of implicit methods is unconditionally stable if $\gamma \geq 1/2$ and $\beta \geq (\gamma + 1/2)^2/4$ whereas, these implicit methods are conditionally stable provided that $\gamma \geq 1/2$ and $\beta < \gamma/2$ with the stability criterion $\omega\Delta t \leq \Omega_{\text{crit}}$. Here, Ω_{crit} denotes the stability condition and ω describes the natural frequency. Typical selection for $\gamma = 1/2$ and $\beta = 1/4$ yields a second-order, implicit and unconditionally stable trapezoidal Newmark scheme. Other Newmark family methods can be found in [69].

These two expressions (G.2a) and (G.2b), combining with second order dynamic equation (G.1) at time step $n+1$, provide the basis for computing $\boldsymbol{u}_{n+1}$, $\dot{\boldsymbol{u}}_{n+1}$ and $\ddot{\boldsymbol{u}}_{n+1}$ at time $n+1$ from the known $\boldsymbol{u}_n$, $\dot{\boldsymbol{u}}_n$ and $\ddot{\boldsymbol{u}}_n$ at time n. In order to achieve

[1] Do not confuse with deformation gradient tensor $\boldsymbol{F}$.

[2] Positive damping is introduced if $\gamma > 1/2$, whereas negative damping for $\gamma < 1/2$.

this, first by noting that (G.2b) can be rewritten as

$$\ddot{\boldsymbol{u}}_{n+1} = \frac{1}{\beta(\Delta t)^2}(\boldsymbol{u}_{n+1} - \boldsymbol{u}_n) - \left(\frac{1}{\beta\Delta t}\right)\dot{\boldsymbol{u}}_n - \left(\frac{1}{2\beta} - 1\right)\ddot{\boldsymbol{u}}_n, \tag{G.3}$$

substitute the above expression into (G.2a) yields

$$\dot{\boldsymbol{u}}_{n+1} = \frac{\gamma}{\beta\Delta t}(\boldsymbol{u}_{n+1} - \boldsymbol{u}_n) - \left(\frac{\gamma}{\beta} - 1\right)\dot{\boldsymbol{u}}_n - \left[\Delta t\left(\frac{\gamma}{2\beta} - 1\right)\right]\ddot{\boldsymbol{u}}_n. \tag{G.4}$$

With the aid of $\ddot{\boldsymbol{u}}_{n+1}$ and $\dot{\boldsymbol{u}}_{n+1}$, the second order dynamic equation (G.1) gives

$$\frac{1}{\beta(\Delta t)^2}\boldsymbol{M}\boldsymbol{u}_{n+1} + \boldsymbol{T}(\boldsymbol{u}_n, \dot{\boldsymbol{u}}_n, \ddot{\boldsymbol{u}}_n, \boldsymbol{u}_{n+1}) - \hat{\boldsymbol{F}}(\boldsymbol{u}_{n+1}) = \boldsymbol{M}\left[\frac{1}{\beta(\Delta t)^2}\boldsymbol{u}_n + \frac{1}{\beta\Delta t}\dot{\boldsymbol{u}}_n + \left(\frac{1}{2\beta} - \right)\ddot{\boldsymbol{u}}_n\right] \tag{G.5}$$

This nonlinear algebraic equations is solvable for $\boldsymbol{u}_{n+1}$ by using the conventional Newton-Raphson iterative method. With $\boldsymbol{u}_{n+1}$ at hand, the values for $\ddot{\boldsymbol{u}}_{n+1}$ and $\dot{\boldsymbol{u}}_{n+1}$ are subsequently obtained (see (G.3) and (G.4)).

G.2.2 Alternative Implementation: Predictor-Corrector Step

An alternative implementation for computing $\ddot{\boldsymbol{u}}_{n+1}$ is presented as follows [69]. By defining predictors as

$$\tilde{\boldsymbol{u}}_{n+1} = \boldsymbol{u}_n + \Delta t\dot{\boldsymbol{u}}_n + \frac{(\Delta t)^2}{2}(1 - 2\beta)\ddot{\boldsymbol{u}}_n; \qquad \tilde{\dot{\boldsymbol{u}}}_{n+1} = \dot{\boldsymbol{u}}_n + (1 - \gamma)\Delta t\ddot{\boldsymbol{u}}_n, \tag{G.6}$$

expressions (G.2a,b) can be consequently re-written as

$$\boldsymbol{u}_{n+1} = \tilde{\boldsymbol{u}}_{n+1} + \underbrace{\beta(\Delta t)^2\ddot{\boldsymbol{u}}_{n+1}}_{\text{corrector}}; \qquad \dot{\boldsymbol{u}}_{n+1} = \tilde{\dot{\boldsymbol{u}}}_{n+1} + \underbrace{\gamma\Delta t\ddot{\boldsymbol{u}}_{n+1}}_{\text{corrector}}. \tag{G.7}$$

First by noting that the residual form is given by

$$\boldsymbol{R}_{n+1} = \hat{\boldsymbol{F}}_{n+1} - \boldsymbol{M}\ddot{\boldsymbol{u}}_{n+1} - \boldsymbol{T}_{n+1}. \tag{G.8}$$

This expression can be approximated linearly by using Taylor series expansion about the known solution $\ddot{\boldsymbol{u}}_{n+1}^{k-1}$ which then yields

$$\boldsymbol{R}_{n+1}^{k} \approx \boldsymbol{R}_{n+1}^{k-1} + \left.\frac{\partial \boldsymbol{R}}{\partial \ddot{\boldsymbol{u}}}\right|_{n+1}^{k-1}\Delta\ddot{\boldsymbol{u}} = \boldsymbol{0}, \tag{G.9}$$

where k is the Newton-Raphson iterative process. By defining tangent stiffness matrix as $\hat{\boldsymbol{M}} = -\partial\boldsymbol{R}/\partial\ddot{\boldsymbol{u}}$, equation above can be rearranged as

$$\Delta\ddot{\boldsymbol{u}} = \left[\hat{\boldsymbol{M}}^{-1}\right]_{n+1}^{k-1}\boldsymbol{R}_{n+1}^{k-1}; \qquad \hat{\boldsymbol{M}} = \boldsymbol{M} + \gamma\Delta t\boldsymbol{C} + \beta(\Delta t)^2\boldsymbol{K}. \tag{G.10}$$

Here, $\boldsymbol{C}$ is the damping matrix. For simplicity, Rayleigh damping (which is a linear combination of stiffness and mass matrices) is used: $\boldsymbol{C} = \xi\boldsymbol{M} + \eta\boldsymbol{K}$ where ξ and

η are the mass and stiffness constants, respectively. Consequently, a new updated accelerating vector at iteration k is then obtained through the increment $\Delta\ddot{\boldsymbol{u}}$ by

$$\ddot{\boldsymbol{u}}_{n+1}^{k} = \ddot{\boldsymbol{u}}_{n+1}^{k-1} + \Delta\ddot{\boldsymbol{u}}. \tag{G.11}$$

For $k = 1$ iteration, the predictor for $\ddot{\boldsymbol{u}}_{n+1}^{k-1}$ at time step $n+1$ is estimated from the converged solution at previous time step n; that is, $\ddot{\boldsymbol{u}}_{n+1}^{0} = \ddot{\boldsymbol{u}}_{n}$. This iterative process continues until a certain convergence criterion is satisfied. Once the converged value $\ddot{\boldsymbol{u}}_{n+1}^{k}$ is obtained, it is trivial to compute $\dot{\boldsymbol{u}}_{n+1}$ and $\boldsymbol{u}_{n+1}$ with the aid of (G.7).

In order to give an overview of the implementation described above, the computational algorithm for standard finite element procedure in conjunction with a family of Newmark time integration schemes is illustrated as follows:

SOLUTION ALGORITHM

- INPUT geometry, material properties and solution parameters.
- FIND mass matrix $\boldsymbol{M}$ (see BOX G.1).
- INITIALISE $\boldsymbol{u}_0$, $\dot{\boldsymbol{u}}_0$, $\ddot{\boldsymbol{u}}_0$, $\boldsymbol{x} = \boldsymbol{X}$ (initial geometry), $\hat{\boldsymbol{F}} = \boldsymbol{0}$, $\boldsymbol{R} = \boldsymbol{0}$.
- LOOP over time
  - SET $\hat{\boldsymbol{F}}$, $i = 0$.
  - PREDICT solution variables: $\tilde{\boldsymbol{u}}$, $\tilde{\dot{\boldsymbol{u}}}$ (see (I.2)).
  - UPDATE geometry: $\boldsymbol{x} = \boldsymbol{X} + \tilde{\boldsymbol{u}}$.
  - FIND $\boldsymbol{T}$ (see BOX G.3), $\boldsymbol{K}$ (see BOX G.4).
  - COMPUTE $\boldsymbol{C} = \xi\boldsymbol{M} + \eta\boldsymbol{K}$, $\hat{\boldsymbol{M}}$ (viz. (G.10b)), $\boldsymbol{R} = \hat{\boldsymbol{F}} - \boldsymbol{M}\ddot{\boldsymbol{u}} - \boldsymbol{T}$.
  - DO WHILE($\|\boldsymbol{R}\|/\|\hat{\boldsymbol{F}}\| >$ tolerance AND $i <$ max. iter)
    - SOLVE $\Delta\ddot{\boldsymbol{u}} = \hat{\boldsymbol{M}}^{-1}\boldsymbol{R}$.
    - UPDATE $\ddot{\boldsymbol{u}} = \ddot{\boldsymbol{u}} + \Delta\ddot{\boldsymbol{u}}$, $i = i + 1$.
    - CORRECT solution variables: $\boldsymbol{u}$, $\dot{\boldsymbol{u}}$ (typically (G.7)).
    - UPDATE geometry: $\boldsymbol{x} = \boldsymbol{X} + \boldsymbol{u}$.
    - FIND $\boldsymbol{T}$, $\boldsymbol{K}$, $\boldsymbol{C}$, $\hat{\boldsymbol{M}}$, $\boldsymbol{R}$.
  - END DO
  - OUTPUT increment results
- END LOOP

G.2.3 Components Required

Elemental Mass Matrix

The elemental consistent mass matrix is given by [115]

$$\boldsymbol{M}_{ab}^{C,(e)} = \left(\int_{V^{(e)}} \rho_0 \hat{N}_a \hat{N}_b \, dV \right) \boldsymbol{I}. \tag{G.12}$$

It clearly shows that the mass matrix does not change with time (since it depends on material density ρ_0 and elemental undeformed volume $V^{(e)}$. This expression does not have to be recomputed during the simulation. In many applications, it is advantageous to use a diagonal (or lumped) mass matrix for computational cost. Making use of the row-sum technique, the diagonal mass matrix is obtained by

$$\begin{aligned} \boldsymbol{M}_{a}^{L,(e)} = \sum_b \boldsymbol{M}_{ab}^{C,(e)} &= \left(\int_{V^{(e)}} \rho_0 \hat{N}_a \left(\sum_b \hat{N}_b \right) dV \right) \boldsymbol{I} \\ &= \left(\int_{V^{(e)}} \rho_0 \hat{N}_a \, dV \right) \boldsymbol{I}. \end{aligned} \tag{G.13}$$

Note that the sum of the shape functions must equal to 1 [114].

BOX G.1: Elemental Mass Matrix $\boldsymbol{M}_{ab}^{(e)}$

- Consistent Mass Matrix:

$$\boldsymbol{M}_{ab}^{C,(e)} = \left(\int_{V^{(e)}} \rho_0 \hat{N}_a \hat{N}_b \, dV \right) \boldsymbol{I}$$

- Lumped Mass Matrix:

$$\boldsymbol{M}_{a}^{L,(e)} = \left(\int_{V^{(e)}} \rho_0 \hat{N}_a \, dV \right) \boldsymbol{I}$$

Constitutive Model

The boxes below summarise three different types of materials. These constitutive equations are presented in an indicial form for simplicity.

BOX G.2.1: 2D PLANE STRAIN COMPRESSIBLE NEO-HOOKEAN

- Cauchy stress tensor:

$$\boldsymbol{\sigma} = \frac{\mu}{J}(\boldsymbol{b} - \boldsymbol{I}) + \frac{\lambda}{J}(\ln J)\boldsymbol{I}; \qquad \sigma_{ij} = \frac{\mu}{J}(b_{ij} - \delta_{ij}) + \frac{\lambda}{J}(\ln J)\delta_{ij}$$

- Spatially isotropic tensor:

$$\mathscr{C} = \lambda' \boldsymbol{I} \otimes \boldsymbol{I} + \mu'(\boldsymbol{\mathcal{I}} + \hat{\boldsymbol{\mathcal{I}}}); \qquad \mathscr{C}_{ijkl} = \lambda' \delta_{ij}\delta_{kl} + \mu'(\delta_{ik}\delta_{jl} + \delta_{il}\delta_{jk})$$

$$\lambda' = \frac{\lambda}{J}; \qquad \mu' = \frac{\mu - \lambda \ln J}{J}; \qquad b_{ij} = F_{iI}F_{jI}$$

BOX G.2.2: 2D PLANE STRAIN NEARLY INCOMPRESSIBLE NEO-HOOKEAN

$$\bar{J} = \frac{v^{(e)}}{V^{(e)}}; \qquad v^{(e)} = \int_{v^{(e)}} dv; \qquad V^{(e)} = \int_{V^{(e)}} dV$$

$$p = \kappa_{2D}(\bar{J} - 1); \qquad \kappa_{2D} = \lambda + \mu$$

$$\bar{\kappa} = \kappa_{2D}\frac{v^{(e)}}{V^{(e)}}$$

$$\sigma'_{ij} = \mu J^{-2}(b_{ij} - \frac{1}{2}I_{\boldsymbol{b}}\delta_{ij}); \qquad I_{\boldsymbol{b}} = \mathrm{tr}(\boldsymbol{b}) = b_{kk}$$

$$\sigma_{ij} = \sigma'_{ij} + p\delta_{ij}$$

$$\hat{\mathscr{C}}_{ijkl} = \frac{\mu J^{-2}}{2}\left[I_{\boldsymbol{b}}(\delta_{ik}\delta_{jl} + \delta_{il}\delta_{jk}) - 2b_{ij}\delta_{kl} - 2\delta_{ij}b_{kl} + I_{\boldsymbol{b}}\delta_{ij}\delta_{kl}\right]$$

$$\mathscr{C}_{p,ijkl} = p(\delta_{ij}\delta_{kl} - \delta_{ik}\delta_{jl} - \delta_{il}\delta_{jk})$$

BOX G.2.3: 2D PLANE STRAIN HYPERELASTIC-PLASTIC IN PRINCIPAL DIRECTIONS

$$\bar{J} = \frac{v^{(e)}}{V^{(e)}}; \qquad \kappa_{2D} = \lambda + \mu$$

$$p = \kappa_{2D}\frac{\ln \bar{J}}{\bar{J}}; \qquad \bar{\kappa} = \frac{\kappa_{2D}}{\bar{J}} - p; \qquad \mathscr{C}_{p,ijkl} = p(\delta_{ij}\delta_{kl} - \delta_{ik}\delta_{jl} - \delta_{il}\delta_{jk})$$

$$\boldsymbol{b}^{(e)}_{trial} = \tilde{\boldsymbol{F}}^{(e)}\boldsymbol{C}_p^{-1,(e)}\tilde{\boldsymbol{F}}^{T,(e)}; \qquad \left[b^{(e)}_{trial}\right]_{ij} = \sum_{\alpha=1}^{3}\left(\lambda^{(e)}_{\alpha,trial}\right)^2 T_{\alpha i}T_{\alpha j}$$

$$\tau'^{,(e)}_{\alpha\alpha,trial} = 2\mu \ln \lambda^{(e)}_{\alpha,trial} - \frac{2}{3}\mu \ln J; \qquad J = \det \boldsymbol{F}^{(e)}_{(2\times 2)}$$

$$f(\boldsymbol{\tau}'^{,(e)}_{trial}, \bar{\varepsilon}_p) \le 0; \quad f(\boldsymbol{\tau}'^{,(e)}_{trial}, \bar{\varepsilon}_p) = \sqrt{\frac{3}{2}(\boldsymbol{\tau}'^{,(e)}_{trial} : \boldsymbol{\tau}'^{,(e)}_{trial})} - \bar{\tau}_y; \quad \bar{\tau}_y = \bar{\tau}^0_y + H\bar{\varepsilon}_p$$

$$\tau'^{,(e)}_{\alpha\alpha} = \tau'^{,(e)}_{\alpha\alpha,trial}; \qquad \Delta\gamma = 0; \qquad \nu_\alpha = 0$$

IF $f > 0$ THEN

$$\nu_\alpha = \frac{\tau'^{,(e)}_{\alpha\alpha,trial}}{\sqrt{\frac{2}{3}}\|\boldsymbol{\tau}'^{,(e)}_{trial}\|}; \qquad \Delta\gamma = \frac{f(\boldsymbol{\tau}'^{,(e)}_{trial}, \bar{\varepsilon}_p)}{3\mu + H}$$

$$\tau'^{,(e)}_{\alpha\alpha} = \left(1 - \frac{2\mu\Delta\gamma}{\sqrt{2/3}\|\boldsymbol{\tau}'^{,(e)}_{trial}\|}\right)\tau'^{,(e)}_{\alpha\alpha,trial}$$

END

$$\sigma^{(e)}_{ij} = \sigma'^{,(e)}_{ij} + p\delta_{ij}; \qquad \sigma'^{,(e)}_{ij} = \sum_{\alpha=1}^{3}\sigma'^{,(e)}_{\alpha\alpha}T_{\alpha i}T_{\alpha j}; \qquad \sigma'^{,(e)}_{\alpha\alpha} = \frac{1}{J}\tau'^{,(e)}_{\alpha\alpha}$$

$$\hat{\mathscr{C}}_{ijkl} = \sum_{\alpha,\beta=1}^{3}\frac{1}{J}\mathscr{C}_{\alpha\beta}T_{\alpha i}T_{\alpha j}T_{\beta k}T_{\beta l} - \sum_{\alpha=1}^{3}2\sigma'_{\alpha\alpha}T_{\alpha i}T_{\alpha j}T_{\alpha k}T_{\alpha l}$$

$$+ \sum_{\substack{\alpha,\beta=1\\ \alpha\neq\beta}}^{3}\frac{\sigma'_{\alpha\alpha}(\lambda^{(e)}_{\beta,trial})^2 - \sigma'_{\beta\beta}(\lambda^{(e)}_{\alpha,trial})^2}{(\lambda^{(e)}_{\alpha,trial})^2 - (\lambda^{(e)}_{\beta,trial})^2}(T_{\alpha i}T_{\beta j}T_{\alpha k}T_{\beta l} + T_{\alpha i}T_{\beta j}T_{\beta k}T_{\alpha l})$$

$$\mathscr{C}_{\alpha\beta} = \left(1 - \frac{2\mu\Delta\gamma}{\sqrt{2/3}\|\boldsymbol{\tau}'^{,(e)}_{trial}\|}\right)\left(2\mu\delta_{\alpha\beta} - \frac{2}{3}\mu\right) - 2\mu\nu_\alpha\nu_\beta\left(\frac{2\mu}{3\mu + H} - \frac{2\mu\sqrt{2/3}\Delta\gamma}{\|\boldsymbol{\tau}'^{,(e)}_{trial}\|}\right)$$

$$\lambda^{(e)}_\alpha = \mathrm{EXP}(\ln \lambda^{(e)}_{\alpha,trial} - \Delta\gamma\nu_\alpha); \qquad b^{(e)}_{ij} = \sum_{\alpha=1}^{3}(\lambda^{(e)}_\alpha)^2 T_{\alpha i}T_{\alpha j}$$

$$\boldsymbol{C}_p^{-1,(e)} = \tilde{\boldsymbol{F}}^{-1,(e)}\boldsymbol{b}^{(e)}\tilde{\boldsymbol{F}}^{-T,(e)}; \qquad \bar{\varepsilon}_p = \bar{\varepsilon}_p + \Delta\gamma$$

Note that $\tilde{\boldsymbol{F}}^{(e)}$ and $\boldsymbol{C}_p^{-1,(e)}$ are described by

$$\tilde{\boldsymbol{F}}^{(e)} = \begin{bmatrix} \boldsymbol{F}^{(e)}_{(2\times 2)} & & 0 \\ & & 0 \\ 0 & 0 & 1 \end{bmatrix} \qquad \boldsymbol{C}_p^{-1,(e)} = \begin{bmatrix} \boldsymbol{C}^{-1,(e)}_{p,(2\times 2)} & & 0 \\ & & 0 \\ 0 & 0 & C^{-1,(e)}_{p,(3,3)} \end{bmatrix}, \tag{G.14}$$

where $C^{-1,(e)}_{p,(3,3)} = 1/\det C^{-1,(e)}_{p,(2\times 2)}$.

Elemental Internal Nodal Forces

The calculation of the equivalent elemental internal nodal forces, $\boldsymbol{T}_a^{(e)}$, depends explicitly on the cauchy stress $\boldsymbol{\sigma}$ (which is found from an appropriate constitutive model). See [7] for futher details.

BOX G.3: EQUIVALENT ELEMENTAL NODAL FORCE $\boldsymbol{T}_a^{(e)}$

$$\boldsymbol{T}_a^{(e)} = \int_{v^{(e)}} \boldsymbol{\sigma}\boldsymbol{\nabla}_{\boldsymbol{x}}\hat{N}_a \, dv; \qquad T^{(e)}_{a,i} = \sum_{j=1}^{3} \int_{v^{(e)}} \sigma_{ij} \frac{\partial \hat{N}_a}{\partial x_j} \, dv.$$

Tangent Substiffness Matrix

The complete elemental tangent substiffness matrix is given by [7]

$$\boldsymbol{K}^{(e)}_{ab} = \boldsymbol{K}^{(e)}_{\mathscr{C},ab} + \boldsymbol{K}^{(e)}_{\boldsymbol{\sigma},ab} + \boldsymbol{K}^{(e)}_{\kappa,ab}, \tag{G.15}$$

where $\boldsymbol{K}^{(e)}_{\mathscr{C},ab}$ denotes the constitutive component of the tangent matrix, $\boldsymbol{K}^{(e)}_{\boldsymbol{\sigma},ab}$ describes the initial stress matrix and $\boldsymbol{K}^{(e)}_{\kappa,ab}$ represents the dilatational tangent stiffness component. $\boldsymbol{K}^{(e)}_{\kappa,ab}$ vanishes if the standard finite element procedure is used.

BOX G.4: COMPLETE ELEMENT TANGENT MATRIX $\boldsymbol{K}^{(e)}_{ab}$

$$\left[\boldsymbol{K}^{(e)}_{ab}\right]_{ij} = \left[\boldsymbol{K}^{(e)}_{\mathscr{C},ab}\right]_{ij} + \left[\boldsymbol{K}^{(e)}_{\boldsymbol{\sigma},ab}\right]_{ij} + \left[\boldsymbol{K}^{(e)}_{\kappa,ab}\right]_{ij}; \quad \forall i,j = 1,2,3$$

$$\left[\boldsymbol{K}^{(e)}_{\mathscr{C},ab}\right]_{ij} = \int_{v^{(e)}} \sum_{k,l=1}^{3} \frac{\partial \hat{N}_a}{\partial x_k} \mathscr{C}_{ikjl} \frac{\partial \hat{N}_b}{\partial x_l} \, dv$$

$$\left[\boldsymbol{K}^{(e)}_{\boldsymbol{\sigma},ab}\right]_{ij} = \int_{v^{(e)}} \sum_{k,l=1}^{3} \frac{\partial \hat{N}_a}{\partial x_k} \sigma_{kl} \frac{\partial \hat{N}_b}{\partial x_l} \delta_{ij} \, dv$$

$$\left[\boldsymbol{K}^{(e)}_{\kappa,ab}\right]_{ij} = \bar{\kappa} v^{(e)} \frac{\partial \hat{N}_a}{\partial \bar{x}_i} \frac{\partial \hat{N}_b}{\partial \bar{x}_j} \quad \text{where} \quad \frac{\partial \hat{N}_a}{\partial \bar{x}_\alpha} = \frac{1}{v^{(e)}} \int_{v^{(e)}} \frac{\partial \hat{N}_a}{\partial x_\alpha} \, dv$$

Appendix H

Library of Curl-Free Schemes

H.1 Introductory Remarks

The evolution of deformation gradient, $\dot{\boldsymbol{F}}$, has to satisfy some compatibility conditions (or the so-called involutions) in order to produce reliable solutions for long-term analysis. A great variety of different techniques have been developed but require a more in-depth study for future works.

H.2 New Governing Equations

This approach modifies the evolution equation (rate of deformation gradient) so that the curl errors in the constraint is advected away. Such approach is used to correct an existing error of the constraint.

The first order hyperbolic system of equations (see Chapter 2) is repeated for the sake of convenience

$$\frac{\partial \boldsymbol{p}}{\partial t} - \boldsymbol{\nabla}_0 \cdot \boldsymbol{P} = \rho_0 \boldsymbol{b}, \tag{H.1a}$$

$$\frac{\partial \boldsymbol{F}}{\partial t} - \boldsymbol{\nabla}_0 \cdot (\boldsymbol{v} \otimes \boldsymbol{I}) = \boldsymbol{0}, \tag{H.1b}$$

where $\boldsymbol{v} = \boldsymbol{p}/\rho_0$. The Rankine-hugoniot jump conditions for the above expressions are denoted by

$$U[\![\,\boldsymbol{p}\,]\!] = -[\![\,\boldsymbol{P}\,]\!]\boldsymbol{N}, \tag{H.2a}$$

$$U[\![\,\boldsymbol{F}\,]\!] = -\frac{1}{\rho_0}[\![\,\boldsymbol{p}\,]\!] \otimes \boldsymbol{N}, \tag{H.2b}$$

which in turn lead to six zero wave speeds. For instance, the jump of $\boldsymbol{F}$ in the direction of $\boldsymbol{T}_\alpha$ (such that $\boldsymbol{T}_\alpha \cdot \boldsymbol{N} = 0$) is

$$U[\![\,\boldsymbol{F}\,]\!]\boldsymbol{T}_\alpha = \boldsymbol{0}; \qquad \forall \alpha = 1, 2.$$

To correct this, it is essential to introduce an additional term into the fluxes of $\partial \boldsymbol{F}/\partial t$ by first noting that $\boldsymbol{\nabla}_0 \boldsymbol{F}^i$ should be symmetric, that is

$$\boldsymbol{\nabla}_0 \boldsymbol{F}^i = (\boldsymbol{\nabla}_0 \boldsymbol{F}^i)^T; \qquad F^i_{I,J} = F^i_{J,I}, \tag{H.3}$$

where $\boldsymbol{F}^i$ is the ith-row of deformation gradient tensor. To this end, a new evolutionary equation for the deformation gradient (based on the assumption that curl $\boldsymbol{F}^i \neq \boldsymbol{0}$) is expressed as

$$\frac{\partial \boldsymbol{F}}{\partial t} = \boldsymbol{\nabla}_0 \cdot \left(\boldsymbol{v} \otimes \boldsymbol{I} + \underbrace{\boldsymbol{F}\boldsymbol{H} \otimes \boldsymbol{I} - \boldsymbol{F} \otimes \boldsymbol{H}}_{\text{additional term}} \right). \tag{H.4}$$

Note that the additional term disappears if $\boldsymbol{F}$ satisfies the compatibility constraint (such as $\boldsymbol{\nabla}_0 \times \boldsymbol{F}^i = \boldsymbol{0}$). By virtue of (H.4), the jump relation becomes

$$U[\![\,\boldsymbol{F}\,]\!] = -\frac{1}{\rho_0}[\![\,\boldsymbol{p}\,]\!] \otimes \boldsymbol{N} - [\![\,\boldsymbol{F}\,]\!]\boldsymbol{H} \otimes \boldsymbol{N} + (\boldsymbol{H} \cdot \boldsymbol{N})[\![\,\boldsymbol{F}\,]\!]. \tag{H.5}$$

Here, $\boldsymbol{H}$ denotes an arbitrary constant wave propagation directional vector and is yet to be defined.

For this purpose, it is necessary to consider the jump of $\boldsymbol{F}$ in the direction of $\boldsymbol{N}$, $[\![\boldsymbol{F}]\!]\boldsymbol{N}$, that has to be identical to (H.2b). This implies that the wave propagation directional vector, $\boldsymbol{H}$, is defined by

$$\boldsymbol{H} = \alpha U_s \boldsymbol{N}; \qquad U_s = \sqrt{\frac{\mu}{\rho_0}}; \qquad \alpha = [0, 1]. \tag{H.6}$$

In contrast, the jump in $[\![\boldsymbol{F}]\!]\boldsymbol{T}_\alpha$ is now convected with travelling speed ($U = \boldsymbol{H}\cdot\boldsymbol{N}$), that is

$$U[\![\boldsymbol{F}]\!]\boldsymbol{T}_\alpha = (\boldsymbol{H}\cdot\boldsymbol{N})[\![\boldsymbol{F}]\!]\boldsymbol{T}_\alpha; \qquad \forall\alpha = 1, 2. \tag{H.7}$$

H.2.1 Linearised Riemann Solver

The interface fluxes (i.e. $\boldsymbol{t}^C$ and $\boldsymbol{p}^C$) at contact point have been derived using exclusively the jump condition of linear momentum variable, that is

$$U[\![\boldsymbol{p}]\!] = -[\![\boldsymbol{P}]\!]\boldsymbol{N}, \tag{H.8}$$

and therefore will not be affected (even with the new terms appeared in space-time evolution of $\boldsymbol{F}$). However, the new additional term in the rate of deformation gradient implies that the contact flux of $\boldsymbol{F}$ component, $\boldsymbol{\mathcal{F}}^C_{N,\boldsymbol{F}}$, is no longer just $-\boldsymbol{p}^C/\rho_0 \otimes \boldsymbol{N}$ but will become

$$\boldsymbol{\mathcal{F}}^C_{N,\boldsymbol{F}} = -\frac{1}{\rho_0}\boldsymbol{p}^C \otimes \boldsymbol{N} + \boldsymbol{\mathcal{H}}_N : \boldsymbol{F}^C, \tag{H.9}$$

where

$$\boldsymbol{\mathcal{H}}_N : \boldsymbol{F}^C = (\boldsymbol{H}\cdot\boldsymbol{N})\boldsymbol{F}^C - \boldsymbol{F}^C\boldsymbol{H}\otimes\boldsymbol{N}. \tag{H.10}$$

Note that the additional term, $\boldsymbol{\mathcal{H}}_N : \boldsymbol{F}^C$, is linear in $\boldsymbol{F}$.

The eigenstructure of $\boldsymbol{\mathcal{H}}_N$ is

$$\boldsymbol{\mathcal{H}}_N : \boldsymbol{F} = (\boldsymbol{H}\cdot\boldsymbol{N})\boldsymbol{F}, \qquad \boldsymbol{F} = \boldsymbol{a}\otimes\boldsymbol{T}_\alpha \tag{H.11}$$

for any arbitrary spatial vector $\boldsymbol{a}$. $\boldsymbol{T}_\alpha$ denotes the vector orthogonal to $\boldsymbol{N}$ ($\boldsymbol{T}_\alpha\cdot\boldsymbol{N} = 0$ where $\alpha = 1, 2$). It is worth noting that the wave speeds vanish if there is a jump of $\boldsymbol{F}$ in the direction of $\boldsymbol{N}$. For instance, $\boldsymbol{\mathcal{H}}_N : \boldsymbol{F} = \boldsymbol{0}$ if $\boldsymbol{F} = \boldsymbol{a}\otimes\boldsymbol{N}$. The above expression then leads to

$$|\boldsymbol{\mathcal{H}}_N| : \boldsymbol{F} = \begin{cases} \boldsymbol{\mathcal{H}}_N : \boldsymbol{F} & \text{if } (\boldsymbol{H}\cdot\boldsymbol{N} > 0) \\ -\boldsymbol{\mathcal{H}}_N : \boldsymbol{F} & \text{if } (\boldsymbol{H}\cdot\boldsymbol{N} < 0) \end{cases}. \tag{H.12}$$

Making use of (H.12) and the linearised Riemann solver (as described in Chapter 2), that is

$$\boldsymbol{\mathcal{H}}_N : \boldsymbol{F}^C = \frac{1}{2}\boldsymbol{\mathcal{H}}_N : (\boldsymbol{F}^- + \boldsymbol{F}^+) - \frac{1}{2}|\boldsymbol{\mathcal{H}}_N| : (\boldsymbol{F}^+ - \boldsymbol{F}^-), \tag{H.13}$$

the additional contact flux can be derived as

$$\boldsymbol{\mathcal{H}}_N : \boldsymbol{F}^C = \begin{cases} \boldsymbol{\mathcal{H}}_N : \boldsymbol{F}^- & \text{if } (\boldsymbol{H} \cdot \boldsymbol{N} > 0) \\ \boldsymbol{\mathcal{H}}_N : \boldsymbol{F}^+ & \text{if } (\boldsymbol{H} \cdot \boldsymbol{N} < 0) \end{cases} \tag{H.14}$$

The complete interface flux of $\boldsymbol{F}$ component at contact point is denoted by

$$\begin{aligned} \boldsymbol{\mathcal{F}}^C_{N,\boldsymbol{F}} &= -\frac{1}{\rho_0}\boldsymbol{p}^C \otimes \boldsymbol{N} + \boldsymbol{\mathcal{H}}_N : \boldsymbol{F}^- \\ &= -\frac{1}{\rho_0}\boldsymbol{p}^C \otimes \boldsymbol{N} + (\boldsymbol{H} \cdot \boldsymbol{N})\boldsymbol{F}^- - \boldsymbol{F}^-\boldsymbol{H} \otimes \boldsymbol{N}, \end{aligned} \tag{H.15}$$

since $\boldsymbol{H} \cdot \boldsymbol{N} > 0$ (see (H.6)).

H.3 Extended Approach for Curl-Preserving Updated Scheme

The locally curl-preserving updated scheme discussed previously might lead to the presence of non-physical low-energy modes. This can be explained by the nodal collocation nature of the averaging algorithm employed. It is possible to remove these unrealistic modes by defining a more refined approach for the computation of the nodal velocity, $\boldsymbol{v}_a$, as

$$\boldsymbol{v}_a = v_a \boldsymbol{\nu}, \tag{H.16}$$

where the magnitude and the direction of the velocity at node a are

$$v_a = \frac{\left\| \sum_k A_k \boldsymbol{v}_k \right\|}{\sum_k A_k} \tag{H.17}$$

and

$$\boldsymbol{\nu} = \begin{cases} \dfrac{\sum_k A_k \boldsymbol{v}_k}{\left\| \sum_k A_k \boldsymbol{v}_k \right\|} & \text{if } \left\| \sum_k A_k \boldsymbol{v}_k \right\| > tol \\ \dfrac{\boldsymbol{v}_{max}}{\|\boldsymbol{v}_{max}\|} & \text{Otherwise} \end{cases}, \tag{H.18}$$

respectively. Here, $\|\boldsymbol{v}_{max}\| = \max \|\boldsymbol{v}_k\|$, tol denotes the tolerance and kth-edge belongs to node a. Note that if $\left\| \sum_k A_k \boldsymbol{v}_k \right\| > tol$ is satisfied, the area-weighted averaging process will simply be recovered, that is

$$\boldsymbol{v}_a = \frac{1}{A_a} \sum_{\substack{k \\ k \in a}} A_k \boldsymbol{v}_k; \qquad A_a = \sum_{\substack{k \\ k \in a}} A_k. \tag{H.19}$$

In principle, the procedure described above eliminates the spurious modes of deformation. However, none of the computational examples demonstrated in this thesis has shown any evidence of spurious (or hourglassing) modes and the area-weighted averaging process has been used throughout.

H.4 Two-Dimensional Orthogonal Curl-Free Projection

Another alternative approach for eliminating curl errors in the context of finite element method will also be introduced (see [173] for detailed explanations). The main idea is to correct the nodal deformation gradient by making use of the orthogonal derivative of the shape functions in an element-wise manner. First by noting that the curl $\boldsymbol{F}$ can be expressed as

$$\boldsymbol{\nabla}_0 \times \boldsymbol{F} = \boldsymbol{F}\boldsymbol{\nabla}_0^{\perp}; \qquad \boldsymbol{F} = \begin{pmatrix} F_{11} & F_{12} \\ F_{21} & F_{22} \end{pmatrix}; \qquad \boldsymbol{\nabla}_0^{\perp} = \begin{pmatrix} -\frac{\partial}{\partial X_2} \\ \frac{\partial}{\partial X_1} \end{pmatrix}. \tag{H.20}$$

Discretise the above curl-free condition gives

$$\boldsymbol{\nabla}_0 \times \boldsymbol{F} = \boldsymbol{F}\boldsymbol{\nabla}_0^{\perp} = \sum_{\substack{a=1 \\ a\in e}}^{Nn_e} \boldsymbol{F}^a \boldsymbol{\nabla}_0^{\perp} \hat{N}_a; \qquad \boldsymbol{\nabla}_0^{\perp} \hat{N}_a = \begin{pmatrix} -\frac{\partial \hat{N}_a}{\partial X_2} \\ \frac{\partial \hat{N}_a}{\partial X_1} \end{pmatrix}. \tag{H.21}$$

Note that $\boldsymbol{\nabla}_0^{\perp}\hat{N}_a$ denotes the orthogonal derivative of the shape functions (such as $\boldsymbol{\nabla}_0^{\perp}\hat{N}_a \cdot \boldsymbol{\nabla}_0 \hat{N}_a = 0$) and Nn_e describes the total number of nodes that belong to the element e.

It is now convenient to introduce a functional Π defined by

$$\Pi(\hat{\boldsymbol{F}}^a, \boldsymbol{\lambda}) = \left(\frac{1}{2} \sum_{\substack{a=1 \\ a\in e}}^{Nn_e} (\hat{\boldsymbol{F}}^a - \boldsymbol{F}^a) : (\hat{\boldsymbol{F}}^a - \boldsymbol{F}^a) \right) + \boldsymbol{\lambda} \cdot \left(\sum_{\substack{a=1 \\ a\in e}}^{Nn_e} \hat{\boldsymbol{F}}^a \boldsymbol{\nabla}_0^{\perp} \hat{N}_a \right), \tag{H.22}$$

where $\hat{\boldsymbol{F}}^a$ describes the corrected deformation gradient at node a and $\boldsymbol{\lambda}$ denotes the Lagrange multiplier vector. The stationary condition of the above functional (H.22) with respect to $\boldsymbol{\lambda}$ and $\hat{\boldsymbol{F}}^a$ will be considered separately. Note firstly that the derivative of Π with respect to $\boldsymbol{\lambda}$ is

$$\frac{\partial \Pi}{\partial \boldsymbol{\lambda}} = \left(\sum_{\substack{a=1 \\ a\in e}}^{Nn_e} \hat{\boldsymbol{F}}^a \boldsymbol{\nabla}_0^{\perp} \hat{N}_a \right) = \boldsymbol{0}. \tag{H.23}$$

This implies that the elemental curl-free condition will be achieved if and only if the summation of all the corrected nodal deformation gradients multiply by their corresponding orthogonal derivative shape functions vanishes. Additionally, the derivative of (H.22) with respect to $\hat{\boldsymbol{F}}^a$ is given as

$$\frac{\partial \Pi}{\partial \hat{\boldsymbol{F}}^a} = \sum_{\substack{a=1 \\ a\in e}}^{Nn_e} (\hat{\boldsymbol{F}}^a - \boldsymbol{F}^a) + \sum_{\substack{a=1 \\ a\in e}}^{Nn_e} \boldsymbol{\lambda} \otimes \boldsymbol{\nabla}_0^{\perp} \hat{N}_a = \boldsymbol{0}. \tag{H.24}$$

Rearrange the above expression gives the corrected deformation gradient as

$$\hat{\boldsymbol{F}}^a = \boldsymbol{F}^a - \underbrace{\boldsymbol{\lambda} \otimes \boldsymbol{\nabla}_0^{\perp} \hat{N}_a}_{\text{correction term}}. \tag{H.25}$$

Once $\boldsymbol{\lambda}$ is determined, the corrected deformation gradient $\hat{\boldsymbol{F}}^a$ can be obtained by substituting $\boldsymbol{\lambda}$ into (H.25). For this reason, it is essential to insert (H.25) into (H.23) for $\hat{\boldsymbol{F}}^a$ which then yields

$$\sum_{\substack{a=1 \\ a\in e}}^{Nn_e} \boldsymbol{F}^a \boldsymbol{\nabla}_0^{\perp} \hat{N}_a - \boldsymbol{\lambda} \sum_{\substack{a=1 \\ a\in e}}^{Nn_e} (\boldsymbol{\nabla}_0^{\perp} \hat{N}_a \cdot \boldsymbol{\nabla}_0^{\perp} \hat{N}_a) = \mathbf{0}. \tag{H.26}$$

Consequently, $\boldsymbol{\lambda}$ is derived as follows:

$$\boldsymbol{\lambda} = \frac{\sum_{\substack{a=1 \\ a\in e}}^{Nn_e} \boldsymbol{F}^a \boldsymbol{\nabla}_0^{\perp} \hat{N}_a}{\sum_{\substack{a=1 \\ a\in e}}^{Nn_e} \boldsymbol{\nabla}_0^{\perp} \hat{N}_a \cdot \boldsymbol{\nabla}_0^{\perp} \hat{N}_a}. \tag{H.27}$$

This ensures that the orthogonal projection onto curl-free space is obtained in an element-wise manner.

H.5 Curl Viscous Flux

To prevent spurious modes for long time integration, it is essential to introduce a diffusive term into the evolution of deformation gradient as [118]

$$\frac{\partial \boldsymbol{F}}{\partial t} - \boldsymbol{\nabla}_0 \cdot \left(\frac{1}{\rho_0} \boldsymbol{p} \otimes \boldsymbol{I} \right) + \underbrace{\alpha_{visc} \boldsymbol{\nabla}_0 \times (\boldsymbol{\nabla}_0 \times \boldsymbol{F})}_{\text{diffusive term}} = \mathbf{0}, \tag{H.28}$$

where $\alpha_{visc} \in [0, 1]$. With the aid of vector calculus identity, the diffusive term can be expanded to

$$\boldsymbol{\nabla}_0 \times (\boldsymbol{\nabla}_0 \times \boldsymbol{F}) = \boldsymbol{\nabla}_0 \cdot [(\boldsymbol{\nabla}_0 \cdot \boldsymbol{F}) \otimes \boldsymbol{I} - \boldsymbol{\nabla}_0 \boldsymbol{F}]. \tag{H.29}$$

Substituting the above expression into (H.28) yields

$$\frac{\partial \boldsymbol{F}}{\partial t} - \boldsymbol{\nabla}_0 \cdot \left[\frac{1}{\rho_0} \boldsymbol{p} \otimes \boldsymbol{I} + \alpha_{visc} (\boldsymbol{\nabla}_0 \boldsymbol{F} - (\boldsymbol{\nabla}_0 \cdot \boldsymbol{F}) \otimes \boldsymbol{I}) \right] = \mathbf{0}. \tag{H.30}$$

This approach has been implemented in two-step Taylor Galerkin framework with only partially successful [64].

Appendix I

Methodologies for New Conservation-Law Formulation

I.1 Two Step Taylor-Galerkin Method

I.1.1 Computational Methodology

In this section, a two-step predictor-corrector scheme (or Runge-Kutta type) is introduced [64]. Such procedure avoids the evaluation of the flux Jacobian matrix, $\boldsymbol{\mathcal{A}}_N$, that appears in one-step Taylor-Galerkin approach [83]. First, it is necessary to predict the unknown variables, $\boldsymbol{\mathcal{U}}$, at half time step $t^{n+1/2}$ with the aid of Taylor series expansion, that is

$$\boldsymbol{\mathcal{U}}^{n+1/2} = \boldsymbol{\mathcal{U}}^n + \frac{1}{2}\Delta t \frac{\partial \boldsymbol{\mathcal{U}}^n}{\partial t} = \boldsymbol{\mathcal{U}}^n - \frac{1}{2}\Delta t \frac{\partial \boldsymbol{\mathcal{F}}_I^n}{\partial X_I}; \qquad \frac{\partial \boldsymbol{\mathcal{U}}}{\partial t} = -\frac{\partial \boldsymbol{\mathcal{F}}_I}{\partial X_I}. \tag{I.1}$$

For simplicity, the source term $\boldsymbol{\mathcal{S}}$ is neglected. We shall then discretise the kinematics in the above expression as

$$\boldsymbol{\mathcal{U}}_a^{n+1/2} = \boldsymbol{\mathcal{U}}_a^n \underbrace{- \frac{1}{2}\Delta t \sum_{\substack{b=1 \\ b\in e}}^{N_{ne}} \boldsymbol{\mathcal{F}}_I^{b,n} \frac{\partial \hat{N}_b}{\partial X_I}}_{\text{elemental increment}}; \qquad \forall a \in e \tag{I.2}$$

or in complete form

$$\boldsymbol{p}_a^{n+1/2} = \boldsymbol{p}_a^n + \frac{1}{2}\Delta t \sum_{\substack{b=1 \\ b\in e}}^{N_{ne}} \boldsymbol{P}_b^n \frac{\partial \hat{N}_b}{\partial \boldsymbol{X}} \tag{I.3a}$$

$$\boldsymbol{F}_a^{n+1/2} = \boldsymbol{F}_a^n + \frac{1}{2}\Delta t \sum_{\substack{b=1 \\ b\in e}}^{N_{ne}} \boldsymbol{v}_b^n \otimes \frac{\partial \hat{N}_b}{\partial \boldsymbol{X}} \tag{I.3b}$$

$$E_a^{n+1/2} = E_a^n + \frac{1}{2}\Delta t \sum_{\substack{b=1 \\ b\in e}}^{N_{ne}} [\boldsymbol{P}^T]_b^n \boldsymbol{v}_b^n \cdot \frac{\partial \hat{N}_b}{\partial \boldsymbol{X}} \tag{I.3c}$$

where $\boldsymbol{\mathcal{F}}_I^{b,n} = \boldsymbol{\mathcal{F}}_I(\boldsymbol{\mathcal{U}}_b^n)$ and N_{ne} denotes the total number of local nodes belongs to element e. This implies that the evolution step is entirely contained in element e, as the elemental increment is evaluated locally.

Unfortunately, the predicted deformation gradient obtained above (see equation (I.3b)), develops some non-physical low-energy modes in the solution [59]. To alleviate this, Izian *et al.* [64] introduced a stiffness stabilisation with the aim at eliminating these spurious modes, which can be written as

$$\boldsymbol{F}_a^{n+1/2} \longleftarrow (1-\bar{\alpha})\boldsymbol{F}_a^{n+1/2} + \bar{\alpha} \underbrace{\left(\sum_{\substack{b=1 \\ b\in e}}^{N_{ne}} \boldsymbol{x}_b^{n+1/2} \otimes \frac{\partial \hat{N}_b}{\partial \boldsymbol{X}} \right)}_{\text{stiffness stabilisation}}; \qquad \boldsymbol{x}_b^{n+1/2} = \boldsymbol{x}_b^n + \frac{\Delta t}{2}\boldsymbol{v}_b^n, \tag{I.4}$$

where $\bar{\alpha} \in [0, 1]$. By virtue of (I.4), the added stabilising term is introduced locally using the standard finite element discretisation for $\boldsymbol{F}^{n+1/2} = \boldsymbol{\nabla}_0 \boldsymbol{x}^{n+1/2}$. The choice

of $\bar{\alpha}$ parameter allows removing of instabilities observed in bending-dominated situations [59]. Here, $\bar{\alpha} = 0$ leads to the Taylor-Galerkin predictor step, whereas $\bar{\alpha} = 1$ recovers the standard finite element formulation for $\boldsymbol{F}^{n+1/2}$, which clearly exhibits overly stiff behaviour [7]. The expression above can also be alternatively represented as

$$\boldsymbol{F}_a^{n+1/2} = (1-\bar{\alpha})\boldsymbol{F}_a^n + \underbrace{\sum_{\substack{b=1 \\ b\in e}}^{N_{ne}} \left(\bar{\alpha}\boldsymbol{x}_b^n + \frac{\Delta t}{2}\boldsymbol{v}_b^n\right) \otimes \frac{\partial \hat{N}_b}{\partial \boldsymbol{X}}}_{\text{elemental contribution}}. \tag{I.5}$$

In addition, the deformation gradient $\boldsymbol{F}_a$ has to be corrected by using curl-free projection in order to satisfy the compatibility constraint:

$$\hat{\boldsymbol{F}}_a^{n+\beta} = \boldsymbol{F}_a^{n+\beta} - \boldsymbol{\lambda}^{n+\beta} \otimes \boldsymbol{\nabla}_0^{\perp}\hat{N}_a; \qquad \boldsymbol{\lambda}^{n+\beta} = \frac{\sum_{\substack{a=1 \\ a\in e}}^{Nn_e} \boldsymbol{F}_a^{n+\beta}\boldsymbol{\nabla}_0^{\perp}\hat{N}_a}{\sum_{\substack{a=1 \\ a\in e}}^{Nn_e} \boldsymbol{\nabla}_0^{\perp}\hat{N}_a \cdot \boldsymbol{\nabla}_0^{\perp}\hat{N}_a}; \qquad \beta = 0, 1/2. \tag{I.6}$$

See Section H.4 for detailed development of this particular approach.

It is now convenient to evolve the unknown variable to full time step t^{n+1} (or corrector-step) by employing conventional Taylor expansion as

$$\boldsymbol{\mathcal{U}}^{n+1} = \boldsymbol{\mathcal{U}}^n + \Delta t\frac{\partial \boldsymbol{\mathcal{U}}^{n+1/2}}{\partial t} = \boldsymbol{\mathcal{U}}^n - \Delta t\frac{\partial \boldsymbol{\mathcal{F}}_I^{n+1/2}}{\partial X_I}, \tag{I.7}$$

where $\boldsymbol{\mathcal{F}}_I^{n+1/2} = \boldsymbol{\mathcal{F}}_I(\boldsymbol{\mathcal{U}}^{n+1/2})$. Multiplying the above expression with shape function $\hat{N}_a$ and integrate over the elemental volume V_e, with the aid of integration by parts, gives

$$\sum_{\substack{b=1 \\ b\in e}}^{N_{ne}} \boldsymbol{M}_{ab}^C \boldsymbol{\mathcal{U}}_b^{n+1} = \sum_{\substack{b=1 \\ b\in e}}^{N_{ne}} \boldsymbol{M}_{ab}^C \hat{\boldsymbol{\mathcal{U}}}_b^n + \Delta t\hat{\boldsymbol{R}}_a^{n+1/2}; \qquad \forall a \in e, \tag{I.8}$$

where

$$\boldsymbol{M}_{ab}^C = \left(\int_{V_e} \hat{N}_a\hat{N}_b\, dV\right)\boldsymbol{I}; \qquad \hat{\boldsymbol{R}}_a^{n+1/2} = \int_{V_e} \frac{\partial \hat{N}_a}{\partial X_I}\hat{\boldsymbol{\mathcal{F}}}_I^{n+1/2}\, dV - \int_{\partial V_e} \hat{N}_a\hat{\boldsymbol{\mathcal{F}}}_N^{n+1/2}\, dA, \tag{I.9}$$

and

$$\hat{\boldsymbol{\mathcal{F}}}_N^{n+1/2} = \hat{\boldsymbol{\mathcal{F}}}_I^{n+1/2}N_I; \qquad \hat{\boldsymbol{\mathcal{F}}}_I^{n+1/2} = \boldsymbol{\mathcal{F}}_I(\hat{\boldsymbol{\mathcal{U}}}^{n+1/2}); \qquad \hat{\boldsymbol{\mathcal{U}}} = (\boldsymbol{p}, \hat{\boldsymbol{F}}, E)^T. \tag{I.10}$$

Here, $\boldsymbol{M}_{ab}^C$ denotes the consistent mass matrix and the interface flux $\boldsymbol{\mathcal{F}}_N$ will be computed based upon nonlinear Riemann solver (see Chapter 5). For computational efficiency, this matrix will be replaced by lumped mass matrix, that is

$$\boldsymbol{M}_a^L = \left(\int_{V_e} \hat{N}_a \sum_{\substack{b=1 \\ b\in e}}^{N_{ne}} \hat{N}_b\, dV\right)\boldsymbol{I} = \left(\int_{V_e} \hat{N}_a\, dV\right)\boldsymbol{I}, \tag{I.11}$$

with the aid of $\sum_{\substack{b=1 \\ b\in e}}^{N_{ne}} \hat{N}_b = 1$.

I.1.2 Solution Procedure

The solution procedure for two-step Taylor Galerkin method satisfying involution is illustrated as follows [173]:

SOLUTION ALGORITHM

- GIVEN $\boldsymbol{\mathcal{U}}_a^n = (\boldsymbol{p}_a^n, \boldsymbol{F}_a^n, E_a^n)^T$.
- FIND lumped mass matrix $\boldsymbol{M}_a^L$ (or consistent mass matrix $\boldsymbol{M}_{ab}^C$); see (I.11b)(or (I.9a)).
- EVALUATE fluxes $\boldsymbol{\mathcal{F}}_I^{a,n} = \boldsymbol{\mathcal{F}}_I(\boldsymbol{\mathcal{U}}_a^n)$.
- LOOP over time
  - UPDATE time increment Δt (see (E.2)).
  - ☐ PREDICTOR STEP: ELEMENT-BASED
  - CORRECT $\boldsymbol{F}_a^n$ by using elemental curl-free projection, $\hat{\boldsymbol{F}}_a^n$ (see (I.6)).
  - PREDICT element nodal unknown variables $\boldsymbol{\mathcal{U}}_a^{n+1/2}$ (use (I.2)).
  - INTRODUCE stiffness stabilisation for $\boldsymbol{F}_a^{n+1/2}$ (viz. (I.4)).
  - CORRECT $\boldsymbol{F}_a^{n+1/2}$ by using elemental curl-free projection, $\hat{\boldsymbol{F}}_a^{n+1/2}$ (see (I.6)).
  - INTERPOLATE corrected local unknown variables $\hat{\boldsymbol{\mathcal{U}}}_a^{n+1/2}$ at Gauss point g (that is, $\hat{\boldsymbol{\mathcal{U}}}_g^{n+1/2}$).
  - COMPUTE fluxes at Gauss point, $\boldsymbol{\mathcal{F}}_I^{g,n+1/2} = \boldsymbol{\mathcal{F}}_I(\hat{\boldsymbol{\mathcal{U}}}_g^{n+1/2})$.
  - FIND viscous first Piola-Kirchhoff stress tensor $\boldsymbol{P}_v$ at Gauss point if necessary (see (E.35)).
  - ☐ CORRECTOR STEP: NODE-BASED
  - EVALUATE the residual vector $\hat{\boldsymbol{R}}_a^{n+1/2}$ (viz. (I.9b)), which consists of the volumental contribution $\boldsymbol{T}_a^{n+1/2}$ and boundary term $\boldsymbol{B}_a^{n+1/2}$ at Gauss point (that is, $\hat{\boldsymbol{R}}_a^{n+1/2} = \boldsymbol{T}_a^{n+1/2} + \boldsymbol{B}_a^{n+1/2}$).
  - UPDATE global unknown nodal variables $\boldsymbol{\mathcal{U}}_a^{n+1} = (\boldsymbol{p}_a^{n+1}, \boldsymbol{F}_a^{n+1}, E_a^{n+1})^T$ using (I.8).
  - APPLY strong boundary conditions on $\boldsymbol{p}_a^{n+1}$ and $\boldsymbol{F}_a^{n+1}$, except for the case where $\boldsymbol{F}_a^{n+1}$ at free surface boundary (see Section I.3).
  - COMPUTE fluxes at node a, $\boldsymbol{\mathcal{F}}_I^{a,n+1} = \boldsymbol{\mathcal{F}}_I(\boldsymbol{\mathcal{U}}_a^{n+1})$.
  - APPLY strong boundary conditions on the first Piola-Kirchhoff stress tensor $\boldsymbol{P}_a^{n+1}$ at free boundary case (see Section I.3).

- UPDATE nodal velocity $\boldsymbol{v}_a^{n+1}$ and mesh coordinates $\boldsymbol{x}_a^{n+1}$.
- OUTPUT increment results.

- END time loop

I.2 Curl-Free Cell Centred Upwind Finite Volume Scheme

I.2.1 Solution Procedure

The solution procedure for cell centred finite volume methodology is presented as belows:

SOLUTION ALGORITHM (Global node a, Centroid of element e)

- GIVEN $\boldsymbol{\mathcal{U}}_e^n = (\boldsymbol{p}_e^n, \boldsymbol{F}_e^n, E_e^n)^T$.
- EVALUATE $\boldsymbol{P}_e^n = \boldsymbol{P}(\boldsymbol{F}_e^n)$ (depends on constitutive model).
- LOOP over time
  - UPDATE time increment Δt (see (4.22)).
  - EVOLVE centroid coordinates $\boldsymbol{x}_e^{n+\frac{1}{\eta}} = \boldsymbol{x}_e^n + \frac{1}{\eta}\Delta t \boldsymbol{v}_e^n$, where η describes the Runge-Kutta stages (viz. (6.6b) and (6.8b)).
  - LOOP over Runge-Kutta stages
    - EXTRAPOLATE averaged component value $\mathcal{U}_e \in \{\boldsymbol{p}_e, \boldsymbol{F}_e, \boldsymbol{P}_e\}$ to contact point k; that is, $\mathcal{U}_{e\alpha}$ where $\{e, \alpha\} \in k$ (See Section 4.4).
    - COMPUTE nonlinear flux, $[\boldsymbol{\mathcal{F}}_N^C]_k$, at contact point k by using Lagrangian contact algorithm (as discussed in Chapter 5).
    - CORRECT the contact traction vector at point k, $[\boldsymbol{t}^C]_k$, for preserving the total angular momentum of a system (see Section 6.3).
    - FIND nodal velocity $\boldsymbol{v}_a$ by making use of the area-weighted averaging technique. Boundary nodal velocities are then corrected via linear extrapolation from interior known values (see Chapter 7).
    - APPLY strong boundary conditions on nodal velocity $\boldsymbol{v}_a$.

- COMPUTE averaged velocity $\boldsymbol{v}_e$ by linearly interpolating nodal velocities, $\boldsymbol{v}_a$, at centroid of the element. This will be used for updating the centroid coordinates $\boldsymbol{x}_e$.
- UPDATE centroid, $\boldsymbol{x}_e$, and nodal coordinates $\boldsymbol{x}_a$, and also the unknown variables $\boldsymbol{\mathcal{U}}_e$ (see (4.21)).
- EVALUATE $\boldsymbol{P}_e^n = \boldsymbol{P}(\boldsymbol{F}_e^n)$ (depends on constitutive model).

- END Runge-Kutta loop
- OUTPUT increment results.

- END time loop

I.3 2D Strong Boundary Conditions: Node-based

Variables (i.e. linear momentum, deformation gradient and first Piola-Kirchhoff stress) have to be corrected at every time step to ensure that they satisfy the correct physical behaviour at the boundary. This correction is of paramount importance and will lead to spurious-free solutions [173]. As discussed previously, three types of boundary conditions are considered:

I.3.1 Sticking Surface Case

The nodal linear momentum vanishes due to no-slip condition [26], which yields

$$\boldsymbol{p}_a = \boldsymbol{v}_a = \boldsymbol{0}, \tag{I.12}$$

(see Figure 5.3). The tangential material line vector, $\boldsymbol{T}$, does not allow for rotation and stretching. This gives the nodal deformation gradient, $\boldsymbol{F}_a$, to be corrected as

$$\boldsymbol{F}_a \longleftarrow \boldsymbol{F}_a - \underbrace{(\boldsymbol{N}\cdot\boldsymbol{F}_a\boldsymbol{T})\boldsymbol{N}\otimes\boldsymbol{T}}_{\text{rotation}} + \underbrace{(1-\boldsymbol{T}\cdot\boldsymbol{F}_a\boldsymbol{T})\boldsymbol{T}\otimes\boldsymbol{T}}_{\text{stretching}}, \tag{I.13}$$

where $\boldsymbol{T}$ is perpendicular to $\boldsymbol{N}$ such that $\boldsymbol{T}\cdot\boldsymbol{N} = 0$. No modification is made to the first Piola-Kirchhoff stress due to the fact that $\boldsymbol{P}_a = \boldsymbol{P}(\boldsymbol{F}_a)$.

I.3.2 Sliding Surface Case

For sliding surface case (see Figure 5.4), it is essential to observe that the velocity only slips over the tangent plane. Mathematically, this condition reveals that

$$\boldsymbol{p}_a \longleftarrow (\boldsymbol{I} - \boldsymbol{N}\otimes\boldsymbol{N})\boldsymbol{p}_a. \tag{I.14}$$

Here, $(\boldsymbol{I} - \boldsymbol{N} \otimes \boldsymbol{N})$ projects the nodal linear momentum, $\boldsymbol{p}_a$, onto the plane orthogonal to $\boldsymbol{N}$; that is, $(\boldsymbol{I} - \boldsymbol{N} \otimes \boldsymbol{N}) = (\boldsymbol{T} \otimes \boldsymbol{T})$. This boundary case restricts the rotation of material line vector, $\boldsymbol{T}$, and gives

$$\boldsymbol{F}_a \longleftarrow \boldsymbol{F}_a - (\boldsymbol{N} \cdot \boldsymbol{F}_a \boldsymbol{T}) \boldsymbol{N} \otimes \boldsymbol{T}. \tag{I.15}$$

Consequently, the first Piola-Kirchhoff stress tensor can be computed by using an appropriate constitutive relationship, $\boldsymbol{P}_a = \boldsymbol{P}(\boldsymbol{F}_a)$.

I.3.3 Free Surface Case

In this case, no correction is made to the linear momentum vector (see Figure 5.5). However, the first Piola-Kirchhoff stress tensor has to be corrected such that the traction vector at the boundary node is in equilibrium with the applied traction vector $\boldsymbol{t}^B$:

$$\boldsymbol{P}_a \longleftarrow \boldsymbol{P}_a + (t_t^B - \boldsymbol{t} \cdot \boldsymbol{P}_a \boldsymbol{N}) \boldsymbol{t} \otimes \boldsymbol{N} + (t_n^B - \boldsymbol{n} \cdot \boldsymbol{P}_a \boldsymbol{N}) \boldsymbol{n} \otimes \boldsymbol{N}, \tag{I.16}$$

where $t_n^B = \boldsymbol{t}^B \cdot \boldsymbol{n}$ and $t_t^B = \boldsymbol{t}^B \cdot \boldsymbol{t}$. Note that $(\boldsymbol{t} \cdot \boldsymbol{n})$ vanishes due to the fact that their directions are perpendicular to each other; that is, $\boldsymbol{n} \perp \boldsymbol{t}$. For simplicity, the correction on the nodal deformation gradient, $\boldsymbol{F}_a$, is not being carried out (since it requires the Newton-Raphson iterative process) due to computational inefficiency (see Appendix F).

Appendix J

Finite Element Shape Functions

J.1 Gradient of a Shape Function

This appendix will derive the gradient of a shape function at centroid of cell e from neighbouring node a, $\boldsymbol{\nabla}_0 \hat{N}_a^e$ where $e \in a$ and $\boldsymbol{\nabla}_0 \equiv \partial/\partial \boldsymbol{X}$. For this purpose, it is convenient to introduce the shape function stated in parent coordinates $\boldsymbol{\xi}$ as [7]

$$\boldsymbol{\nabla}_0 \hat{N}_a^e(\boldsymbol{X}) = \left(\frac{\partial \boldsymbol{X}}{\partial \boldsymbol{\xi}}\right)^{-T} \boldsymbol{\nabla}_{\boldsymbol{\xi}} \hat{N}_a^e(\boldsymbol{\xi}); \qquad e \in a, \tag{J.1}$$

where $\boldsymbol{\nabla}_{\boldsymbol{\xi}} \equiv \partial/\partial \boldsymbol{\xi}$.[1] The derivative of material coordinates with respect to parent coordinates (also known as Jacobian matrix) is typically expressed by

$$\frac{\partial \boldsymbol{X}}{\partial \boldsymbol{\xi}} = \sum_{\substack{a=1 \\ a \in e}}^{Nn_e} \boldsymbol{X}_a \otimes \boldsymbol{\nabla}_{\boldsymbol{\xi}} \hat{N}_a^e, \tag{J.2}$$

where Nn_e denotes the total number of nodes that belong to a given cell e.

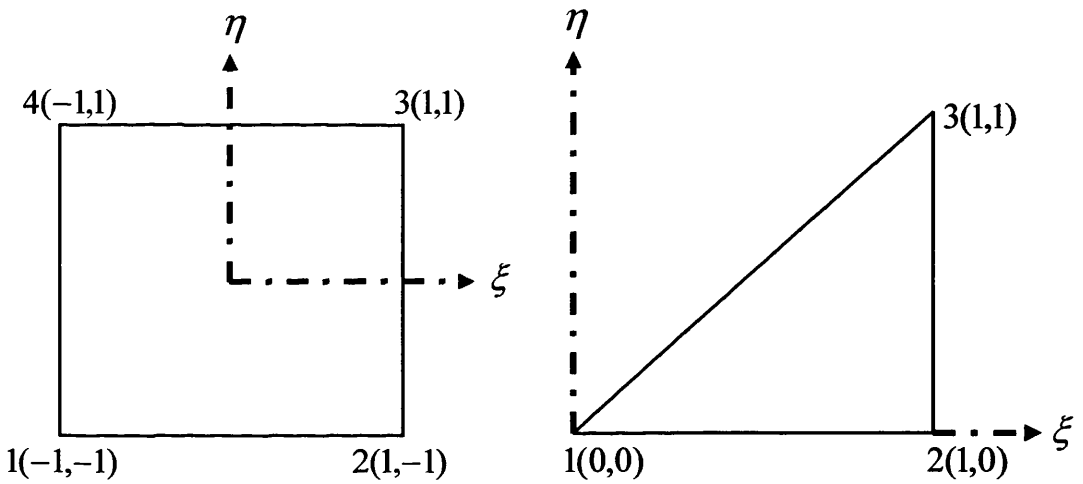

Figure J.1: Two dimensional isoparametric linear shape functions: (a) Quadrilateral mesh; and (b) Triangular mesh.

J.1.1 Quadrilateral Mesh

The shape function in parametric coordinates is written as

$$\hat{N}_a = \frac{1}{4}(1 + \xi_a \xi)(1 + \eta_a \eta), \tag{J.3}$$

and its derivatives are

$$\nabla_{\xi} \hat{N}_a = \frac{1}{4}\xi_a(1 + \eta_a \eta); \qquad \nabla_{\eta} \hat{N}_a = \frac{1}{4}\eta_a(1 + \xi_a \xi), \tag{J.4}$$

[1] Shape functions in parent coordinates are clearly discussed in [38, 82, 107, 145, 174].

$\forall a = 1, 2, 3, 4$ (see Figure J.1a). Note that the gradient of the shape function is computed at the centroid of cell e, that is the origin of the parametric coordinates $(\xi = 0, \eta = 0)$, which can be concluded as

$$\nabla_0 \hat{N}_a^{NE} = \begin{pmatrix} -1/(2\Delta x) \\ -1/(2\Delta y) \end{pmatrix}; \qquad \nabla_0 \hat{N}_a^{NW} = \begin{pmatrix} 1/(2\Delta x) \\ -1/(2\Delta y) \end{pmatrix}; \tag{J.5}$$

and

$$\nabla_0 \hat{N}_a^{SW} = \begin{pmatrix} 1/(2\Delta x) \\ 1/(2\Delta y) \end{pmatrix}; \qquad \nabla_0 \hat{N}_a^{SE} = \begin{pmatrix} -1/(2\Delta x) \\ 1/(2\Delta y) \end{pmatrix}. \tag{J.6}$$

J.1.2 Triangular Mesh

It is well known that shape functions of linear triangle are defined by (see Figure J.1b)

$$\hat{N}_1 = 1 - \xi, \qquad \hat{N}_2 = \xi - \eta, \qquad \hat{N}_3 = \eta. \tag{J.7}$$

Their derivatives can be easily obtained as

$$\nabla_{\boldsymbol{\xi}} \hat{N}_1 = \begin{pmatrix} -1 \\ 0 \end{pmatrix}, \qquad \nabla_{\boldsymbol{\xi}} \hat{N}_2 = \begin{pmatrix} 1 \\ -1 \end{pmatrix}, \qquad \nabla_{\boldsymbol{\xi}} \hat{N}_3 = \begin{pmatrix} 0 \\ 1 \end{pmatrix}. \tag{J.8}$$

As usual, it is now necessary to evaluate the transformation (or Jacobian) matrix, $\partial \boldsymbol{X}/\partial \boldsymbol{\xi}$, in preparation for the development of the material gradient of an interpolating function. To this end, $\nabla_0 \hat{N}_a^e$ are summarised as follows:

$$\nabla_0 \hat{N}_a^{NW} = \begin{pmatrix} 1/\Delta x \\ -1/\Delta y \end{pmatrix}; \qquad \nabla_0 \hat{N}_a^{NN} = \begin{pmatrix} 0 \\ -1/\Delta y \end{pmatrix}; \qquad \nabla_0 \hat{N}_a^{NE} = \begin{pmatrix} -1/\Delta x \\ 0 \end{pmatrix}; \tag{J.9}$$

and

$$\nabla_0 \hat{N}_a^{SW} = \begin{pmatrix} 1/\Delta x \\ 0 \end{pmatrix}; \qquad \nabla_0 \hat{N}_a^{SS} = \begin{pmatrix} 0 \\ 1/\Delta y \end{pmatrix}; \qquad \nabla_0 \hat{N}_a^{SE} = \begin{pmatrix} -1/\Delta x \\ 1/\Delta y \end{pmatrix}. \tag{J.10}$$

Graphical representation is depicted in Figure 7.2b.

Part VII

References

Bibliography

[1] L.E. Malvern, *Introduction to the mechanics of a continuous medium.* Prentice-Hall, 1969.

[2] J. Simo and T. Hughes, *Computational inelasticity.* 1998.

[3] G. Holzapfel, *Nonlinear solid mechanics: a continuum approach for engineering.* Wiley and Sons, 2000.

[4] Y. Fung and P. Tong, *Classical and computational solid mechanics.* World Scientific, 2001.

[5] J. Lubliner, *Plasticity theory.* Dover Publication(reprinted), 2008.

[6] E. S. Neto, D. Perić, and D. Owen, *Computational methods for plasticity: theory and applications.* John Wiley and Sons, 2008.

[7] J. Bonet and R. Wood, *Nonlinear continuum mechanics for finite element analysis.* 2 ed., 2008.

[8] S. Timoshenko and J. Goodier, *Theory of elasticity.* McGraw-hill, 1970.

[9] L. Felton and R. Nelson, *Matrix structural analysis.* John Wiley and Sons, 1997.

[10] O. Zienkiewicz and R. Taylor, *The finite element method : solid mechanics*, vol. 2. Butterworth-Heinemann, 5 ed., 2000.

[11] R. Hibbeler, *Structural analysis.* Prentice-Hall, 6 ed., 2002.

[12] D. Schodek, *Structures.* Prentice-Hall, 4 ed., 2000.

[13] M. E. Gurtin, *An introduction to continuum mechanics.* Academic Press, 1981.

[14] G. Backus, *Continuum mechanics.* Samizdat Press, 1997.

[15] G. Mase and G. Mase, *Continuum mechanics for engineers.* CRC, 2 ed., 1999.

[16] S. Nair, *Introduction to continuum mechanics.* Cambridge University Press, 2009.

[17] O. Zienkiewicz, J. Rojek, R. Taylor, and M. Pastor, "Triangles and tetrahedra in explicit dynamic codes for solids," *International Journal for Numerical Methods in Engineering*, vol. 43, pp. 565–583, 1998.

[165] Pijaudier, G. Cabot, L. Bode, and A. Huerta, "Arbitrary eulerian lagrangian finite element analysis of strain localization in transient problems," *International Journal for Numerical Methods in Engineering*, vol. 38, pp. 4171–4191, 1995.

[166] M. Papadrakakis, G. Babilis, and P. Braouzi, "Efficiency of refinement procedures for the p-version of the adaptive finite element method," *Engineering Computations*, vol. 14, pp. 98–118, 1997.

[167] G. Georgi and R. Silverman, *Linear algebra.* Dover Publications, 1977.

[168] H. Schneider and G. P. Barker, *Matrices and linear algebra.* Dover Publications, 1973.

[169] J. Heinbockel, *Introduction to tensor calculus and continuum mechanics.* Trafford, 2001.

[170] Y. Fung, *A first course in continuum mechanics: for physical and biological engineers and scientists.* Prentice Hall, Englewood Cliffs, New Jersey, 3 ed., 1994.

[171] B. Boley and J. Weiner, *Theory of thermal stresses.* Dover Publications, 1997.

[172] N. Newmark, "A method of computation for structural dynamics," *Journal of Engineerign Mechanics Division*, vol. 85, pp. 67–94, 1959.

[173] A. K. Izian, *Two-step taylor galerkin formulation for explicit solid dynamics large strains problems.* PhD thesis, Swansea University, 2011.

[174] D. Henwood and J. Bonet, *Finite elements: a gentle introduction.* Palgrave Macmillan, 1997.